Carbon nanotubes and boron nitride nanotubes under high pressure

Silvio Domingos Silva Santos

To cite this version:

Silvio Domingos Silva Santos. Carbon nanotubes and boron nitride nanotubes under high pressure. Other [cond-mat.other]. Université de Lyon, 2017. English. NNT : 2017LYSE1286 . tel-01771200

HAL Id: tel-01771200

https://theses.hal.science/tel-01771200v1

Submitted on 19 Apr 2018

N° d'ordre NNT : 2017LYSE1286

THÈSE DE DOCTORAT DE L'UNIVERSITÉ DE LYON
opérée au sein de
l'Université Claude Bernard Lyon 1

École Doctorale ED52
PHYSIQUE ET ASTROPHYSIQUE DE LYON (PHAST)

Spécialité de doctorat : Physique

Soutenue publiquement le 14/12/2017, par :
Silvio Domingos SILVA SANTOS

Nanotubes de carbone et de nitrure de bore sous haute pression

---

Devant le jury composé de :

M. Laurent Alvarez, Maître de Conférences, Université de Montpellier	Rapporteur
M. Pascal Puech, Maître de Conférences, Université Paul Sabatier	Rapporteur
Mme. Nedjma Bendiab, Maître de Conférences, Université Grenoble Alpes	Examinatrice
M. David Dunstan, Professeur, Queen Mary University of London	Examinateur
Mme. Catherine Journet, Professeure, Université Lyon 1	Examinatrice
Mme. Vittoria Pischedda, Maître de Conférences, Université Lyon 1	Examinatrice
M. Antonio Gomes de Souza Filho, Professeur, Université Fédérale du Ceará	Examinateur
M. Alfonso San Miguel, Professeur, Université Lyon 1	Directeur de thèse

N° d'ordre NNT : xxx

DOCTORAL THESIS OF UNIVERSITÉ DE LYON
submitted to
Université Claude Bernard Lyon 1

Doctoral School ED52
PHYSICS AND ASTROPHYSICS OF LYON (PHAST)

for the degree of
Doctor of Sciences

presented at 14/12/2017, by :
Silvio Domingos SILVA SANTOS

Carbon nanotubes and boron nitride nanotubes under high pressure

---

Doctoral Committee :

M. Laurent Alvarez, Maître de Conférences, Université de Montpellier	Referee
M. Pascal Puech, Maître de Conférences, Université Paul Sabatier	Referee
Mme. Nedjma Bendiab, Maître de Conférences, Université Grenoble Alpes	Co-referee
M. David Dunstan, Professeur, Queen Mary University of London	Co-referee
Mme. Catherine Journet, Professeure, Université Lyon 1	Co-referee
Mme. Vittoria Pischedda, Maître de Conférences, Université Lyon 1	Co-referee
M. Antonio Gomes de Souza Filho, Professeur, Université Fédérale du Ceará	Co-referee
M. Alfonso San Miguel, Professeur, Université Lyon 1	PhD supervisor

Acknowledgements

This thesis work was done at Université Claude Bernard Lyon 1, Institut Lumière Matière with the financial support of the Conselho Nacional de Desenvolvimento Científico e Tecnológico (CNPq) from the brazilian scientific program “science without borders”.

I would like to express my deepest gratitude to my PhD supervisor Prof. Alfonso San Miguel for his fundamental guidance, his wise advices and his invaluable support throughout of this thesis work.

I would like to thank also:

PhD co-supervisor Denis Machon for the discussions on various theoretical aspects of thesis.

Prof. Catherine Journet, for her fundamental collaboration in the boron nitride nanotubes research work.

Franck Legrand, Sylvie Le Floch and Régis Debord, for their help on various engineering and theoretical issues.

Prof. David Dunstan, for many interesting discussions and for the collaboration in the DAC helium loading project.

Nicholas Blanchard, for his support with transmission electron microscopy characterizations of carbon nanotubes systems.

Rémy Fulcrand, for the support on Focused Ion Beam equipment to develop new devices.

Rafael Silva Alencar, Aude Stolz and Colin Bousige, Antonio Gomes for collaboration in different parts of this thesis. Even if not included in this thesis, I would like to express my gratitude to collaborators with whom I have been interacting for other research projects:

- Patrick Weisbecker (†) and Gerard Vignoles from the LCT and University of Bordeaux and Geeth Manthilake from the LMV of Clermont-Ferrand in the study of pyrocarbons at high pressures.
- Fabio Medeghini, Paolo Maioli, Fabrice Valée, Mike Hettich and Natalia del Fatti in the development of Spatial Modulation Spectroscopy (SMS) at high pressure.

I would like also to thank:

all technicians, the administrative staff and lab directors of Institut Lumière Matière for providing a favorable environment to develop this work.

I am grateful also to:

Abraão Cefas Torres-Dias, Ashwani Tripathi, Yang Wang, Tung To, Wenwen Cui, Jingming Shi, Cassandre Miralaei, Alexis Forestier and those who my memory does fails to remember, for their friendship.

Lastly but not less important, I would like to present my greatest thanks to my family, Maria Emi Silva Beltrão, Carolina Costa Moda Beltrão, my parents Maria Salvelina Silva Santos, Carlos Roberto de Lima Santos, my brother Carlos Matheus Silva Santos (including, his daughter and wife) and all from the Beltrão and Silva families for their continuous support even far, love and understanding.

Contents

Introduction **11**

1 Basic concepts of carbon nanotubes and boron nitrite nanotubes **15**

1.1 Carbon nanotubes . . . 16

1.1.1 General aspects . . . 16

1.1.2 Geomectric structure . . . 16

1.1.2.1 Nanotube reciprocal lattice . . . 19

1.1.3 Electronic structure . . . 20

1.1.3.1 Tight-binding model and zone-folding method . . . 21

1.1.3.2 Density of states . . . 23

1.1.3.3 Kataura plot . . . 25

1.2 Phonons modes of carbon nanotubes . . . 26

1.2.1 Raman spectroscopy of carbon nanotubes . . . 27

1.2.2 Radial breathing mode (RBM) . . . 28

1.2.3 Tangential modes–G band . . . 28

1.3 Carbon nanotubes under high pressure . . . 29

1.4 Specific aspects of BN nanotubes . . . 35

1.4.1 Electronic structure of BN nanotubes . . . 36

1.4.2 Phonon structure of BN nanotubes . . . 38

1.4.3 Raman spectroscopy of BN nanotubes . . . 39

2 Synthesis methods of carbon nanotubes and experimental methodology **42**

2.1 Introduction . . . 43

2.2 Synthesis methods . . . 43

2.2.1 Electric arc-discharge . . . 43

2.2.2 Laser ablation . . . 44

2.2.3 Chemical vapour deposition-CVD . . . 45

2.3 Experimental methods . . . 46

2.3.1 High pressure technique . . . 46

2.3.2 Transmission electron microscope . . . 48

2.4 Experimental setup for Raman spectroscopy and TEM . . . 51

2.4.1 Theoretical Basis of Raman Scattering . . . 51

2.4.2 Raman at high pressure . . . 55

2.5 Transmission electron microscopes . . . 58

3 (6,5)-Enriched single walled carbon nanotubes at high pressure **61**

3.1 Introduction . . . 62

3.2 Sample preparation. Aqueous Two-Phase (ATP) separation method . . . 62

3.2.1 (6,5) SWCNTs enrichment . . . 63

3.3 High pressure study. Results and discussion 66
    3.3.1 Radial breathing modes - RBM 70
    3.3.2 Tangential modes - G bands 77
    3.3.3 Reversibility limits of (6,5) SWCNTs 80
    3.3.4 Conclusions 85

4 Triple walled carbon nanotubes at high pressure **87**
4.1 Introduction 88
4.2 Triple walled carbon nanotubes 88
    4.2.1 TWCNTs synthesis 88
    4.2.2 General aspects and previous works 89
    4.2.3 Results and discussion 90
        4.2.3.1 Radial breathing modes analysis 91
        4.2.3.2 Tangential modes - G band analysis 95
        4.2.3.3 Pressure-induced nanotubes irreversibility and unzipping 99
    4.2.4 Conclusions 102

5 Boron nitride multiwalled nanotubes under high pressures **105**
5.1 Introduction 106
5.2 Boron nitride multiwalled nanotubes 106
    5.2.1 Synthesis 106
    5.2.2 General aspects and previous work 107
    5.2.3 Results and discussion 109
    5.2.4 Conclusions 117

General conclusion **119**

Annexes **123**

A Suplementary information of the Chapter 2 **124**
A.1 Experiments of Raman spectroscopy 124
    A.1.1 SWCNTs 124
    A.1.2 TWCNTs 124
    A.1.3 Boron nitride multiwalled nanotubes 125
A.2 Experiments of transmission electron microscopy 125
    A.2.1 SWCNTs 125
    A.2.2 TWCNTs 126
    A.2.3 BNMWNTs 126

Bibliography **143**

Introduction

Materials based on carbon (carbonaceous materials) have the capability to form different bondings schemes, thus a wide families of allotropes are possible. This is the case of fullerenes (0D), carbon nanotubes (1D), graphene (2D) or diamond (3D), among many others. Each one of these carbon forms need specific synthesis conditions (thermodynamics) in which pressure and temperature are key parameters. Due to the peculiar bond ”flexibility” feature of the carbon atom, in the last decades the scientific community has payed great attention to investigate the elaboration of novel carbon materials, leading to new discoveries as well as new technologies. Between, the more investigated materials are fullerenes,carbon nanotubes or graphene.

Fullerenes were discovered in 1985 by Kroto, Heath, O’Brien, Curl and Smalley [1] (Kroto, Curl and Smalley were laureated with the Chemistry Nobel prize in 1996). Shortly thereafter in 1991, Iijima in a pioneer work (even if other observations of carbon nanotubes took place earlier) suggested a new carbon structure, in which graphite sheets should be enrolled up in cylindrical fashion (helical microtubes), better known now as multi wall carbon nanotubes (MWCNTs) [2]. Two years after the MWCNTs model was introduced independently by Iijima et al. [3] *et al.* and Bethune *et al.* [4] who reported the first experimental evidence of single wall carbon nanotubes (SWCNTs). Soon after the first production in scale enough for handling, carbon nanotubes became of great interest for the scientific community, in particular due to the possibility for many different applications. In fact, carbon nanotube showed a number of exceptional and promising properties, as for instance, high mechanical stability (high Young’s modulus values ranging from GPa to TPa, for radial and axial directions, respectively), unique optical and electronic characteristics, high chemical stability or efficient thermal conductivity [5, 6, 7]. Graphene isolation was obtained only in 2004 by Novoselov and Geim via the mechanical exfoliation method [8]. Nowadays a lot of progress has been done in the understanding of graphene properties which is particularly relevant both from a fundamental and applied point of view to understand the proprieties of many other carbonaceous systems.

Fullerenes, nanotubes or graphene are nano-systems or nanoscale materials. The properties of matter at the nanoscale can strongly differ from those of bulk bringing new insights in the material science for applications. From a fundamental point of view to understand how the physical properties of the nanosystem depended on its size or its geometry is one of the most challenging questions. This is in particular true in the case for carbon or BN nanotubes in which - due to their 1D nature - their nanometer scale size is characterized by a single number: their diameter. The low dimensionality, sp^2 hybridization associated to the tubular geometry of carbon nanotubes give them the capability to investigate confined molecular systems. This is a particularly exciting subject with a potential for a major control in terms of nanostructuration engineering (nanofluidic applications [9] for instance). Insertion of water or fullerenes has revealed the potential for different geometrical configurations, as well as change their initial properties [10]. At the same time in high pressure experiments there is the potential of the inner invasion of the pressure transmitting medium which will strongly modify the pressure response. In any case, applying pressure means bringing atoms or molecules closer to the studied object and a possible enhancement of chemical or mechanical interactions associated to the proximity of this environment with the surface of a bulk material. Some studies have presented such effects as important and others as not having much effect on the measured properties. Clearly this needs clarification.

There have been deployed very important efforts to understand the mechanical response of carbon nanotubes under uniaxial stress. Also some research groups in the world have been working to understand the response of carbon nanotubes to radial deformation including due to effect of high pressure application. In that way, the radial mechanical stability at high pressure of carbon nanotubes has been investigated through theoretical means as well as experimental methods which include optical spectroscopies (absorption, photoluminescence), X-ray or neutron diffraction and particularly Raman spectroscopy. In fact, the studies in literature using this combination have demonstrated that the environment and filling have influence on the mechanical response of nanotubes under pressure.

Today, the scientific community agrees on the existence of a radial instability of carbon nanotubes which has been well characterized in single wall carbon nanotubes. This so called collapse process takes place at a pressure which is in general inversely dependent on the nanotube diameter, d with most works pointing ot a d^{-3} dependence for tubes having a diameter of $d > 1nm$. Nevertheless we do not have a complete view on the collapse of lower diameter tubes, the dependence of the collapse process with the number of walls or how the atomic nature of the tubes. This PhD thesis is placed in that context and tries to provide new elements to clarify how the mechanical stability of nanotubes under cold compression can depend on geometrical parameter as its size, but also to the number of walls of the tube or even its atomic nature (carbon versus BN nanotubes).

The interplay between nanometer-scale physical effects and environment effects in high pressure experiments is probably at the origin of many of the contradictions, confusions and difficulties of interpretation. We will try to take this into account in all the different parts of this thesis work.

The PhD manuscript is organized in 5 chapters followed by general conclusions. The first two chapters are devoted to contextualize the study, while the next 3 chapters concentrate on the experimental results obtained in the study of the three systems of the thesis: chirality enriched SWCNTs, triple-wall carbon nanotubes (TWCNTs) and boron nitride multi-wall nanotubes (BNMWTs).

Chapter 1 is an introduction to the structure and physical properties of carbon nanotubes. In this chapter is first introduced the geometrical description of carbon nanoutubes in direct and reciprocal space, their electronic structure and their dynamics (phonos). In a second part of the chapter a bibliographic survey on the high pressure properties of carbon nanotubes is introduced. Finally the chapter concludes, without entering into much detail, with a short introduction to the specific aspects of BN nanotubes

In Chapter 2 the experimental aspects of the synthesis of carbon nanotubes and the experimental methodology used in the thesis are presented. Even if this thesis work does not include any nanotube synthesis aspect, they are so important to define the tubes characteristics, radial distribution or presence of impurities, that we have made a short presentation of the main methods of carbon nanotubes elaboration. We then present the different experimental methods which have been used in the thesis work: high pressure techniques, transmission electron microscopy

(TEM) and Raman spectroscopy. Finally, the experimental details of TEM and Raman at high pressure used in the three systems (SWCNTs, TWCNTs and BNMWNTs).

Chapters 3 to 5 constitute the core of results of the thesis in which is explored the effect on the radial stability with pressure or the integrity of nanotubes considering the size or chirality (Chapter 3), number of walls (Chapter 4) or nature of the tubes (Chapter 5). In all cases the combination of in situ Raman spectroscopy at high pressure and ex situ characterization of samples after pressure cycles up to pressures in some cases of 80 GPa has been essential to drive our main conclusions. In all these 3 Chapters we have included a specific section to precise the elaboration method of the samples, the analysis and results from the radial breathing modes (RBMs), the analysis and results form the tangencial modes (TMs) and the irreversibly aspects in which the TEM analysis has played an important role. Only for the case of the BNMWNTs the RBM section is absent as such signal is not detected in BNMWNTs. All these Chapters include an Introduction and a Conclusion sections trying to summarize the main conclusions.

The General conclusion tries to summarize the main findings of this thesis work confronting the results of the different chapters to try to derive some general ideas. Finally, some annex and a bibliography complete the work. Overall, we have tried to modestly contribute to a better understanding of the mechanical stability and the pressure response of nanotubes, a rich family of fascinating nano-objects.

1

Basic concepts of carbon nanotubes and boron nitrite nanotubes

Sommaire :

1.1 Carbon nanotubes 16
  - 1.1.1 General aspects 16
  - 1.1.2 Geomectric structure 16
    - 1.1.2.1 Nanotube reciprocal lattice 19
  - 1.1.3 Electronic structure 20
    - 1.1.3.1 Tight-binding model and zone-folding method 21
    - 1.1.3.2 Density of states 23
    - 1.1.3.3 Kataura plot 25

1.2 Phonons modes of carbon nanotubes 26
  - 1.2.1 Raman spectroscopy of carbon nanotubes 27
  - 1.2.2 Radial breathing mode (RBM) 28
  - 1.2.3 Tangential modes–G band 28

1.3 Carbon nanotubes under high pressure 29

1.4 Specific aspects of BN nanotubes 35
  - 1.4.1 Electronic structure of BN nanotubes 36
  - 1.4.2 Phonon structure of BN nanotubes 38
  - 1.4.3 Raman spectroscopy of BN nanotubes 39

1.1 Carbon nanotubes

1.1.1 General aspects

The carbon nanotube structure can be described as an one-atom-thick sheet of carbon arranged in a hexagonal lattice (graphene layer), which is rolled up into a hollow cylindrical shape (Fig. 1.1). This arrangement gives a high length-to-diameter ratio ($> 10^3$) for the carbon nanotubes (CNTs), which in turn form an interesting system class for the study of low-dimensional physics, at the theoretical or experimental levels. The following subsections will address basic concepts of carbon nanotubes, as for instance geometrical and electronic structures, which are important to describe its fundamental properties.

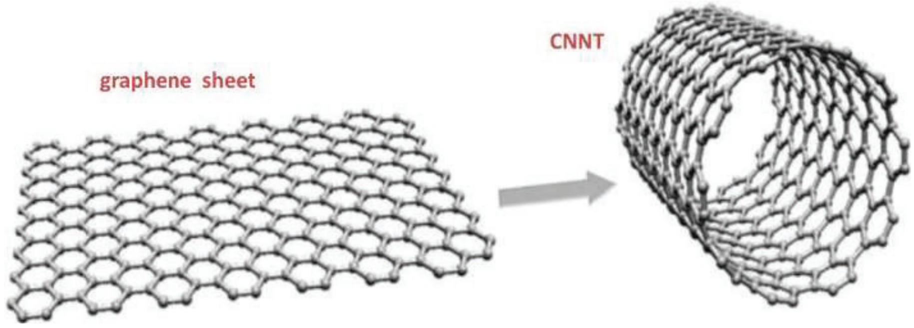

Figure 1.1 – Wrapping of graphene layer to generate CNNT [11].

1.1.2 Geomectric structure

Carbon nanotubes are usually classified according to the cylindrical layers (walls) number that constitute them. Thus, the tubes can be single-, double-, triple- and multiwall carbon nanotubes (SWCNTs, DWCNTs, TWCNTs, and MWCNTs, respectively). In particular, DWCNTs and TWCNTs are special cases of the MWCNTs class.

There are an infinity of possible ways to roll up the graphene layer (bi-dimensional [2D] hexagonal lattice or honeycomb structure), but these seemingly immense rolling up fashions, when studied under a symmetry standpoint show two helical forms, known as achiral (symmorphic) or chiral (non-symmorphic) geometries. The chirality concept is introduced to describe the reflection symmetry between an object and its mirror image, thus *an object is chiral when itself cannot be superimposed on its mirror image* and *achiral if the object is superimposable.* Furthermore, the nanotubes achiral geometry can be grouped in two types, *armchair* or *zigzag*, according to their cross-sections. Comprehension of the chirality notion is an essential key to categorize the physical and electronic properties of CNNTs.

The 2D hexagonal lattice is generated (parametrized) by two primitive vectors, $\vec{a}_1$ and $\vec{a}_2$, which uniquely define the nanotube structure by chiral vector $\vec{C}_h$ (Fig. 1.2), this vector spans the circumference of the cylinder when the graphene sheet is rolled up into a tube. The chiral vector is written as:

$$\vec{C}_h = n\vec{a}_1 + m\vec{a}_2, \tag{1.1}$$

where n and m are integers, related by the inequality $0 \leq m \leq n$. The indexes n and m provide the simplified notation to $\vec{C}_h \equiv (n, m)$. This notation is extensively used to categorize

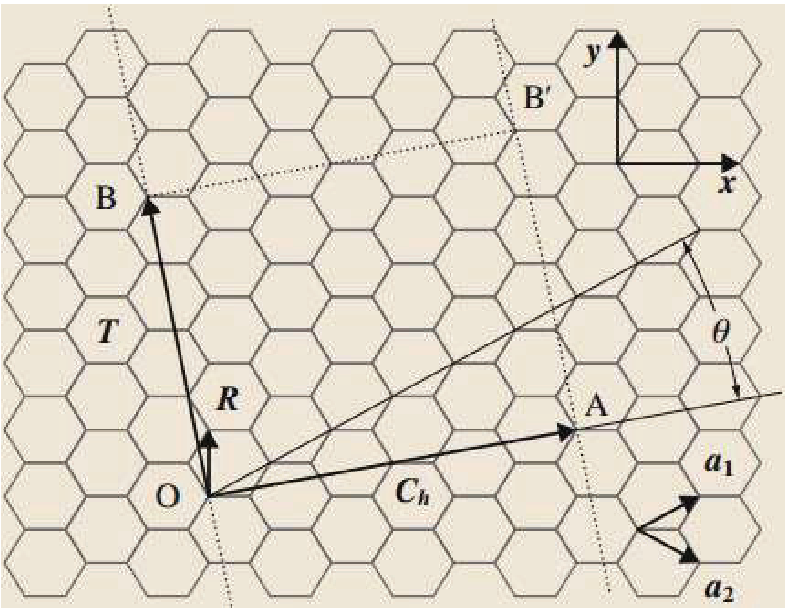

Figure 1.2 – The scheme of an unrolled nanotube unit cell projected on graphene sheet. The figure show the chiral angle θ together with vectors chiral $\vec{C}_h$, translational $\vec{T}$ and the primitive vectors $\vec{a}_1$ and $\vec{a}_2$ of graphene layer. The crystallographically equivalent points (O with A) and (B with $B^{'}$), that overlapping form the nanotube. Adapted from [12].

the nanotube geometry. The other way to characterize the nanotube geometry is by giving its diameter d_t and its chiral angle θ, where both parameters are related to the chiral indexes n and m. Assuming the lattice constant $a = \sqrt{3}a_{C-C} = |\vec{a}_1| = |\vec{a}_2|$ for graphene layer and that $a_{C-C} = 1.42\text{Å}$ carbon bonding length, it can be deduced d_t in function of the circumference length $|\vec{C}_h|$, as follows:

$$\begin{aligned} d_t \equiv \frac{|\vec{C}_h|}{\pi} &= \frac{\sqrt{\vec{C}_h \cdot \vec{C}_h}}{\pi} = \frac{\sqrt{(n\vec{a}_1 + m\vec{a}_2)\cdot(n\vec{a}_1 + m\vec{a}_2)}}{\pi} \\ &= \frac{\sqrt{n^2\vec{a}_1\cdot\vec{a}_1 + 2nm\vec{a}_1\cdot\vec{a}_2 + m^2\vec{a}_2\cdot\vec{a}_2}}{\pi}\,, \end{aligned}$$

where the scalar product $\vec{a}_1 \cdot \vec{a}_2 = |\vec{a}_1||\vec{a}_2|\cos 60° = \frac{a^2}{2}$,

then

$$\boxed{d_t = \frac{a}{\pi}\sqrt{n^2 + nm + m^2}\ ;\ \ |\vec{C}_h| = a\sqrt{n^2 + nm + m^2}} \tag{1.2}$$

The chiral angle θ defines the $\vec{C}_h$ orientation in relation to the primitive vector $\vec{a}_1$ Fig. 1.2, then considering eqs. 1.1, 1.2 and the inner product $\vec{C}_h \cdot \vec{a}_1$, follows that

$$\begin{aligned} \vec{C}_h \cdot \vec{a}_1 &= |\vec{C}_h||\vec{a}_1|\cos\theta \\ (n\vec{a}_1 + m\vec{a}_2)\cdot\vec{a}_1 &= a\sqrt{n^2 + nm + m^2}a\cos\theta \\ (2n + m)\frac{a^2}{2} &= a^2\sqrt{n^2 + nm + m^2}\cos\theta \\ &\Downarrow \end{aligned}$$

$$\boxed{\cos\theta = \frac{2n + m}{2\sqrt{n^2 + nm + m^2}} \iff \theta = \arccos\left(\frac{2n + m}{2\sqrt{n^2 + nm + m^2}}\right)} \tag{1.3}$$

Due to the sixfold rotational symmetry of the graphene, all CNNTs can be constructed with chiral angles $\theta \leq 60°$ and furthermore, for each tube with $0° \leq \theta \leq 30°$ an equivalent tube

$30° \leq \theta \leq 60°$, but because of the reflection symmetry (chirality) the tube changes from right-handed to left-handed. Therefore, we can restrict our considerations to the case $0° \leq \theta \leq 30°$, corresponding to $0 \leq m \leq n$. And as already aforementioned, the tubes can be classified in 3 groups, based on their chiral angles (see Figure 1.3):

- armchair nanotube (achiral), where $\theta = 30°$ or n = m ,
- zig-zag nanotube (achiral), where $\theta = 0°$ or m = 0 ,
- chiral nanotube, $0° < \theta < 30°$ or $n \neq m$.

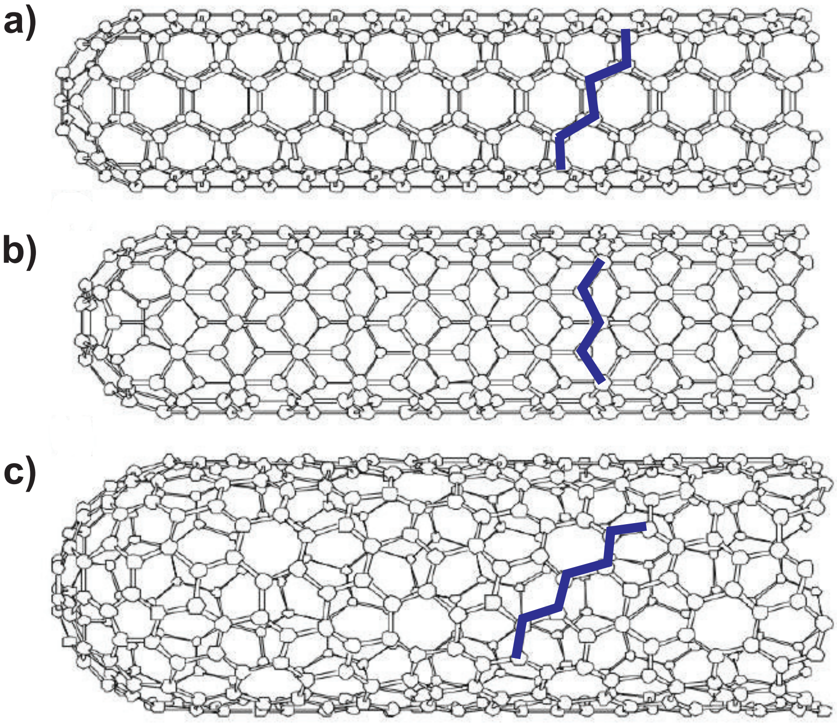

Figure 1.3 – Schematic model for three different groups of single-walled carbon nanotubes. The blue line is a guide to the eyes. a) Armchair. b) Zigzag. c) Chiral [13].

The nanotube unit cell unrolled on honeycomb lattice forms a rectangular area bounded by vector $\vec{C}_h$ and translational symmetry vector $\vec{T}$ (Fig. 1.2). The vector $\vec{T}$ is collinear to the tube axis and perpendicular to $\vec{C}_h$. Besides it links the nearest two equivalent atoms in this direction. We can express $\vec{T}$ in function of vectors $\vec{a}_1$ and $\vec{a}_2$, as

$$\vec{T} = t_1\vec{a}_1 + t_2\vec{a}_2 \equiv (t_1, t_2) \tag{1.4}$$

In order to express t_1 and t_2 based on indexes (n, m), it should be noted that due to definition $\vec{C}_h \perp \vec{T}$, the inner product $\vec{C}_h \cdot \vec{T} = 0$ and that also leads to the fact that the greatest common divisor (gdc) of the integers (t_1, t_2) is equal to one, that is gdc(t_1, t_2) = 1. Otherwise, if t_1 and t_2 were multiple with each other, the perpendicularity property would be unsatisfied. Then, by eqs. 1.1, 1.4 and with $0 \leq m \leq n$, we have

$$\begin{aligned} \vec{C}_h \cdot \vec{T} &= 0 \\ nt_1a^2 + nt_2\frac{a^2}{2} + mt_1\frac{a^2}{2} + mt_2a^2 &= 0 \\ t_1(2n+m) + t_2(2m+n) = 0 &\implies t_1 = -t_2\frac{(2m+n)}{(2n+m)} \text{ or } t_2 = -t_1\frac{(2n+m)}{(2m+n)} , \quad (1.5) \end{aligned}$$

tanking in account that $\forall a, b$ integers $gdc(-a, b) = gdc(a, -b) = gdc(-a, -b) = gdc(a, b)$, follows

$$\begin{aligned} gdc(t_1, t_2) &= gdc\left(-t_2\frac{(2m+n)}{(2n+m)}, t_2\right) = gdc\left(-t_2\frac{(2m+n)}{(2n+m)}, -t_2\overbrace{\frac{(2n+m)}{(2n+m)}}^{1}\right) \\ &= -\frac{t_2}{2n+m}\overbrace{gdc(2m+n, 2n+m)}^{=d_R} = 1 \implies \boxed{t_2 = -\frac{2n+m}{d_R}} \quad (1.6) \end{aligned}$$

by substituting eq.1.6 in eq.1.5,

$$t_1 = -t_2\frac{(2m+n)}{(2n+m)} \implies \boxed{t_1 = \frac{2m+n}{d_R}} \quad (1.7)$$

The calculation of the number of hexagons contained in unit cell can be obtained by unit cell area divided by graphene unit cell:

$$N = \frac{\left|\vec{C}_h \times \vec{T}\right|}{|\vec{a}_1 \times \vec{a}_2|} = \frac{2(n^2 + mn + m^2)}{d_R} , \quad (1.8)$$

with N corresponding to the hexagons number inside of the nanotube unit cell projected on graphene. Knowing that each graphene unit cell contains two equivalent carbon atoms, we can deduce that in this nanotube unit cell there will be 2N carbon atoms.

1.1.2.1 Nanotube reciprocal lattice

The reciprocal lattice of graphene can be constructed by the orthogonal relation,

$$\vec{a}_i \cdot \vec{b}_j = 2\pi\delta_{ij} . \quad (1.9)$$

Writing the primitive vectors $\vec{a}_1$ and $\vec{a}_2$ of the hexagonal lattice in Cartesian coordinates, we have

$$\begin{aligned} \vec{a}_1 &= a\cos 30°\hat{\imath} + a\sin 30°\hat{\jmath} = a\frac{\sqrt{3}}{2}\hat{\imath} + \frac{a}{2}\hat{\jmath} \\ \vec{a}_2 &= a\cos 30°\hat{\imath} - a\sin 30°\hat{\jmath} = a\frac{\sqrt{3}}{2}\hat{\imath} - \frac{a}{2}\hat{\jmath} , \end{aligned}$$

then using the previous expressions together with eq. 1.9, the reciprocal lattice of graphene is given by,

$$\begin{aligned} \vec{b}_1 &= \frac{2\pi}{a\sqrt{3}}\hat{k}_x + \frac{2\pi}{a}\hat{k}_y \\ \vec{b}_2 &= \frac{2\pi}{a\sqrt{3}}\hat{k}_x - \frac{2\pi}{a}\hat{k}_y , \quad (1.10) \end{aligned}$$

where $\vec{b_1}$ and $\vec{b_2}$ are the reciprocal primitive vectors, $\hat{k}_x$ and $\hat{k}_y$ reciprocal space unit vectors (dual basis of the $\boldsymbol{k}$-space or dual space).

The nanotube unit cell projected on the graphene layer is defined by vectors $\vec{C}_h$ and $\vec{T}$ (Fig. 1.2), and the analogous representation for the nanotube on reciprocal lattice of graphene is given by vectors $\vec{K}_1$ and $\vec{K}_2$ (corresponding to $\vec{C}_h$ and $\vec{T}$, respectively) and constructed by relations,

$$\begin{aligned} \vec{C}_h \cdot \vec{K}_1 &= \vec{T} \cdot \vec{K}_2 = 2\pi \quad \text{(normalization)} \\ \vec{C}_h \cdot \vec{K}_2 &= \vec{T} \cdot \vec{K}_1 = 0 \quad \text{(orthogonality).} \end{aligned} \tag{1.11}$$

From the eqs. 1.6, 1.7, 1.8, and 1.11, the vectors $\vec{K}_1$ and $\vec{K}_2$ are expressed by:

$$\vec{K}_1 = \frac{-(t_2\vec{b_1} - t_1\vec{b_2})}{N}, \; \vec{K}_2 = \frac{(m\vec{b_1} - n\vec{b_2})}{N}. \tag{1.12}$$

The modules of the two vectors from eq. 1.12 are given by,

$$\left|\vec{K}_1\right| = \frac{2}{d_t}, \; \left|\vec{K}_2\right| = \frac{2\pi}{\left|\vec{T}\right|}. \tag{1.13}$$

It should be noted that the wave vector $\vec{K}_2$ is collinear with the translational vector $\vec{T}$, and that the collinearity property is also verified between the wave vector $\vec{K}_1$ and the chiral vector $\vec{C}_h$(nanoscale size in this direction), it follows for this correspondence that the nanotube unrolled reciprocal lattice is quantized along the $\vec{K}_1$ direction and is continuous in $\vec{K}_2$ direction.

Then, the vectors $\mu\vec{K}_1$ (with $\mu = 0, \ldots,$ N - 1; $\forall$ N even) form the set of N wave vectors quantized in direction $\vec{K}_1$ of the nanotube unfolded reciprocal lattice. Each one of these N quantized states correspond to a line segment of length $K_2 = \frac{2\pi}{|\vec{T}|}$ in the direction $k\frac{\vec{K}_2}{|\vec{K}_2|}$ (with $-\frac{\pi}{T} < k < \frac{\pi}{T}$), this length corresponds to the 1D first Brillouin zone. Thus, these N line segments constructed from wave vectors $\vec{K}_1$ and $\vec{K}_2$, define parallel equidistant lines (cutting lines) in the unrolled reciprocal lattice of the nanotube. The separation between two neighbor cutting lines is given by the vector $\vec{K}_1$, while the length and orientation of each of these cutting lines is given by $\left|\vec{K}_2\right|$ and $\vec{K}_2$, respectively. It is interesting to note that the vector $\vec{K}_2$ is a reciprocal lattice vector, while $\mu\vec{K}_1$ is not.

1.1.3 Electronic structure

Graphene as well as carbon nanotubes possess sp^2-hybridized electrons (mixing of valence electronic states or atomic orbitals). The carbon atom has two electrons in 1s orbitals (strongly bound to the core) and four valence electrons, occupying the orbitals: $2s, 2p_x, 2p_y, 2p_z$, with the z-axis perpendicular to the carbon hexagonal network. The sp^2 hybridization, the $2s$ and $2p$ orbitals mix form three in-plane covalent bonds σ and σ^* (anti-bonding state), which characterize the binding energy in graphene plane. The out-of-plane orbitals p_z create the delocalized bonds π and π^* (anti-bonding state) which are relevant for the transport properties.

The understanding of the electronic and optical properties of the carbon nanotubes is obtained by knowing the electronic band structure. In order to achieve this aim, firstly is introduced the *tight-binding* (TB) approximation for graphene followed by the zone-folding method of nanotubes.

1.1.3.1 Tight-binding model and zone-folding method

The tight-binding model is an approach to the calculation of the electronic band structure in a periodically-repeating environment (crystalline lattice), using for this purpose a set of Bloch functions, that is by writing a linear combination of lattice atoms wavefunctions, differing on a phase as below,

$$\Phi_i(\vec{k},\vec{r}) = \frac{1}{\sqrt{N}}\sum_{\vec{R_m}} e^{i\vec{k}\cdot\vec{R_m}}\varphi_i(\vec{r}-\vec{R_m}), \quad (i=1,\cdots,n) \tag{1.14}$$

where φ_i denotes the i-th atomic orbital (state or energy level) and $\vec{R_m}$ is the atomic site position in unit cell, moreover for a given $\vec{k}$ there are n Bloch functions.

The eigenfunctions or Bloch wavefunctions in the atomic network can be expressed by a linear combination of Bloch functions as follows,

$$\Psi_i(\vec{k},\vec{r}) = \sum_{i'=1}^{n} C_{ii'}(\vec{k})\Phi_{i'}(\vec{k},\vec{r}), \tag{1.15}$$

where $C_{ii'}$ are coefficient to be determined.

The unit cell of graphene is formed by two distinct carbon atoms A and B (or sublattices), which Bloch orbitals are given by

$$\Phi_A(\vec{k},\vec{r}) = \frac{1}{\sqrt{N}}\sum_{\vec{R_A}} e^{i\vec{k}\cdot\vec{R_A}}\varphi_z(\vec{r}-\vec{R_A}), \tag{1.16}$$

$$\Phi_B(\vec{k},\vec{r}) = \frac{1}{\sqrt{N}}\sum_{\vec{R_B}} e^{i\vec{k}\cdot\vec{R_B}}\varphi_z(\vec{r}-\vec{R_B}), \tag{1.17}$$

with the wavefunctions $\varphi_z(\vec{r}-\vec{R_A})$ and $\varphi_z(\vec{r}-\vec{R_B})$ describing the p_z electrons. In this way, the electronic structure of the graphene π-bands can derived from the Schrödinger equation by substituting the eigenfunctions $\Psi(\vec{k},\vec{r})$ (which are written as a linear combination of Bloch functions of each sublattice eqs. 1.16, 1.17):

$$\begin{aligned} \Psi(\vec{k},\vec{r}) &= \sum_{j=A,B} C_j\Phi_j((\vec{k},\vec{r}) \\ H\Psi(\vec{k},\vec{r}) &= E_g(\vec{k},\vec{r})\Psi(\vec{k},\vec{r}), \end{aligned} \tag{1.18}$$

$$\Downarrow$$

$$H\Big[\overbrace{C_A|\Phi_A(\vec{k},\vec{r})\rangle + C_B|\Phi_B(\vec{k},\vec{r})\rangle}^{=|\Phi\rangle\text{ (Dirac's notation)}}\Big] = E_g(\vec{k},\vec{r})\Big[C_A|\Phi_A(\vec{k},\vec{r})\rangle + C_B|\Phi_B(\vec{k},\vec{r})\rangle\Big], \tag{1.19}$$

and through the multiplication by one of the eigenstates $\langle\Phi_A|$ or $\langle\Phi_B|$ on left side of the eq. 1.19, it follows

$$\begin{Vmatrix} H_{AA}(\vec{k}) - E_g(\vec{k})S_{AA}(\vec{k}) & H_{AB}(\vec{k}) - E_g(\vec{k})S_{AB}(\vec{k}) \\ H_{BA}(\vec{k}) - E_g(\vec{k})S_{BA}(\vec{k}) & H_{BB}(\vec{k}) - E_g(\vec{k})S_{BB}(\vec{k}) \end{Vmatrix} \begin{Vmatrix} C_A(\vec{k},\vec{r}) \\ C_B(\vec{k},\vec{r}) \end{Vmatrix} = 0, \tag{1.20}$$

with the matrix elements given by $H_{ij}(\vec{k}) = \langle\Phi_i|H|\Phi_j\rangle$ and $S_{ij}(\vec{k}) = \langle\Phi_i|\Phi_j\rangle$.

By considering only nearest-neighbor interactions, we have that the carbon atom A(B) interacts with itself and also with the three carbon atoms B(A) in sublattices, thus yielding the Hamilton forms and the overlap matrix elements $H_{AA} = H^{\star}_{BB}$, $H_{AB} = H^{\star}_{BA}$, $S_{AA} = S_{BB}$ and $S_{AB} = S^{\star}_{BA}$

[1]. Using the matrices H and S and solving the characteristic equation 1.20, the eigenvalues $E(\vec{k})$ are given as a function $\omega(\vec{k})$, k_x and k_y:

$$E_g(\vec{k}) = \frac{\epsilon_{2p_z} \pm \gamma\omega(\vec{k})}{1 \pm s\omega(\vec{k})} \tag{1.21}$$

where the + (-) signs in the numerator and denominator provide the bonding π energy band (anti-bonding π^* band), while the function $\omega(\vec{k})$ is given by

$$\omega(\vec{k}) = \sqrt{1 + 4\cos\frac{\sqrt{3}k_x a}{2}\cos\frac{k_y a}{2} + 4\cos^2\frac{k_y a}{2}} \tag{1.22}$$

and with ϵ_{2p_z}, γ and s written as

$$\begin{aligned} \epsilon_{2p_z} &= \langle\varphi_A(\vec{r} - \vec{R_A})|H|\varphi_A(\vec{r} - \vec{R_A})\rangle \\ \gamma &= \langle\varphi_A(\vec{r} - \vec{R_A})|H|\varphi_B(\vec{r} - \vec{R_B})\rangle \\ s &= \langle\varphi_A(\vec{r} - \vec{R_A})|\varphi_B(\vec{r} - \vec{R_B})\rangle. \end{aligned} \tag{1.23}$$

It is worth mentioning that, the valence and conduction bands go through the K- and K$^{'}$-points have the Fermi level (E$_F$) equal to zero. Thus, the expansion of the cosines around these high symmetry points in eq. 1.21 gives

$$E_g^{\pm}(\vec{k} + K) = E_g^{\pm}(\vec{k} + K^{'}) = \pm\frac{\sqrt{3}\gamma_0 a}{2}\sqrt{k_x^2 + k_y^2}, \tag{1.24}$$

which leads to a quasi-linear dispersion of the graphene electronic structure, known as *Dirac cones.* At the K and K$^{'}$ valleys the electrons behave like mass-less particles or Dirac fermions. The band structure of graphene by nearest-neighbor tight-binding approach is shown in Fig.(1.4). After building the energy dispersion relations for graphene, the electronic structure of SWCNTs can be obtained from the ones of graphene. As shown in Subsect. 1.1.2.1, by the periodic boundary conditions $\Big(\Phi(\vec{r} + \vec{C}_h) = \Phi(\vec{r}) \Longleftrightarrow \exp(i\vec{k}\cdot\vec{C}_h) = 1\Big)$ in the direction of the chiral vector $\vec{C}_h$ (along the circumference), the wave vector $\vec{K}_1$ becomes quantized, while along the nanotube axis the wave vector $\vec{K}_2$ associated to the translational $\vec{T}$ remains continuous for the case of tubes with infinite length. Thus in the dual space (reciprocal space of graphene), the wave vectors pair $(\vec{K}_1, \vec{K}_2)$ defines cutting lines one-dimensional that when crossing the graphene conduction and valence bands create the 1D energy subbands of nanotubes and this approximation is so-called of *zone-folding or confinement.* Finally, the 1D energy dispersion relations are expressed as

$$E_\mu(k) = E_g\left(\mu\vec{K}_1 + \frac{k\vec{K}_2}{|\vec{K}_2}|\right),\ (\mu = 0, \cdots, N-1)\,\text{and}\,k \in\,]-\pi/\|\vec{T}\|, \pi/\|\vec{T}\|] \tag{1.25}$$

Near to the K-point or close to the Fermi level, the energy dispersion behaves linearly in first approach, yielding the energy dispersion of subband μ given as

$$E_\mu^{\pm}(k) \approx \pm\frac{\sqrt{3}\gamma_0 a}{2}|\vec{k}_\mu - \vec{k}_F|, \tag{1.26}$$

with $\vec{k}_F$ being the Fermi wave vector.

---

[1] The calculations development and deeper discussions can be seen in Ref. [5, 6]).

The cutting lines behavior close to the Dirac point are essential for nanotubes properties. In other words, the electronic nature of the nanotubes depend on the position of the cutting lines in relation to the K (K') point. So, when one of these lines crosses the graphene Dirac point, the tube is considered metallic. Otherwise, if no line touches the K-point, the tube exhibits a separation between the valence and the conduction bands (energy *gap*) and it is semiconducting. In addition, carbon nanotubes can be classified according to the rule $\nu \equiv n - m(\text{mod}3)$[2], setting thus **nanotube families**

1. $\nu = 0$, metallic (M);
2. $\nu = +1$, semiconducting (SC) of family type I;
3. $\nu = -1$, semiconducting (SC) of family type II.

The armchair nanotubes are always metallic, whereas zig-zag and chiral nanotubes can be semiconducting or metallic. Moreover, the energy dispersion graphs for the SC and M tubes can be calculated from (1.26), showing that the subband indices (μ = 0, ±1,±2,...) of metallic tubes are identical at the Fermi levels from the Dirac points (K and K' valleys). On the other hand, in semiconducting CNTs, the subband quantum numbers closest to E_F are opposite at K and K' valleys.

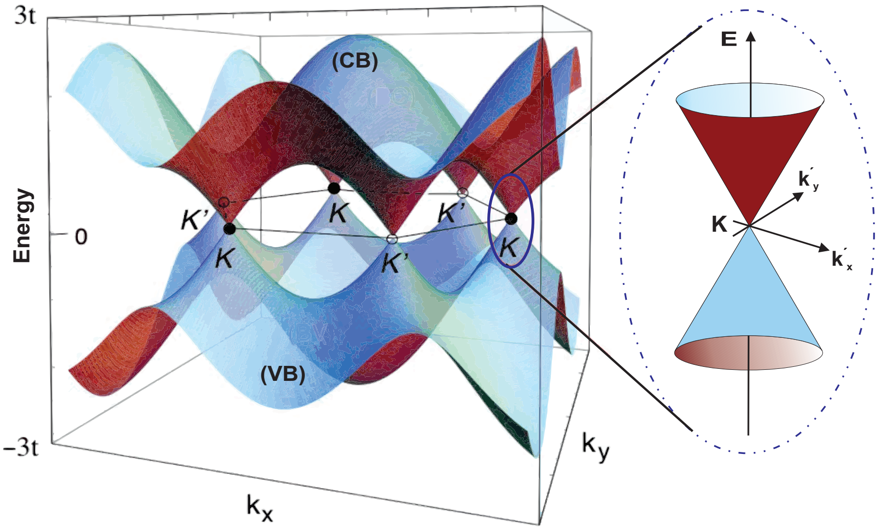

Figure 1.4 – The electronic energy dispersion of graphene (adapted from Ref. [14]).

1.1.3.2 Density of states

An important property related to the energy bands of CNNTs is density of states (DOS), which informs about the density of mobile electrons or holes present in the system. Each of the cutting lines (except for the one that touches the Dirac point) give rise to a local maximum at the valence band (or minimum at the conducting band) in the DOS diagram, known as a 1D *van*

---

[2] In particular, the electronic states are restricted to the wave vectors that fulfill the condition $\vec{k} \cdot \vec{C}_h = 2\pi q$ (q integer) and since the K-point is at $\frac{1}{3}(\vec{b}_1 - \vec{b}_2)$, a nanotube is metallic if $\vec{K} \cdot \vec{C}_h = 2\pi q = \frac{1}{3}(\vec{b}_1 - \vec{b}_2)(n\vec{a}_1 + m\vec{a}_2) = \frac{2\pi}{3}(n - m)$ or $3q = n - m \Rightarrow n \equiv m(\text{mod}\,3)$ Ref. [5].

Hove singularity (VHS). The contribution for energy band with index μ in the density of states is mathematically express as

$$\rho(E) = \frac{2}{N} \sum_{\mu=1}^{N} \int \left[\frac{\partial E_\mu(k)}{\partial k} \right]^{-1} \delta \left[E_\mu(k) - E \right] dk, \tag{1.27}$$

where the factor 2 in the numerator is included due to the spin degeneracy, and N represents the number of pairs of energy dispersion curves.

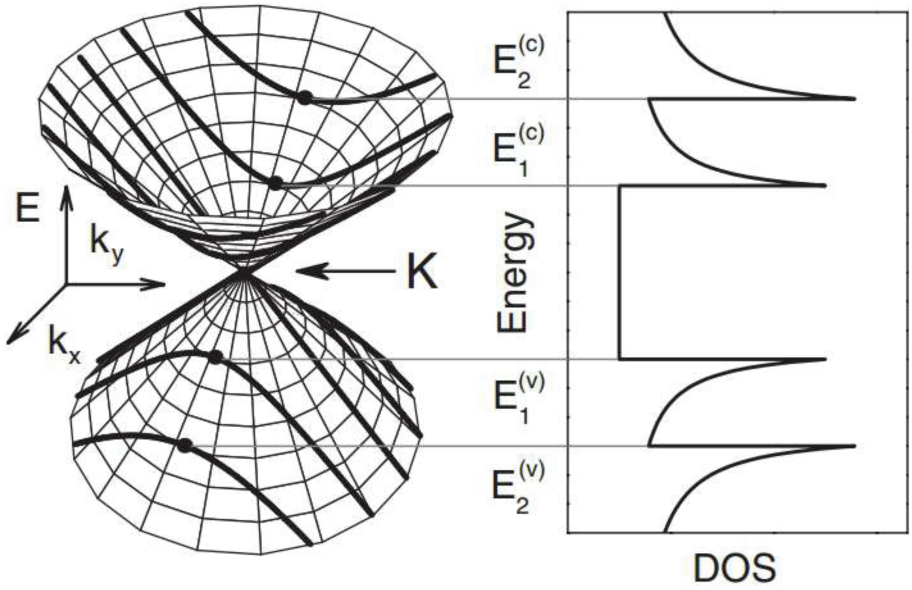

Figure 1.5 – The energy-momentum contours for valence abd conducting bands for graphene (double cone). The cutting lines of these contours denote the dispersion relation of nanotube, given rise to different energy sub-bands in the DOS plot (left panel). Adapted from [13].

Close to the K-point the DOS can be expressed in an analytic form using the eq. 1.26. Thus, for a given subband μ, the extreme values of the conduction and valence bands (minimum and maximum, respectively) are written

$$E_\mu^{\pm} = \pm \frac{a\gamma_0}{\sqrt{3}d} |3\mu - n - m| = \pm E_0 |3\mu - n - m|, \tag{1.28}$$

where the Fermi energy is set to zero. Then, the density of states becomes

$$\rho(E) = \frac{4a}{\pi^2 d\gamma_0} \sum_{\mu} g(E, E_\mu), \;\; g(E, E_\mu) = \begin{cases} |E| / \sqrt{E^2 - E_\mu^2}, & \text{if } |E| > |E_\mu| \\ 0, & \text{if } |E| < |E_\mu| \end{cases}. \tag{1.29}$$

The function $g(E, E_\mu)$ diverges at the band-edges of the valence and conduction subbands ($E = E_\mu$). Thus 1D nanotube DOS has a sharp threshold and a decaying tail.

In the case of metallic nanotubes, the desity of states at the Fermi level presents no bandgap (available electronic states), however the van Hove singularities are observed from $E/E_0 = \pm 3, \pm 6, \ldots$, thus a pseudo bandgap is defined for the metallic CNNTs between the first singularities conduction and valence energy bands, i.e.

$$M_{11} = 6E_0 = \frac{6a\gamma_0}{\sqrt{3}d}. \tag{1.30}$$

For semiconducting nanotubes, the DOS at the region around the Fermi energy presents a bandgap where no states are available, showing also van Hove singularities at positions $E/E_0 = \pm 1, \pm 2, \pm 4, \pm 5, \ldots$. The region without available states is expressed by

$$S_{11} = 2E_0 = \frac{2a\gamma_0}{\sqrt{3}d}. \tag{1.31}$$

1.1.3.3 Kataura plot

The first experimental observation of the density of electronic states in SWCNTs was accomplished via scanning tunneling spectroscopy, however other techniques based on optical spectroscopy, have also been able to measure the DOS. More precisely, the optical techniques (like Raman scattering) do not directly measure the electronic density of states, because some selection rules are imposed on the electronic transitions in the band structures. A plot that depends on density of valence-conduction states fulfilling these selection rules, which are available for optical transitions as a function of the excitation photon energy is known as *joint density of states* (JDOS) graph and written as,

$$\rho(E) = \frac{\sqrt{3}a^2}{2\pi^2 d} \sum_{\mu} \int dK_2 \delta(K_2 - k_\mu) \left\| \frac{\partial(E^- - E^+)}{\partial K_2} \right\|. \tag{1.32}$$

By considering the energy transitions E_{ii} (where the i correspond to the valence and conduction bands at the same cutting line or symmetry) from the van Hove singularities in JDOS plot, it is possible to build a graph that relates the nanotube diameters and their bandgap energies, so-called *Kataura plot*. In other words, the symmetric transitions between VHS of each nanotube of a given chirality (n, m) shape a vertical set of points on Kataura's plot at the tube diameter. These transitions are excited in the nanotube using parallel light polarization to the tube axis. The nanotubes transition energies can be displayed in branches with $2n + m$ constant providing for each E_{ii} a herringbone arrangement Figure 1.6 a).

In practice, since the Kataura graph provides the relation between E_{ii} vs. d_t, then a prediction about which nanotubes sort (chiralities) will be excited in a sample for a specific laser energy can be performed, see Figure 1.6 b) (it shows a semiconducting (6,5)-tube in resonance with the excitation energy of 2.16 eV - yellow line). In this sense, the Kataura plot becomes an important tool for the study of CNNTs by Raman spectroscopy, as well as by photoluminescence. Still by the Figure 1.6 b), we can also observe the empirical fitting model reasonably mimics the experimental findings, however some models, e.g. tight-binding, can underestimate the transition energies, so some adjustments are required to improve the empirical fitting functions, as in the formula below

$$E_{ii}(p, d_t) = a\frac{p}{d_t}\left[1 + b\log\frac{c}{p/d_t}\right] + \beta_p \cos 3\theta / d_t^2, \tag{1.33}$$

with a = 1.049 eV nm, b = 0.456 and c = 0.812 nm^{-1}. This functional form carries both the linear dependence of E_{ii} on p/d_t, expected from the quantum confinement of the 2D electronic structure of graphene, and the many-body logarithmic corrections [15, 16] (they are important for the study of CNTs in different environments).

Not less important, it should be noted that the transition energies Kataura plot needs to be corrected by the excitonic nature of the optical transition energies, which is supported by theories and experiments [19, 20]. The theoretical predictions previous (using tight-binding model, *ab initio* calculations) usually take in account only the electron-phonon coupling strength which are based on the free-particle picture, so not including the excitonic effects [21, 22]. In this way, Jiang et al. [23] within the framework of the tight-binding model calculated the Raman intensities (signal) by inclusion of excitonic states, showing that the exciton–photon matrix element

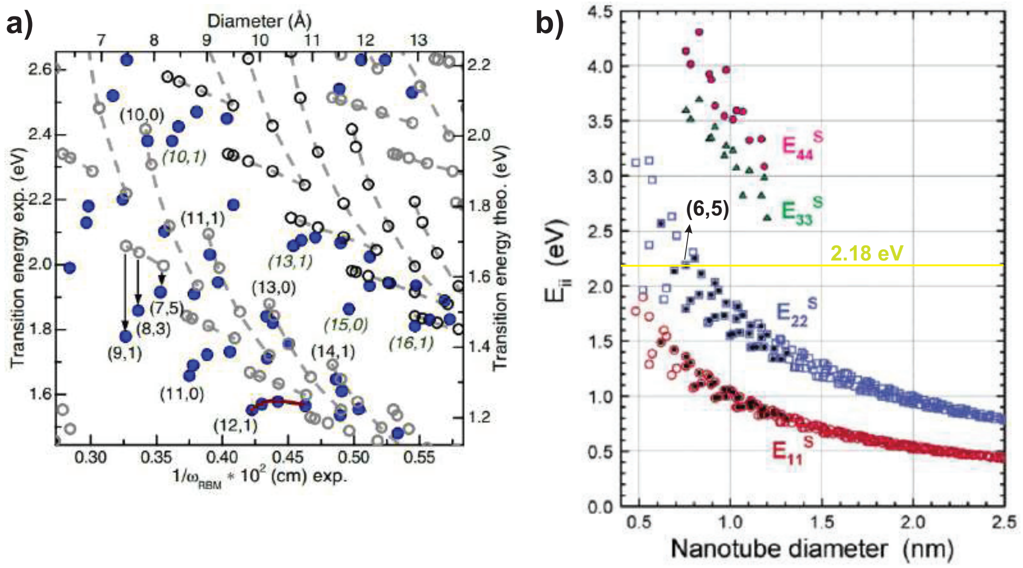

Figure 1.6 – a) Kataura plot from experimental data points (filled circles) and third neighbor tight-binding calculations (open circles) with the gray and black indicating semiconducting (E^S_{22} and E^S_{33} optical transitions) and metallic tubes, respectively. The gray dashed lines correspond to the tubes from the same branch 2n + m = const. (adapted from [17]). b) Optical transitions energies vs tube diameter for semiconducting SWCNTs. The black dots are experimental data, while the open symbols are predictions of E_{11} (circles) and E_{22} (squares) from the empirical fitting functions. The yellow line marks the excitation energy of 2.18 eV for which the semiconducting (6,5)-SWCNT (black arrow) is in resonance (adapted from [18]).

$\mathcal{M}_{\text{ex-op}}$ depends upon tube diameter $1/d_t^2$ but without the tube type or chiral angle dependence. Whereas the exciton–phonon matrix elements $\mathcal{M}_{\text{ex-ph}}$ hardly displayed any deviation from results based on the free-particle picture (descibres the tube type and chiral anlgle dependences, but underestimates the diameter dependence, especially for small diameter SWNTs).

1.2 Phonons modes of carbon nanotubes

The phonon dispersion curves of the graphene layer can be calculated via the force constant model. Since there are two non-equivalent carbon atoms (A and B) in the graphene until cell, we need considering 6 degrees of freedom, so the secular equation to be solved is a 6×6 dynamical matrix $\mathcal{D}$. Through some calculations and under certain constrains [3], it is remarkable that the inclusion of the fourth-neighbor interactions is sufficient to reproduce the phonon relations of graphene. In this context, there are six phonon dispersion curves (branches), which originate from the Γ-point in the Brillouin zone. Three from these six phonon branches correspond to *acoustic modes*

- an out-of-plane transverse mode (oTA),
- an in-plane tangential mode (iTA),
- an in-plane longitudinal mode (iLA).

---

[3] For more details see Ref. [5].

The remaining three branches match to *optical modes*

- one out-of-plane transverse mode (oTO),
- two in-plane modes (iTO-tangential and iLO-longitidinal).

In a similar way, to the zone-folding procedure used in the treating of eletronic structure of carbon nanotubes, it can be also employed to obtain the phonon dispersion curves of CNNTs from the graphene ones. The first approximation arises by superimposing of the N cutting lines (constructed by wave vectors $\vec{K}_1, \vec{K}_2$) on the six phonon surfaces in the reciprocal space of the graphene sheet. Thereby, the one-dimensional phonon energy dispersion relation for the nanotubes is given as,

$$\omega_{1D}^{m\mu}(q) = \omega_g^m \left(\mu \vec{K}_1 + q \frac{\vec{K}_2}{|\vec{K}_2|} \right), \quad \left(\begin{array}{c} m = 1, \ldots, 6 \\ \mu = 0, \ldots, N-1, \end{array} \text{ and } -\frac{\pi}{T} < q \leq \frac{\pi}{T} \right), \tag{1.34}$$

where ω_g^m is the 2D phonon frequency relations in the graphene for the m branch, q is 1D wave vector, T is modulus of the translational vector $\vec{T}$, and μ is the cutting line index (N is given by formula 1.8). This procedure yields $6N$ phonon modes for each carbon nanotube. In addition, the $6(N/2-1)$ pairs of phonon modes related with cutting lines of indices μ and $-\mu$ (where $\mu = 1, \ldots, (N/2-1)$) are expected to be doubly degenerated, while the phonon modes arising from the cutting lines for the $\mu = 0$ and $\mu = N/2$ are non-degenerate, and therefore, resulting in a total number of $(3N+2)$ distinct phonon branches.

Even though these is a huge number of phonon frequencies in carbon nanotubes, experimentally just few modes are Raman- or infrared-active and this feature appears due to symmetry selection rules. The selection rules governing the aforementioned processes are usually obtained via group theory. But, at the same time, these rules are closely related to the cutting lines concept, and thus they can be also derived from the zone-folding scheme.

According to the group analysis [24], the Raman and infrared optical modes in CNNTs are represented by

$$\begin{aligned}
\mathscr{D}_{\text{zigzag}}^{\text{Raman}} &= 2A_{1g} + 3E_{1g} + 3E_{2g} \Rightarrow 8 \text{ modes;} \\
\mathscr{D}_{\text{zigzag}}^{\text{infrared}} &= A_{2u} + 2E_{1u} \Rightarrow 3 \text{ modes;} \\
\mathscr{D}_{\text{armchair}}^{\text{Raman}} &= 2A_{1g} + 2E_{1g} + 4E_{2g} \Rightarrow 8 \text{ modes;} \\
\mathscr{D}_{\text{armchair}}^{\text{infrared}} &= 3E_{1u} \Rightarrow 3 \text{ modes;} \\
\mathscr{D}_{\text{chiral}}^{\text{Raman}} &= 3A_1 + 5A_1 + 6E_2 \Rightarrow 14 \text{ modes;} \\
\mathscr{D}_{\text{chiral}}^{\text{infrared}} &= A_2 + 5E_1 \Rightarrow 6 \text{ modes.}
\end{aligned} \tag{1.35}$$

1.2.1 Raman spectroscopy of carbon nanotubes

Carbon nanotubes when probed through of the resonant Raman spectroscopy (RRS) show further enhanced spectral intensities and this is due to the huge density of states available for the optical transitions, which in turn are characterized by the E_{ii} excitonic transitions present in VHs (associated with the quantum confinement of electronic states in the chiral vector direction). This characteristic makes of the RRS a tool of choice to access many properties and physical phenomena in this 1D carbon allotrope. In the following, we address the well-established studies from the literature about electronic and phonon structures of carbon nanotubes via resonant Raman spectroscopy.

1.2.2 Radial breathing mode (RBM)

The radial breathing mode (RBM) Raman feature corresponds to the totally symmetric vibrations of the C atoms in the radial direction, as if the tube was breathing. Usually, this mode appears between 100 cm^{-1} $< \omega_{RBM} <$ 500 cm^{-1}, being very useful for characterizing nanotube diameters through the expression

$$\omega_{\mathrm{RBM}} = A/d_t + B \tag{1.36}$$

where A and B are parameters determined experimentally and are dependent on the environment surrounding the nanotubes. For SWCNTs (within diameter range 1-2 nm) in bundles, A = 234 cm^{-1} and B = 10 cm^{-1} and for isolated, A = 248 cm^{-1} and B = 0. Nevertheless, for large diameter tubes, $d_t > 2$ nm, the RBM peak intensities are weak and are difficult to measures. For $d_t < 1$ nm the expression 1.36 does not hold the same form due to high-curvature effects that distort the nanotube lattice leading to a chirality dependence of ω_{RBM}.

As fastly pointed out in the Subsec.1.1.3.3, the Kataura plot is useful to the RRS study of CNNTs, once that this plot displays E_{ii} versus d_t, being directly related to the RBM modes via relation 1.36 (given E_{ii} vs. ω_{RBM} or $1/d_t$).

1.2.3 Tangential modes–G band

The Raman tangential modes in graphene are observed at around 1582 cm^{-1} (similar by to the graphite), and are referred as G band. The G band is associated with the doubly degenerated in-plane phonons modes (iTO and iLO), which involve a first-order Raman scattering process (Figure here). Unlike graphene, the tangential G band in SWNTs gives rise to a complex spectral characteristics (multi-peaks). However, due to the confinement scheme of the phonons vector wave in the chiral direction as well as to the symmetry breaking effects linked with the nanotube curvature, the Raman spectra usually show two strong G peaks that are labeled G^{+} (ω_{G^+} high frequency originates from atomic vibrations along the tube axis) and G^{-} (ω_{G^-} low frequency originates from atomic displacement along the circumferential direction).

The G^{-} lineshape of metallic SWCNTs is broadened in comparison with the Lorentzian shape of semiconducting tubes, and this broadening is explained by the coupling of a discrete phonon with the electronic continuum spectrum, and is fitted using the asymmetric Breit-Wigner-Fano (BWF) line shape. Moreover, the G^{-}(G^{+}) vibrational directions in metallic tubes are reversed in relation to that of semiconducting.

An experimental study over isolated SWCNTs has shown that the G-band allows estimating the nanotube diameters. More precisely the frequency ω_{G^-} as a function of d_t is expressed as

$$\omega_{G^-} = \omega_{G^+} - \frac{C}{d_t^2} \tag{1.37}$$

where $\omega_{G^+} = 1591$ cm^{-1}, $C = 47.7$ cm^{-1} nm^{-2} for semiconducting tubes and $C = 79.5$ cm^{-1} nm^{-2} for metallic tubes.

The results about G-band mentioned above offer a characterization proposal for nanotubes, where the line shape of G^{-} peak indicates electronic feature (metallic or semiconducting) and the frequency difference of G^+ and G^- provides an alternative approach for the tube diameter determination.

In addition, other Raman active modes are also observed in carbon nanotubes. Structural defects in the nanotube lead to a band at around 1350 cm^{-1} known as D-band, which is originated from a double resonant Raman scattering process involving one-phonon and one elastic scattering. The "overtone" mode related to the D-band is named the $G^{'}$ band (previously this mode has been called D^* or 2D band [25, 26]), this mode being originated from a double-resonant Raman process where a two-phonon scattering takes place independently of structural defects [13].

1.3 Carbon nanotubes under high pressure

Carbon nanotubes can have their mechanical and electronic properties tuned by external physical parameters, as temperature, pressure, electric field and others. Thus, the ability to tune the nanotubes properties represents an enormous potential for the development of novel technologies. However, a deeper understanding of how the external parameters modify these properties and their control is still required. In this context, the high pressure (as external force) has shown to be an important tool for straintonics investigations.

Many experimental and theoretical studies about high-pressure structural investigations on carbon nanotubes are seeking to understand the behavior of this material at extreme conditions. Theoretical studies based on molecular dynamics, tight-binding methods or density functional theory (DFT) + tight-binding models have shown that SWCNTs bundles undergo a radial cross-section modification towards a collapsed conformation under high pressure. These geometrical changes depends on the nanotube diameter.

Modelizations show that in low pressures regime, tubes with large diameters tend to assume a polygonal shape, while smaller diameter tubes can to assume a ovalized cross-section [27]. Moreover, when the SWCNTs bundles are submitted to high pressures conditions their cross-sections can evolve to peanut or dog-bone like shapes (large diameters) and to racetrack or elliptical shapes (samll diameters) [28].

The pressure threshold for the collapse has been suggested to depend inversely to the nanotube diameter, with a d_t^{-3} dependence Lévy-Carrier law [29]. This corresponds to the other forms of collapse dependence as d_t^{-1} have been proposed [27].

In a very recent study, it has been proposed a modified version of Lévy-Carrier law $P_c d_t^3 = \alpha(1 - \beta^2/d_t^2)$ combining experiments and models. This modeling reveals a deviation from continuum mechanics in relation to that of $P_c \propto d_t^{-3}$ for the smallest tubes below ~ 1 nm in diameter [30].

Experimentally the collapse of SWCNTs has been widely investigated by resonant Raman spectroscopy and other techniques. It has been proposed that tubes with diameter $d_t \geq 4.16$ nm tend to the auto-collapse at ambient conditions [27] and this theoretical predictions corroborate with the experimental result of high resolution transmission electron microscope image Fig.1.7 for diameters ranging from 4.6 nm to 6.2 nm [31].

Some high-pressure Raman spectroscopy studies on SWCNTs (1.33-1.46 nm diameter range) reported the disappearance or total loss of RBM signal and in the pressure ranges from 1.5 to 2.6 GPa and associated this loss with a structural change [32, 33]. In other studies, the RBM signal loss at low pressures was also followed by a significant decreasing of the G-band intensity

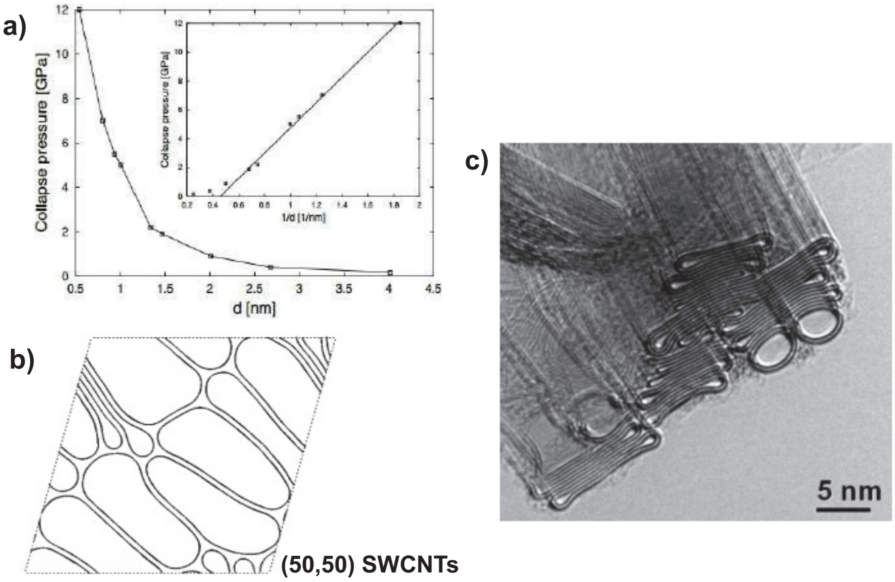

Figure 1.7 – a) The collapse pressure following the d_t^{-1} law. b) Auto-collapse of (50,50) SWCNT bundles at ambient conditions (adapted from [27]). c) HRTEM image shows the collapsed tubes [31].

or an abrupt change of the G-band pressure derivatives (α_G) [34, 35]. Supported by theoretical calculations, these effects were interpreted as a signature of the cross-section transformation from circular to ovalized. An investigation using X-ray and Raman spectroscopy has reported the disappearance of a diffraction peak together with a change of the G-band pressure derivative. Theses events were again assigned as a structural modification of the radial cross-section at 2 GPa for SWCNT of mean diameter 1.49 nm [36].

Other evidences of collapse have been found for tube diameters ranging between 0.6 – 1.6 nm, with or without pressure transmitting medium (PTM) [37, 38]. Yao *et al.* [37] observed a G-band plateau process ($\partial\omega/\partial P = 0$), showing also changes on the RBMs full width at half maximum (FWHM). An intensity decreasing of RBM modes close to the plateau. Above the plateau region the RBM and G-band profiles presented a strong decrease of intensities, however in the plateau the intensities did not have an appreciable change. In addition, theoretical simulations suggested that before the onset of the G-band plateau, the cross-section of the nanotubes changes from circular shape to an elliptical (which was observed from the FWHM changes in the RBMs near to the plateau onset) and then to flattened oval shape till the end plateau.

Experiments of high pressures on single-walled carbon nanotubes (1.35 ± 0.1 nm average tubes) in bundles filled with C_{70} fullerenes were perfomed by Raman spectroscopy and compared with the behavior of nonfilled SWCNTs [39]. In this work, the authors detected two successive transitions. The first transition was characterized by the change in the RBM broadening, occurring in the 2–2.5 GPa range (Figure 1.8(b)) independently of the choice of the PTM and of the filling or not of the tubes. This transition is explained by the change of the nanotube cross-section from circular profile to elliptical or polygonized. The second transition took place in the range of 10 – 30 GPa with high dependence on the PTM choice and was pointed out by G-band frequency downshift ($\partial\omega_G/\partial P < 0$). The behavior of the second transition was assigned as a cross-section transformation from ovalized or polygonized to a racetrack shape or peanut-like (Figure 1.8(c)).

A work related to the collapse of empty and filled SWCNTs was published by Torres-Dias *et. al.* [41]. The mechanical stability of individualized empty (closed, pristine) and water-filled (opened) SWCNTs with different chiralities at high pressure was studied by high-resolution res-

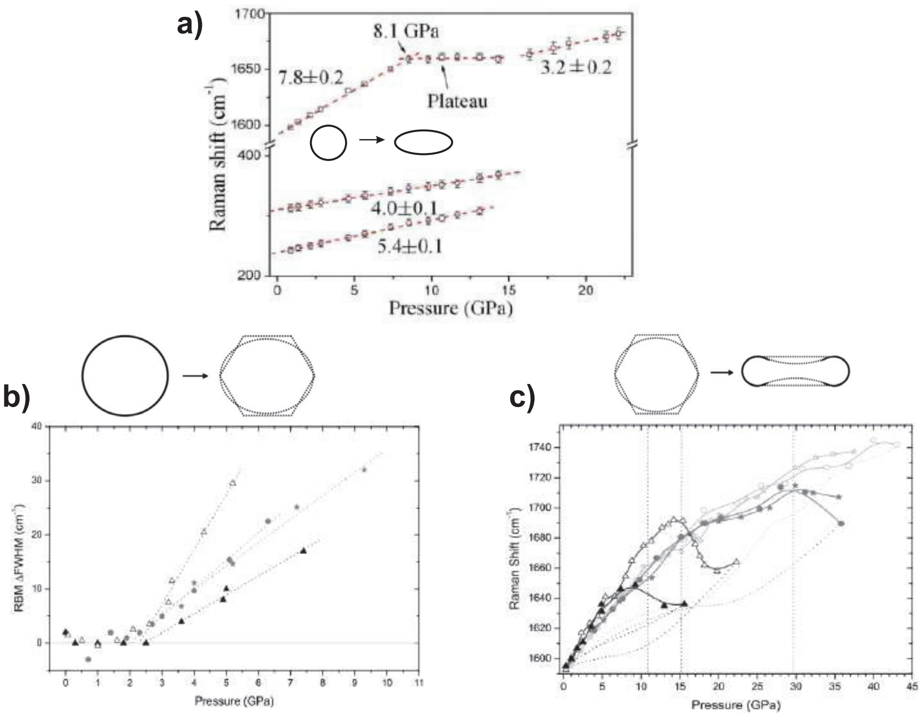

Figure 1.8 – a) The RBM and G^+ frequencies evolution as a function of pressure. The plateau onset marks the structural transformation from circular shape to racetrack [40]. b) Pressure variation of the RBM linewidth of the C_{70} peapods and empty nanotubes in different means. c) The G band evolution of filled SWCNTs with C_{70} peapods (full symbols) and empty SWCNTs (hollow symbols). The vertical dashed lines mark the pressures values in which the G band slope decreases [39].

onant Raman and fluorescence-excitation spectroscopy. For empty SWCNTs (average diameter of 1.32 nm) an abrupt collapse took place at 3.8 GPa, being identified by the RBMs disappearance as shown Fig. 1.9(a). The collapse onset for empty tubes was identified by a plateau of the G-band frequency and an inflection in the G-band evolution as a function of pressure for water-filled tubes. The collapse end of empty SWCNTs was associated to the RBMs frequency disappearance, which happened simultaneously with the plateau end of the G-band. Moreover, the results displayed that the filling presence in same-diameter tubes (1.32 nm) provides a higher mechanical stability, delaying the collapse final pressure from 4 GPa to high values (in the range of 14 – 17GPa) (Fig. 1.9(b)). In turn, these results have elucidated the permanent contradictions between experiments and theory on the interpretation of the collapse values ascribed in the literature for PTMs differences as due to the tube filling.

In a very recent study, Torres-Dias *et al.* [30] have identified through of experimental and theoretical aspects a deviation in the Lévy-Carrier law for nanotubes of small diameters. In this work, the deviation from continuum mechanics was ascribed to a modified Lévy-Carrier law $P_c d_t^3 = \alpha(1 - \beta^2/d_t^2)$ (where β is associated to discretization of the elastic compliance and α is the bending stiffness of graphene) and compared with the experimental RBMs data from Ref. [41]. The result analysis determined that the onset and completion of the RBMs quenching are in excellent agreement to the onset (P_c) and end (at ~ 1.5 P_c) collapse predicted by models, see Fig. 1.9(c - d).

Beyond the aforementioned geometrical transformations in SWCNTs, the pressure effects can

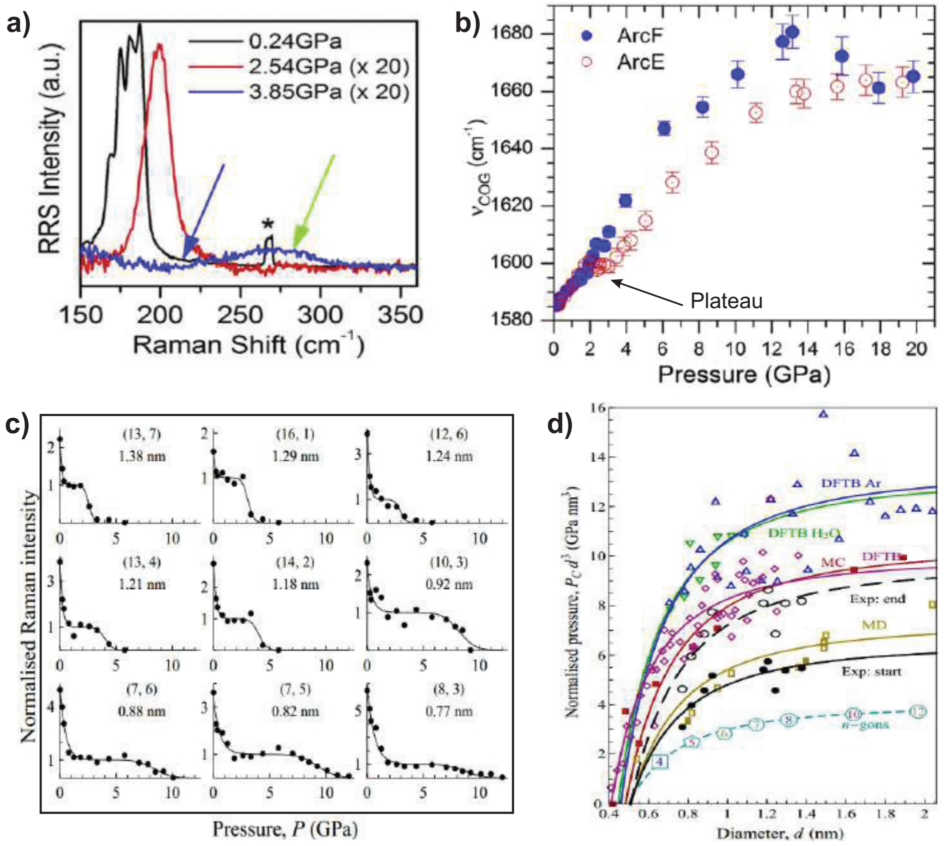

Figure 1.9 – a) The RBM spectra at three different pressures, where at 3.85 GPa the signal is quenched. b) Comparison of the G-band evolutions of the empty (hollow circles) and filled (full circles) SWCNTs. The black arrow indicates a plateau for empty tubes [41]. c) The normalised Raman peak area of nine chiralities plotted as a function of pressure. d) Comparison between the experimental collapse pressures and theoretical simulations in the from P$_C$d^3 plotted against d [30].

also change their optical properties (electronic structure). By means of theoretical and experimental studies, it has been demonstrated that under pressure carbon nanotubes undergo resonance change (optical transitions), which are related to the gap tunability. Lammert *et al.* [42] have showed through tight-binding calculations that (n,n) armchair tubes (metallic) when collapsed become semiconductors and (3n,0) zig-zag tubes can be metallized. Capaz *et al.* [43] have investigated electronic properties of (n,0) semiconducting SWCNTs under compression using a combination of theoretical techniques and revealed that the signal pressure coefficients of the band gap (dE$_g$/dP) of these SWCNTs can be negative or positive, when the division n/3 produces remainders equals to 2 or 1, respectively. Other feature found was that the magnitude of dE$_g$/dP seems to increase with diameter. Experimental evidence of resonance changes were reported by Ghandour *et al.* [44]. They have performed high-pressure resonant Raman experiments on bundled SWCNTs using two different laser energies and observed that at 3.5 GPa the intensity G-band profile at 1.96 eV (composed by metallic and semiconducting SWCNTs at ambient conditions when excited with this energy) was similar to the intensity profile of that one excited with 2.41 eV (only semiconducting SWCNTs have been observed when probed for this laser energy at ambient conditions). This behavior was associated to a redshift in the transition energies of metallic tubes (E$_{11}$) induced by pressure. Shan *et al.* and Wu *et. al.* [45, 46] studied, the pressure effects on the optical transitions in individualized semiconducting single wall carbon nanotubes of different diameters and chiralities by means of optical absorption and photoluminescence spectroscopy. Their results showed that the pressure coefficients of band-gap energies are negative (E_{11} and E_{22}) and dependent on the chirality, being less sensitive fo the second van Hove transitions. For the case of larger diameter tubes the sensitivity is more pronounced.

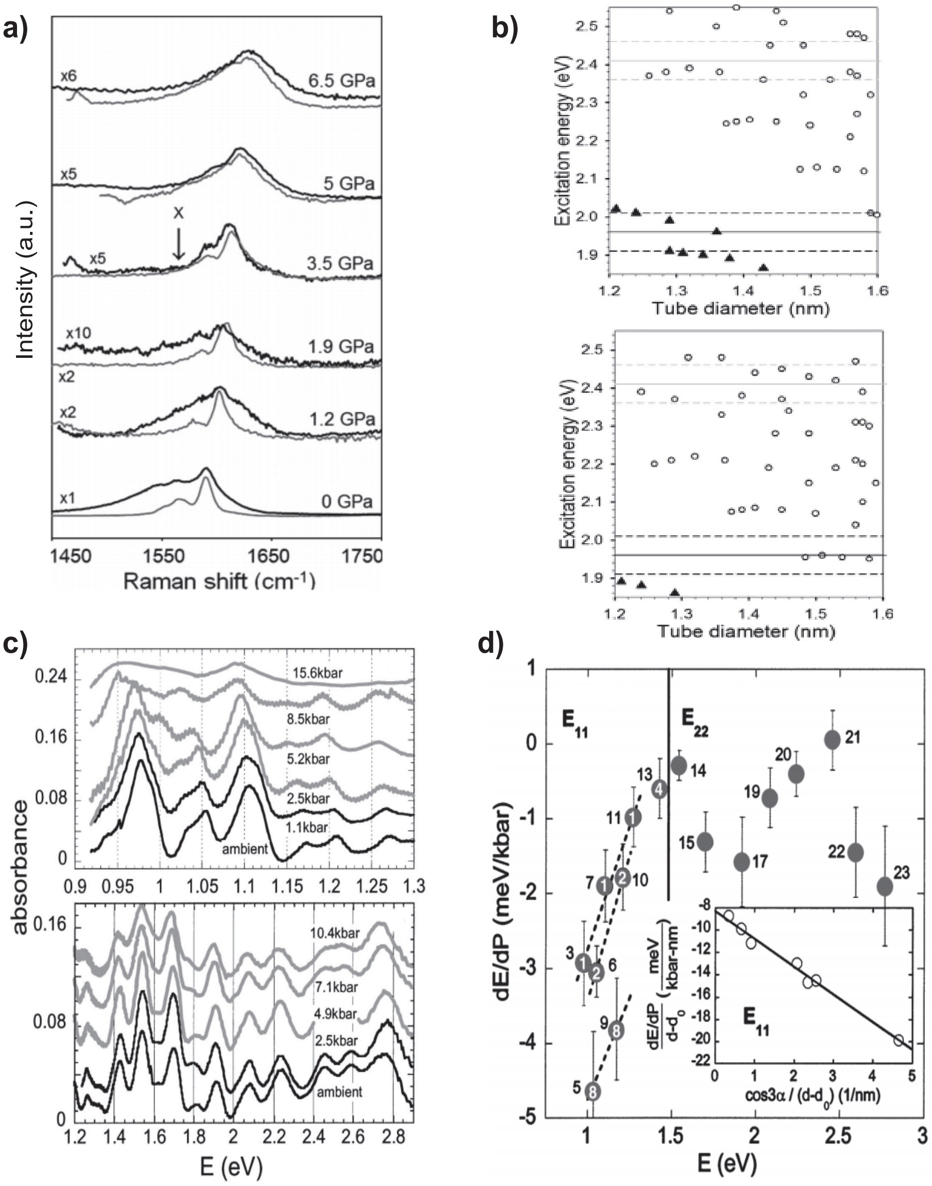

Figure 1.10 – a) G-band spectra at high pressure excited by two different laser lines (1.96 eV in black and 2.41 eV in gray). The point marked “X” shows the resonance change. b) Kataura plots at ambient conditions (upper panel) and at 3.5 GPa (lower panel) close to the excitation energies of 1.96 eV and 2.41 eV. The black triangles represent the metallic tubes whereas the opnen circles are semiconducting SWCNTs. The resonance windows are also limited by dashed lines [44]. c) Absorption spectra at high pressures taken at two different energy ranges (first from 0.9 - 1.3 eV; second from 1.2 - 2.8 eV). d) Measured linear pressure coefficients as function of peak energy observed from the absorption spectra for transition energies E_{11} and E_{22}. The dashed lines connect families with equal n-m values [46].

Structural changes also have been investigated in DWCNTs. Through molecular dynamics it was observed that isolated DWCNTs undergo a pressure induced phase transition, with the tube cross-section changed from circular to elliptical shape simultaneously for outer and inner tubes, evolving to peanut. The critical transition pressure was observed to depend strongly of the inner tube diameter, following the same inverse cubic law (d^3_{inner}) for SWCNTs [47]. On the other hand, the mechanical stability in DWCNTs bundles has been studied using different theoretical techniques and the results show that the phase transition depends on symmetry and diameter of DWCNTs bundles, having the collapse pressure governed by inverse cubic law. However in that work the diameter dependence of the collapse pressure is proposed to be dependent on the average of the inner and outer tube diameters [48].

The pressure effect on electronic bands and structural stability of DWCNTs bundles was investigated by combining a tight-binding model, a classic force field and first-principle calculations [49]. The results pointed out that the outer tube acts as a protective shield for the inner tube, which increases the mechanical stability of the outer tube (the resistance to the external pressure). Furthermore, it has been observed that the structural phase transition induces a pseudogap along the ΓX–line in the electronic band structure of armchairs tubes (metallic) and the DWCNTs bundles optical properties display a strong anisotropy in the collapse. After the collapse these properties changed considerably.

Another experimental study on the response to pressure application of double-wall nanotubes by means of Raman spectroscopy also showed the outer tubes effect [50]. The pressure screening in DWCNTs bundles based on radial breathing modes behavior was studied by Arvaniditis *et al.* [51, 52]. They proposed that the normalized pressure coefficient vs initial RBM frequencies ($\Gamma_i = (1/\omega_i)(\partial\omega_i/\partial P)$) is attenuated due to shielding effect provided by outer tubes to the inner, which leads the normalized pressure coefficient values of inner tubes to be closer of those for individual tubes with the same diameter. The pressure response of inner tubes was attributed to the intratube coupling and their tube spacing dependence, indicating thus the existence of specific inner-outer tube combinations.

The cold compression effect on DWCNTs optical properties using absorption/transmission spectroscopy has been reported in two works by Anis *et al.* [53, 54]. These works investigated the evolution of the pressure-induced absoprtion bands comparing the redshifts of empty SWCNTs and DWCNTs. The smaller redshift of the absorption bands in DWCNTs indicated that the outer tubes are stabilized by the inner tubes, moreover, an anomaly in the pressure-induced shifts took place at 12 GPa pointing out the structural deformation onset of the tubular cross-sections.

The experimental collapse in DWCNTs was also investigted by high-pressure resonance Raman technique in two different PTM (paraffin oil and NaCl) in the work of Aguiar *et. al* [55]. They observed the collapse onset by a inflection in the slope of the G^+ pressure coefficient. The collapse process was seen as a two steps mechanism: (i) the outer tube is destabilized at a higher pressure than SWCNTs with same diameter (evidence of mechanical support), followed (ii) by the inner tube destabilization as response to the outer tube deformation at a lower pressure collapse than for the corresponding SWCNT. Calculations in that same work indicated that the collapse pressure appears to follow inverse cubic law $1/d^{-3}_{tav}$ (d_{tav} the average diameter from the inner and outer tubes). They also observed experimentally that the collapse process is independent of the PTM nature (chemical screening).

In very recent study, Alencar *et .al* [56] studied collapse of few-wall (2 and 3) carbon nanotubes.

They performed high pressure resonant Raman experiments in DWCNTs of inner and outer diameters larger than 1 nm (more precisely, inner and outer diameters averaging 1.5 nm and 2.0 nm, respectively) and observed experimentally the onset and end of the radial collapse process between 2 GPa and 5 GPa, through of the G-band slope modification together with quenching of the RBMs. These experimental results were found to be in good agreement with the modified Lévy-Carrier formula $\mathrm{P}_c d_t^3 = \alpha(1 - \beta^2/d_t^2)$.

In brief, despite of many efforts to understand the collapse process, it shows still quite complex scenarios without a consensus in the literature, mainly for the case of few-wall nanotubes. The difficulties can have different origins, among them, the samples synthesis method providing huge diameter distributions, chiralities, the tubes bundling as well as the number of defects, beyond the external and inherent parameters control that disturb the mechanical stability and also changed the electronic properties. Motivated for these limiting factors, we accomplished high pressure experiments in different carbon nanotubes systems, which will be discussed along this work.

1.4 Specific aspects of BN nanotubes

Boron Nitride Nanotubes (BNNTs) can be seen as hexagonal boron nitride (h-BN) sheets that have been concentrically rolled into cylinders Figure 1.11 a). This corresponds to the geometrical analogy used for graphene wrapping to form carbon nanotubes (CNTs). BNNTs were initially predicted by computational simulation in 1994 [57, 58] and synthesized by arc-discharge method in 1995 [59]. Compared to CNTs, which can be metallic or semiconducting depending on chirality, BNNTs have a large band gap beyond 5 eV [60] (insulating nature) with weak dependence on chirality. They also exhibit enhanced thermal stability, high thermal conductivity and significant yield strength [61]. These properties are sometimes complementary to those of CNTs and make BNNTs promising candidates for advanced material technologies, such as in the development of photoluminescence or optoelectronic devices or piezoelectric materials [61, 62] Figure 1.11 b). However, their development and production for practical applications still depend of trustworthy synthesis methods, analytical characterizations, together with an improved knowledge of the structure-property relationships.

A variety of methods, such as laser ablation [65], chemical vapor deposition (CVD) [66], ball-milling [67], substitution reaction [68] were invented and adopted to synthesize BNNTs. These synthesis methods provided BNNTs with different purity, diameters and structures in order to meet the requirements for detailed physical property investigations. Nevertheless, the absence of an effective method for the large-scale synthesis of BNNTs with high purity and small diameters is still a prime obstacle in a route toward further understanding BNNT characters and their real practical prospects. In order to overcome these hindrances, we present in Chapter 5 a synthesis route developed for the our BNNTs study, know as Boron Oxide Chemical Vapor Deposition (BOCVD) following a catalytic “Vapor-Liquid-Solid (VLS) Growth Mechanism”.

The BNNTs, as an inheritor of h-BN sheet, show the same advantageous properties of this 2D material (summarized in Fig. 1.11 b)). Thus, when we are exploring the BNNTs physical properties (as electronic and phonon structures, mechanical aspects, Raman modes) under certain restrictions we are also exploring the h-BN layer physical properties. The BN allotropes will be

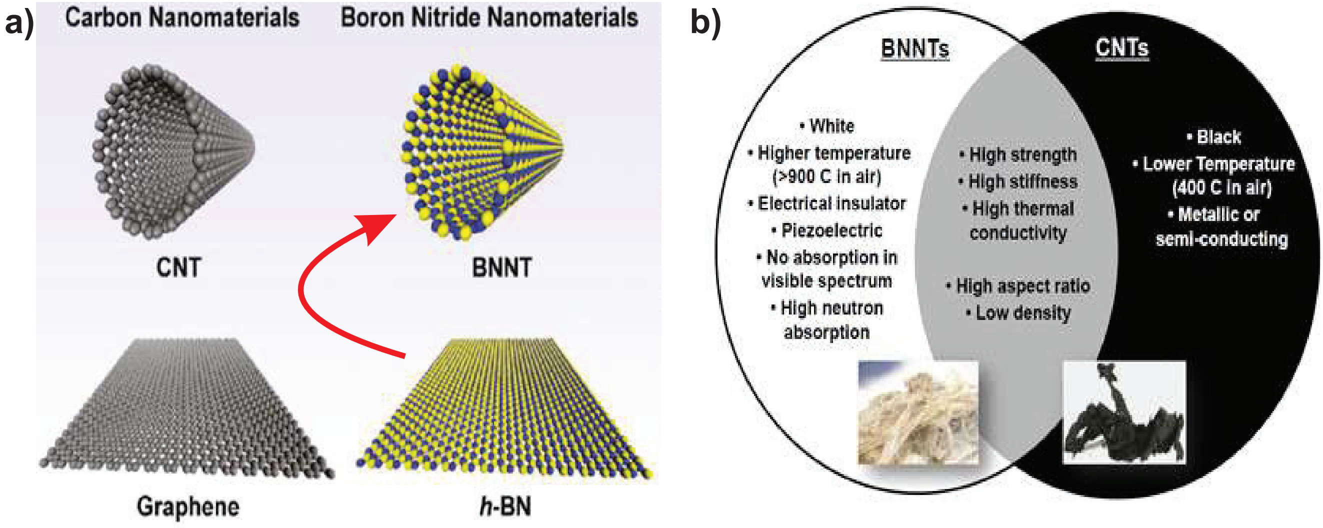

Figure 1.11 – a) The representation of a hexagonal boron nitride sheet generating a BNNT (red arrow - adapted from [63]). b) BNNTs vs CNTs properties comparison (adapted from [64]).

invoke insofar as be interesting to compare their properties with the BNNTs.

A theoretical work by generalized tight-binding molecular dynamics reveals that unlike CNTs, BNNTs possess a wave-like or "rippled" surface in which B atoms rotate inward to an approximately planar configuration, whereas the N atoms move outward into a corresponding pyramidal configuration. More interestingly, it was found that a zig-zag BNNT may favor a flat end, while in an arm-chair tube the conical tube closure is more energetically favored and a "chiral" tube may have the amorphous end. This discovery made it possible to find out the chirality of BNNTs by simply checking TEM images of the BNNTs' ends. However, the exact relationship between chirality and tip morphology has not been verified yet because of very few relevant experimental works [69].

1.4.1 Electronic structure of BN nanotubes

In spite of structure similarity, BNNTs possess totally different electronic structures with CNTs. With a constant wide band gap at 5.0–6.0 eV, unmodified BNNTs can be considered as insulating materials. A dielectric constant of 5.90 was predicted by theoretical calculations which is universal for all BNNTs, regardless of their radius and chirality. High-resolution transmission electron microscopy (HRTEM), electron energy loss spectroscopy (EELS) [70], transport experiments [71], measurements of the optical properties by means of absorption [72], and low-loss EELS [73] were performed on these tubes. These measurements confirmed the predicted large band gap.

To illustrate the band gap properties of h-BN and BNNTs, we introduce the Figure 1.12 a) which displays the band gap structure of hexagonal boron nitride, whereas the Figure 1.12 b) shows the electronic structures for isolated (left panel) and bundled (right panel) (8,8)-BNNT.

According the tight-binding method calculations for the BNNTs' electronic strcuture [57], it was found that the semiconducting has direct or indirect band gaps. Theoretically, the band gap may become rather small ($\sim$2 eV) in very tiny tubes with a diameter $>$1 nm, however,

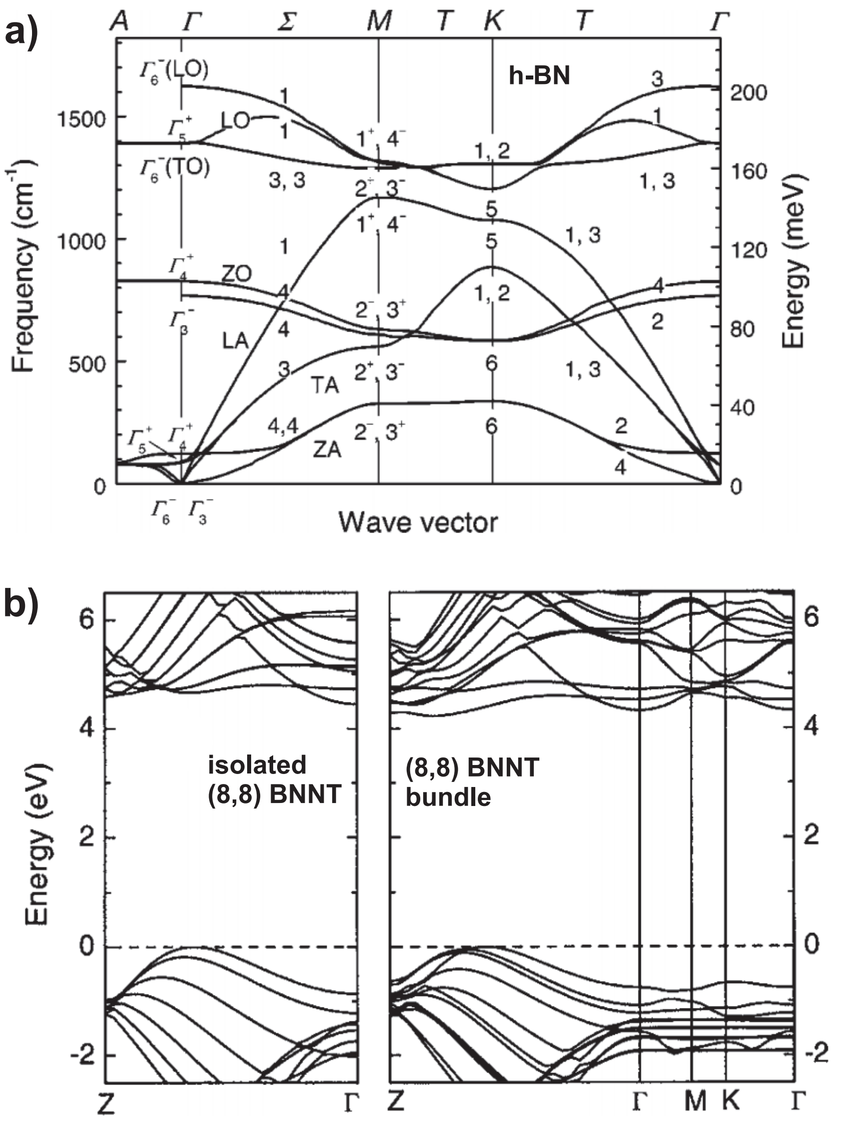

Figure 1.12 – a) Electronic structure of hexagonal boron nitride (adapted from [74]). b) Electronic band structures of isolated (8,8) BNNT (left panel) and (8,8) BNNT bundle along several high-symmetry directions in the hexagonal Brillouin zone (adapted from [75]).

such narrow BN tubes have never been experimentally reported. In the studies based on local density functional (LDA) calculations proved that it is energetically more favorable to fold a hexagonal BN sheet into a BNNT than to create a CNT from a graphite sheet [76] and the gaps are stable at ∼4 eV according to LDA. In another calculation using density functional theory (DFT), the bands of BNNTs were found to be saturated at 5.03 eV for all tubes with realistic diameters [77]. However, other works point out that the flattening deformation (for instance, pressure application [78, 79]) may cause a band gap decrease.

In fact, various methods were attempted to tune the electronic structure of BNNTs, such as applying an electrical field [80], strain [75], doping [81, 82], introducing defects [83], or modifying the tube surface [84]. Thus, BNNT band gap could be directly reduced by a field or a strain or modified by introducing localized energy levels inside the gap under chemical treatments. For instance, the BNNT band gap change was investigated by applying an 0.2 V/Å electric field and the band gap of an arm-chair (10,0) BNNT was reduced from 4.0 to ∼0.5 eV 1.13 a). Under compression the higher diameter tubes, such as (12,0) BNNTs bundles had its band gap energies decreased from 4.0 to 2.75 eV 1.13 b).

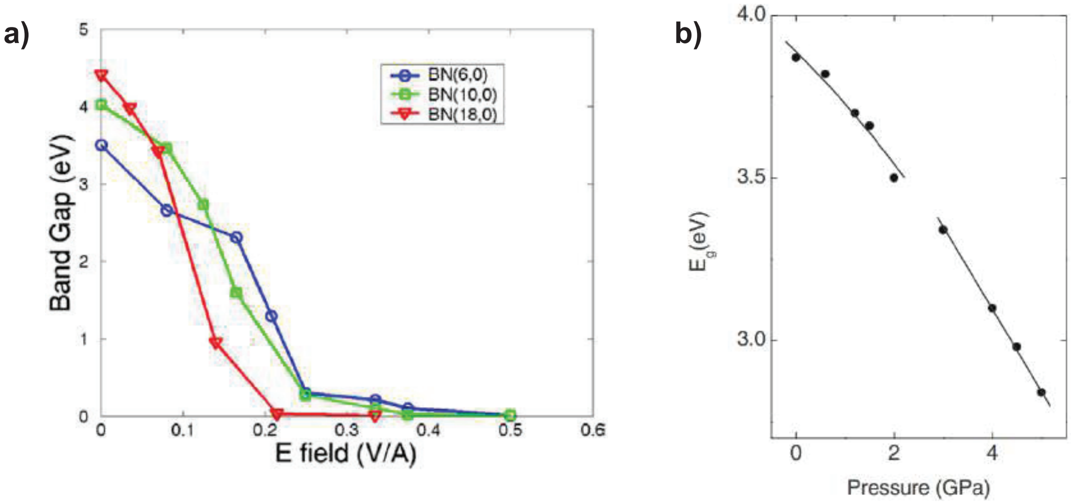

Figure 1.13 – a) The band gaps of (6,0), (10,0) and (18,0) BNNTs are plotted as a function of field strength (adapted from [80]). b) Band gap evolution as a function of pressure for zigzag (12,0) (adapted from [78]).

Some studies on photoluminescence and cathodoluminescence showed that BNNTs are an effective violet and ultra-violet light emission material [85]. The strong luminescence is attributed to excitonic effects, more precisely to excitons bound to the structural defects: dislocations, facets, which are observed along the walls. Structural defects have already been identified in h-BN to be responsible for the D-band emission between 5.4 and 5.65 eV and for its spatial localization. In that case, D-band luminescence was found to be mainly due to the recombination of trapped excitons at defects such as grain boundaries. This is in contrast with the case of the MWBNNTs, where the junction lines between the facets, which are grain boundaries analogues, are not the dominant sites for recombination [86]. In fact, such excitonic effects were found to be more important in BNNTs compared to CNTs.

1.4.2 Phonon structure of BN nanotubes

According to the group-theoretical analysis, the number of active modes is found by determining how often each irreducible representation appears in the (reducible) representation of the symmetry group (C_{2nv}, C_{2nh}, or C_N, respectively) which is given by the 12n vibrational degrees of freedom of the unit cell. For zigzag tubes this leads to 14 Raman-active modes (3 with A_1 symmetry, 5 with E_1 symmetry, and 6 with E_2 symmetry, where the E_1 and the A_1 modes with vanishing frequency have already been subtracted). Out of these modes, 8 modes ($3A_1$ and $5E_1$) are also IR active. In the case of chiral tubes, there are 15 Raman active modes (4A, $5E_1$, and $6E_2$) out of which 9 modes (4A and $5E_1$) are also IR active. The small difference in the number of active modes between zigzag and chiral tubes stems from the fact that the additional vertical reflection symmetry of the zigzag tube causes a distinction between Raman+IR active A_1 modes and nonactive A_2 modes. The sets of Raman- and IR-active modes for BN armchair tubes are disjoint: 9 modes are Raman active (3 with A_g symmetry, 2 with E_{1g} symmetry, and 4 with E_{2g} symmetry) and 4 modes are IR active (1 with A_u symmetry and 3 with E_{1u} symmetry) [87, 88]. Series of calculations of phonon in BNNT's have been performed using tight-binding model, density-functional theory, and valence shell model (these calculations of phonons have also been performed for graphite and carbon nanotubes). In particular, a force constants model in which the interatomic force constants up to the fourth-nearest-neighbor interaction was fitted to experimental data for phonons in boron nitride nanotubes [89]. This approach is very fast and, in combination with the zone-folding method (i.e., the construction of phonons in the tube from the phonons of a sheet which is rolled up to form the tube), allows a good intuitive understanding of phonons in nanotubes.

The Figure 1.14 a) shows the phonon spectrum of 2D h-BN (right graphic - where also the experimental points are included by the open circles) in comparison with the phonon dispersion of a (10,10) BNNT, obtained through the valence shell model. Fig. 1.14 b) offers a sight of the radial buckling (R), longitudinal (L), tangential (T) vibrational modes for a zigzag BNNT.

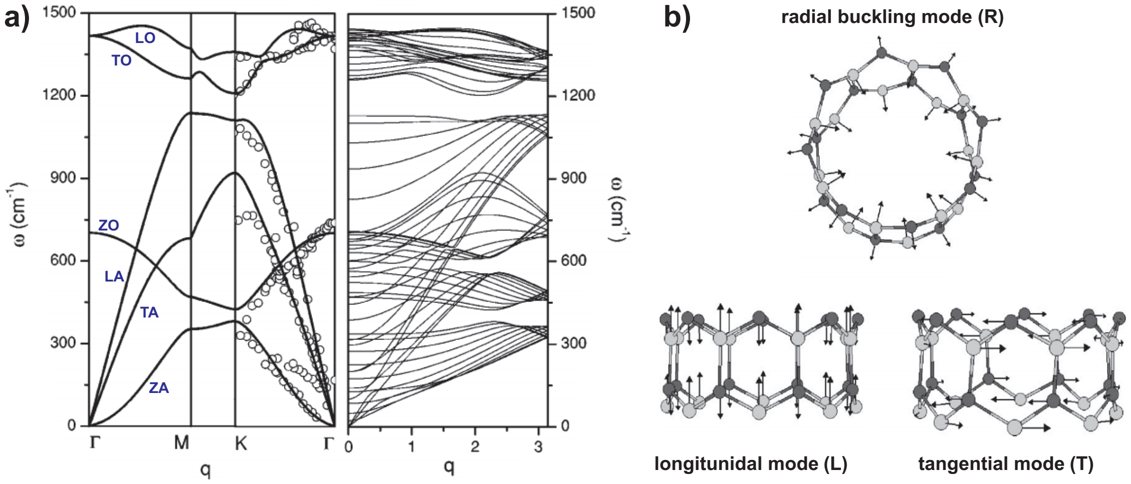

Figure 1.14 – a) Phonon dispersion relation for 2D h-BN (left graphic) in comparison with (10,10) BNNT (adapted from [89]). b) Sketch of radial buckling (R), longitudinal (L) and tangential (T) modes in a BN zigzag tube (adapted from [88]).

1.4.3 Raman spectroscopy of BN nanotubes

The infrared and Raman active modes of individual single BNNTs have been predicted by different theoretical approaches as above-mentioned: zone-folding [90] combined with bond polarizability parameters of carbon [76, 59, 91], tight binding approach [92], and ab initio calculations [88, 93], see Figure 1.15.

Interestingly from these theoretical studies, it was confirmed that the radial breathing mode (RBM) in boron nitride nanotubes (as well as in carbon nanotubes) is inversely proportional to the tube diameter. However, Ghavanloo *et al.* [94] presented an analytical formulation for predicting the radial breathing mode (RBM) frequency of boron nitride nanotubes (BNNTs) with arbitrary chirality. The main results pointed out that **i)** the frequency of the RBM is

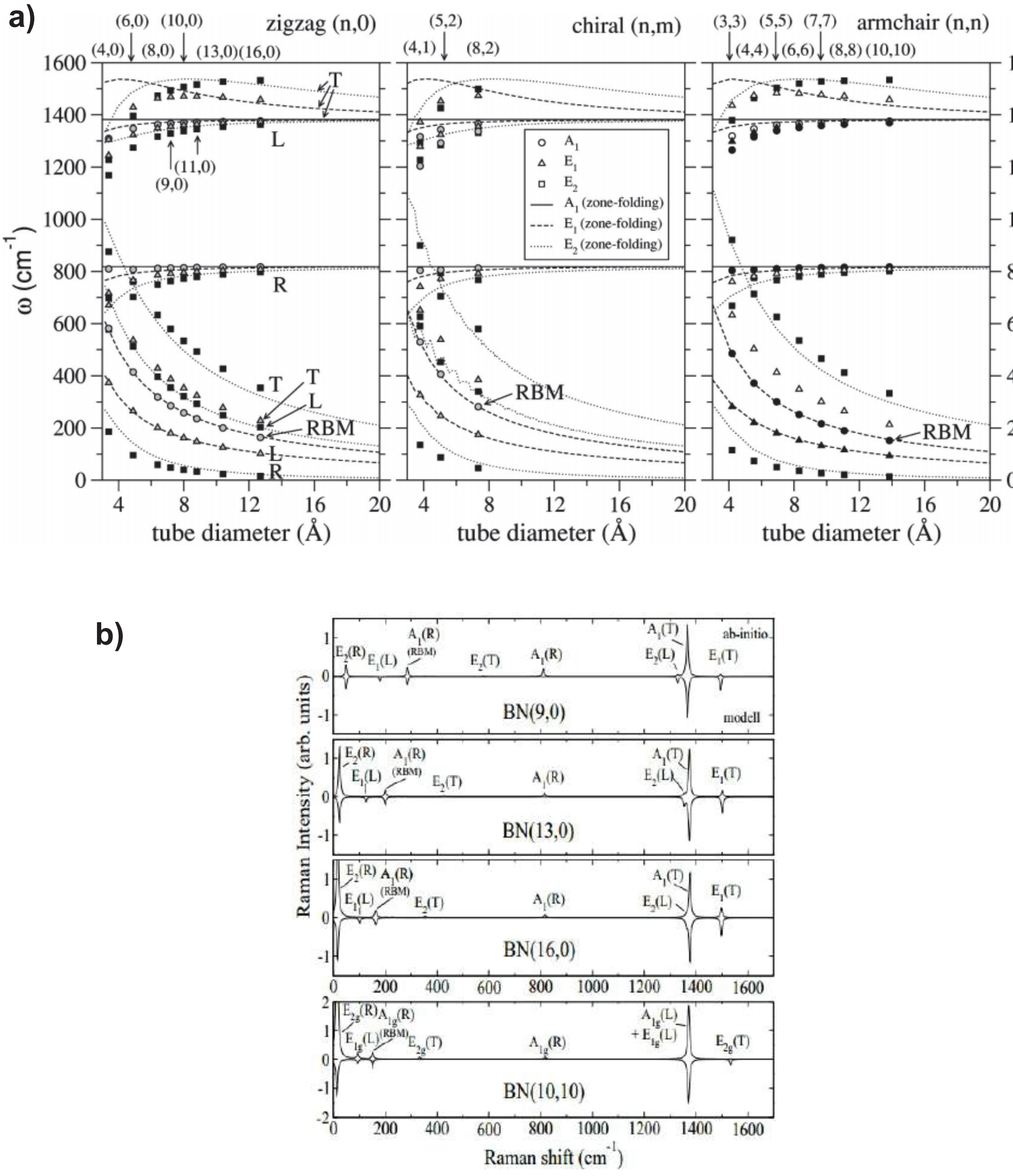

Figure 1.15 – a) Frequencies of Raman- and IR-active modes in BN nanotubes as a function of tube diameter: comparison of ab initio values (symbols) with zone-folding method (lines). Black and white filling mark modes which are Raman and IR actives, respectively. Whereas, the gray filling stands for modes which are both Raman and IR active. The shape of the symbols denotes the symmetry of the modes, see legend (adapted from [88]). b) Raman spectrum for different BN tubes: Comparison of ab-initio calculations (positive axis) with the bond polarization model (inverted axis). Symmetry assignment follows [87] (adapted from [93]). In the both graphics, the letters R,T,L denote the character of the corresponding phonon oscillation: radial, transverse, or longitudinal.

not inversely proportional to the diameter of the BNNTs as predicted by the previous studies aforementioned and **ii)** the BNNT with a smaller chiral angle has a lower RBM frequency when considering the tubes with the same diameter.

Despite of the wide number of informations about the RBMs frequencies of BNNT given by calculations, no clear experimental evidence of these modes has been reported. Due to this latter large electronic band gap of the BNNTs, the Raman scattering of light is expected to be nonresonant in contrast to carbon nanotube in which the process is resonant. A experimental study of Raman spectroscopyof SW-BNNTs (unpurified BNNTs prepared by laser vaporization process) have been carried out using visible and UV excitation energies [95]. This work showed that in the visible range, the effect of contaminants is important, since it can hide the spectroscopic response of BNNTs. In the UV range, Raman scattering at 229 nm excitation wavelength provided pre-resonant conditions and allowed to identify the tangential modes at high-frequency (1370 cm^{-1}). In contrast to SWCNTs, no dependence on the excitation wavelength was observed confirming the insulating character of BNNTs. Other Raman experiments were performed on double-walled and multiwalled boron nitride nanotubes samples [96, 97] and yielded contradictory results in relation to that one previously mentioned.

The essential test on the performance of Raman spectroscopy for the characterization of BN nanotubes is the comparison of the spectra of nanotube samples with the spectra of crystalline h-BN. At low-frequency the radial buckling mode has its intensity decreased with increasing diameter, making it difficult to characterize. At high frequency, bulk h-BN displays a single Raman line due to the E$_{2g}$ LO/TO mode. It was also observed that the E$_{2g}$ mode in multiwalled tubes displays a similar upshift as the isolated sheet, this feature was explained considering the increased interlayer distance and the noncommensurate stacking in multiwall tubes, where both effects reduce the interlayer interaction [98].

In short, despite of many studies about the BNNTs physical properties, still some optical and mechanical features stay not totally clear, as for example, the diameter dependence of the RBM frequencies of the tubes as well as a more accurate assignment of RBM frequencies (among others) by means of experiments from well-synthesized samples. Thus, in order to understand these limiting factors, we have carried out a study of BNNTs at high pressures, which is shown and also compared with previous works in Chapter 5 of this manuscript.

2

Synthesis methods of carbon nanotubes and experimental methodology

Sommaire :

2.1 Introduction **43**
2.2 Synthesis methods **43**
  2.2.1 Electric arc-discharge 43
  2.2.2 Laser ablation 44
  2.2.3 Chemical vapour deposition-CVD 45
2.3 Experimental methods **46**
  2.3.1 High pressure technique 46
  2.3.2 Transmission electron microscope 48
2.4 Experimental setup for Raman spectroscopy and TEM **51**
  2.4.1 Theoretical Basis of Raman Scattering 51
  2.4.2 Raman at high pressure 55
2.5 Transmission electron microscopes **58**

2.1 Introduction

In this chapter, we first describe the more common synthesis methods of carbon nanotubes found in the literature, to provide with a brief overview on the most important aspects of this key aspect which determine the main characteristic of samples used in experiments. Besides this, for each one of the samples studied in this thesis, their synthesis or purification processes are detailed including more specific aspects in the their respective Chapters from 3 to 5. In the following sections of this Chapter are presented basic concepts about the high pressure techniques using the operational principle of the diamond anvil cell (DAC), transmission electron microscopy technique and Raman spectroscopy. They are the main techniques used to study the materials throughout this thesis. The experimental set up descriptions are given in last part of this Chapter.

2.2 Synthesis methods

In this section we make a brief review on the most important methods used for the synthesis of CNTs. All these methods have as common aspects three ingredients, **1)** the carbon precursor; **2)** the catalysts nanoparticles, which depending on mixture can favor a good yield; **3)** the presence of an energy source that will sublimate or decompose a carbon precursor. It is worthy to mention that during the synthesis process many residual materials can be produced, as fullerenes, carbon nanocages or carbon amorphous among others.

2.2.1 Electric arc-discharge

In 1997 C. Journet *et al.* developed this method Ref.[99]. In this method, two graphite rods (anode which also contains a metallic catalyst and chatode) are placed in a reactor surrounded with a inert gas as helium or argon (Figure 2.1). The anode is moved towards the cathode creating an electric which is generated by a potential difference. The anode is continuously translated to keep a constant distance (gap of 1-2mm) from the cathode. In the arc is created a plasma of very high temperature $\sim$ 4000-6000 K (electrical breakdown of a gas), which sublimes the anode. The plasma is constituted of a mixture of carbon vapor, the rare gas and the vapors of catalysts. From the deposits of the plasma, some zones rich in carbon nanotubes are obtained.

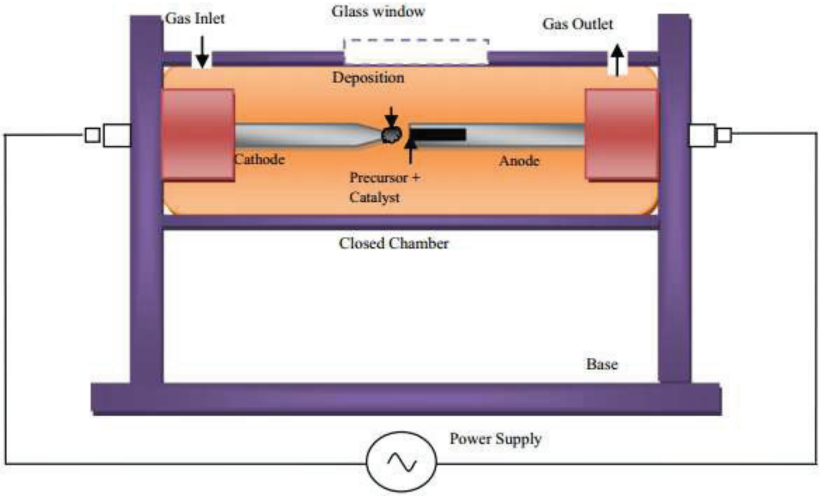

Figure 2.1 – Scheme of an arc discharge setup, adapted [100].

The nature of CNTs depends on the anode composition (graphite purity or doping by metallic nanoparticles). If SWCNTs are preferable, then the anode has to be doped with metal catalyst, such as Fe, Ni, Co. Usually, the carbon nanotubes are set up in bundles and the synthesis production yield can reach 80% [99, 100].

2.2.2 Laser ablation

In 1995 Guo et al.[101] developed by the first time the high quality CNTs growth by laser ablation. In this technique, intense laser pulses (for instance, Nd:YAG laser) ablate a carbon target which is placed in an oven heated to 1200 °C. During the process an inert gas flows by the chamber (quartz tube) to carry the grown nanotubes until a cooled collector (Figure 2.2). As the temperatures involved in this method is very high (4000 °C), a certain percentage of carbon target is evaporated. The carbon nanotubes are formed in bundles and the diameters range is narrow.

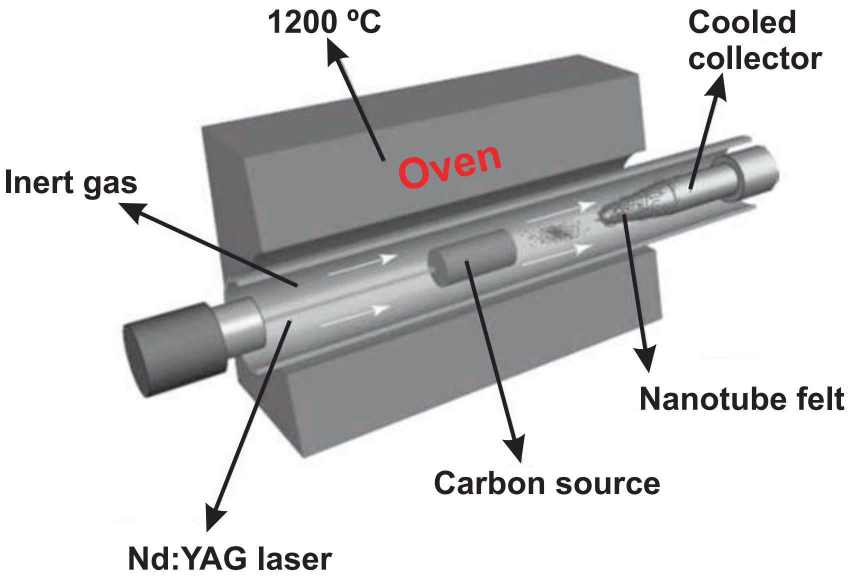

Figure 2.2 – Scheme of the laser ablation method setup [102].

2.2.3 Chemical vapour deposition-CVD

The catalytic techniques (or chemical vapour deposition) present some advantages over the arc and laser methods aforementioned. The catalysis is more amenable to scale-up the processes to produce SWCNTs and MWCNTs in large scale. Moreover this method offers greater control upon the growth process since it uses mild conditions (moderate temperature in relation to arc and laser methods). For these reasons the CVD is commonly employed for industrial purposes.

In the CVD method a substrate covered with metallic catalysts nanoparticles (Ni, Co, Fe or their mixture) is heated typically between temperatures of 600-1200 °C. The catalysts are the responsible for the nucleation growth of the tubes (Fig. 2.3(b)). The growing takes place when two gases flow through the tube furnace, a carrier gas like nitrogen or hydrogen and the other of organometallic type (hydrocarbons, as acetylene (C_2H_2) or methane (CH_4)) (Figure 2.3(a)). The synthesis production yield can reach 90%. By the control of catalysts nanoparticles size it is possible to obtain variable diameter distribution, even for SWCNTs.

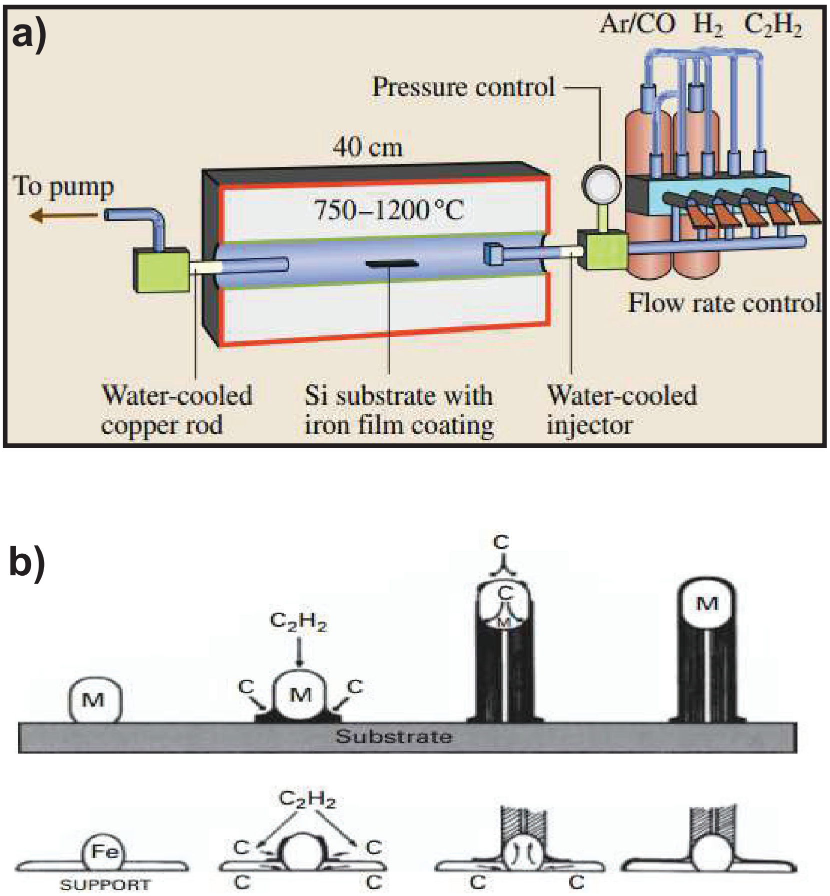

Figure 2.3 – a) Schematic of CVD system setup utilized in CNTs growth [12]. b) Illustration of tip (upper diagram) and base (lower diagram) growth mechanisms of CNTs growing [102].

2.3 Experimental methods

2.3.1 High pressure technique

Since the pioneering work of the American physicist P. W. Bridgman, during the early part of the 20th century, until the late 1960s, massive hydraulically driven Bridgman-anvil and piston-cylinder apparatus ruled high-pressure science. From the advent of the diamond anvil cell (DAC), in mid 1960s, many non-specialized laboratories became able to develop high pressure experiments [103]. Diamond is the hardest known bulk material. Besides it possess high incompressibility and transparency, being ideal to be employed as a high-pressure device.

The DAC works like a pressure chamber constituted by flat parallel faces (culets) of two opposed diamond anvils. Between them is fitted a holed metallic foil (gasket), creating a cavity (Figure 2.4(a)). The operational principle of the DAC consists on pressing the sample by means of some external force transmitted until the diamond culets (Figure 2.4(a)). The culet diameters can range from 200 μm or even less to 1000 μm. The smaller the culet, the higher the pressures which can be reached.

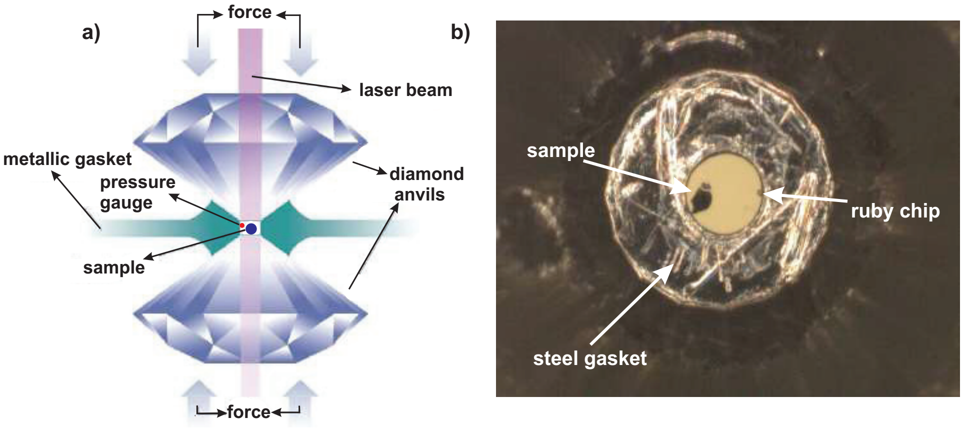

Figure 2.4 – a) Scheme of the DAC operational principle. The external forces drive one diamond against the other, which in turn compress the specimen (blue circle) and the pressure gauge (red dot). The black arrows help to identify better the DAC diagram. b) Optical image of loading of a specimen (Pyrocarbon) and ruby chip inside of steel gasket, having as PTM the salt NaCl. The hole diameter is about 116 μm.

The gasket placed between the diamonds has a thickness of the order of 200 μm in our experiments and can be typically made in rhenium, tungsten, steel, cooper or Cu-Be. The aim of the gasket is to protect the diamonds against fractures occasioned by direct contact of the culets, beyond of to limit and confine the sample volume in the cavity. The gasket is pre-indented by the anvils (this indentation is made to avoid major plastic deformation during the compression) and after a hole is pierced at its center by the electrode of an electrical discharge machining or using a micro-driller (Figure 2.4(b)). Usually, the optimized hole diameter value corresponds to 30% from that one of the culet, hence the electrode diameter is selected according to this value. The sample can be placed together with ruby chips (Al_2O_3:Cr^{3+}) that work as gauges to determine the pressure in the chamber through of the fluorescence emission of the R1 line. To provide hydrostatic conditions a pressure transmitting medium (PTM) is required in order to fill the volume created by the hole. The PTMs with higher hydrostatic levels are helium and neon that even at pressures around 50 GPa remain with pressure gradients less than 0.5 GPa (less than 1%) [104]. However, liquids PTMs as 4:1 methanol-ethanol mixture which remaining hydrostatic until 10.5 GPa can be used due to its easy handling. In the case of solid PTMs, those introducing shear forces and high compressibility are more used, as NaCl, KCl, KBr (soft solids) [105, 103].

The diamond anvil cells can have different designs depending on the force-generating mechanisms. The simplest devices are those controlled manually, as lever-arm or of force generation through bolts. However to attain a specific pressure value, the control is not very accurate. In addition the DAC must be removed from the probing position to be tightened when pressure is increased. By contrast to this, a pneumatic mechanism allows to change the pressure smoothly and remotely by tuning the gas pressure of a ring-like membrane that acts on the diamond support (piston) [103]. The Figure 2.5 shows the DACs having force generation via screws (a) and pneumatic together with the gas supplier (b).

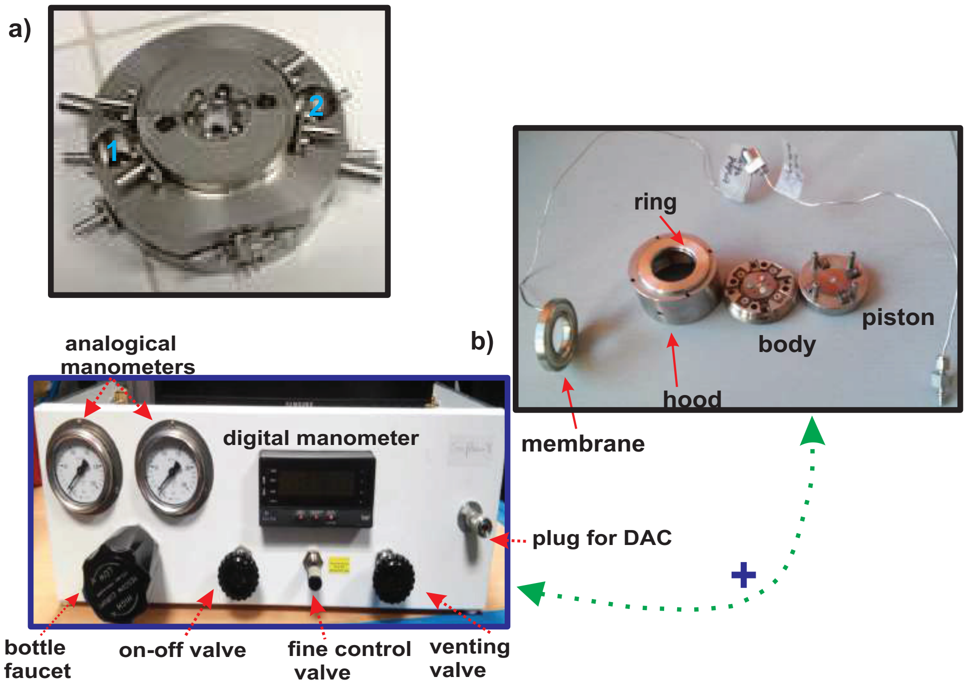

Figure 2.5 – a) DAC controlled by tighten screws/bolts mechanism (the number 1 and 2 in blue indicate the entrance for bolts (adapted from [106]). b) The left image shows the gas supply system for the DAC (right image) controlled by pneumatic mechanism, besides the components of gas supply + DAC system (blue cross) are also shown.

The commonly method used to measure the pressure values inside the DAC is the calibration from ruby fluorescence emission R_1. The ruby R_1 fluorescent line undergoes a blueshift (higher energies) upon pressure application. Equation 2.1, which is valid until 80 GPa with a incertitude of about 5% gives the calibration law [107].

$$P(\mathrm{GPa}) = \frac{1904}{7.665}\left\{\left[1+\left(\frac{\Delta\lambda}{\lambda_0}\right)\right]^{7.665}-1\right\}, \tag{2.1}$$

in this equation the pressure is obtained in GPa, the values 1904 and 7.665 are the calibration parameters, $\lambda_0 = 694.2$ nm is the R_1 wavelength at ambient pressure and $\Delta\lambda$ is the shift of R_1 due to pressure.

In Raman spectroscopy is more common to use the wavenumber $\bar{\nu}$ (cm^{-1}) instead of wavelength λ(nm). In order to express eq. 2.1 in terms of excitation wavelength (λ_{laser}) and $\bar{\nu}$, we need rewrite this equation as

$$\begin{aligned} P(\text{GPa}) &= \frac{1904}{7.665}\left\{\left[\underbrace{1+\left(\frac{\Delta\lambda}{\lambda_0}\right)}_{=\gamma}\right]^{7.665} - 1\right\} \\ &= \frac{1904}{7.665}\left\{\left(\frac{\lambda_f}{\lambda_0}\right)^{7.665} - 1\right\}, \end{aligned} \tag{2.2}$$

where λ_0 and λ_f are respectively the initial and final wavelengths of the R_1 emission band. A pratical writting of the above expression, when using a Raman spectrometer is:

$$P(\text{GPa}) = \frac{1904}{7.665}\left\{\left[\frac{\frac{10^7}{\lambda_{\text{laser}}} - \Delta\bar{\nu}_0}{\frac{10^7}{\lambda_{\text{laser}}} - \Delta\bar{\nu}_f}\right]^{7.665} - 1\right\}, \tag{2.3}$$

with $\Delta\bar{\nu}_i$, $\Delta\bar{\nu}_f$ the ambient pressure and measured wavenumber at pressure P respectively and λ_{laser}, the excitation wavelength given in inverse centimeters (cm^{-1}) and nanometers (nm), respectively.

An example of ruby fluorescence spectra measured in a Raman spectrometer is shown in Fig.2.6.

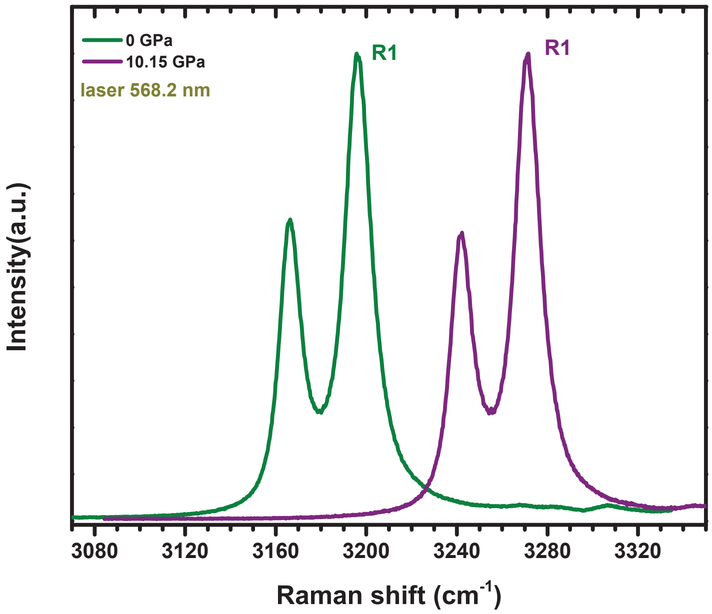

Figure 2.6 – Shift of ruby fluorescences lines R1 with pressure measured in a Raman spectrometer when at using a laser excitation of 568.2 nm (2.18 eV).

2.3.2 Transmission electron microscope

Historically transmission electron microscopy (TEM) was developed to overcome the image resolution limitation of optical microscopes, which is imposed by the wavelength of visible light and whose magnification is about 1000 times. Electron microscopes can reach magnifications of the order of 10^6. The first manufactured TEM was developed by Max Knoll and Ernst Ruska (1932). They manufactured the first TEM with resolution greater than light in 1933 and the commercial TEMs were first produced only 4 years after. The Metropolitan-Vickers EM1 was the first of such instrument and was produced in the UK in 1936, however it didn't work properly and the regular production of TEMs for sale was really initiated by Siemens and Halske in Germany in 1939. After the end of World War II several others companies as Hitachi, JEOL, Philips and RCA started their productions [108].

The TEM basic operational principle is based on transmission of electron beams through a specimen to form an image. A TEM equipment is shown in Figure 2.7(a). A TEM is composed of several components, which include an electron emission source (electron gun) that is connected to a high voltage source ($\sim 100 - 300$ keV), a vaccum system (airlock) that permits the beam travel through the instrument undisturbed (increasing the mean free path) and keeps the specimen clean, a specimen stage to insert the sample holder (arm + TEM grid), a series of electrostatic plates and electromagnet lenses that guide the electron beams and a viewing screen (fluorescent) as well as CCD camera. All these components are assembled along of a column Figure 2.7(b).

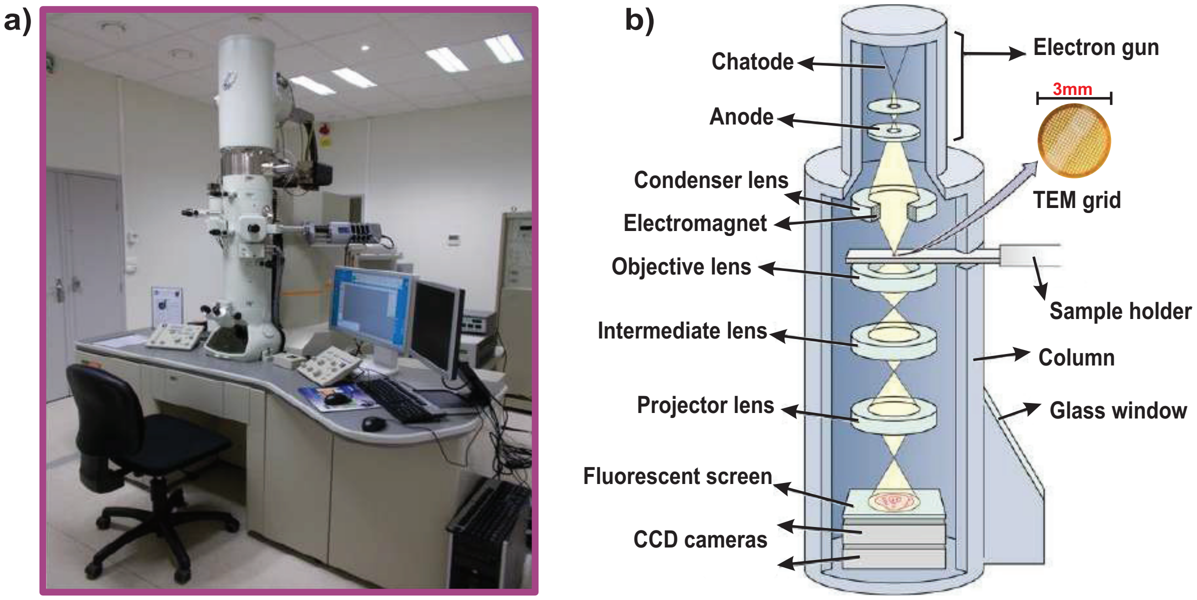

Figure 2.7 – a) TEM JEOL JEM-2100F from the Centre Technologique des Microstrcutures (CTμ) of Lyon1. b) Layout of components in a basic TEM.

The sample preparation in TEM can be a challenge, as specimens should be less than 100 nm thick, thus making sample size the major limitation for TEM characterizations. Thereby, some preparation protocols can be useful depending of the specimen kind (solids or liquids), bulk sample, thin films, fibers or powders. A short scheme about sample preparation is shown in Fig 2.8. For biological samples a cutting technique from material sections in thin slices (microtome) is usually used.

In particular, the specimens in powders or in buckypaper shape (nanotubes) with about few microns[1] were prepared following a simple procedure:

---

[1] obtained in this thesis after a pressure cycle in a diamond anvil cell.

1. the specimen directly recovered from the DAC gasket or from the diamond culet is placed in a microtube (eppendorf) or small glass bottle and if possible visualized under optical microscope to confirm its presence and position;
2. by means of a micropipette (maximum volume 2μL) some liquid drops (preferably ethanol absolute anhydrous) are spilled dispersing a little the sample in the container;
3. the set is stirred in an ultra-sonication bath of low power for about 20 min, in order to homogenize and improve the sample dispersion;
4. lastly the liquid + specimen pieces are pumped with a micropipette and dropped on the TEM grid, and waiting a time for the liquid evaporation.

TEM imaging is usually obtained via two different methods: **a)** through the electron diffraction pattern, which is formed in the focal point of the objective and collected on a sensitive screen after that the electrons beam to cross the sample or **b)** by a charge-couple device, which uses the Fourier transform of the electron diffraction (magnetic lenses works in the beam convergence) to form a plane sample image. Thus, all times the crystallographic information as well as the analytical can be related to the image of the sample. It is important noting that TEM images interpretation requires certain attention as it presents us 2D images of 3D specimens. In other words, a single TEM image does not provide depth sensitivity.

However, to overcome this limitation some TEM apparatus provide specialized holder designs with the capability to move the specimen in high angles, called tilt sample holders. The combination of a sequence of images taken at different tilts and improved by reconstruction software can create a 3D image of the sample, this technique is known as electron tomography.

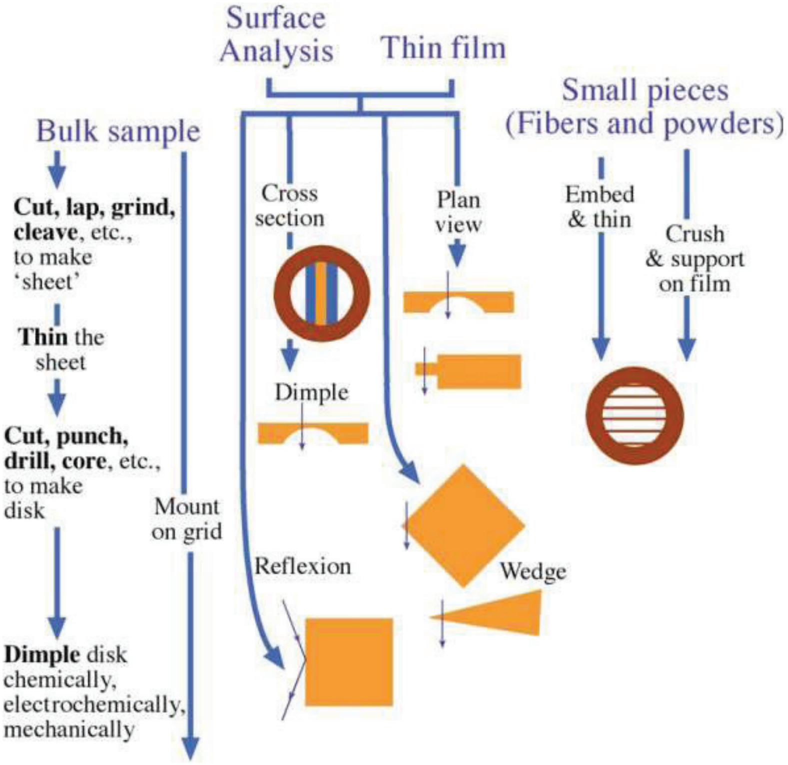

Figure 2.8 – Flow chart of sample preparation for solid phase TEM investigations, adapted from [108].

2.4 Experimental setup for Raman spectroscopy and TEM

2.4.1 Theoretical Basis of Raman Scattering

When the electromagnetic radiation (ER) interacts with matter, this radiation may be absorbed or scattered, or may not interacts with the material and simply pass through it. Thus, to study different kinds of radiation (ER) on the matter, there are several spectroscopies techniques dedicated to each electromagnetic frequency region and of which the Raman spectroscopy is part. We show in Table 2.1 some technical aspects of these techniques

Table 2.1 – Spectral regions and their origins.

Spectroscopy technique	Radiation range ($\bar{\nu}$,cm^{-1})	Origin
Gamma ray	10^{10} – 10^{8}	Rearrangement of elementary particles inside of nuclei
X-rays (EDX, XPS)	10^{8} – 10^{6}	Transitions between the energy levels of inner electrons of atoms and molecules
UV-visible	10^{6} – 10^{4}	Transitions between energy levels of valence electrons of atoms and molecules
Raman and Infrared	10^{4} – 10^{2}	Transitions between vibrational levels (change of configuration)
Microwaves	10^{2} – 1	Transition between rotational levels (change of orientation)
Electron spin resonance (ESR)	1 – 10^{-2}	Transition between the spin levels in magnetic field
Nuclear magnetic resonance (NMR)	10^{-2} – 10^{-4}	Transition between nuclear spin levels in magnetic fields

The Raman spectroscopy, basically, it is a phenomenon of scattering of a incident monochromatic light on some material medium, the light arising from this scattering is polychromatic. Much of the scattered light is not modified, having the same feature from that incident monochromatic, and the name of this process is **elastic scattering** or **Rayleigh**. A small quantity of the light undergoes the **inelastic scattering** or **Raman** (1 in every 10^{6} – 10^{8} photons[2]).

Historically, the Raman scattering has been described in terms of both classical and quantum theories. The classical is based on wave theory of light (classic electromagnetism) is incomplete, in the sense that it does not take into account the quantum nature of the molecular vibrations. In addition to not being able to explain in more details the relation between molecular properties and the Raman spectra nature as quantum theory.

From now on, we introduce the two theoretical aspects (classical and quantum) of the spectroscopy Raman. Starting by the wave theory treatment and following to the quantum approach, which considers the light as a particle – photon – with discrete energy.

The classical description of Raman scattering is illustrated in Fig., it shows a induced polarization in a molecule through the oscillating electric field of a monochromatic light. This field induces

---

[2] explained later in text

a dipole, which in turn radiates the scattered light, with ou without energy exchange with the molecule vibrations. The induced polarization force (induced dipole momentum), P, is given by the polarizability, α, and an external electric field, E:

$$\vec{P} = \overset{\leftrightarrow}{\alpha}\vec{E}. \tag{2.4}$$

In the matrix form the equation 2.4 becomes,

$$\begin{Bmatrix} P_x \\ P_y \\ P_z \end{Bmatrix} = \begin{Bmatrix} \alpha_{xx} & \alpha_{xy} & \alpha_{xz} \\ \alpha_{yx} & \alpha_{yy} & \alpha_{yz} \\ \alpha_{zx} & \alpha_{zy} & \alpha_{zz} \end{Bmatrix} \begin{Bmatrix} E_x \\ E_y \\ E_z \end{Bmatrix}. \tag{2.5}$$

In both classical and quantum treatments of the Raman scattering the equation 2.4 is used. The classical treatment follows the effects of molecular vibrations due to polarizability α. So, we start by considering a incident electric field in the form:

$$E = E_0 \ \cos 2\pi\nu_0 t, \tag{2.6}$$

where ν_0 is the source light frequency (laser). The molecular vibrations, usually are composed of normal modes Q_k, of which 3N-6 (or 3N-5 for a linear molecule) can be found in a molecule with N atoms and these modes are given as

$$Q_k = Q_k^0 \ \cos 2\pi\nu_k t, \tag{2.7}$$

where ν_j is the harmonic frequency of mode normal j-th. The polarizability of electrons in the molecule will be modulated by molecular vibration, thus it can be expended in Taylor series as a function of normal coordinates (Q_j) around the equilibrium point, that is

$$\begin{aligned} \alpha_{ij} &= (\alpha_{ij})_0 + \sum_k \left(\frac{\partial \alpha_{ij}}{\partial Q_k}\right) Q_k + \frac{1}{2!}\sum_{k,k'} \left(\frac{\partial^2 \alpha_{ij}}{\partial Q_k \partial Q_{k'}}\right) Q_k Q_{k'} \\ &+ \frac{1}{3!}\sum_{k,k',r} \left(\frac{\partial^3 \alpha}{\partial Q_k \partial Q_{k'} \partial Q_r}\right) Q_k Q_{k'} Q_r \ldots . \end{aligned} \tag{2.8}$$

Beginning from the equation 2.4, the induced dipole is the product between the eqs.2.6, 2.8. For small variations of Q_k, taking into account the trigonometric relation $\cos a \cos b = \left[\cos(a+b) + \cos(a-b)\right]/2$ and that the high order terms can be left aside in 2.8, we can write

$$P = (\alpha_{ij})_0 E_0 \cos 2\pi\nu_0 t + E_0 Q_k^0 \left(\frac{\partial \alpha_{ij}}{\partial Q_k}\right)\left(\frac{\cos 2\pi(\nu_0+\nu_k)t + \cos 2\pi(\nu_0-\nu_k)t}{2}\right) \tag{2.9}$$

After we have assumed (classically) that the polarized electrons will radiate light in the oscillation frequencies, the equation 2.9 demonstrates that the light will be scattered in three frequencies. The first term corresponds to Rayleigh scattering, which is in the same laser frequency and has magnitude proportional to $(\alpha_{ij})_0$, inherent polarizability of the molecule. The second term is the anti-Stokes Raman scattering, that happens at $\nu_0 + \nu_k$, and the third term is the Stokes scattering at $\nu_0 - \nu_k$. The transitions associated with the Rayleigh and Raman scatterings make part of quantum nature of the vibrations, however we will extract some informations from classical construction.

In order to have contributions from second term of eq. 2.9, it is necessary that $\frac{\partial \alpha_{ij}}{\partial Q_k} \neq 0$, in other words, only the vibrations that change the polarizability contribute to the Raman scattering. This statement is the base for the first selection rule of Raman activity. Another fact that arises is $\frac{\partial \alpha_{ij}}{\partial Q_k}$ changes significantly for different molecules and vibrational modes, taking to huge variations in the Raman scattering intensity.

The Raman intensity observed is proportional to the scattering cross section, σ_k, with measure unit of area (cm^2) per molecule. The magnitude of σ_k is related to $\frac{\partial \alpha_{ij}}{\partial Q_k}$ and a direct consequence is the variation of intensity Raman, I$_R$ (frequency dependent), be given by

$$I_R = \mu(\nu_0 \pm \nu_k)^4 \alpha_{ij}^2 Q_k^2, \tag{2.10}$$

where μ is a constant. By equation 2.10, we can realize that the Raman intensity change with the fourth power of the observed frequency for a normal Raman scattering, which in turn depends of laser frequency. The fourth power factor arises from the classic scattering treatment of a oscillating induced dipole, where the intensity has unit of watts (W). Thus, we could advance on this reasoning line and get more insights about Raman scattering from the point of view of classical theory. Meanwhile, as aforementioned, there are some limitations when dealing with the vibrational nature in this line, one of them that can not explained classically, is the intensity difference between the Stokes and anti-Stokes scatterings observed experimentally.

Now, we begin to deal with quantum approach. According to the quantum mechanics, when a molecule interacts with incident photon, a energy transfer happens from the photon to molecule, written in form

$$\Delta E = h\nu = h\frac{c}{\nu} = hc\bar{\nu}. \tag{2.11}$$

The equation 2.11 shows the energy difference between two quantized states, comparing the energies orders express in terms of wavenumber (common in spectroscopy) $\bar{\nu}$ (cm^{-1}), λ (cm) and ν (Hz). By this equation, we can understand better as happen the Rayleigh and Raman scattering mechanisms.

The Raman lines intensity is given by changes in molecular polarizability during the vibrational transitions. The element of polarizability tensor α_{ij} for a transitions of initial vibronic state m to final vibronic state n is written by quantum mechanics as,

$$(\alpha_{ij})_{nm} = |\psi_m\rangle \alpha_{ij} \langle \psi_n| = \int_{-\infty}^{\infty} \psi_n^* \alpha_{ij} \psi_m d\tau, \tag{2.12}$$

where $\psi_{m,n}$ are vibronic wavefunctions from initial and final states. This indicate that the Raman scattering involves a two-photon process and it will be clear when show a general form of the molecular polarizability.

In case of small molecular vibrations, we use again the expansion in Taylor series for the polarizability in the normal coordinates for derivatives taken in a equilibrium geometry of molecule. So, combining the eqs. 2.8 and 2.12 and neglecting high order terms, it follows

$$(\alpha_{ij})_{mn} = (\alpha_{ij})_0 \int_{-\infty}^{\infty} \psi_n^* \psi_m d\tau + \left(\frac{\partial \alpha_{ij}}{\partial Q_k}\right)_0 \int_{-\infty}^{\infty} \psi_n^* Q_k \psi_m d\tau, \tag{2.13}$$

The first term in eq.2.13 correspond to the Rayleigh scattering, and the second term provides the Raman scattering, if two conditions are satisfied (without resonant conditions):

1. the polarizability derivative $\left(\frac{\partial \alpha_{ij}}{\partial Q_k}\right) \neq 0$, i.e, the molecular polarizability must change during a particular vibrational transition;

2. the integral $\int_{-\infty}^{\infty} \psi_n^* Q_k \psi_m d\tau \neq 0$. This condition requires that the vibrational quantum number of transition differs by 1 for Stokes scattering and -1 for theanti-Stokes.

The scattered intensity in a Raman experiment is proportional to the overall power emitted by the induced dipole moment, hence the p-th Stokes line is given by

$$I_p = I_0 N_{\omega_i} \overbrace{\frac{2^7\pi^5}{3^2c^4}\frac{\hbar}{\omega_i}(\omega_0 - \omega_i)^4 \frac{1}{e^{-\hbar\omega_i/kT} - 1} \sum_{i,j} |(\alpha_{ij})_p|^2}^{=\sigma_p}, \tag{2.14}$$

where I_0 and ω_0 are the intensity and frequency of incident photon (laser), respectively. The σ_p is the Raman cross-section, $|(\alpha_{ij})_p|^2$ is modulus squared of the probability amplitude, N_{ω_i} is the molecules number in the vibrational state i with frequency ω_i, c is the light speed, and $\hbar = h/2\pi$ is the Planck constant. The term $\frac{1}{e^{-\hbar\omega_i/kT}-1}$ is the vibrational partition function for photons (the photons are bosonic particles, which in turn are ruled by a distribution function (Bose-Einstein) provided in the statistical mechanics).

Based on quantum mechanics and in particular perturbation theory, Kramer and Heisenberg (1925) and Dirac (1927) derived a quantum description (KHD expression) of molecular polarizability tensor (**here the (i,j) and (m,n) indexes pair are substituted by (p,q) and (f,i), respectively**):

$$(\alpha_{pq})_{fi} = \sum_r \left\{ \frac{\langle\psi_f|\mu_p|\psi_r\rangle\langle\psi_r|\mu_q|\psi_i\rangle}{\hbar\omega_{ri} - \hbar\omega_0 - i\Gamma_r} + \frac{\langle\psi_f|\mu_q|\psi_r\rangle\langle\psi_r|\mu_p|\psi_i\rangle}{\hbar\omega_{rf} - \hbar\omega_0 - i\Gamma_r} \right\}, \tag{2.15}$$

where p and q are the incident and scattered polarization directions, while ψ_i, ψ_r and ψ_f refer to the initial, intermediate, and final states of the Raman scattering process. ω_0 is the laser frequency, ω_{ri} and ω_{rf} quantify the energy differences between the respective states. The damping constant Γ_r is introduced phenomenologically in order to mimic the line widths of band profile. In particular, the resonant Raman scattering occurs for the excitation wavelength chosen to be resonant with a molecular electronic transition, which approaches the denominator of the first term of the eq. 2.15 to a small value and this term dominantly contributes to the molecular polarizability tensor and then to the Raman scattering.

For case of the Stokes Raman scattering process, a molecule in its ground state is excited by a photon with energy $h\nu_0$ and is promoted to a virtual state, which is not necessarily a true quantum state (as a electronic state), but may be considered a distortion very quick from electronic cloud. At followed the molecule passes to *nth* excited vibronic state $h\nu_n$ and a photon is scattered in the process, having lower energy than that incident photon $h\nu_0 - h\nu_n$. For the anti-Stokes Raman scattering, the molecule is in a excited vibronic state and by interacting with a incident photon of energy $h\nu_0$, it is promoted to the ground state with a scattered photon of energy $h\nu_0 + h\nu_n$ to the process end. It is important to underline that the processes described here (Stokes and anti-Stokes) are non-resonant, thus a priori the electronic energy levels of molecule are not excited.

In the Rayleigh scattering, the molecule in its ground state is excited by a incident photon ($h\nu_0$) and undergoes a transition to virtual state. At followed the molecule returns to the its ground state and a photon is re-radiated with same energy of that incident ($h\nu_0$). The Figure 2.9 illustrates the Rayleigh, Stokes and anti-Stokes scattering mechanisms.

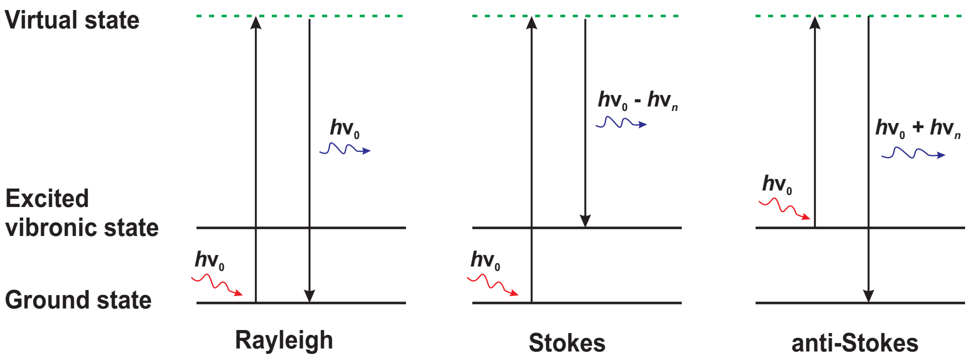

Figure 2.9 – Schematic diagram of elastic (Rayleigh) and inelastic (Stokes and anti-Stokes) scattering processes.

2.4.2 Raman at high pressure

Thanks the wide transparency in the electromagnetic spectrum and hardness, the diamond anvils allow the illumination of sample by different photon energies, among them the visible light (laser), which is widely used in most conventional micro-Raman spectrometers for Raman high pressure experiments. Below, we show these devices used to study the samples in this thesis (in all experiments the beam laser was focused with 50x magnification objective lens), Table 2.2. The laser power at source was tuned by means of optical filters according to the necessity of each experiment and sample. It is worthy to mention that the mirrors from our different setups also causes a loss of throughput, however not as important as the filters. The Figure 2.10 provides a sketch of a common Raman spectrometer used to carry out experiments at high pressures.

Table 2.2 – Micro-Raman spectrometers used in this thesis. More experimental details in Annex A.1.

Sample	**Raman spectrometer**	**spectral resolution** (cm^{-1})	**laser type and power**	
SWCNTs	Acton 2500i	1	514 nm argon-ion	15 mW
	LabRAM HR800	0.6	568.2 nm krypton-argon	2.10, 3.3 and 8 mW
	LabRAM HR Evolution	0.5	532 nm state solid	$\ll$ 15 mW
TWCNTS	Acton 2500i	1	514 nm argon-ion	15.4 mW
	LabRAM HR Evolution	0.5	532 nm state solid	$\ll$ 15 mW
BNMWTs	Acton 2500i	1	514 nm argon-ion	20 mW
	LabRAM HR Evolution	0.5	532 nm state solid	< 20 mW

The Figure 2.11 displays the heating tests on samples used in our studies (see Table 2.2). For this purpose, the spectra were collected by Acton 2500i Raman spectrometer with 514 nm laser

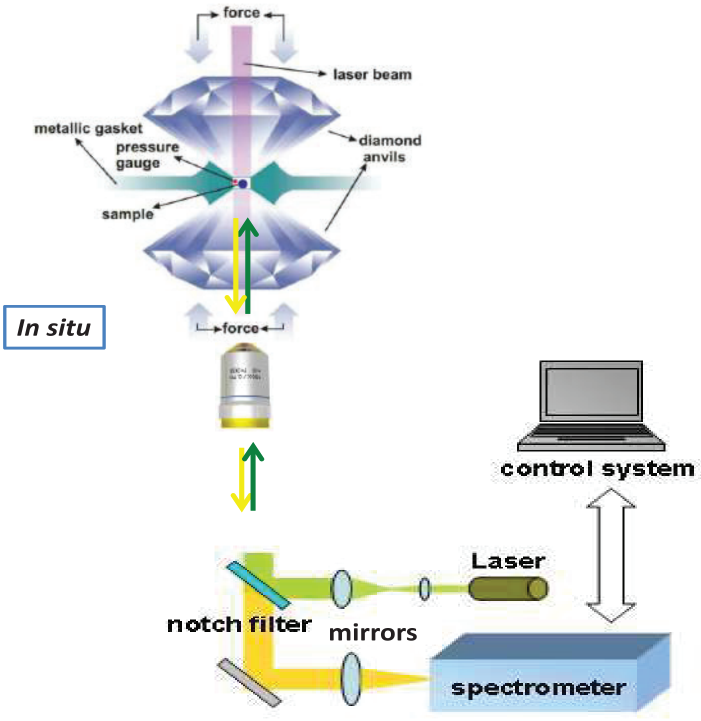

Figure 2.10 – Diagram of a typical Raman spectrometer for high pressure experiments in backscattering geometry (adapted from internet).

energy. The labels ascribed in the figures by 1st and 2nd filters mean the obstruction levels for the laser in our filter wheel from our Raman set-up (there are 3 levels). Thus, 1st filter blocks more the laser power, whereas the 2nd filter lets pass a little bit more of power.

In fact, before and after each experimental characterization we have optimized the laser power on samples in order to avoid the heating effects in our spectral signals.

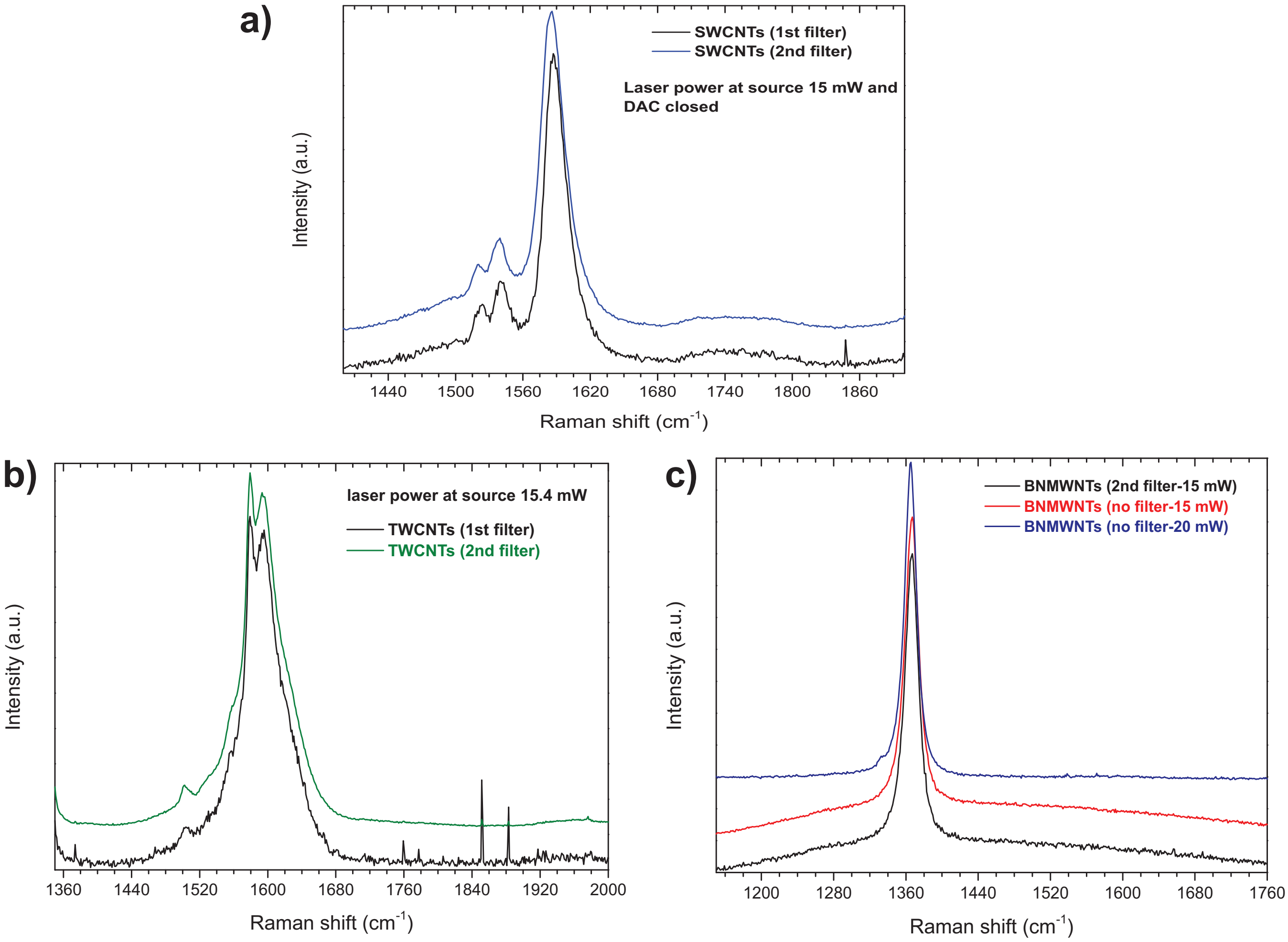

Figure 2.11 – a) Comparison between the G-band spectra of SWCNTs collected with the laser power of 15 mW, taken in different filters. b) Comparison between the G-band spectra of TWCNTs collected with the laser power of 15.4 mW, taken in 1st and 2nd filters from our set-up. c) Tangential modes comparison of BNMWNTs using the intermediate filter and no filter.

2.5 Transmission electron microscopes

All samples characterized in this work were transfered by means of procedure described in the subsection **2.3.2**: a dispersion in ethanol, followed by ultrasonication of low power and dropping on the TEM grid (see Figure 2.12 a)). The TEM tomography was used to investigate the recovered samples of BNMWNTs and a sketch is displayed in Figure 2.12 b).
The table 2.3 summarizes the transmission electron microscopes that we have used,

Table 2.3 – TEM equipments. For more details see Annex A.2.

Sample	**TEM model**	**acceleration** (kV)	**exposure time** (s)	**emission source**
SWCNTs	JEOL 2100	80 and 200	2.0 and 1.0	LaB_6
TWCNTS	JEOL 2100	120	1.0	LaB_6
BNMWTs	JEOL JEM-2100F	200	0.5 and 1.0	FEG

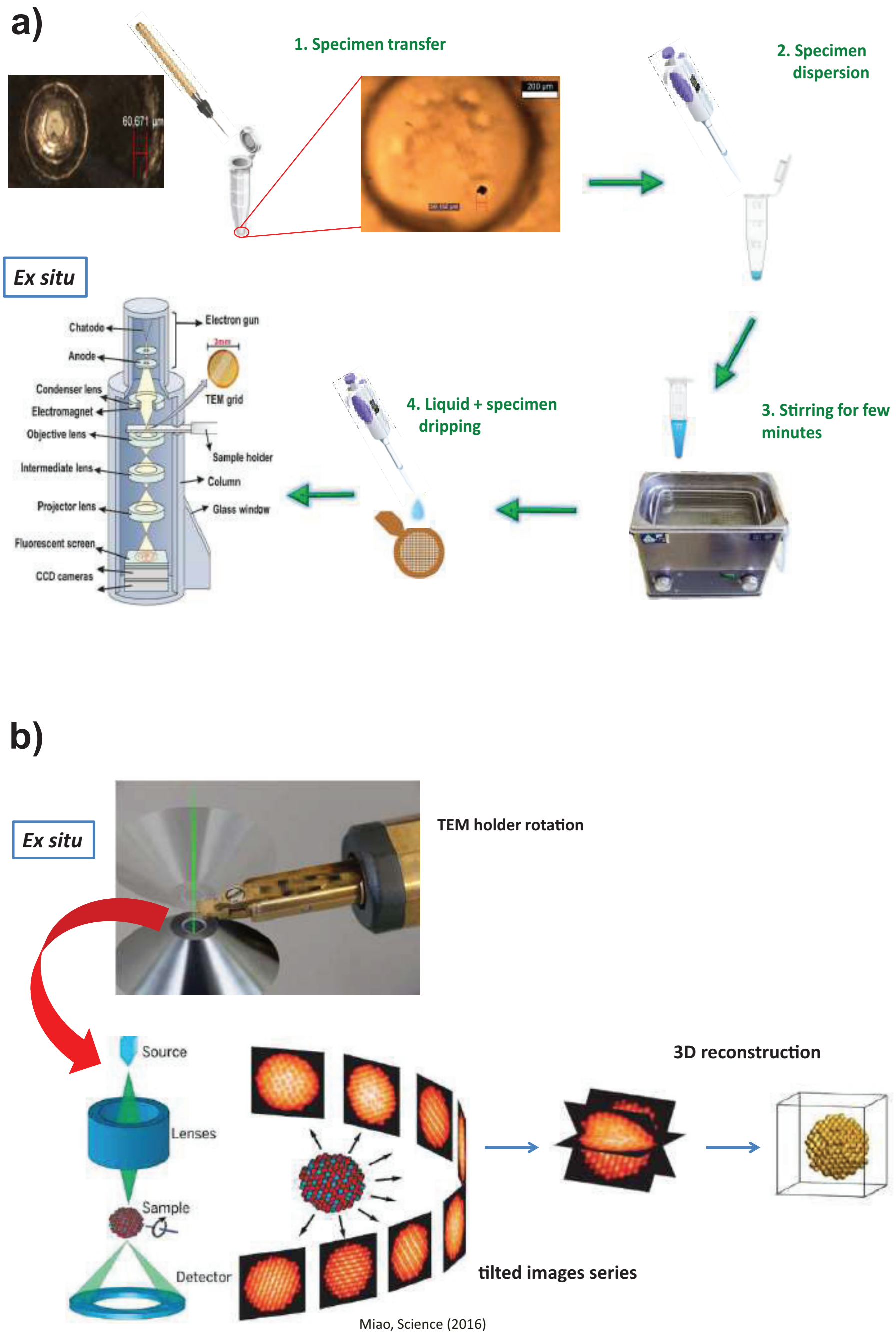

Figure 2.12 – a) Schematic diagram about the transfer method of samples for *ex situ* TEM characterization. b) Illustration of the TEM tomography characterization for recovered samples of BNMWNTs (adapted from [109]).

3

(6,5)-Enriched single walled carbon nanotubes at high pressure

Sommaire :

3.1 Introduction 62

3.2 Sample preparation. Aqueous Two-Phase (ATP) separation method 62

  3.2.1 (6,5) SWCNTs enrichment 63

3.3 High pressure study. Results and discussion 66

  3.3.1 Radial breathing modes - RBM 70

  3.3.2 Tangential modes - G bands 77

  3.3.3 Reversibility limits of (6,5) SWCNTs 80

  3.3.4 Conclusions 85

3.1 Introduction

In this first chapter we will explore the high pressure response of low diameter SWCNT in different environments. The study will include both individualized and bundled tubes and different pressure transmitting media. For this we concentrate on the high pressure behavior of (6,5) chirality-enriched SWCNTs. Both water filled and empty tubes were probed. Chirality selection is obtained by means of aqueous two-phase (ATP) method and the high pressure behavior is investigated by resonant Raman spectroscopy. The collapse pressure domain was studied and further compression allowed us to reach the irreversible structural transformations of the tubes. TEM images from the recovered samples provided additional information on the structural evolution for this low-diameter single-wall carbon nanotubes.

This chapter is organized in two main sections. In the first one (3.2) we detail the methods and protocols to produce the (6,5) enriched samples. This was the subject of the thesis of Aude Stolz in our team [110]. We thought that it was important to make a description of the chirality selection method in order to understand the detail characteristics of the different samples studied in this thesis. The high pressure study on these samples is then presented in the following section (3.3) including *in situ* Raman and *ex situ* TEM characterizations. We will first consider the information from RBM, then for tangencial modes and finally discuss the irreversible transformation including the valuable contribution of TEM images.

3.2 Sample preparation. Aqueous Two-Phase (ATP) separation method

As discussed in Chapter 2, the different synthesis methods of SWCNTs do not allow to provide samples exhibiting a single chirality. The ATP method has been used to separate single-wall CoMoCAT carbon nanotubes selecting particular chiralities. ATP is based on the spontaneous redistribuition of the carbon nanotubes into two aqueous solutions with relatively different hydrophobicity. The two phases are formed by mixing two water-soluble polymers, such as polyethylene glycol (PEG) and dextran. In the demixed liquid, the bottom phase, rich in dextran, is more hydrophilic than the top phase, which is mainly constituted of PEG [111, 112].

The two-phase aqueous procedure for enrichment of (6,5) single-walled carbon nanotubes used in this theses has followed basically the protocol established by Subbaiyan *et al.* [111, 113], however with subtle adaptations on the initial samples rate and pre-dispersion conditions Ref.[110]. The precursor nanotubes (which we will refer as **Stock** in the following) marketed by Sigma-Aldrich Co. LLC., under the specification SWeNT SG65i, contain mostly (6,5) single wall carbon nanotubes ($\geq$ 40% of (6,5) tubes with 93% of the semiconducting nanotubes present in total weight). The Stock sample is presented as a dried powder. The tubes themselves are prepared by Catalytic Chemical Vapor Deposition method (CoMoCAT CVD) which uses the cobalt and molybdenum chemical elements as catalysts. These *bundled* nanotubes have different chiralities providing diameters in the 0.7-0.9 nm range. In Figure 3.1(a) is shown the photoluminescence characterization of our Stock sample in which five different chiralities were detected: (6,4), (6,5), (7,3), (7,5) and (8,3). These chiralities are in good agreement with previous studies following the same protocol [114, 111]. The Raman spectroscopy characterization of the samples is in good agreement with photoluminiscence and will be further discussed at the end of this section. Various TEM images of the Stock sample are also shown in Figure 3.1(b-d). Despite the high percentage in SWCNTs, some residual material as catalysts particles or others carbon forms (amorphous or nanocages) may be found in the samples (Figure 3.1.c). The precise determination of the chirality distribution given by the TEM setup is complicated in particular due to the lack of resolution and also due to the creation of defects by knock-on effect.

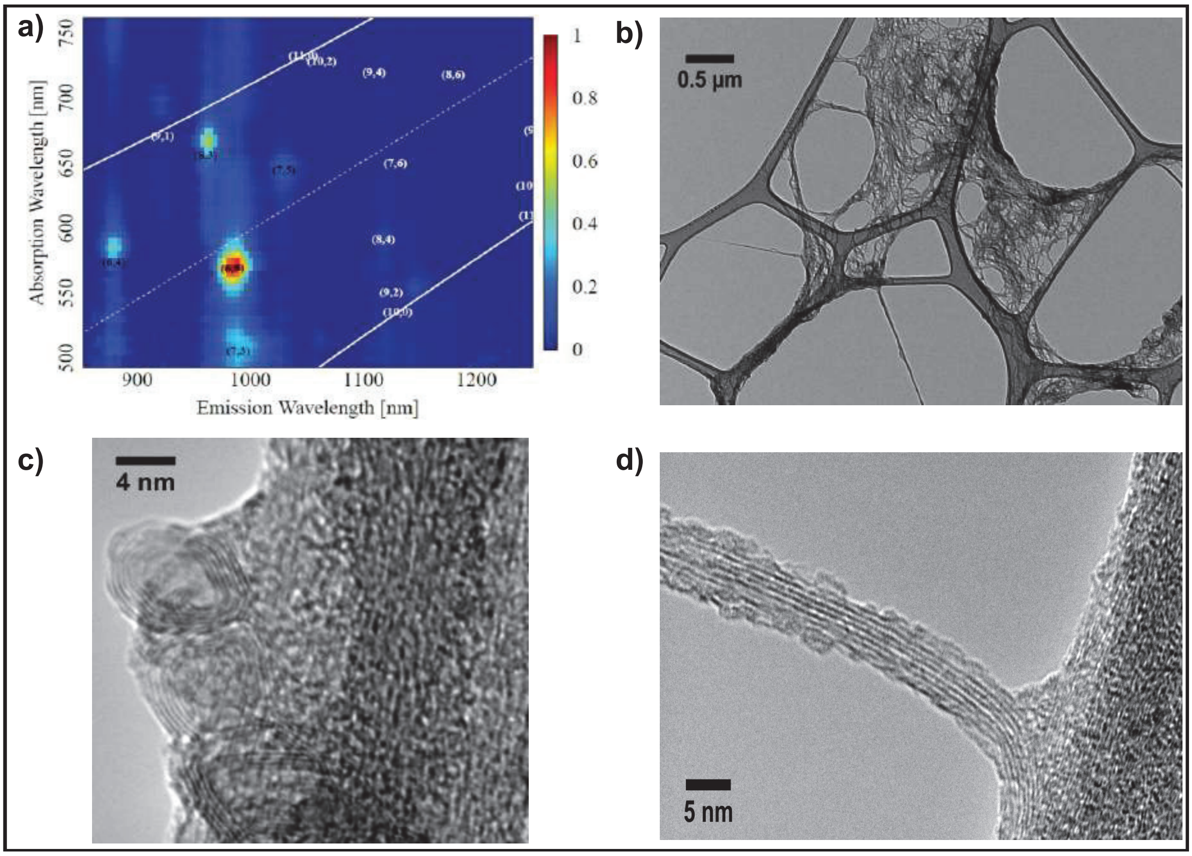

Figure 3.1 – a) Photoluminescence characterization of Stock sample. b) TEM image shows the dispersion of bundled SWCNTs of the Stock suspended on carbon films of the TEM grid. c) TEM image of a nanocages or nano-onions present in the Stock specimen. d) Bundle of few SWCNTs of Stock wrapped by a residual material left during the synthesis process.

3.2.1 (6,5) SWCNTs enrichment

Starting from the above described Stock sample, the first step of the chirality enrichment process is to individualize the nanotubes from the bundles by using a surfactant solution. Starting from the (6,5) SWCNTs Stock sample, a pre-dispersion of the sample was done in an aqueous solution of sodium deoxycholate (DOC) in 1% mass by volume (m/v), achieving a final concentration at nanotubes of 1mg/mL. This mixture was placed in an ice bath and submitted to the ultrasound treatment with the use of an ultrasonic tip during 1h for homogenization. Ultrasonication makes possible at the same time that already at this step some nanotubes are broken, becoming then opened-end tips, which in turn favors the tubes filling by water. The next step is the aqueous two-phase (ATP) separation process itself, in which two immiscible polymers - polyethylene glycol

(PEG) and dextran - both soluble in water, were prepared together with different concentrations of the SC, SDS, DOC surfactants and salt (NaCl-sodium chloride). For this purpose, two solutions Stock-1 and Stock-2 were created under the following conditions, described below (see Table 3.1).

Table 3.1 – The concentration of the Stock-1 and Stock-2 solutions.

Reagents	Stock-1	Stock-2
PEG-MW 6.000	56.4 g	29.0 g
dextran-MW 64.000-76.000	19.6 g	4.66 g
SC	1.96 g	—
SDS	4.46 g	3.60 g
DOC	—	0.095 g
NaCl	0.56 g	—
distilled water	400 mL	200 mL

After one overnight of dissolution, the ATP separation was iniciated by adding 8 mL of the SWCNTs pre-dispersion, 16 mL distilled water and 153 mL of Stock1. Along the process, the initial solution - SWCNTs-DOC dispersion + water + Stock1 - was centrifuged, in order to speed up the separation in two phases which we name Bottom 1 and Top 1 (see Fig.3.2). The product named Bottom 1 was then added to Stock 2 to be centrifuged, thus obtaining a highly (6,5) chirality-enriched phase of *individualized* tubes, called **Top 2**. The scheme below shows the process steps,

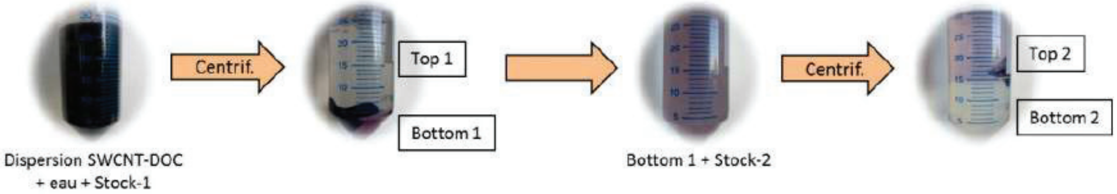

Figure 3.2 – The sequential steps of our ATP process.

The confirmation of the almost single (6,5) chirality in Top 2 solution was obtained through different characterization techniques, as photoluminescence (PL) and UV-visible absorption spectroscopy (UV-vis). The obtained results are provided in Fig. 3.3.

The addition of inorganic salt (NaCl or $MgCl_2$) to the individualized (6,5) enriched SWCNTs in Top 2 solution allowed the rebundeling of the nanotubes. Basically, the higher electric permeability of the salty solution screens the electrostatic repulsion between anionic surfactants wrapping the SWCNTs and then favoring bundling.

After the formation of chirality enriched nanotubes bundles, the solution follows a filtration process, in which the SWCNTs bundles are filtered by a membrane (pore size 0.1 microns-PTFE-

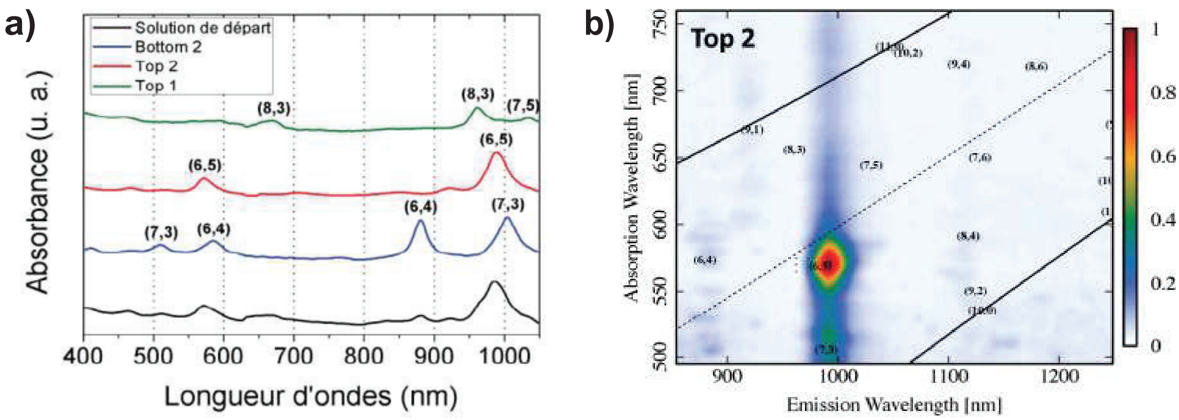

Figure 3.3 – a) The graph shows the UV-visible spectra of each solution along of ATP process (labeled colorful lines in the graph caption) with the chiralities proportions at each phase. b) The red circle shows the high ratio of (6,5) chirality SWCNTs in Top 2 solution when probed by photoluminescence technique. Other chiralities as (7,3), (8,3), (6,4) and (7,5) can be found at low ratios. Adapted from [110].

Merck Millipore). Throughout the filtration process successive and repeated washing with water, ethanol and acetone was performed, in order to try to remove as much as possible polymers, surfactants and salt. At then end, a thin film of bundled carbon nanotubes (buckypaper) was formed on the membrane filter and the (6,5) bundled SWCNTs dried bucky sample was isolated with a spatula that scraped off the thin film from the membrane. The final samples obtained from this method (later referred as **Set 1** and **Set 2** for different purifications protocols) consist on buckypaper scraps.

A number of characterizations were done in order to verify the efficiency of polymer and surfactant removal after the filtration process in order to select the best samples. Thermogravimetric analysis (TGA), infrared spectroscopy (IR) as well as transmission electron microscopy (TEM) techniques were used showing always the presence of bundles and of some residual surfactant/polymer around the bundles (for more details see [110]).

Based on the aforementioned purification post-treatment process, we have chosen two different protocols, including thermal treatments, to improve the buckypaper quality:

- **Set 1** : Heating during 2h at 600 °C (ramp up rate 10°C/min) in argon (Ar) atmosphere. Providing on average a (6,5) chirality-enriched open- and closed-ends nanotubes ratio of about 50% – 50%. The single wall nanotubes are obtained in bundles.
- **Set 2** : In order to further reduce the polymers (as well as others residual materials), the Set 1 buckypaper scraps were submitted to a sonication process in water by 1h followed by filtration. This process was repeated 3 times. The final product after 3 filtrations was heated during 6h at 800 °C in an argon atmosphere. Also in this case the tubes are bundled.

Details of the characterization of these samples are provided in Ref. [110]). In both Set 1 and Set 2 the complete elimination of polymer residues was not possible.

A comparison between Raman spectra of the Stock and of the Set 1 samples at ambient conditions excited with a 568 nm laser is shown in Fig.3.4. The RBM and G-band regions of both samples provide information on the contribution of each chirality, which are labeled in the spectra. The chirilaties present in the Stock RBMs agree with those found in the photoluminescence experiment (Fig.3.1(a)). The enrichment of (6,5)-SWCNTs of Set 1 can be clearly observed.

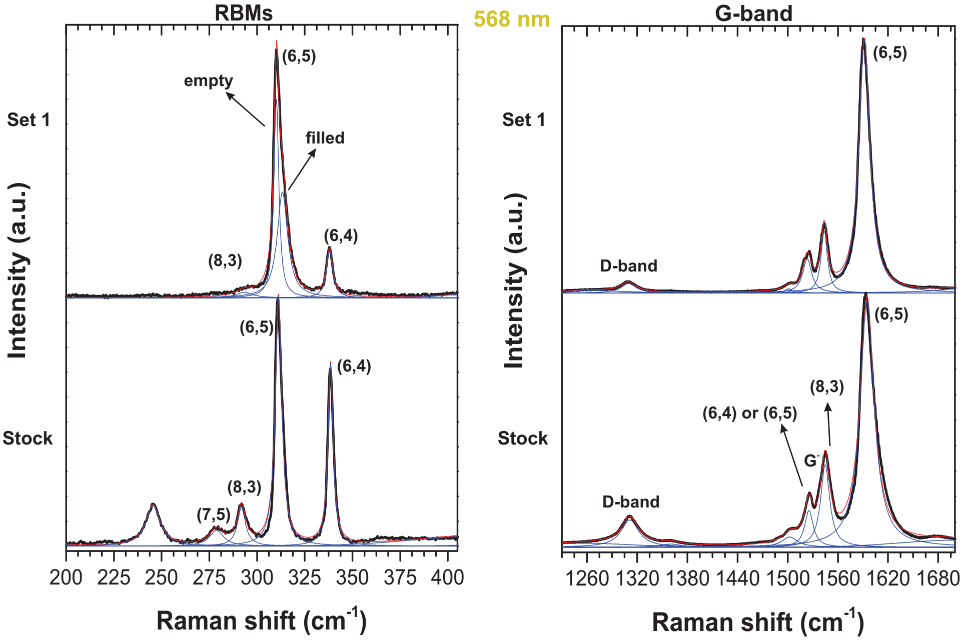

Figure 3.4 – Comparison of spectra measured at ambient and resonant conditions for Stock (empty tubes) and Set 1 (empty and water-filled (6,5) tubes) specimens. The left panel shows the RBM region with the chiralities conveniently labeled and the same is done for G band region (right panel). The peaks are fitted by the blue Lorentzian lines, while the data and the global fitting correspond to black and red lines, respectively.

In our work proposal of (6,5)-enriched SWCNTs, the Stock, Top 2 solution, Set 1 and Set 2 samples were used for Raman high pressure studies. The high pressure studies are addressed in next section.

We summarize in Table 3.2, some of the characteristics of the studied the samples in our experiments

The Stock sample is made of closed-ended (then empty) tubes, while for all other samples, both empty and filled tubes are found as it will be discussed in the study of the Raman RBM signal in the next section.

3.3 High pressure study. Results and discussion

We investigate the high pressure evolution and the mechanical stability of the four above mentioned enriched-(6,5) single wall carbon nanotubes. The samples were studied by *in situ* Resonant Raman spectroscopy (RRS). Resonant conditions for the (6,5) tubes are best obtained using the 2.18 eV energy (568 nm), which is absorbed by the symmetric (6,5) E_{22} transition energy (see Fig.1.6 b)) and consequently improving the RBMs and G-band profiles. Nevertheless in experiments done with different excitation energies (2.41 eV or 2.33 eV), we are still able to detect the (6,5) RBM peaks (both for filled and empty tubes) in the purified samples. In an

Table 3.2 – Summary of the different (6,5) chirality-enriched SWCNT samples studied in our work. Note that Top 2 is made of individualized CNT and all others are bundled tubes.

Samples	(n,m)	d_t (nm)	$\theta_{\mathrm{ch}}(^\circ)$
Top 2	(6,4)	0.68	23.4
	(6,5)	0.75	27
Set 1 and Set 2	(6,4)	0.68	23.4
	(6,5)	0.75	27
	(8,3)	0.77	15.3
Stock	(6,4)	0.68	23.4
	(6,5)	0.75	27
	(8,3)	0.77	15.3
	(7,5)	0.82	24.5

attempt explain this we can provide the following arguments:

1. The (6,5) tubes have a phonon sideband in their optical absorption spectrum, which should be a combination of the transition energies (symmetric E_{ii} or asymmetric E_{ij} bands) [115];
2. The purification process increases the (6,5) species percentage, which in turn increases the local field induced by the applied field (excitation energy), thus making these transitions more easy to be observed.

Nevertheless, we do not have a robust explanation for the observation of the Raman signal out of conventional resonance conditions [116]. In table 3.3 are given the parameters used in the different experiments.

Table 3.3 – Summary of the different high pressure Raman spectroscopy experiments on (6,5) chirality enriched SWCNT done in our work. Are given for each experiments the excitation wavelength, the maximum pressure attained and the used pressure transmitting medium

Initial sample	excitation laser nm	Max. pressure GPa	PTM
Top 2	568 (2.18 eV)	26	polymer + surfactant + water
Set 1	568 (2.18 eV)	26	4:1 – M:E
Set 2	514 (2.41 eV)	40	4:1 – M:E
	514 (2.41 eV)	50	
	532 (2.33 eV)	50	
Stock	514 (2.41 eV)	80	4:1 – M:E

More details on the experimental set-up used can be found in section 2 and in the annexes. The two first experiments in Top 2 and Set 1 samples had as main goal the observation and characterization of the (6,5) tubes pressure collapse. We then used the 568 nm laser excitation to match the resonance conditions to obtain the best signal. We used diamond anvils allowing to reach easily 30 GPa of maximum pressure. A first analysis of these data (Top 2 and Set 1) was already presented in the PhD thesis of Aude Stolz [110]. Here we will comment again these data for which in particular the data fitting of the Set 1 sample was redone again to verify a certain number of points. Experiments on Set 1, Set 2 and Stock samples were on their side designed to explore the maximum pressure stability of the tubular structure. Not having an easy access to the 568 nm laser excitation, we used other wavelengths and coupled the in situ Raman observation with the ex situ characterizations after the pressure cycle. 4:1 methanol:ethanol was always used as pressure transmitting medium except for the Top 2 experiment for which the own solution of the nanotubes was used.

Before discussing the different details of the experiments in the following subsections, we would like to present here some characteristic spectra evolution with pressure as well as the fitting method.

The Figure 3.5(a) shows the Raman spectra stacking of RBM (left panel) and G band (right panel) regions for the Set 1 specimen for different pressure values. As was shown in Fig. 3.4, the dominant contributions in these samples are coming from (6,5) tubes but also include some presence of (6,4) and a marginal detection of (8,3) tubes. In both panels spectra were normalized in order that their intensities are between 0 and 1 after background substraction. In general, both RBM and G modes become broader with pressure and their intensities decrease. For the RBM spectra, the green and blue curves represent the Lorentzian fits of water-filled and empty (6,5) SWCNTs, respectively[41]. The gray Lorentzian curves are used for the (6,4) and (8,3) RBM modes, as well as for the non-identified peak at around 420 cm^{-1}. The G band spectra were also fitted by Lorentzian functions. The black line is the fitting to the SWCNTs G^+ peak (with a dominant contribution from (6,5) tubes), while blue lines are fitted to the G^- peaks of (6,4) and (6,5) nanotubes at low and high frequencies, respectively.

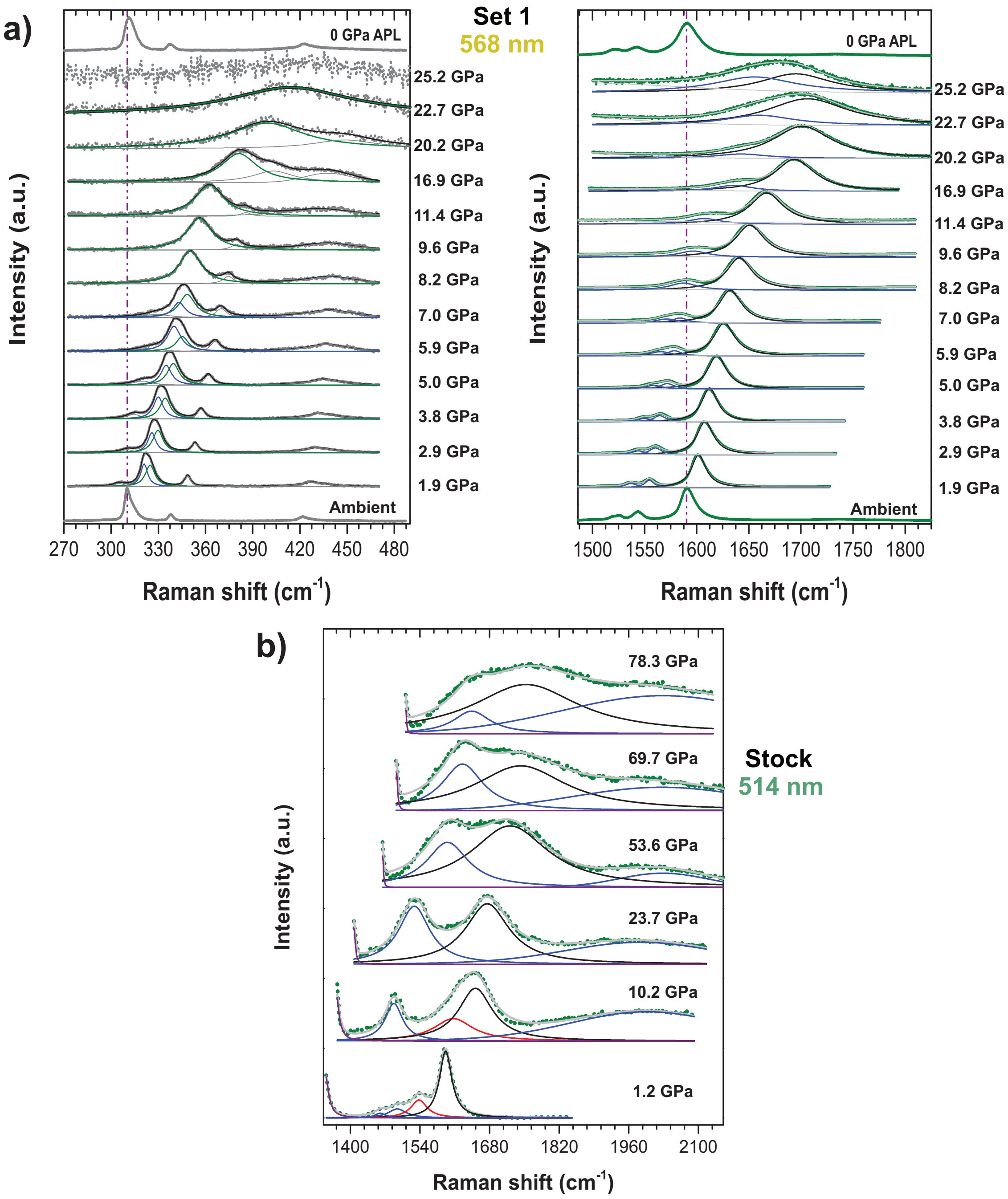

Figure 3.5 – a) Peak fittings of RBM (left panel) and G-band (right panel) spectra of the Set 1 (bundles of water-filled and empty (6,5) SWCNTs) sample taken with laser energy of 568 nm. b) The G-band spectral peak fittings of Stock (bundles of empty (6,5) SWCNTs) sample at laser excitation of 514 nm.

Figure 3.5(b) shows G-band Raman spectra (normalized from 0 to 1) for the Stock specimen in six different values of pressure (with the maximum at $\sim$ 80 GPa) taken with a laser energy of 2.41 eV. This was the experiment done to the highest pressure. The red (G^-) and black (G^+) curves correspond to the Lorentzian fittings, while the purple (arising from diamond anvil peak) and blue (for the background) curves are Voigt profiles. Similar spectral fittings were done for the others high pressure experiments. In fact, we have only displayed two different data treatments in order to give a qualitative aspect of the spectral fittings. Spectra evolution in the other experiments is included in the annexes.

In the next subsections, we prefer presenting the obtained results separately for the RBM and G band evolutions as a function of pressure. Their analysis will be used to discuss the collapse pressure and the nanotube geometry stability. Finally we will devote a specific subsection to the irreversibly process. All results will be confronted with know works present in the literature.

3.3.1 Radial breathing modes - RBM

Individualized SWCNTs and Collapse – We start our discussion with the individualized tubes (Top 2). We have completed the analysis started in th PhD thesis of Aude Stolz in our group[110]. Figure 3.6(a) presents the evolution of the frequency of the RBM peaks in the Top 2 solution . We could linearly fit the evolution of the 3 RBM peaks up to their maximum pressure of detection. We will discuss later in this section the fitting parameters. We have also represented in Fig. 3.6(a) as discontinuous lines the obtained fit for the same (6,4) and empty + water-filled (6,5) tubes in the work of Torres-Dias *et al.* [41]. In that work their data needed the use of a quadratic fit, which clearly does not corresponds to the evolution observed in our Top 2 sample. The main difference between our Top 2 sample and the one in the work of Ref. [41] is the tube environment which in our case contains polymers which interact with the carbon nanotubes in addition to the DOC surfactant. We may then suggest that the differences in the ambient pressure wavenumber of the RBM modes as well as the type of linear evolution (linear or quadratic) strongly depends on the nature of the environment shell wrapping the nanotube. We will further discuss this aspects for the bundled tubes.

Figure 3.6(b) shows the evolution of the normalised RBM peak area as a function of pressure for the Top 2 solution ((6,5)-individualized SWCNTs). This graph shows a strong drop of the normalized peak area value between 0 and 1 GPa, a plateau region and a second drop in the $\sim$ 16 GPa. The normalization of the RBM peak area of filled/empty tubes was accomplished through the spectrum of the neon lamp for different pressure values, i.e., for each value of achieved pressure, the RBMs (filled and empty), ruby shift (pressure measurement) and neon lamp spectra were collected. At followed, the RBM integrated intensity for one specific pressure value was divided by the neon lamp integrated intensity at the same pressure (the neon calibrator is a good reference, because it keeps the same peak position under pressure and its peak area changes very little), thus allowing to plot the evolution of normalized RBM peak area as a function of pressure. This general evolution of the RBM peak area with pressure in individualized tubes is in perfect agreement with the observations in Ref.[30] (empty tubes). The second drop of the peak area was seen to correspond to the collapse pressure. The data were fitted as in Ref.[30] by means of least-squares method given by function $1/2(I_0\exp(-bP) + a)(\mathrm{erf}(\omega/P_0(P - P_0)))$, where the Gauss error function (erf) provides an approach that describes the plateau and collapse regions.

However, the normalized peak area plot in our sample takes in account both water-filled and empty tubes, while that in Ref.[30] the signal is ascribed to empty tubes. From our data, the collapse pressure onset for the Top 2 individualized (6,5) tubes is of ∼ 16 GPa. We can compare this value with the predictions of the collapse pressure as function of the tube diameter given by Ref. [29] and Ref. [30] which are respectively of 16.3 GPa and 10.2 GPa. Filled tubes can show a collapse pressure up to 3 times larger than empty tubes [41]. In addition it has been observed that for the Top 2 solution, the G-band frequency deviates from linearity also at ∼ 16 GPa[110] and this result will be revisited together with the G-band analysis of other specimens (Stock, Set 1, Set 2) in the section **Tangential modes - G bands**. We may then assign the observed attenuation of the RBM (6,5) peak area at 16 GPa to the collapse of the empty tubes.

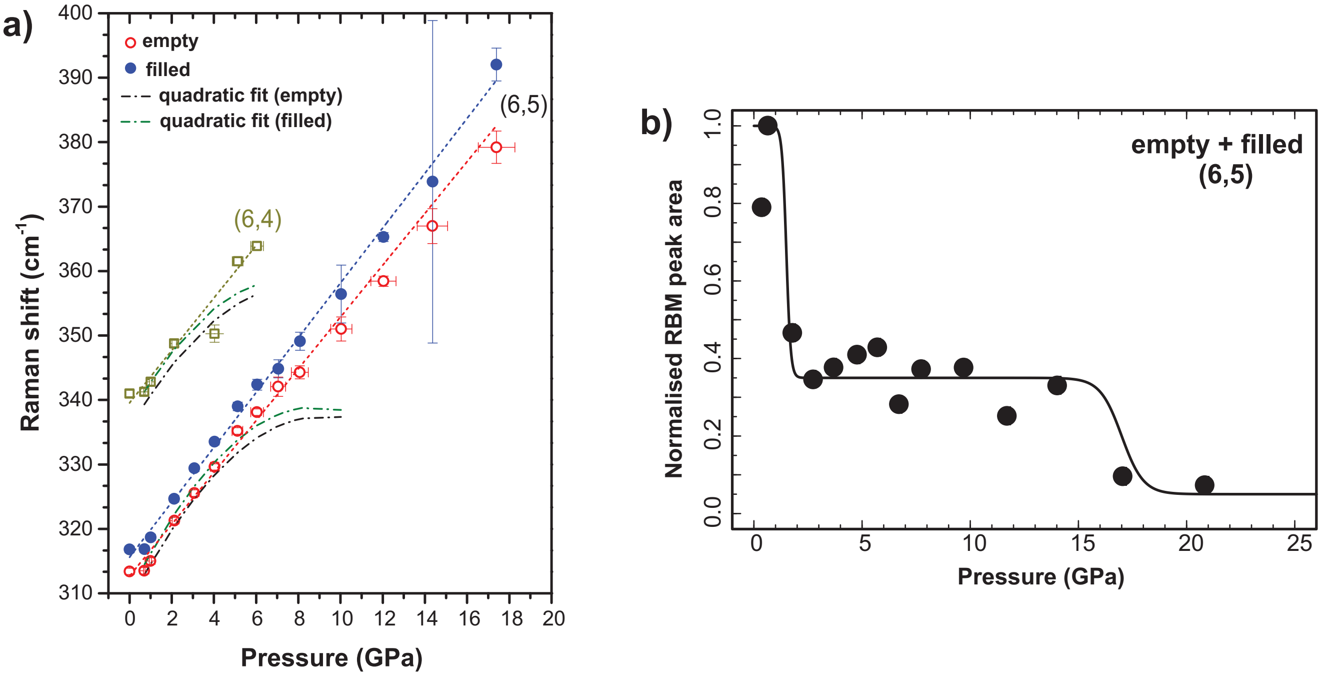

Figure 3.6 – Top 2 high pressure experiment. a) The left panel shows the RBM frequencies evolution of (6,4) and water-filled and empty (6,5) tubes together with their respective linear fits (blue dashed line - filled; black dashed line - empty). The corresponding quadratic evolution from Ref.[41] are also shown b) The normalised RBM peak area) evolution of our empty + water-filled (6,5)-individualized SWCNTs, calculated according to Ref.[30]. The pressure transmitting medium corresponds to the solution of surfactants, polymers and water.

Bundled SWCNTs – The (6,5)-enriched bundled samples in our study are Set 1, Set 2 and Stock (bundles in 4:1 M-E PTM). We start discussing the results of the Set1 sample which spectra evolution with pressure was shown in Fig 3.5.a. The result of the fit of the RBM signal is shown in Figure 3.7(a). In this figure is shown the compared evolution of RBMs and their FWHMs as a function of pressure for the tubes (6,4) (yellow pentagons), (8,3) (blue pentagons) and (6,5) water-filled (wine dots) and empty (green circle) for Set 1 sample. The gray dashed vertical line marks the pressure point where the methanol:ethanol PTM is solidified (about 10 GPa). We do not observe any clear modification in the spectra evolution associated to the PTM solidification. The frequency of the (8,3) tube RBM increases steadily up to 7 GPa as well as does its FWHM. Probably the fitting error bars for (8,3) tubes in Figure 3.7(a) are underestimated (background substraction effect on a weak peak). The (8,3) tubes can not be observed beyond 7 GPa, probably due to the attenuation of they already very weak intensity. For the (6,4) tubes, the RBM evolution also has a monotonic increasing up to ∼ 17 GPa, however the FWHM evolution experiences a jump close to 12 GPa (above from the PTM solidification point). The empty (6,5) tubes display a similar RBM evolution than the (8,3) tubes but we can initially fit both the contributions of empty(E) and filled(F) tubes. Nevertheless, the E/F signal cannot be fitted separately for the (6,5) tubes from about 7 GPa. We have then only fitted one peak - associated to the filled (6,5) tubes from that pressure. This explains the observed accident in the (6,5) filled tube FWHM and wavelength at this pressure. Filled (6,5) tubes evolve steadily - apart of the above mentioned accident at 7 GPa - up to 17 GPa.

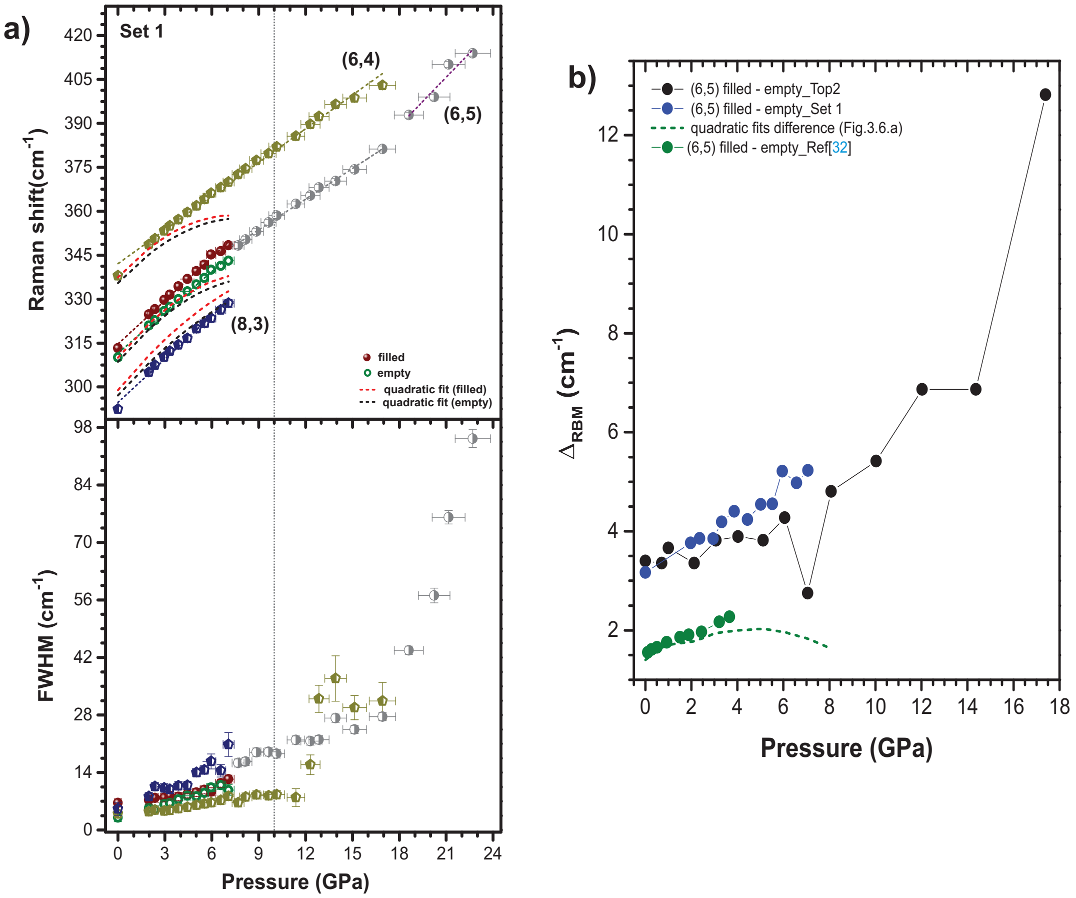

Figure 3.7 – a) RBM Raman shift as a function of pressure for (6,4) (yellow), (6,5) (green and wine for empty and water-filled tubes, respectively) and (8,3) (blue) chiralities of the Set 1 sample. The data linear fittings (following their respective colors) are provided at each pressure range and compared with the quadratic from of Ref.[41], where the grey circles data points represent the signal coalescence of (6,5) tubes. The attached lower panel shows the FWHM pressure evolution for these chiralities with same encoding. The gray dashed line marks the pressure point of PTM solidification. b) Difference of RBM positions of water-filled (6,5) SWCNTs with respect to empty ones, $\Delta_{\text{RBM}} = \omega_{\text{filled}} - \omega_{\text{empty}}$, compared with the quadratic fits (Fig.3.6a) and data points from Ref. [41].

Following the work of Ref. [41] we fitted using linear or quadratic polynomials the frequency evolution of the different peaks for the Top 2 and Set 1 experiments as well as for the Stock sample. Results are shown in Table 3.4 and compared with the work of Torres-Dias *et al.*[41]. In this table we see that we have been able to measure the signal of the RBM peaks of the (6,5) and (6,4) peaks to much higher pressures than for Ref. [41]. Moreover, the difference in the wavenumber between filled/empty tubes (with same chirality, as displayed in Table 3.4) could be attributed to different orientations of water molecules in the filled tubes, which provides large shifts of the electronic transitions [117]. However, in a general way Cambré et al. [117] observed that the shifts of the RBM frequency upon water filling showed a complex nonmonotonic dependence on the diameter and chirality and considering water filling of tubes well in the diameter range where only a single file of water molecules fits inside the tube. Nevertheless, the slope of the filled/empty tubes aforementioned present very close values, this behavior may be ascribed by the increasing of the dielectric constant of the environment originated from the compression of polymers and surfactant layers wrapping the SWCNTs, which in turn changes the electronic resonances [41] having an effect on the RBM modes evolution with pressure. We can actually realize that the ambient pressure wavenumber of the different (n,m) peaks can significantly vary upon determined experimental conditions.

This is much better seen in Table 3.5 where we have grouped the obtained results by tube chirality and in which the results of Ref. [41] have also been included. The incertitudes of ω_0 are estimated to ±1 cm^{-1}. We can see that differences in the ω_0 values depending on the environment can be as large as 4-5 wavenumbers. We see also that the two Set 2 experiments are consistent within error bars. The results from Set 1, Set 2 and Stock, all for bundled tubes differ both in ω_0 values and pressure slopes for the (6,5) tubes. This the high sensitivity of the RBM tubes to the tube environment as it has already been reported in literature [118]. Finally we may also note that for the same experiment (environment) there is no difference for the pressure slopes of the (6,5), (8,3) and (7,5) tubes. The weaker (6,4) seems on its side have a lower slope.

The comparison of our values for the α parameter and the ones of Ref. [41] are not really significant as in that work a quadratic term was also needed. This is better seen in Fig 3.5.a. We have also compared the evolution of the F/E RBM position with pressure in Fig 3.5.b where the difference between the two signals is plotted. We see that at ambient pressure the difference of signal in our experiments (Top 2 and Set 1) is of about 3 cm^{-1}, i.e., the double than in Ref. [41]. This differences increases with pressure at a similar rate than for Ref. [41], except for the very last point measured in the Top 2 sample and an anomalous point at 7 GPa.

Finally for the Set 1 sample, we note in Fig 3.5.a a change of slope in the (6,5) RBM evolution at 18±2 GPa associated with a high increase of the associated FWHM which could be associated with the collapse of the empty tubes. In fact, the collapse of the empty (6,5) tubes or others of similar diameter, will probably lead to the development of a large local non-hydrostatic strain field affecting then the filled tubes FWHM. This hypothetical assertion would need further support.

We would like now compare in more detail the RBM evolution for the 3 experiments done for the "Set" samples (one for Set 1 and two for Set 2). This is done in Figure 3.8.a which provides the observed evolution for the (6,5) water-filled tubes (RBM and its FWHM). The (6,5) RBM wavenumber evolution coincides for the 3 experiments up to $\sim$ 7-8 GPa. The trend in the FWHM is more scattered up to 4 GPa. From that pressure the FWHM is similar for the 3

Table 3.4 – RBM pressure derivatives of different SWCNTs nanotube chiralities of the studied samples in our work compared with the results obtained from Ref. [41]. Values for empty (E) and water-filled (F) tubes are given when available. The peaks positions evolution were fitted according their trends (linear or quadratic) in each pressure range. ω_0 are the RBM frequencies at ambient conditions. α and β are the linear and quadratic coefficients of the pressure fit. The pressure domain in which the fit was done is indicated.

Initial sample	(n,m)	d_t nm	P range (GPa)	E/F	ω_0 (cm^{-1})	α ($cm^{-1}GPa^{-1}$)	β ($cm^{-1}GPa^{-2}$)
Top 2	(6,4)	0.68	0 - 6	—	341	4.1 ± 0.3	—
	(6,5)	0.75	0 - 17.3	E	313.4	4.0 ± 0.1	—
				F	316.8	4.3 ± 0.1	—
	(8,3)	0.77	—	—	294.3	—	—
Set 1	(6,4)	0.68	0 - 17	—	337.9	3.8 ± 0.1	—
	(6,5)	0.75	0 - 7	E	310.1	4.6 ± 0.1	—
				F	313.3	4.9 ± 0.1	—
			7 - 17	E and/or F		3.5 ± 0.1	—
			17 - 22.7	E and/or F		5.5 ± 1.1	—
	(8,3)	0.77	0 - 7	—	293.5	4.9 ± 0.2	—
Set 2 (prepared for cylce of 40 GPa)	(6,5)	0.75	0 - 7.22	E	313.1	6.3 ± 0.1	-0.3 ± 0.1
			0 - 12.7	F	317.3	5.9 ± 0.3	-0.2 ± 0.1
	(8,3)	0.77	—	—	295.2	—	—
Set 2 (prepared for cycle of 50 GPa)	(6,5)	0.75	0 - 6.8	E	314.2	6.6 ± 0.1	-0.4 ± 0.1
			0 - 13.6	F	318.2	5.3 ± 0.4	-0.2 ± 0.1
	(8,3)	0.77	—	—	296.2	—	—
Stock	(6,4)	0.68	—	E	338.5	—	—
	(6,5)	0.75	—	E	311.2	—	—
	(8,3)	0.77	—	E	291.8	—	—
	(7,5)	0.82	—	E	278.8	—	—
Reference [41] DOC-D_2O solution	(6,4)	0.68	0 - 3.64 GPa	E	335.5	5.6 ± 0.1	-0.4 ± 0.1
				F	337.4	5.8 ± 0.1	-0.4 ± 0.1
	(6,5)	0.75	0 - 3.64	E	308.6	6.3 ± 0.1	-0.4 ± 0.1
				F	310.0	6.6 ± 0.1	-0.4 ± 0.1
	(8,3)	0.77	0 - 11	E	297.1	6.0 ± 0.3	-0.2 ± 0.1
			0 - 13	F	298.9	6.5 ± 0.1	-0.3 ± 0.1
	(7,5)	0.82	0 - 11	E	282.6	6.2 ± 0.2	-0.2 ± 0.1
			0 - 13	F	284.4	6.2 ± 0.2	-0.2 ± 0.1

Table 3.5 – RBM frequencies at ambient conditions ($\omega_\circ$) and pressure slopes α comparison between our specimens and Ref.[41].

Sample	**(6,4)**		**(6,5)**	
	ω_0 (cm^{-1})	α (cm^{-1}GPa^{-1})	ω_0 (cm^{-1})	α (cm^{-1}GPa^{-1})
Stock	338.5	–	311.2	–
Top 2	341	4.1 ± 0.3	E 313.4	4.0 ± 0.2
	–	–	F 316.8	4.2 ± 0.10
Reference [41]	E 335.5	5.7 ± 0.2	E 308.6	6.3 ± 0.2
	F 337.4	5.7 ± 0.2	F 310.0	6.5 ± 0.2
Set 1	337.9	3.8 ± 0.1	E 310.1	4.6 ± 0.2
	–	–	F 313.3	4.9 ± 0.2
Set 2 (40 GPa)	–	–	E 313.1	6.3 ± 0.2
	–	–	F 317.3	5.9 ± 0.4
Set 2 (50 GPa)	–	–	E 314.2	6.5 ± 0.2
	–	–	F 318.2	5.3 ± 0.4

	(8,3)		**(7,5)**	
	ω_0 (cm^{-1})	α (cm^{-1}GPa^{-1})	ω_0 (cm^{-1})	α (cm^{-1}GPa^{-1})
Stock	291.8	–	278.8	–
Top 2	294.3	–	–	–
	–	–	–	–
Reference [41]	E 297.1	6.0 ± 0.3	E 282.6	6.2 ± 0.2
	F 298.9	6.5 ± 0.1	F 284.4	6.2 ± 0.2
Set 1	293.5	4.9 ± 0.2	–	–
	–	–	–	–
Set 2 (40 GPa)	295.2	–	–	–
	–	–	–	
Set 2 (50 GPa)	296.2	–	–	–

samples. We should underline that in Figure 3.8.a the grey symbols correspond to the change to a single peak-fitting and may be attributed most probably to filled tubes too, but which could be affected by the presence of a weak empty tube component in the fit. Again, differences in the pressure behavior of all these bundled (6,5) tubes may be due to the environment differences. In Figure 3.8.b is shown the (6,5) F/E evolution for the Set 2 experiments (RBM and FWHM). Again, with our present knowledge it is difficult to assign the particularities of the evolution with respect to Set 1 to other reasons that the environment effects.

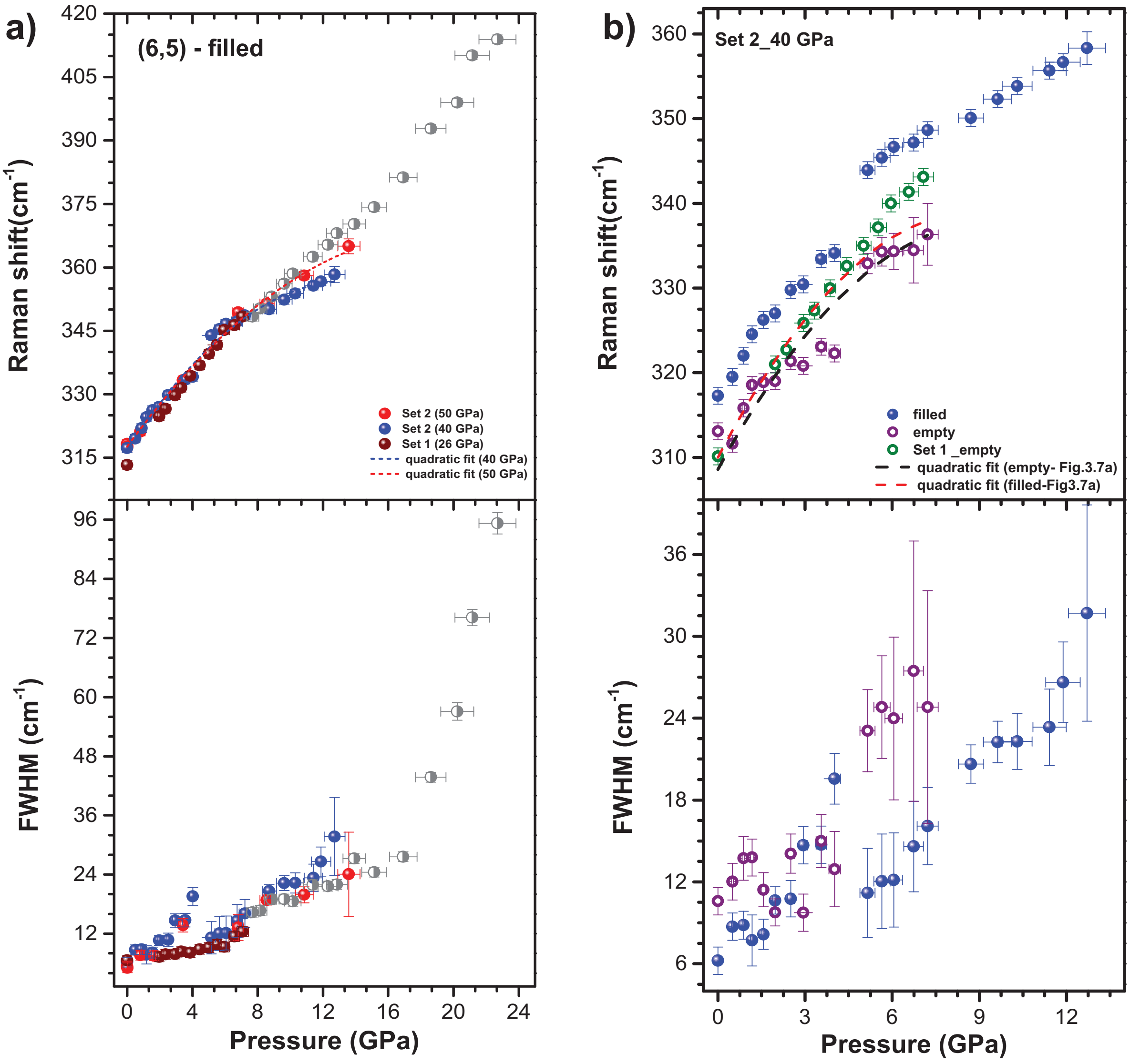

Figure 3.8 – a) Comparison of RBM pressure evolutions of water-filled (6,5) tubes of Set 1 and Set 2 samples at each pressure cycle. The quadratic fittings are provided by blue (Set 2-40 GPa) and red (Set 2-50 GPa) dashed curves. The gray circles is the continuation of data points for the Set 1. Pressure evolution of line width is shown in the same colors. b) RBM shift as a function of pressure of empty (purple hollow dots) and water-filled (blue solid dots) (6,5) tubes from Set 2 (cycled up to 40 GPa) sample. These data are compared with Set 1_empty and with the second order degree polynomial curves of empty (black line) and water-filled (red line) from [41].

3.3.2 Tangential modes - G bands

Before to start the discussion on our own data, it is important to mention the common methodology found in the literature to make the G band analysis. At lower pressure values, the G^- and G^+ profiles are well distinguishable, making easy the peaks fit. At high pressures, the G^- loses its intensity together with the line width broadening and the G^+ increases its frequency. Different fitting strategies can be adopted. In our study, we have fitted the G^- contribution with a Lorentzian function without locking its parameters. In other words, when we fit the G^+ and G^- peaks (ω_{G+} and ω_{G-}, respectively) and no divergence appears, we consider the contribution of the G^- as relevant.

In a general way, the G band spectral adjustments were performed by background subtraction with a linear function usually close to horizontal. The spectra were then fitted after normalization (this same procedure was use in the RBM fittings).

We have used two FWHM values for the G-band: one considering a zero normalization on one left side of the G^+ band and the other taking a background subtraction in which the right side (high frequency region) of the G^+ band is fitted properly by a Lorentzian function. The final value was the average between these two, giving $\big(\langle FWHM\rangle = \big[FWHM_1 + FWHM_2\big]/2\big)$. While, their error bars were provided by 2 methods of error propagation, $\sigma_{\langle FWHM\rangle} = \sqrt{\sigma^2_{HWHM_1} + \sigma^2_{HWHM_2}}$ (HWHM — half-width at half-maximum) and $\sigma_{\langle FWHM\rangle} = \frac{|FWHM_1 - FWHM_2|}{2}$, where the higher value between these two methods has been chosen. The G bands (G^+ and G^-) frequencies of Set 1, Set 2 and Stock samples did not show significant variations when estimated in this same way.

We still underline that the G^+ band signals of Set 1, Set 2, Stock and Top 2 samples may have their origin mainly coming from water-filled and empty (6,5)-tubes (high relative intensity in RBMs spectra) when compared with the other chiralities (low ratio in RBMs spectra) and this is due to the fact that the tubes (in particular for Set 1, Set 2 and Top 2 samples) enrichment process (chirality sorting) allows us to analyze unambiguously the G-band in macroscopic sampling, as well investigated in references [119, 120]. However, we need to keep in mind that these modes are less weakened by rehybridization (induced by symmetry-breaking of circular cross-section) and thus yielding a much smaller softening of the phonon, which in turn becomes the chirality distinguishable in the sample a hard task. Unlikely to the G^+ band, the G^- band has its frequency associated with a more pronounced phonon softening (rehybridization increasing) and this makes the G^- band chirality dependent [121, 120], as for instance displayed in Fig. 3.4 about the G-band (lower spectrum from left panel).

The Figure 3.9 shows the G^- peaks evolution of the Set 1, Set 2 and Stock samples cycled at different pressures. We have assigned the observed peaks to the chiralities (6,4), (6,5) and (8,3) up to 7 GPa, based on resonant Raman studies on the diameter, chiral angle, and family dependence of the high-energy modes, G^- and G^+, in small-diameter semiconducting SWCNTs suspended in solution [120]. After this pressure, all modes are overlapped, making the chiralities identification not more unambiguous.

Table 3.6 summarizes the main features from Fig. 3.9, the experimental data points were linearly fitted until pressure below of ∼7 GPa. The parameters obtained from our G-band pressure data were compared with previous works about the DWCNTs G-band pressure response in the

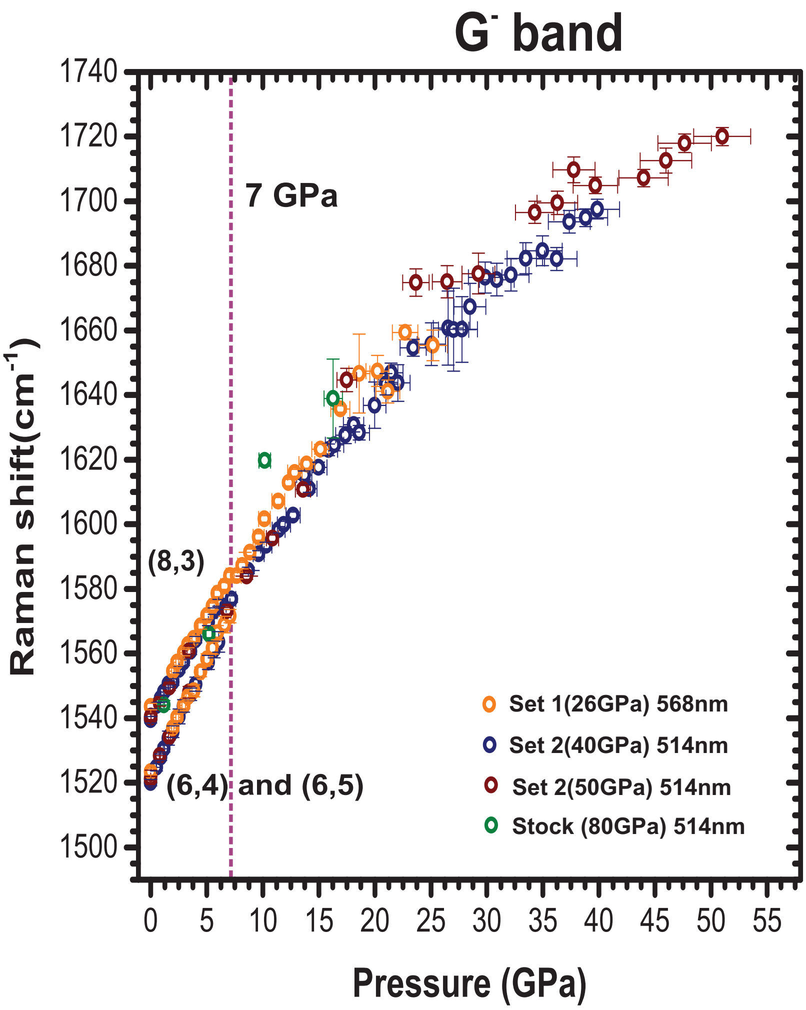

Figure 3.9 – G$^-$ peaks as function of pressure for bundled tubes Set 1 (empty + water-filled (6,5) SWCNTs), Set 2 (empty + water-filled (6,5) SWCNTs), Stock (empty tubes). Dashed purple line marks the pressure value from which the chiralities can not be more distinguished. The colorful labels provide the sample names with pressure cycles values and also the excitation energies.

presence of different pressure transmitting media (see Table 3.6) and they display similar pressure coefficients values in relation to the outer tubes (nearly the same shift, this could correspond to a pure mechanical effect with strain minimization). In contrast, the pressure coefficients of inner tubes DWCNTs refs.[51, 122, 55] are consistently much lower than the outer tubes as well as to the our experimental findings. This fact also indicates the screening effect on inner tubes provided by outer tubes. In addition, we will observe in the part about G$^+$ peaks pressure evolutions that its pressure slopes have a common linear coefficient and that this value is in good agreement with the G$^-$-peaks shown here.

Figure 3.10(a) shows the comparison of the pressure evolution of the G$^+$ band and line width evolutions for the Set 1, Set 2 and Stock samples. All the samples follow a common linear behavior up to 10 GPa with a pressure common slope of 6.36 cm^{-1}GPa^{-1}, thus, we can estimate that our G-mode pressure coefficient ranges 5-7.6 cm^{-1}GPa^{-1} in good agreement with the displayed values for tubes wrapped by environments (surfactant, PTM) and/or bundled/individualized from literature.

Table 3.6 – The SWCNTs G^{-} peaks at ambient conditions (ω_i) and its pressure derivatives α, as well as the intercept of each mode when extrapolated to the pressure of 0 GPa.

G^{-}- peak (n,m)	Sample	ω_i (cm^{-1})	linear fitting Intercept (cm^{-1})	 α (cm^{-1}/GPa)	 Pressure range (GPa)
G^{-}-peak **(8,3)** 4M:1E	Set 1 (26 GPa)	1543.60	1543.38	5.72 ± 0.07	0 - 7
	Set 2 (40 GPa)	1539.50	1541.50	5.28 ± 0.17	0 - 7.22
	Set 2 (50 GPa)	1540.26	1541.04	4.95 ± 0.28	0 - 6.8
	Stock (80 GPa)	–	1537.64	5.46	0 - 5.2
G^{-}- peak **(6,4)** and/or **(6,5)** 4M:1E	Set 1 (26 GPa)	1523.36	1523.45	6.93 ± 0.08	0 - 7
	Set 2 (40 GPa)	1520.06	1521.21	7.58 ± 0.34	0 - 6.1
	Set 2 (50 GPa)	1521.13	1521.96	7.26 ± 0.15	0 - 3.42
G^{+}_{inner}	DWCNTs	–	–	5.1 ± 0.2	0 - 10
G^{+}_{outer}	[55]	–	–	8.3 ± 0.2	0 - 10
G^{+}_{5} (inner)	DWCNTs [50]	–	–	3.3	0 - 10
G^{+}_{6} (outer)	4M:1E	–	–	6.1	0 - 10
G^{+}_{inner}	DWCNTs [122]	–	–	3.3 - 5.1	–
G^{+}_{outer}	4M:1E, Ar, O_2	–	–	5.8 - 8.6	–

Around 10 GPa pressure the FWHM of the G^{+} peak start to broaden progressively up to approximately 20 GPa. After this pressure, broadening continues steadily but at a lower rate. In all this samples the PTM is 4:1 methanol:ethanol which solidifies at 10 GPa. We may then hypothesize that the G-band frequency evolution spread of values after the PTM solidification may be due to differences in the inhomogeneous stress field generated by the PTM. We may nevertheless note that only the G band evolution of Stock (empty tubes only) presents a more pronounced deviation which starts being evident at around 15 GPa and progressively approaching the graphite pressure evolution of the G-band. We can then - following previous works in our group - assign this deviation at around 15 GPa to the collapse pressure of the empty tubes of the Stock specimen in which empty (6,5) tubes are majority. This interpretation matches then the one we did when analyzing the RBM contributions.

As discussed, above the collapse region, the ω_{G+} of the Stock sample (empty tubes) as function of pressure evolves gradually until reaching a graphite-like behavior close to 60 GPa, while the Set 2 samples (empty and water-filled tubes) continue raising up until their respective maximum pressures (40 GPa and 50 GPa). This graphite-like trend in the Stock sample from ∼ 60 GPa and up to the maximum pressure of 80 GPa is associated to a much prominent FWHM increase, which suggests important structural changes. As we will discuss in the next section such evolution is coherent with a total loss of the nanotubes mechanical stability or "unzipping" taking place from 60 GPa. This value may be considered as the threshold for the transformation between the tubular geometry (whatever its radial cross-section) and a graphite-like structure. The gray vertical rectangle marks the region of the proposed irreversible transformation.

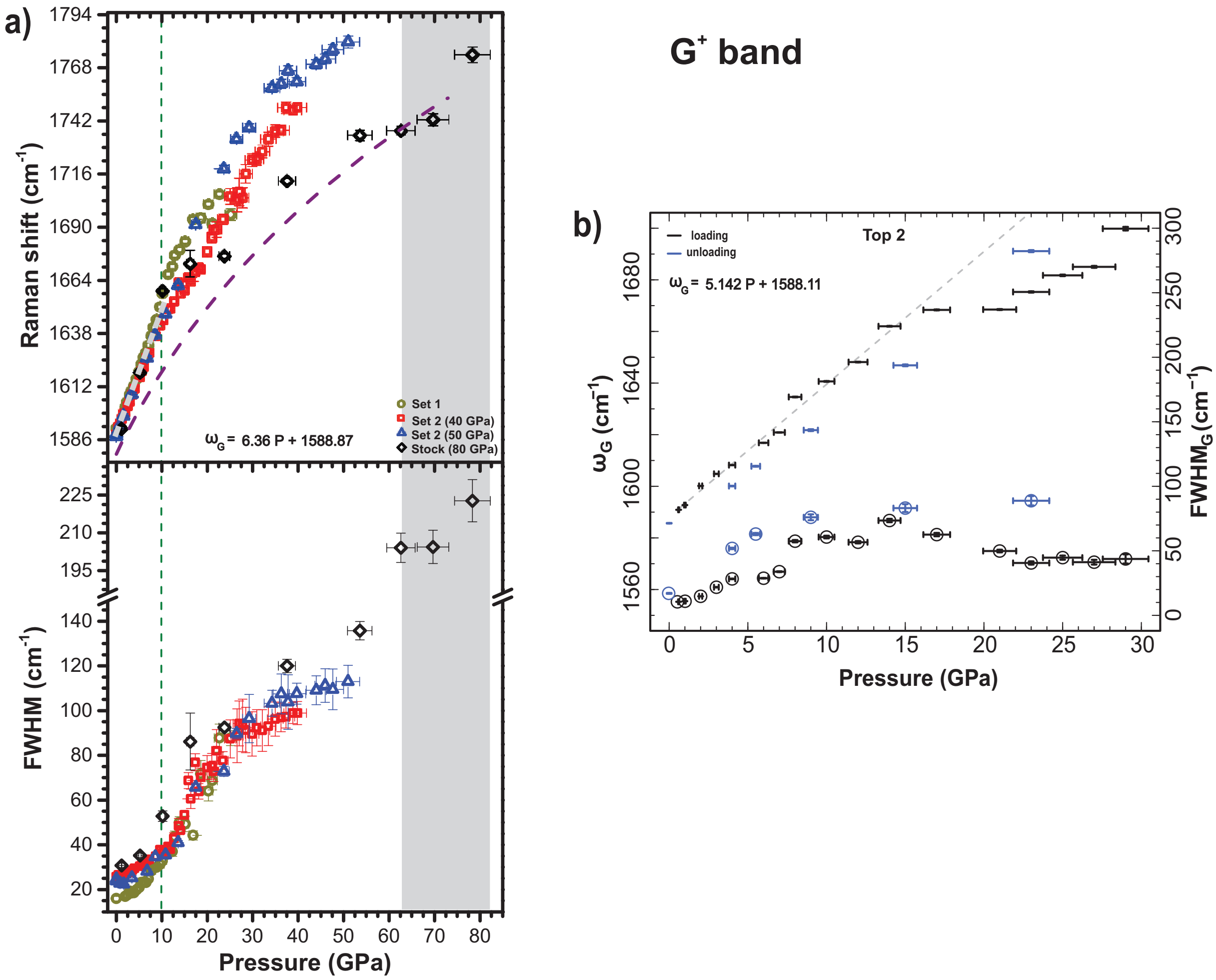

Figure 3.10 – a) G^+ band as function of pressure for bundled tubes Set 1 (empty + water-filled (6,5) SWCNTs), Set 2 (empty + water-filled (6,5) SWCNTs), Stock (empty tubes). Purple curve shows the graphite G-band evolution and the green vertical line is the PTM solidification pressure point. The large gray line represents the all data linear fittings up to solidification point (the linear equation is also provided). Line width evolution with the pressure is equally shown (lower panel). The gray rectangular area indicates the pressure range where the Stock and graphite G-band evolutions match. b) The G-band (dots) and FWHM_G (circles) evolutions with the pressure of the Top 2 solution (empty + water-filled (6,5) SWCNTs). The black color represents the loading pressure, while the blue the unloading. A linear fitting is displayed by gray dashed line as well as its equation.

3.3.3 Reversibility limits of (6,5) SWCNTs

In order to obtain a better insight on the permanent pressure-induced changes in the tube structure we will examine the Raman signal after pressure cycle as well as TEM images. The irreversible changes have been already suggested by the G-band evolution in the Stock experiment. The RBM and G band spectra of Set 1, Set 2 and Stock samples measured before (BPL) and after (APL) the pressure loading are compared in Figure 3.11. The labels indicate the maximum pressure attained for each cycle. In Fig.3.11(a), the RBMs for the spectrum 26 GPa_Set 1 shows that the (8,3) tubes, water-filled- and empty-(6,5) and (6,4) tubes are recovered after pressure cycle up to 26 GPa, however the RBM peak area of filled-(6,5) increased, which means that the ratio of filled tubes increased during the pressure experiment.

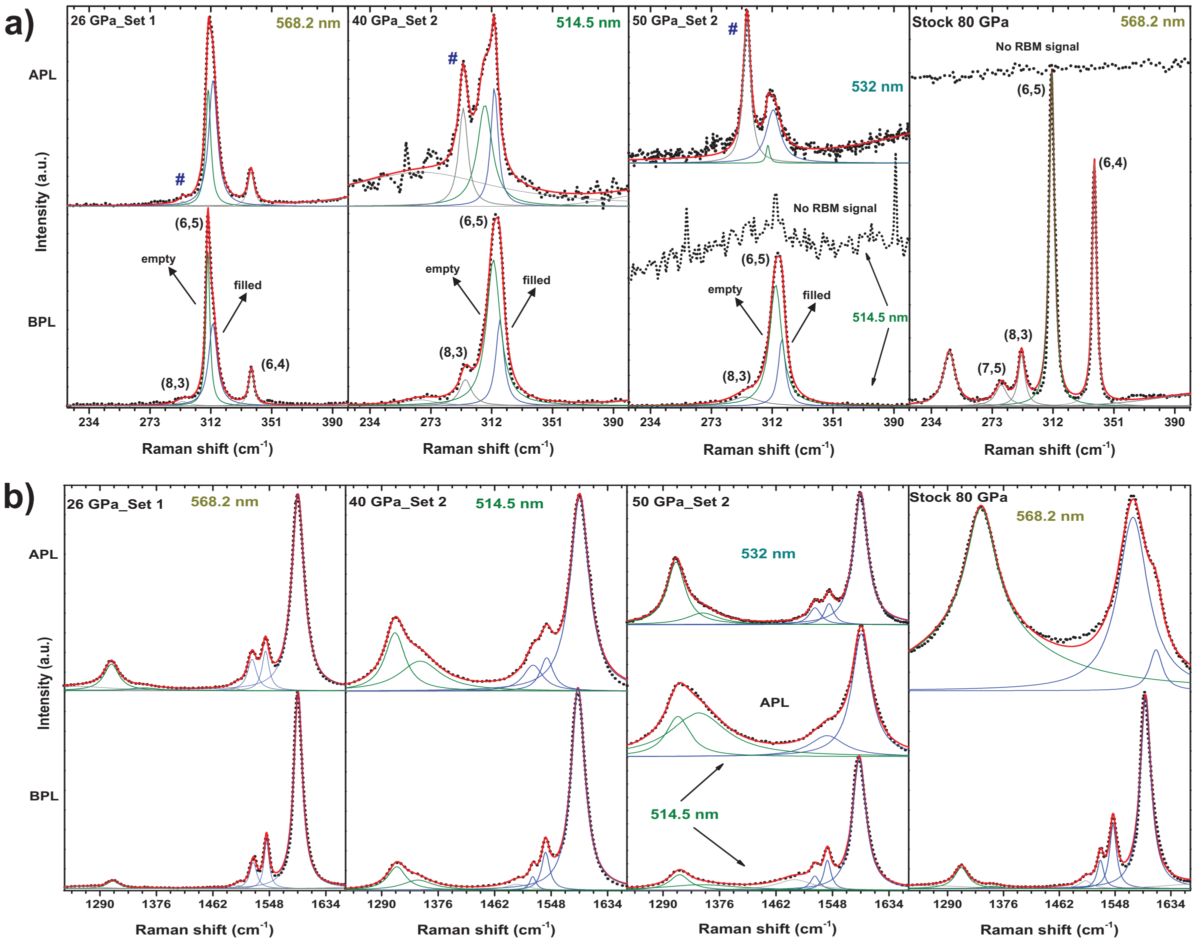

Figure 3.11 – The Set 1 and Set 2 samples contain empty + water-filled (6,5) SWCNTs, while the Stock has only empty tubes. a) RBM spectra comparisons of Set 1, Set 2 and Stock samples before (BPL) and after (APL) pressure loadings. In each panel, the labels indicate until which pressure the samples were cycled and for which laser energies the specimens have been characterized, as well as their chiralities. The blue hash symbol (#) indicates the RBM position of (8,3) tubes. b) G-band spectra comparisons of Set 1, Set 2 and Stock samples before (BPL) and after (APL) pressure loadings. In each panel, the labels indicate until which pressure the samples were cycled and at which laser energies the specimens are excited.

For the 40 GPa_Set 2 RBM spectrum, the (8,3) and water-filled- and empty-(6,5) tubes have their profiles substantially modified after the pressure cycle. We note also that the tube signal is much weaker (lower S/N ratio). The ratio of empty/filled-(6,5) tubes is roughly unchanged with respect to the experiment up to 26 GPa. The most significant change is that the (8,3) RBM peak area has now become comparable to the (6,5) one (E or F). The progressive prominence of the (8,3) peak with increasing maximum pressure is confirmed in the 50 GPa_Set 2 experiment taken with a 532 nm eV laser : the (8,3) signal becomes more intense than the (6,5) one. It is important to note that the characterizations at ambient conditions for Set 1 and Set 2 (see Figs.3.4, 3.11) do not offer a enough resolution to distinguish the filling effect in the (8,3) and (6,4) tubes. Surprisingly, the (6,5) signal of the 50 GPa_Set 2 shows similar frequencies to the (6,5)-empty tubes. We note that no RBM signal is observed for the 50 GPa_Set 2 sample APL when excited with the 514 nm laser wavelength. Nevertheless, in the corresponding G-band spectra Figure 3.11(b)(third panel from left to right), the G^{-} peak in the APL still is resolved, therefore demonstrating a reminiscent tubular feature. Consequently, the RBM signal losses with the 514 nm excitation can be attributed to resonance conditions. Finally the Stock sample cycled up to 80 GPa did not show any sign of RBM and its G-band did not show any sign of G^- peak. This seems to indicate the unzipping or destruction of all tubular structures.

We may look to the G-band spectral of Fig. 3.11(b) with more detail. They reveal that with increasing the maximum pressure, the D band (structural defects) intensities increase. The evolution of the proportion of defects can be described quantitatively by the evolution of I_D/I_G which are given in Table 3.7. The I_D/I_G maximum ratio of 0.98 found for Stock is usually ascribed in some works from literature [123, 124], as a indicative of structural transformations. This information becomes evident when we connect the I_D/I_G values evolution and the G^- bands (tubular aspect) profiles of other recovered materials, since that these peaks can be resolved up to 50 GPa but not for 80 GPa. It is also interesting to mention that the G^- peaks are assigned as contributions of (6,4) (low frequency) and (6,5) (high frequency) tubes, by comparing with the G-band spectra at ambient conditions Figure 3.4.

Overall our analysis of the cycled Raman spectra shows that the small diameter tubes (empty or filled) can support pressures up to 50 GPa with the presence of structural damages (the low peak intensity and the background signal-to-noise increasing). At pressures of 80 GPa all tubes have been irreversibly transformed. Interestingly there are clear differences on the tube pressure stability between tubes having different chiralities and similar diameters. This is the case of the (8,3) tubes which showed to better survey to pressures cycles up to 40 GPa and 50 GPa.

Table 3.7 – Comparison between our studied samples after each maximum pressure loading. The collapse pressure for each sample is addressed together with the reversibility aspect. The defects density is provided by ratio I_D/I_G (6th column). The percentage of filling measured with the same energy excitation for the samples before and after pressure cycles is given by ratio I_{APL}/I_{BPL} (7th column).

Initial sample	laser λ (nm)	$P_{\max}$	Collapse Pressure	Reversibility	I_D/I_G	I_{APL}/I_{BPL}	
						E	F
Top 2	568.2	26 GPa	17 GPa (onset)	reversible	–	–	–
Set 1	568.2	26 GPa	17 GPa (onset)	reversible	0.20	1.00	1.55
Set 2	514	40 GPa	17 GPa (onset) - 30 GPa (end)	reversible	0.41	0.76	1.25
Set 2	514	50 GPa	17 GPa (onset) - 30 GPa (end)	reversible	0.6	–	–
Set 2	532	50 GPa	single acquisition (APL)	reversible	0.5	–	–
Stock	514	80 GPa	$\sim$ 15 GPa	irreversible	0.98	–	–

To further explore the structural irreversibility undergone by nanotubes of Stock cycled to 80 GPa, a set of TEM images were collect from the recovered material Figure 3.12. The Figure 3.12(a) shows an open field image of a piece from Stock sample recovered after loading of 80 GPa. In Fig. 3.12(b) is shown a region of the sample exhibiting a turbostratic carbon structure (upper left image). The electron diffraction (SAED) pattern of this material was taken and the distance between two brighter curves (red numbers labeled by 1 and 2) confirms that the interlayer distance is graphite-like with about 0.337 nm ($D = 1/(\frac{L}{2})$, where $L = 5.922\ \text{nm}^{-1}$ in reciprocal space). The weak secondary rings are also visible in the SAED, being associated with

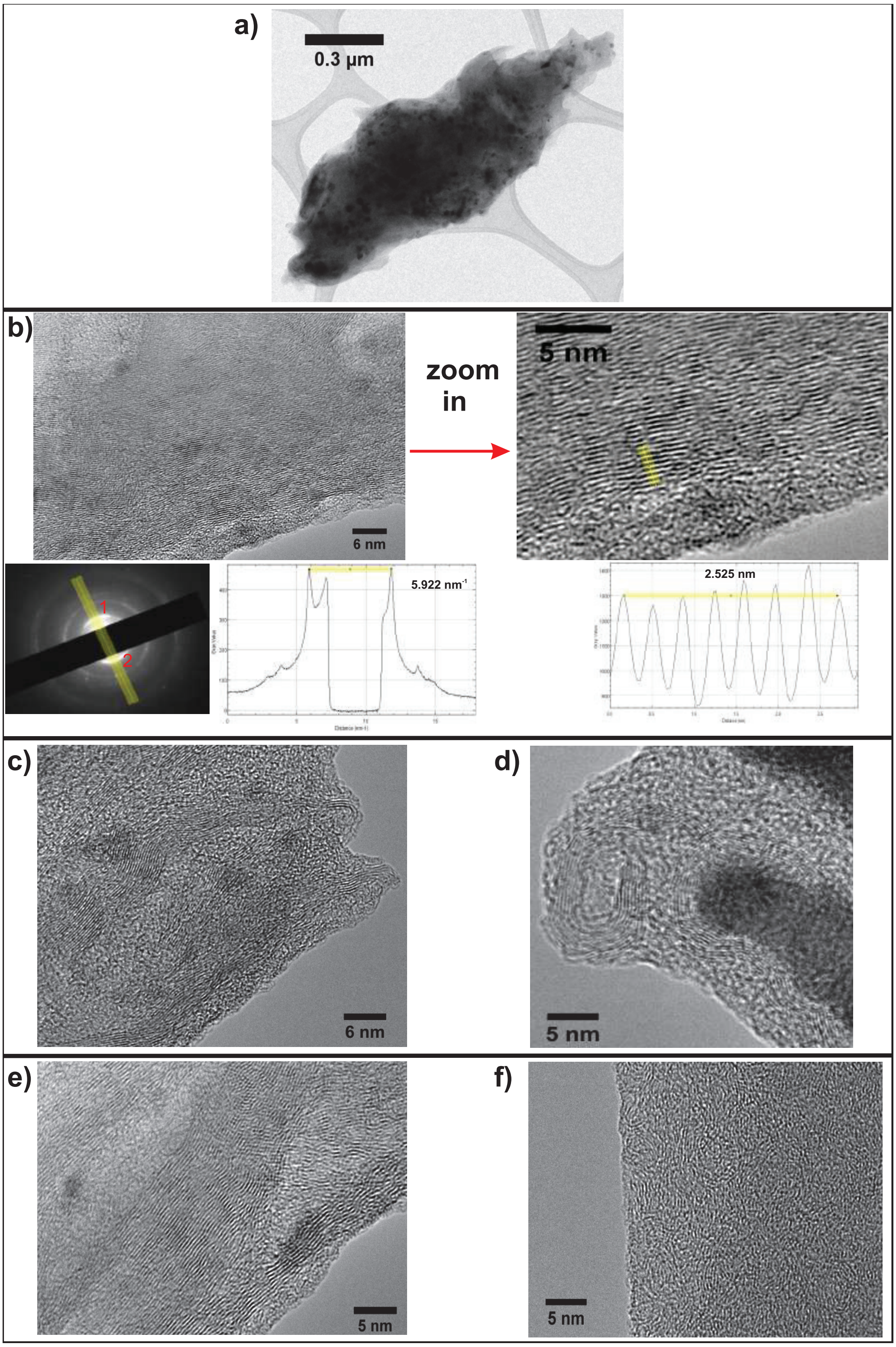

Figure 3.12 – TEM images of Stock (empty tubes) sample after pressure cycle of 80 GPa. a) Zoom out of a piece from the Stock recovered specimen after 80 GPa. b) TEM image of a region of the turbostratic carbon (right side). The SAED pattern shows two brighter opposite curves close to the beam center (numbered by 1 and 2 in red color) and the plan distance is given in the lower left graph, secondary rings also are shown by electron diffraction pattern. The right image corresponds to the zoom in from right one and the yellow line marks the plan distance provided in the lower right graph. c) Non-graphitic carbon planes. d) Nanocages present after 80 GPa. e) Overlapped non-graphitic carbon planes. f) Amorphous carbon region. The scales bar are provided in each image.

the sample polycrystallinity. A zoom from the previous image (upper right image) allowing to display a better view of the layers stacking and texture. The yellow line on that zoom image allowed to measure the distance between planes providing a distance around 0.360 nm (associated with the turbostratic carbon structure [125]). Other nanosctructures are also formed (see Figure 3.12), as non-graphitic carbon planes c), overlapped non-graphitic carbon planes e) and amorphous carbon f), all providing strong evidence of the nanotube irreversible transformation. Nano-onions or nanocages with inter-plane distances close to graphitic planes (Fig.3.12(d), distance $\sim$ 0.344 nm) are also observed; however these structures are also present in the Stock pristine sample Fig. 3.1(c). Some works in the literature report that the nanocages can support pressures higher than nanotubes [126, 127].

3.3.4 Conclusions

We have performed a resonant and non-resonant Raman study at high pressures of chirality-enriched (6,5) single walled nanotubes in bundles and individualized tubes. We observed that the RBM frequencies as well as their pressure dependence are strongly dependent of the surrounding environment of the tubes. The collapse pressure of empty (6,5) was estimated at around 16 GPa, while for the water filled (6,5) tubes no feature indicating a possible collapse appeared up to 50 GPa. For pressure cycles up to 50 GPa, empty and filled tubes survive, but nevertheless a large proportion of damaged tubes can be evidenced both by defects density (I_D/I_G) as well as by the RBM Raman peak areas of filled and empty tubes before and after pressure loadings ($I_{\mathrm{APL}}/I_{\mathrm{BPL}}$).

The instability (unzipping) of empty (6,5) (and other chiralities) is full at 80 GPa with the creation of others nanostructures, as turbostratic graphite planes and amorphous carbon. In addition, the mechanical stability response of nanotubes seems to depend of chirality. In fact we have observed a higher structural instability for empty + water-filled (6,5) tubes in comparison to the empty (8,3) tubes after recovering the samples from pressure cycles at different maximum pressures.

This first study in this PhD thesis on low diameter (0.75 nm) nanotubes point out to three important results: a)there is no significant PTM effect on the collapse pressure, but nevertheless an important effect on the RBM signal evolution, b) it appears to be an important chiral effect on the tube stability and c) nanotube stability for these low diameter tubes is found between 50 and 80 GPa.

4

Triple walled carbon nanotubes at high pressure

Sommaire :

4.1 Introduction **88**
4.2 Triple walled carbon nanotubes **88**
  4.2.1 TWCNTs synthesis 88
  4.2.2 General aspects and previous works 89
  4.2.3 Results and discussion 90
    4.2.3.1 Radial breathing modes analysis 91
    4.2.3.2 Tangential modes - G band analysis 95
    4.2.3.3 Pressure-induced nanotubes irreversibility and unzipping 99
  4.2.4 Conclusions 102

4.1 Introduction

After having explored the effect of the pressure transmitting medium, diameter and even chirality in the mechanical stability of SWCNTs, we will now turn to the effect of the number of walls. For this we will consider in this chapter triple-wall carbon nanotubes (TWCNTs). There have been a number of works on the high pressure response of DWCNTs but the study on the pressure response of TWCNTs is newer and counts only with a single experimental study[128] limited to a maximum pressure of 6 GPa. That study, makes part of an ongoing collaboration of several years between our ILM group of the University of Lyon and the Physics Department of the Federal University of Ceara (Fortaleza, Brazil) and the present chapter is a continuation of that work to explore at higher pressures the stability of TWCNTs. In this chapter we first describe the elaboration and main properties of the TWCNTs specimen used together with works previously reported in literature about this sample. Subsequently, we introduce our results obtained by high pressure resonant Raman experiments and electron microscopy characterization, discussing them throughout the text. As in the previous chapter we will first consider the RBM signal, then the G band contribution before considering at last the irreversible transformation of the sample. We finished the chapter by summarizing the main conclusions of this chapter.

4.2 Triple walled carbon nanotubes

4.2.1 TWCNTs synthesis

Highly crystalline and uniform TWCNTs were synthesized by Muramatsu *et al.* [129]. To obtain this sample, a high-temperature thermal treatment of catalytically grown high-purity DWCNTs was performed at 2400 °C by means of a graphite furnace in argon atmosphere to enlarge the diameter of the tubes via the coalescence mechanism. The thermally annealed DWCNTs presented inner diameters optimized to encapsulate C_{60} ranging from 1.0 - 1.8 nm. The cap structure of the DWCNTs was removed by an air-oxidation treatment carried out in air. This was followed by the encapsulation of the fullerenes in DWCNTs. For this C_{60} and nanotubes were sealed into a glass tube under vacuum, and the mixture was annealed at 600 °C for 5 h. DWCNTs encapsulating fullerenes (peapods) were washed by toluene to remove the residual fullerenes in adhesion on tubes surfaces. In order to transform C_{60}@DWCNTs into TWCNTs (to coalesce the fullerenes and form the inner tubes of TWCNTs), a thermal treatment was carried out at temperatures of 1500 - 2400 °C (the optimal temperature for transformation was of 2000 °C) using a graphite furnace in argon for 30 min. The number of TWCNTs with regard to SWCNTs and DWCNTs was estimated to be ca. 45% (considering the filling ratio as well as the conversion rate of peapods).

The TWCNTs characterization was performed using TEM, Raman spectroscopy, photoluminescence (PL) and optical absorption spectroscopy. For more details about the synthesis and characterizations see [129].

It is important to emphasize that the basic geometrical features (diameters evaluation, the possible chiralities) of the TWCNTs were studies by Raman spectroscopy, whereas the TEM + PL studies were carried out more for the diameter distribution as well as the formation ratio of TWCNTs at high temperature. However, none of these studies associated with the diameter distribution provide a quantitative approach about the inter-layer (wall to wall) distance, but we think that by the average values shown in the Figure 4.1(c) (similarly in Figure 2 and Table S2 of the Supporting Information from [129]) the inter-layers distance seems to follow the nominal van der Waals value (~ 0.34 nm). A way to access the information concerning to the wall-to-wall distance could be the use of X-Ray diffraction, where e.g., the (002) peak position displays the wall to wall distance, as shown in the work about the DWCNTs systems [130].

4.2.2 General aspects and previous works

TWCNTs[1] offer an ideal structure to study and understand in what way the environment can influence the general properties of both SWCNTs and DWCNTs, as well as other hybrid systems and their reciprocal relation, in this sense a well-established knowledge on mechanical and electronic properties is required.

The first detailed study using RRS for characterization of bundled and individual TWCNTs was carried out by Hirschmann *et al.* [131]. In this work was demonstrated that inner nanotubes are chirality-dependent isolated (i.e. partially) by outer nanotube. Once it has been observed that the innermost semiconducting tubes are more sensitive than metallic nanotubes, being effect by the surroundings and high-curvature intertube. In another study (extension of the previous one), Hirschmann *et al.* [132] have pointed out that metallic inner tubes show broadened resonant peaks profiles when compared with those narrow peaks of the semiconducting tubes in a RBM spectrum region. By means of comparison the Raman results for bundled as well as individual fullerene-peapod derived double wall carbon nanotubes and TWCNTs, it was possible discuss a correlation between wall-to-wall distances and the frequency upshifts of RBMs. These results provided more informations about fundamental properties of DWCNTs and TWCNTs, as the intertube interactions depending on diameter-, chirality-, high-curvature-dependent. This has then, showed the role of intratube interactions in TWCNTs electronic structure.

In other characterization work about the G' band (also known as 2D band - double resonant Raman scattering process independent of structural defects) of individual TWCNTs taken at different laser wavelengths, Hirschmann *et al.* [133] has shown that each concentric nanotubes contributes independently to the G' band from one another. In fact the G' band shows a clear triple-peak structure, thus indicating a weak coupling of the system. In bundles the G' band frequency and intensity revealed an important dependence on the nanotube chirality and diameter of inner tubes.

Through the pressure application on bundled TWCNTs, Alencar *et al.* [128] demonstrated that the host (intermediate) tubes experience electronic screening and mechanical support effects at the same time, making then TWCNTs distinguishable from DWCNTs in the mixture. In addition, the radial breathing modes (RBMs) of the innermost tubes of TWCNTs under different resonance and pressure conditions showed similarities, which evidenced the pressure-induced band-gap tunability.

Albeit these works provide some fundamental insights to a better understanding of mechanical and electronic properties in TWCNTs, the collapse picture of TWCNTs and the tube stability are not known.

In next sections, we will address these problems using *in situ* resonant Raman spectroscopy at

---

[1] Always corresponding to the synthesized sample by Muramatsu *et al.* [129]

high pressure and post-modern TEM study.

4.2.3 Results and discussion

The experimental details of the TWCNTs experiments are reported in the Annex. We will focus here on the results obtained from our experiments together with the existing literature.

Figure 4.1 shows the high resolution transmission electron microscopy (HTREM) of DWCNTs and TWCNTs as prepared in Ref. [129]. Our samples are the same ones. We can notice by Figs. 4.1(a)-(b) that the specimen does not contain an homogeneous distribution of walls number (the TWCNTs rate is 45% with regard to that of DWCNTs). Therefore, we may observe that the resonant Raman spectra collected from this sample contains contributions of both DWCNTs and TWCNTs. We should note that it has been proposed that the frequency of the RBM modes in DWCNTs can be modified by the coupling of the tubes [134] and in this context we should then speak about BLMs (Breathing-Like Modes). Nevertheless, the often found incommensurability between the two adjacent layers in DWCNTs has been proposed as a limitation for such coupling [135, 136] which may exist for some particular DWCNTs. Our samples being powders we assume that not coupling is dominant.

To estimate the inner, intermediate and external diameter of TWCNTs, we used the zero-order approximation $\omega_{\mathrm{RBM}} = 218.3/d_t + 15.9$ cm^{-1} as suggested by Muramatsu et .al [129], where ω_{RBM} is the radial breathing mode and d_t is the tube diameter. The intermediate and outer tube diameters of TWCNTs are similar to those of DWCNTs. The diameter distributions of TWCNTs are shown in Fig. 4.1(c) (the average diameter of innermost, intermediate and outer tube from TWCNT are 0.83 nm, 1.45 nm and 2.23 nm). The loading configuration of sample before the pressure cycling is shown in Fig.4.1(d), the white arrows designate the ruby chip, pieces of sample and NaCl PTM (used to avoid filling of the tubes).

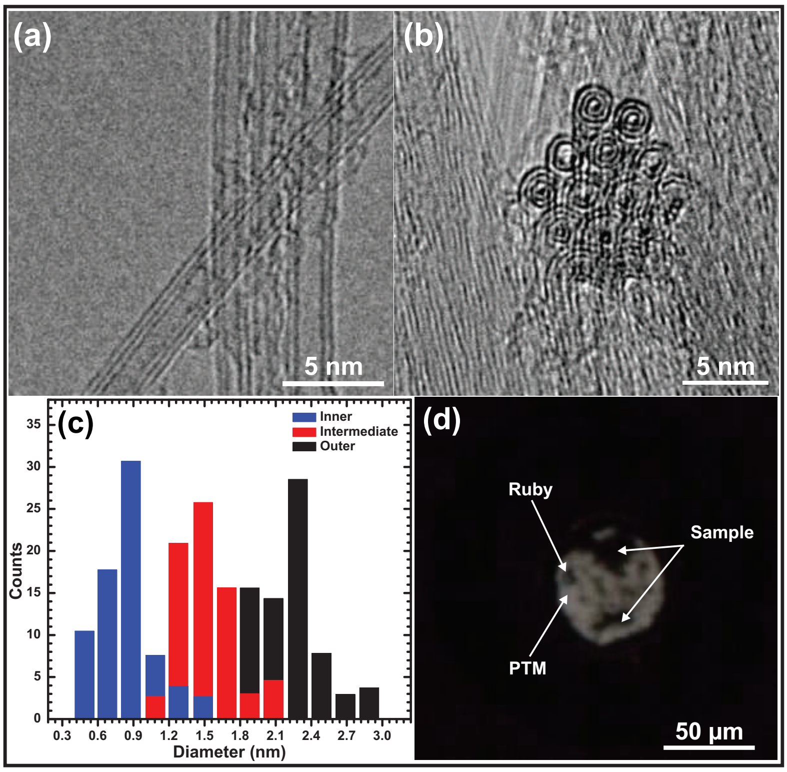

Figure 4.1 – (a) HRTEM image of a TWCNT on DWCNTs at ambient conditions (scale bar in image). (b) circular cross-sections of pristine samples (scale provided in image).(c) the colorful histogram displays the diameters distribution of inner (blue), intermediate (red) and outer (black) tubes from our specimen.(d) optical image from DAC gasket volume filled by NaCl PTM, a ruby chip and sample pieces at few microns size before the pressure cycle.

4.2.3.1 Radial breathing modes analysis

Figure 4.2(a) shows the RBM like Raman spectra at different pressure values (from ambient conditions up to 18.7 GPa) of TWCNTs taken with an excitation energy of 2.41 eV. All spectra were background subtracted with a linear function and normalized (0 to 1).

Our measurements which containing some visible RBM signal extend up to 15 GPa, whereas the previous study of the TWCNTs RBM evolution was limited to 10.4 GPa (Ref. [128]). In general, with the increase of pressure all RBM modes broaden and their intensities present a global attenuation, in agreement with previous studies [55, 56, 128]. However, for the RBMs frequencies above of 360 cm^{-1}, the relative intensities change with the pressure increase, being observable up to 14.6 GPa. As suggested in Ref. [128], this result can be attributed to changes in the electronic transition energies from inner tubes (discussed along the text).

Due to the non-homogeneity of the sample (DWCNTS and TWCNTs) and the diameters distribution to be narrow, it is difficult to distinguish directly the origin of the peaks contribution in the Raman spectra. In other words, we do not know if theses peaks belong to the inner tubes of DWCNTs or to the intermediate tubes of TWCNTs, when measured at ambient conditions.

Thus, for a deeper analysis of the RBM spectra, each peak was fitted with one Lorentzian component, resulting in twelve peaks, which are shown in Table 4.1. The peak marked with hash symbol is a spurious signal, since both frequency and intensity (relative to the noise) do not change with pressure. The other two peaks labeled with stars are laser plasma line (see

Fig.4.2(a)).

The RBMs frequencies follow a linear behavior with the pressure, having the experimental data fitted with $\omega(P) = \omega_0 + \alpha P$ (where ω_0 and α correspond to the extrapolated frequency at 0 GPa and the pressure coefficient, respectively). These RBM peaks as a function of pressure are shown in Figure 4.2(b). The R1 and R3 peaks, disappear at the two first pressure points, and consequently, do not provide enough experimental points to carry out a reliable fitting. All other RBM modes evolve linearly with pressure, but with different rates.

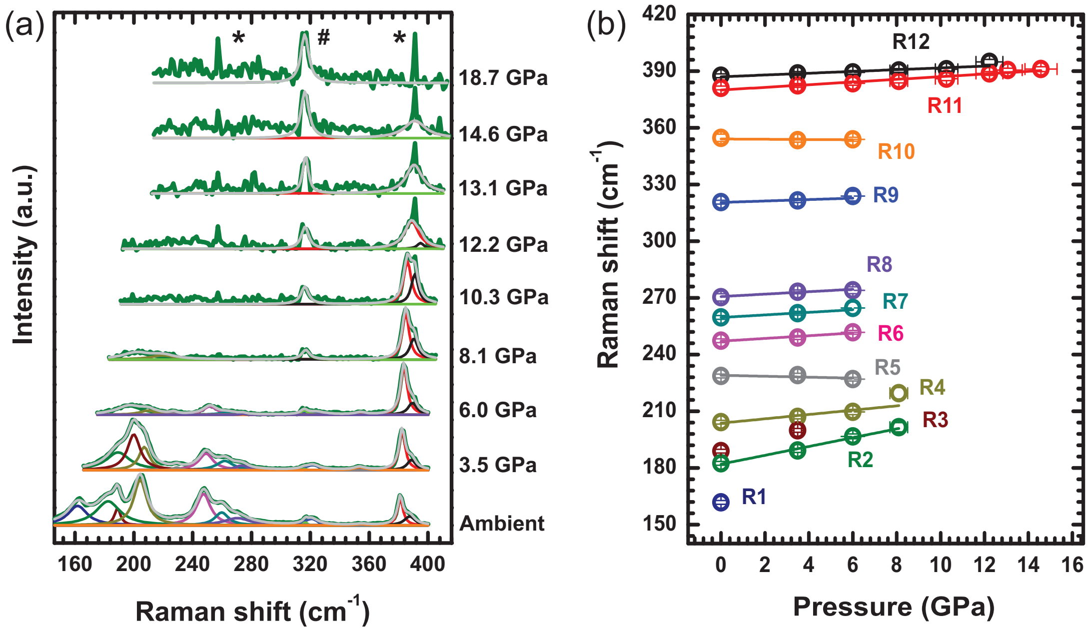

Figure 4.2 – (a) RBM Raman spectra stacked at different pressures values. The green and light gray colors designate the spectral data and fitting, respectively. The another colors emphasize the RBM features until their disappearance. The symbols labelled by stars and hash represent spurious signals, whose origin is discussed throughout the text. (b) RBM frequencies of all twelve observable peaks from spectrum (a) as a function of pressure.

By normalizing the pressure coefficient for each frequency value ω_0 is possible plot a graph of normalized pressure coefficient vs initial frequencies. By means of this plotting, a previous high pressure resonant Raman study on fullerene-peapod-derived TWCNTs (the same specimen used in our work) using different three excitation energies showed that the presence of the innermost tube of the TWCNT provides a structural support for the intermediate tube, an result associated to a smaller normalized pressure coefficient $[(1/\omega_0)(\partial\omega/\partial P)]$ when compared with the inner tube of DWCNTs with similar diameter [128]. This behavior is related to structural support. In fact, the radial stability against pressure of carbon nanotubes is strongly dependent on the tube diameter and on the number of walls [56, 30].

Thus, by comparing the $(1/\omega_0)(\partial\omega/\partial P)$ from our data Figure 4.2(b) with those of Ref. [128] in Figure 4.3, it can be observed that only the R2 peak comes from the DWCNTs (inner DWCNTs). Furthermore, the innermost tubes of the TWCNTs have a similar behavior to those of the inner rings model of DWCNTs (clear yellow square) from the reference [137], whose the values of the normalized pressure slopes are smaller than those for single rings with the same diameters,

Table 4.1 – RBM frequencies at ambient conditions ($\omega_\circ$) and pressure derivatives $\partial\omega/\partial P$, as well as the intercept of each mode when extrapolated to the pressure of 0 GPa.

		linear fitting using NaCl as PTM				
Mode	$\omega_\circ$ (ambient pressure) (cm^{-1})	Intercept (cm^{-1})	$\partial\omega/\partial P$ (cm^{-1}/GPa)	d$_t^*$ (nm)	(n,m)	wall type
R1	161.8	–	–	1.49	–	intermediate
R2	182.4	182	2.3 ± 0.2	1.31	–	intermediate
R3	188.9	–	–	1.26	–	intermediate
R4	204.3	203.7	1.1 ± 0.2	1.15	–	intermediate
R5	228.6	229	-0.2 ± 0.2	1.02	–	intermediate
R6	247.3	247.1	0.7 ± 0.2	0.94	–	innermost
R7	259.7	259.6	0.7 ± 0.4	0.89	–	innermost
R8	270.3	270.7	0.6 ± 0.4	0.85	–	innermost
R9	320.6	320.5	0.4 ± 0.3	0.71	–	innermost
R10	354.7	354.1	-0.1 ± 0.2	0.64	–	innermost
R11	381.1	380	0.7 ± 0.1	0.59	(5,4)	innermost
R12	387.5	387	0.5 ± 0.1	0.58	(7,1)	innermost

*Diameters calculated by relationship suggested in Ref. [129], see text.

reflecting the pressure screening effect of the outer tube, and the decrease of the interlayers distance (ranging of 0.34 to 0.38 nm, see Fig.4.3) causes the RBMs frequencies upshift (the increase of the layers interaction) with a more efficient pressure transmission to the innermost tube (larger $(1/\omega_0)(\partial\omega/\partial P)$). It is important to mention that although the model coupled anharmonic oscillators for DWCNTs of Christofilos *et al.* [137] provides constant curves (dashed yellow lines) of intratube spacing (0.34-0.38 nm (blue) Fig.4.3) for various some of inner rings diameters (0.6-1.0 nm (yellow) Fig.4.3), we are not be able to use it in order to estimate the wall-to-wall distance of our TWCNTs innermost (black triangles Fig.4.3), since the error bars size are large. Summarizing, for the excitation energy of 2.41 eV, the largest contribution for the RBM Raman spectra is originated from the TWCNTs. The R5 and R10 peaks present a small negative $\partial\omega/\partial P$. A similar result has been found for DWCNTs, although not explained [55]. Additional information would be need to clarify such singular behavior.

The RBMs contributions of the TWCNTs innermost tubes are kept above 8 GPa, evidencing the screening effect against pressure [138, 139, 122]. These tubes were assigned as having (5,4) and (7,1) chiralities, the explanation arises from the following arguments:

1. According to the characterization work of TWCNTs bundles at ambient conditions [131], the low diameter tubes excited at 2.41 eV localized in the Kataura plot of individual DWCNTs of similar diameters correlated with a experimental 2D map of intensities, are tubes of chirality (5,4) and (7,1). Besides, the authors affirm that the smaller tubes found in this specimen are (5,4)[2]. The RBM frequency displayed in this work has a good agreement with that of the Table 4.1, taking in account that interactions between tubes lead to blue

---

[2] This statement is given by the RBM and G$^-$ peaks values. In addition, the G$^-$ assignment at 1511.5 cm^{-1} of this study is coherent with that one of our study - see in the next section, the G$_1^-$ position at 0 GPa.

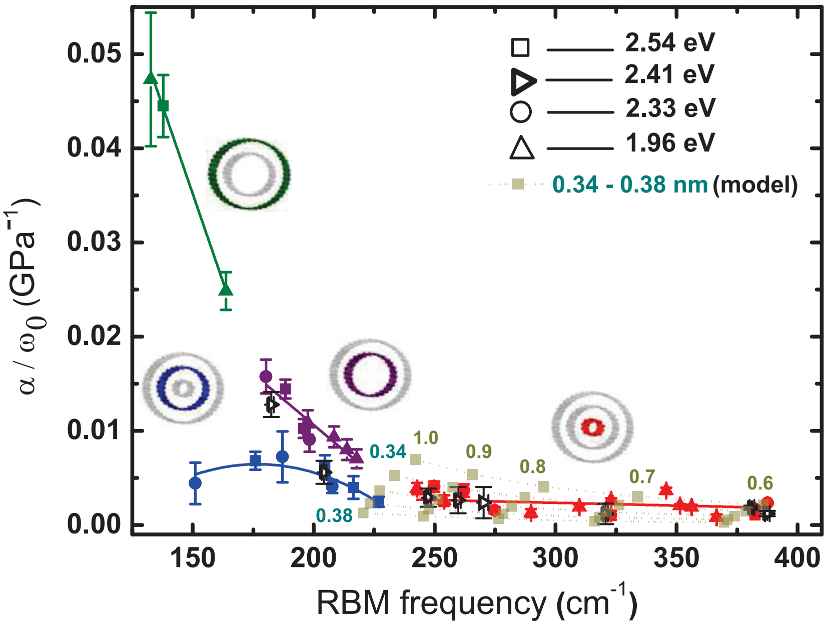

Figure 4.3 – Normalized pressure coefficients ($\alpha/\omega_0 = 1/\omega_0 \partial\omega/\partial P$) as a function of RBM frequencies obtained from the Raman spectra acquired with the excitation energy of 2.41 eV from our experimental data (highlighted horizontal black triangles) compared with those from Ref. [128]. The dashed yellow curves correspond to the coupled oscillators model of DWCNTs from [137] with the layers distance ranging from 0.34 to 0.38 nm (blue numbers) for different inner tube diameters (yellow numbers).

shift of modes. Besides, the (5,4) resonance condition is very intense at 2.41 eV, while for (7,1) tube this condition is more close to 2.33 eV.

2. The next argument arises from the first work already referred about TWCNTs under high pressure excited by different laser energies [128], where innermost tubes probed by laser 2.41 eV at ambient conditions showed profiles and peaks positions similar to those at a pressure of 5 GPa, but excited with an energy of 2.33 eV. In other hands, the tubes probed with these two energies were the same, but resonance conditions were tuned with pressure.

3. Combining the above assumptions 1 and 2, we can suggest that in our experiment of high pressures the innermost tubes (5,4) have the their resonance conditions less affected than (7,1) tubes until at least 14.6 GPa, because these tubes already are at strong resonance and loss slowly this resonance, in opposition to (7,1). This similar result was observed in Ref.[128], where the (5,4) and (7,1) enter in resonance only with the pressure increase.

A priori until the value of 8 GPa, no structural transformations is expected, taking in account that the collapse in SWCNTs and DWCNTs (with similar diameter) has been observed only above 10 GPa [55, 39, 140, 141]. At the same time, if we consider the collapse pressure relying on d^{-3} (equivalent to modified Lévy-Carrier law in the larger tubes regime) and that the TWCNTs outer tubes are > 1.5 nm, we could point out surely that inner tubes provide the structural support, which in turn delays the collapse pressure of the all system [47, 43, 55, 128, 56].

On the other hand, our previously discussed RBM data and results do not offer a clear indication about the collapse of TWCNTs As reported in Ref.[128] and briefly quoted in the text, the compression in smaller diameter tubes lead to deep changes in their transition energies (E_{ii}). This results explain the modifications seen in the RBMs profiles of our experiments (Figure 4.2(a)).

4.2.3.2 Tangential modes - G band analysis

Figure 4.4(a) shows the G-band Raman spectra at different pressure values for excitation energy of 2.41 eV. As in case of the RBM spectra, the G-band were also normalized so that their intensities are between 0 and 1. Commonly, the G-band broadens and its intensity decreases as pressure increases, in agreement with previous studies in DWCNTs and TWCNTs [128, 55, 56]. For a detailed analysis of the G-band, we fitted the G-band profile with six Lorentzian components (black lines in 4.4(a)), following a similar procedure as in Ref [128]. Due to the fact that our sample contains a mixture of DWCNTs and TWCNTs, we have nominated the three highest frequency components as G_1^+, G_2^+ and G_3^+ modes Figure 4.4(b). Since, we could expect the G_2^+ and G_3^+ contributions being originated from intermediate and outer tubes of DWCNTs and TWCNTs, whereas the G_1^+ component could be only attributed to innermost tubes of TWCNTs. A similar proposition would be used to assign the three lowest peaks G_1^-, G_2^- and G_3^-. Here the numeral labels refer to the tube position, with 1 being the innermost tube [55, 128]. Moreover, we also used a Voigt component (blue lines in Figure 4.4(a)) for a lower energy component to improve the fitting. This broad band has been assigned in other works to the D-band [142].

In addition, a recent study [143] considering the mechanical coupling between the layers of individual suspended DWCNTs (unambiguously index-identified) at ambient conditions has shown the G-mode frequencies dependence on the distance between the inner and outer layers and this is well understood through the effect of an effective pressure felt between these two layers. It was stated that when the intertube distance is larger than 0.34 nm (the nominal van der Waals value), larger is the downshift (upshift) of the longitudinal (LO) and transverse (TO) G-modes of inner-layer (outer-layer) with respect to the corresponding modes in equivalent SWCNTs. By contrast, our work deals with bundled TWCNTs (containing in a certain rate DWCNTs and SWCNTs) whose configuration leads to the overlapping of all modes, thus making the investigation on the TWCNTs innermost tube more complex and limiting in this particular case the of this approach.

The pressure-dependence of the six G-band modes from Figure 4.4(a) is shown in Figure 4.4(b). Because of the fast attenuation of the G^- peaks and the increase of the D-band intensity (blue lines in Figure 4.4(a)), we concentrate our analysis on the G^+ components. These components blue shift steadily with then a positive - but different from each other - pressure coefficient ($\partial\omega_{G^+}/\partial P$) up to 21.7 GPa (blue arrow in Figure 4.4(b)). At this pressure value, both G_2^+ and G_3^+ components present an inflection point evolving towards a negative $\partial\omega_{G^+}/\partial P$ up to 27.5 GPa. After this pressure they follow a behavior close to graphite (dashed red line in Figure 4.4(b)). Differently, the G_1^+ component exhibits a plateau between 24.8-36.8 GPa. After that, it also evolves with a similar $\partial\omega_G/\partial P$ to graphite. Beyond 60 GPa (one pressure point) we used only one Lorentzian component to fit the G-band. The reason to follow such procedure will be discussed later.

The Table 4.2 shows the pressure response of the TWCNTs G-band frequencies for the inner,

intermediate and outer tubes compared also with DWCNTs from literature [50, 55]. The slope of G^{+}_{inner}-peak has a smaller value than $G^{+}_{intermediate,outer}$-peaks, reflecting again the larger deformation of the outer tubes and the pressure shielding effect for inner tubes (as already pointed out in the RBMs case). When the TWCNTs G^{+}_{inner}-peak is compared with that one of compressed DWCNTs at sodium chloride (NaCl), as well as in methanol:ethanol mixture, its slope is close to than of DWCNTs inner tubes. However, the slope of the external (outer) tubes probed in different pressure transmitting media considerably change, suggesting the environment effect on the outer tube and the chemical screening to inner tube (in agreement with [55]).
In Figure 4.5 is also included for comparison the pressure-dependence of the G^{+} components (blue squares) from DWCNTs [55]. The DWCNTs studied in Ref. [55] are the same used as precursor (catalytically grown high-purity DWCNTs) in the synthesis of our TWCNTs (by means of diameter-enlarged DWCNTs encapsulating fullerenes) used in this thesis.

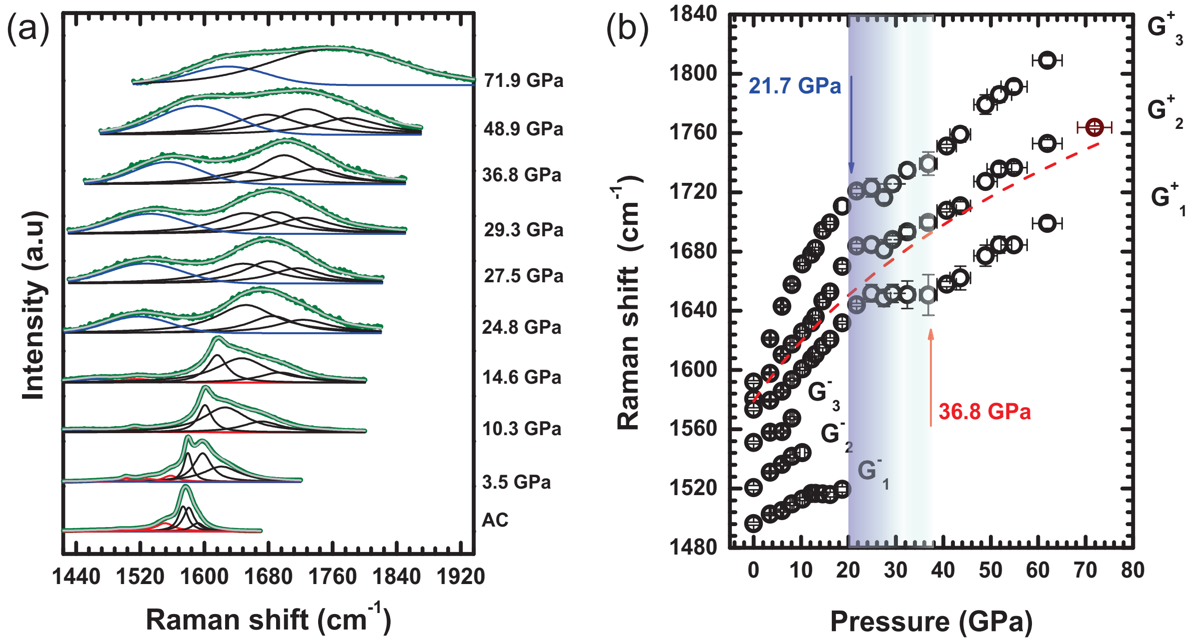

Figure 4.4 – (a) G-band Raman spectra collected at different pressures values. The green and light gray indicate the spectral data and fitting, respectively. Black and red Lorentzian curves represent the three components of the G^{+} and G^{-} peaks, respectively. Blue Voigtian profile at low frequency region is commonly assigned as the D-band. (b) Raman frequencies of the G^{+} and G^{-} components labelled as 1, 2 and 3 for the inner, intermediate and outer tubes, respectively, as a function of pressure. The red dashed line indicates the graphite evolution. The blue and red arrows indicate the onset at $\sim$ 22 GPa and end of collapse $\sim$ 37 GPa, respectively. The colorful rectangular vertical area displays the collapse region. The wine symbol at 71.9 GPa marks the value where the TWCNTs have lost the tubular feature.

The Raman signature of the radial collapse for SWCNTs as well as the value of the collapse pressure depends significantly of the tube filling [41, 144, 56]. For empty SWCNTs, the beginning and the end of a plateau on the G-band pressure derivative ($\partial\omega_G/\partial P \sim 0$) are associated to the onset and the end of the radial collapse, respectively. On the other hand, for water-filled SWCNTs the onset of the radial collapse is related to change on sign of the pressure derivative

Table 4.2 – The TWCNTs G-band frequencies at ambient conditions (ω_i) and its pressure derivatives $\partial\omega/\partial P$, as well as the intercept of each mode when extrapolated to the pressure of 0 GPa.

G-band	ref	ω_i (cm^{-1})	**linear fitting from 0-10 GPa** Intercept (cm^{-1})	$\partial\omega_i/\partial P$ (cm^{-1}/GPa)	Normalized slope (GPa^{-1})
G^+_{outer}	this work	1591.9	1593.4	7.84 ± 0.28	0.005
$G^+_{intermediate}$		1580.58	1581.8	4.41 ± 0.19	0.003
G^+_{inner}		1573.5	1571.6	2.68 ± 0.26	0.002
G^+_o(1.56±0.54nm)	DWCNTs [55]	–	1596.0	8.0 ± 0.1	0.005
G^+_i(0.86±0.25nm)	NaCl	–	1579.2	4.6 ± 0.1	0.003
G^+_o	DWCNTs [50]^a	$1592^a/1594^b$	–	$6.1^a/5.8^b$	$0.004^a/0.004^b$
G^+_i	[122]^b 4M:1E	$1579^a/1582^b$	–	$3.3^a/3.3^b$	$0.002^a/0.002^b$
G^-_{outer}	this work	1551.0	1550.7	1.82 ± 0.46	0.001
$G^-_{intermediate}$		1520.6	1521.6	2.47 ± 0.14	0.002
G^-_{inner}		1496.3	1496.4	1.59 ± 0.08	0.001

[50]^a: d_t^{outer}=1.38±0.05 nm, d_t^{inner}=0.69±0.08 nm; [122]^b: DWCNTs with diameter ranging from 0.6-3.0 nm.

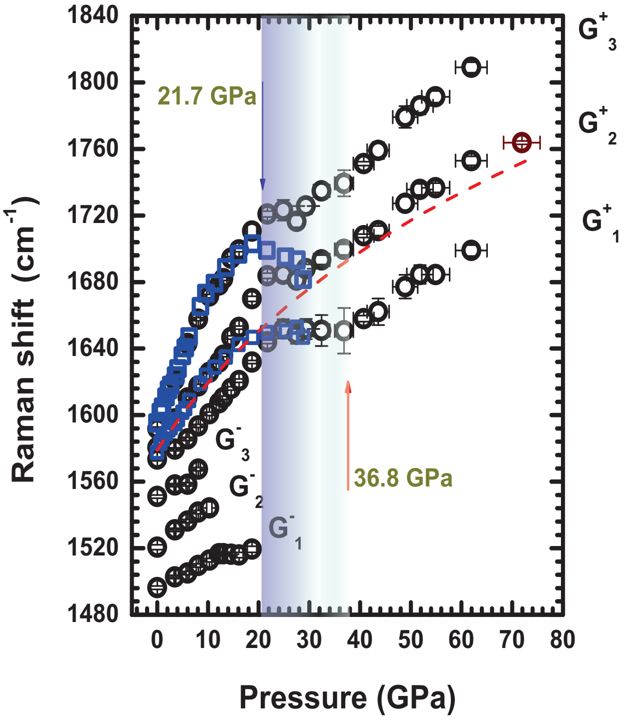

Figure 4.5 – The blue squares represent the G^+ components from DWCNTs Ref.[55] evolving as a function of pressure in comparison with the data of the present work. The collapse region is represented by colourful vertical rectangular with the onset at 21.7 GPa and the end at 36.8 GPa. The red dashed curve belongs to graphite evolution and the sole wine point marks the irreversible transformation explained in the main text.

whereas the full collapse is associated with the pressure at which the G-band frequency evolves with a graphite-like behavior [39, 37, 41]. For DWCNTs, as in water-filled SWCNTs, the onset of radial collapse is also attributed to a inversion of $\partial\omega_G/\partial P$ [55], being completed when the G-band frequencies achieve a behavior similar to the one of graphite [56]. The disappearance of the RBM modes can also be an indicative of the radial collapse, specially in individualized tubes [30]. However change of resonance conditions and drastic variations on the tube cross section, as previously mentioned can also lead to loss of RBM modes [41, 56, 128, 44, 34, 35, 145, 142].

Theoretically the collapse process of DWCNTs and TWCNTs is predicted to follow a cascade effect, with a pronounced volume reduction before the full collapse [144, 56]. Firstly the outer tube deforms, being supported by the inner tube (intermediate and inner tube in TWCNTs), which in turn, is screened by the outer one. On the other hand, the outer tube cross-section polygonization induces a radial strain on the inner tube and, consequently, the full collapse. Differently, SWCNTs present a more abrupt transition to collapsed form which nevertheless spans in a pressure domain in hydrostatic conditions from P_c to $1.5Pc$ [146, 30], much less pronounced than found in DWCNTs, P_c to $2.5P_c$ [56].

In this sense, the pressure behavior of the G^+ components from Figure 4.4 is interpreted as follows. The outer and intermediate tubes collapse onset takes place at $\sim$ 22 GPa, i. e., 3 GPa higher than the one found for the DWCNTs collapse onset (blue squares in Figure 4.5), even if we take into account the diameters distribution difference between the precursor DWCNTs [55] and enlarged DWCNTs by annealing studied here. Thereby, such difference might be related to the further structural support provided by the innermost tubes in the TWCNTs system and more clearly, the components G_1^-, G_2^- and G_3^- evolution may be attributed to inner, intermediate and outer walls of TWCNTs, respectively. The inner tube from TWCNTs seems to begin the collapse only at $\sim$ 25 GPa, which suggests a cascade effect, however the position differences have close incertitudes making the accuracy difficult. A similar effect is also observed in DWCNTs (Figure 4.5 blue squares), in which the inner tube also starts to collapse only 4 GPa after the outer one. The graphite-like behavior of both G_2^+ and G_3^+ components after 29 GPa is interpreted into two regimes. In the 29-37 GPa the pressure-evolution of both G^+ components indicate that the inter-wall separation of these two tubes has reached that of graphite at the same pressure, although they are not completely collapsed, since the inner tube is still in collapse process. After 37 GPa, the end of the plateau, the inner tube also assume a graphite-like behavior (red arrow). This pressure is assigned as being the full radial collapse of the TWCNTs, where all shells evolve similar to the graphite with pressure, i.e., all tubes shells achieved a peanut-shape cross-sections [56] (or racetrack for the innermost tubes). A scheme about collapse picture is proposed in Figure 4.6.

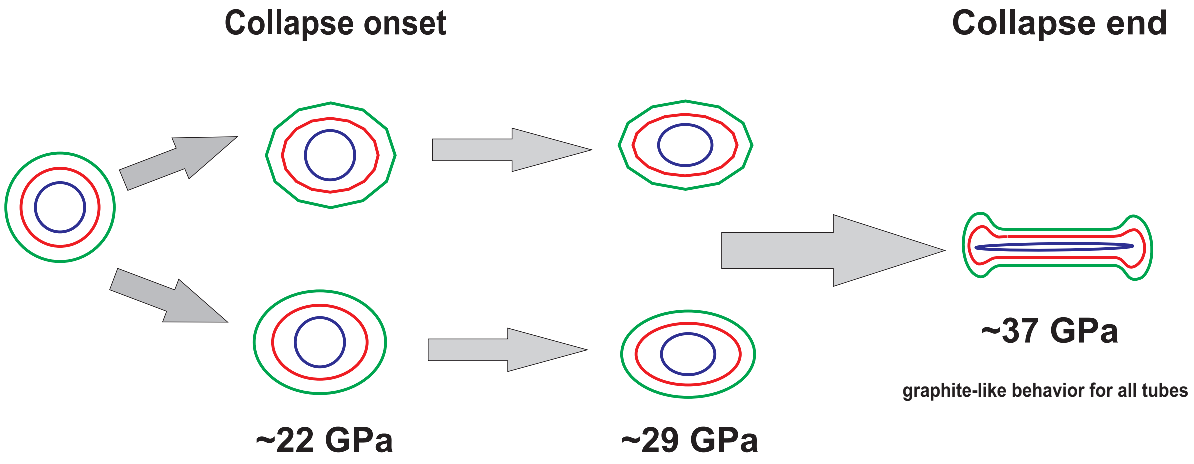

Figure 4.6 – Collapse scheme for TWCNTs, where the green, red and blue circles correspond to the outer, intermediate and inner tubes, respectively. The collapse onset happens ∼22 GPa, showing two possible shapes for the cross-sections of outer and intermediate tubes (polygonized or ovalized). The same aspect is shown at ∼29 GPa with a pronounced ovalization of the inner tube cross-section. At ∼37 GPa the collapse end takes place and all tube walls enter in a graphite-like regime.

4.2.3.3 Pressure-induced nanotubes irreversibility and unzipping

In order to investigate possible transformations in the TWCNTs after pressure loading up to 72 GPa, we have recovered the specimen and characterize it by TEM. Figure 4.7 shows a long and compacted bunch of filaments (Figure 4.7(a)), which are characterized by films disclosed of any tubular geometry profile, Figures (4.7(b)-(d)). Such findings suggest that for pressure far away from the collapse, the collapsed peanut-shape cross-section of the tube transforms into nanoribbons-like graphitic structures Figure 4.7(c). The pressure-induced nanoribbons are stacked in few layers. Some previous studies have shown that the carbon nanotubes can be transformed into graphene nanoribbons (GNRs) via unzipping by chemical and sonochemical treatment [147, 148, 149, 150, 151, 152]. Besides, studies of hypervelocity impact of nanotubes against a solid target reported the obtaining nanoribbons by the longitudinal unzipping of the nanotubes, as well as nanodiamonds and covalently interconnected nanostructures [124, 153]. However, such nanotubes unzipping by static compression (extreme pressure conditions) has not yet been reported in literature (including those experiments on single- and multi-walled carbon nanotubes at extreme pressures [154, 155, 156]).

We have carried out other three high pressure experiment cycles aiming better confine the about the threshold pressure for TWCNTs irreversible transformation. Figure 4.8 shows the comparative RBM, D- and G-band Raman spectra after decompression of different pressure cycles with the pristine one. After 36 GPa a slight intensity decrease of the RBM modes and a low value of $I_D/I_G = 0.1$ show that still exists a high percentage of remaining TWCNTs and DWCNTs. For the decompression after 52 GPa, the presence of RBM modes at the region from 240 to 390 cm^{-1}, which belongs to the TWCNTs, according to Figure 4.3, indicates that TWCNTs can still hold that pressure value, although considered increasing of I_D/I_G ratio and a decreasing of the signal-to-noise intensity radio indicate induced structural damages on the tube.

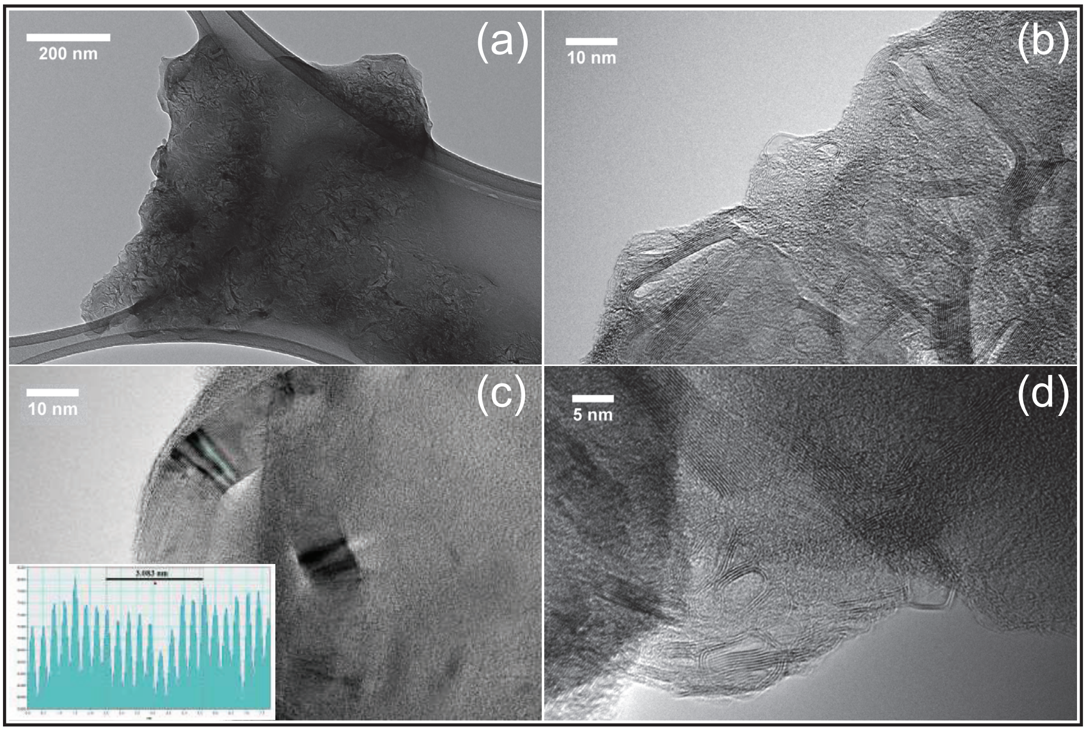

Figure 4.7 – (a)TEM image of the recovered sample after 71.9 GPa pressure loading on carbon grid. This image displays clearly grouping of well-distributed long filaments. (b) The zoom in shows a better definition of the filament structures, which are constituted by stacking of few layers. (c) The blue straight line on TEM image reproduces the graphite-like structure with graphitic plane distance of 0.334 nm between, showing the TWCNT transformation into nanoribbons-like structures. (d) The image emphasizes of absence of any tubular feature, thus addressing a irreversible transformation of the TWCNTs. The scale bars are provided in each image.

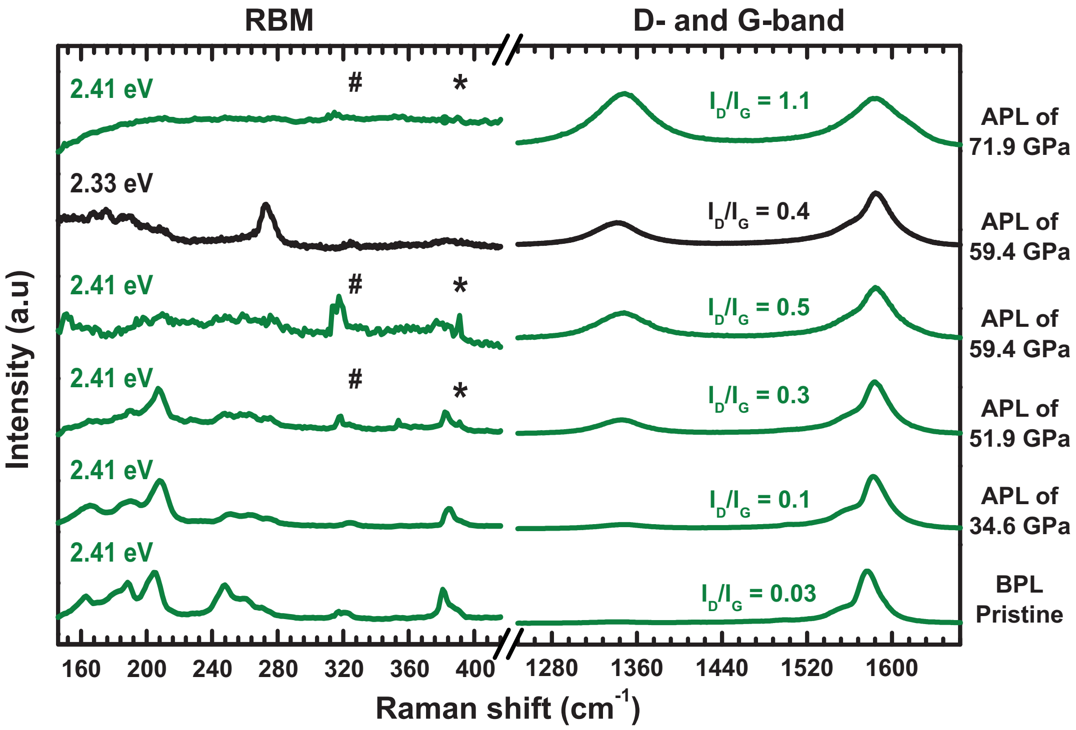

Figure 4.8 – Raman spectra collected before and after several pressure cycles: 34.6 GPa, 51.9, 59.4 and 71.9 GPa acquired with two 2.33 eV and 2.41 eV excitation energies. The star and hash symbols represent spurious signals, whose origin is discussed throughout the text. The I_D/I_G ratio for all cycles are also displayed. (BPL: before pressure loading; APL: after pressure loading)

The spectra after pressure loading of 60 GPa were excited by two different laser wavelengths. For the 2.41 eV excitation energy, the RBM region displays no clear presence of modes, only the aforementioned spurious signals (hash and star marks), indicating a deeper level of defect on the nanotube structure, which in turn, may induce changes on the resonance conditions [41]. However, the G-band presents an asymmetric profile (in its low frequency region), which denotes a G^{-} component similar to the others spectra at low pressures. Since this feature comes from the nanotube curvature aspect[157, 158, 159, 160, 161], it suggests a residual tubular structure after 60 GPa. Based on this hypothesis, we recorded another spectra with 2.33 eV excitation energy of the recovered sample in the same spectral window for 2.41 eV ones. The residual circular tube cross-section is confirmed by the presence of the RBM signature in the low energy region of the spectrum, validating our previous assumption.

We find the irreversible transformations threshold of TWCNTs between 60 and 72 GPa. The carbon nanotubes transformation into nanoribbons is well supported by the TEM images, as already shown at the beginning of this section. The 72 GPa APL (after pressure cycle) Raman spectrum corroborates the ribbon-like transformation, as it does present any appreciable RBM modes and shows a symmetric G-band profile, as well as an I_D/I_G ratio higher than unity, which are features of nanoribbons [162, 124, 153, 151].

The already done analysis on the structural transformations of the TWCNTs from RBM, -D and G-bands Raman provides a coherent qualitative scenario of the structural changes. The G$^{'}$ band, which is originated from a double resonant Raman scattering process involving a two-phonon scattering and showing a well-developed triple-peak structure in the TWCNTs (individual and bundles) system [133], provides an additional tool to study these transformations. This triple-peak structure reveals that each concentric nanotubes contributes separately from one another. The Raman G'-band of the recovered samples shows a 3 components profile up to 60 GPa whereas the 72 GPa APL shows a single component as shown in Fig.4.9. Besides, the G'-band spectrum measured after pressure loading of 71.9 GPa is compared with the spectra of single- (SLG) and bi-layer graphene (BLG) from reference [163] (grown by chemical vapor deposition - CVD graphene), showing a slight difference between the peak position of the SLG and 72 GPa APL spectra. Nevertheless, the G'-band profile of 72 GPa APL is broader than that one of SLG spectrum (also to BLG), this broadening could be originated by means of residual strain, disordered stacking distribution of the nanoribbons-like structures after 72 GPa (as supported by TEM images). Details of Raman spectra data analysis, as also the comparison of individual TWCNT components and peaks distances from Ref.[133] with our Raman spectra of the G' bands are provided in the Figure 4.9 and Table 4.3. The evolution of the G' band is coherent with the proposed scenario of irreversible transformation of TWCNTs. In addition the evolution of the relative intensities of the components of the G'-band is also coherent with the presence of some irreversible effects (defect creation?) appearing first in the other tubes (attenuation of their signal).

Table 4.3 – Differences between the G' frequencies of inner and host tubes (Δ_{ih}) and host and outer tubes (Δ_{ho}). Sample (GNRs) provides the peak position for the single component. All results are obtained of the spectra from Figure 4.9.

Sample (TWCNTs)	excitation source (eV)	Δ_{ih}(cm^{-1})	Δ_{ho}(cm^{-1})
individual TWCNT (Ref)	2.41	25.50	36
BPL Pristine	2.41	27.32	28.76
APL 51.9 GPa	2.41	28.52	27.41
APL 59.4 GPa	2.41	27.81	29.07
APL 54.9 GPa	2.33	27.83	31.11
Sample (GNRs)	excitation source	G'-band	
APL 71.9 GPa	2.41 eV	2682.8 cm^{-1}	

4.2.4 Conclusions

We performed a resonant Raman study at high pressures on highly-quality TWCNTs bundles. We also studied *ex situ* by transmitting electron microscopy the recovered samples after a maximum loading of 72 GPa. The RBM frequencies broaden with pressure and their signal showed a quenching between 14.6 – 18.7 GPa. Moreover it was evidenced that major contribution in RBMs is originated from the TWCNTs. This was supported by the normalized pressure coefficients plot of Figure 4.3. The G-band spectra analysis revealed that the G^- peaks do not provide a clear way to describe G-band evolution with pressure, and this might be associated to the strong intra- and inter-tube interactions enhanced by the tube curvature (which weakens the carbon bonds by orbitals rehybridization). This mode is then quite sensitive to the application of pressure. The three TWCNTs G^+ components evolved monotonically with pressure until

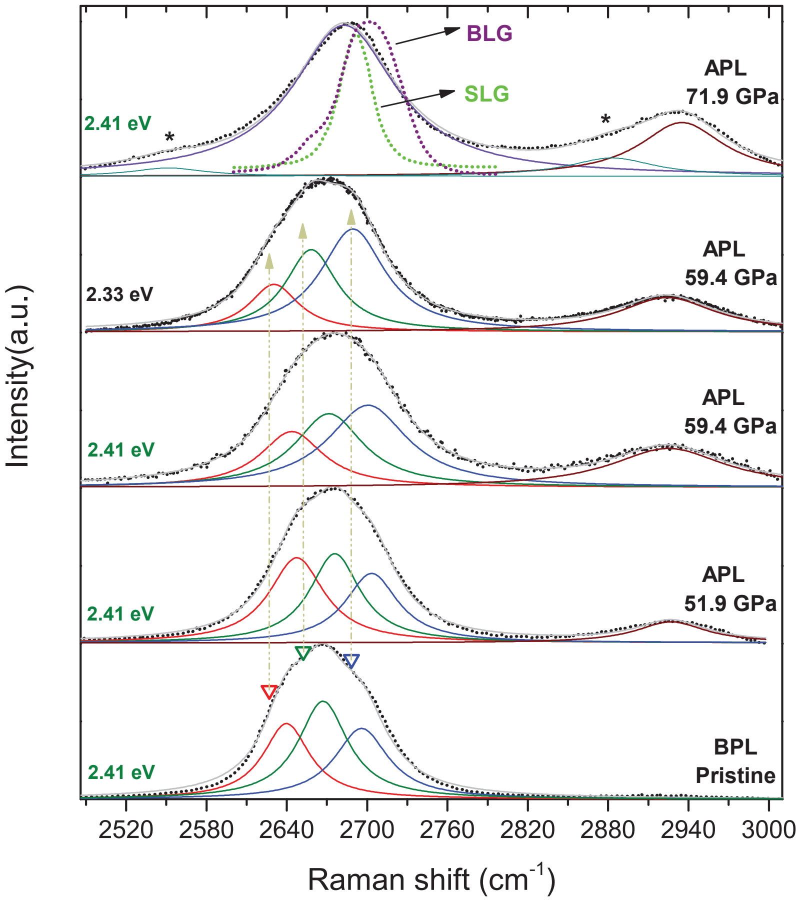

Figure 4.9 – G' band Raman spectra of pristine and recovered samples after pressure treatments (51.9, 59.4 and 71.9 GPa) measured at 2.33 eV and 2.41 eV excitation energies. The three triangles (red, green and blue) indicate the triple-peak structure of individual TWCNT from Ref. [133] and the three arrows are guides for the eyes for comparison with the triple-components to spectra until 59.4 GPa. After pressure loading of 71.9 GPa a single component was used for the G'-band spectral fitting and its spectrum is compared with the spectra of single- (SLG-green) and bi-layer graphene (BLG-purple) taken at 2.41eV laser energy from Ref. [163]. The two star symbols represent two auxiliary components used to improve the fitting. For all spectra after pressure cycles a new band above of 2900 cm^{-1} appears.

reaching the collapse region, with the onset at 21.7 GPa and the end at 36.8 GPa. The collapse process could be interpreted as a sequential process progressing from the outer tube to the inner one. From 29 GPa the two outer tubes reach the graphitic-like behavior while the inner tube continues its collapse up to the plateau end at 37 GPa. After 37 GPa the inner tube enter also a graphite-like regime. This complex picture of collapse process could be ascribed to an inhomogeneous compression of inner tubes by outer, as well as the non-hydrostaticity of pressure transmitting medium, however in our experiments we have avoided the unintentional filling of the tubes. Experimentally we have determined a threshold value for which pressure-induced structural transformations of TWCNTs are irreversible, being shown for the located well above the collapse region, between 60 GPa and 72 GPa. In addition, we have shown by first time via electron microscopy a direct transformation of fell-wall tubes into a nanoribbon-like structure. On the other hand, we expect that theoretical predictions assist to discriminate better this global scenario of structural transformations.

5

Boron nitride multiwalled nanotubes under high pressures

Sommaire :

5.1 Introduction . . . 106
5.2 Boron nitride multiwalled nanotubes . . . 106
  5.2.1 Synthesis . . . 106
  5.2.2 General aspects and previous work . . . 107
  5.2.3 Results and discussion . . . 109
  5.2.4 Conclusions . . . 117

5.1 Introduction

In the previous chapters we have been examining the effect of size, number of walls and even chirality in the pressure stability of carbon nanotubes. In this chapter we will become interested on the way the nature itself of the atoms of the tube can affect the pressure stability. We will consider one of the closest variant of carbon nanotubes which are Boron Nitride nanotubes. They were briefly presented in Chapter 1. In particular, this chapter is devoted to the high pressure response of well-characterized BN multiwall nanotubes (BNMWNTs). We may be confronted to the effects of some particularities of the BN tubes which are to be related with the iono-covalent character of their bond. In fact, this imposes an important constraint in MWNTs which are in general considered as having equal or close chiralities for the concentric tubes. We will here again combine Raman spectroscopy and TEM imaging to try to obtain the clearest view on the structural evolution of BNMWNTs under high pressure. We will see that changes with pressure appear to be very rich and that TEM (including HRTEM tomography) on cycled samples reveals as a extremely powerful tool. The chapter organization includes two first sections to introduce the synthesis used to produce our specimens and the general aspects (theoretical and experimental) of BNMWNTs behavior at high pressure found in literature. The third section is dedicated to our experimental results of BN-tubes under high pressure and their TEM characterizations. The discussion about our findings is developed throughout the text. In the last part, we summarize the more findings of our study.

5.2 Boron nitride multiwalled nanotubes

5.2.1 Synthesis

Boron nitride nanotubes (BNNTs) have been synthesized via Boron Oxide Chemical Vapor Deposition (BOCVD) following a catalytic "Vapor-Liquid-Solid (VLS) Growth Mechanism" [164, 165, 166]. A mixture of powder precursors (boron B) and catalysts (magnesium oxide MgO and iron boride FeB) in a molar ratio of 1: 2: 1 respectively, was used as a starting material. This mixture was placed in an alumina combustion boat and introduced in a horizontal induction tube furnace closed at both ends (Figure 5.1(a)). The tube furnace was first evacuated and then heated up to 1500 °C. As a result, B_2O_2 vapors and liquid or partially-melted nanosize catalyst particles were formed. NH_3 gas was then introduced into the tube furnace at a rate of 150 sccm for one hour at a pressure of 1000 mbar. At this temperature NH_3 decomposed into N_2 and H_2. The oxygen of the as-formed B_2O_2 vapors reacted with H_2 to form water vapor while the boron reacted with N_2 to form BN-species. These species were then diffused into the condensed catalysts and aggregated with the passage of time until it supersaturated and precipitated into the form of BNNTs.

BNNTs thus obtained were multiwall nanotubes (MWNTs) in pure form, with an average outer diameter of approximately 50 nm, a length greater than 10 mm and almost no impurity was present in the final product. The nanotubes were straight with concentric tubular structure containing no defects and were uniformly dispersed (Figure 5.1(b)-(c)).

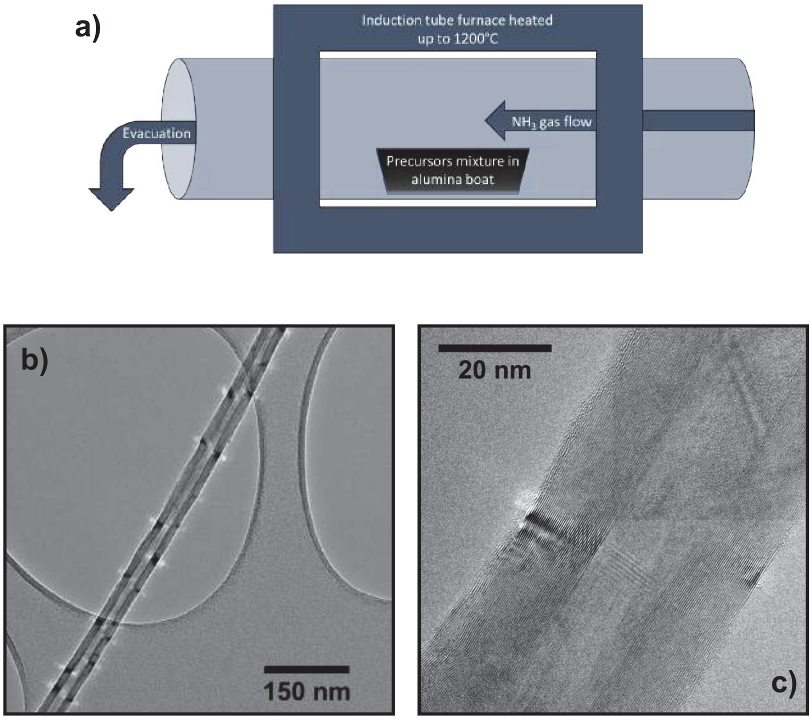

Figure 5.1 – a) Schematic representation of the experimental set-up used for the synthesis of BNNTs by BOCVD. b) BNMWNT with black contrast pattern induced by incident electron beam on the different faceted tube orientations, which is typical in BNNTs (refs.[167, 168]). c) HRTEM image showing the inner tube surrounded by approximately 40 concentric tubes.

5.2.2 General aspects and previous work

The characterization of mechanical properties of nanotubes constitutes a particularly important subject in view of applications [169]. In particular, the effective radial elastic modulus of SW-BNNT is smaller than for SWCNTs [170], but - as in CNTs - it increases rapidly with the number of walls [171]. In carbon nanotubes, the radial cross-section under high pressure evolves through different geometries depending on radius and number of walls. This has been extensively studied both theoretically[27, 172, 29] and experimentally[39, 37, 55, 128, 30].In particular as it was discussed in Chapter 1, theoretical and Raman experimental works agree that collapse pressure, P$_c$, of single-wall CNTS follows a modified Lévy-Carrier law $P_c d^3 = \alpha\left(1-\beta^2/d^2\right)$ law (d tube diameter or the internal diameter in few-wall tubes and α and β parameters) [29, 41, 30].

Some works have explored theoretically the high pressure evolution of BNNTs. For single-walled BNNTs (SWBNNTs) bundles, density-functional theory (DFT) simulations showed that the collapse pressure, P$_c$, decreases when the tube diameter increases[78]. DFT calculations in a (10,0)@(17,0) double-walled BNNTs (DWBNNT) bundle [79] revealed basically two regimes of structural transformation with a change to an elliptical cross-section first($\sim$ 1 GPa) followed by a first-order flattening transition at ($\sim$ 10 GPa). The deformation of the outer tube is transmitted to the inner one similarly to the cascade transition type observed in DWCNT [55]. Similarly to SWBNNTs bundles, the energy gap reduces sharply at the transition region. However, other calculations [173] show that the electronic structure of individualized BNNTs with various number of walls can present very different regimes upon radial deformation.

Raman spectroscopy is a powerful characterization tool widely used for the experimental investigation of the electronic and mechanical properties of CNTs under extreme conditions. This technique enables following *in situ* nanotube structural transformations [174, 37, 128]. For BNNTs and the four BN polytypes [h-BN (graphite-like), rhombohedral (r-BN), cubic (c-BN; diamond-like) and wurtzite (w-BN)], infrared (IR) spectroscopy is an intersting technique thanks to its sensitivity to polar/ionic bondings. IR Spectroscopy can then provide details about the nature of the different BN-vibrations [175, 176, 97, 177]. UV Raman measurements can also be used to evaluate the volume fraction between h-BN and c-BN in thin BN films [74]. High pressure Raman spectroscopy in BNNTs suffers from limitations associated with sample purity, fluorescent BNNTs background and the closeness of the main Raman tangential mode (E_{2g}) of BNNTs to the prominent diamond Raman mode (1332 cm^{-1} [178]) arising from the use of diamond anvil cell pressure apparatus. Nevertheless it remains a practical technique to explore the high pressure properties on BNNTs in particular thanks to the parallel which can be done with the high pressure study of CNTs.

Many works have reported high- pressure and/or temperature transformations in bulk h-BN, as well as in another BN allotropes. It has been shown that h-BN can be converted into more closely packed w-BN or c-BN structures [179, 180, 181, 182, 183, 184, 185, 186, 187, 188, 189] and c-BN $\leftrightarrow$ r-BN [190], depending to the P-T parameters. There are on the other side very few high-pressure experimental studies of BNNTs reported in literature [191, 192, 193, 194].

Saha et al. [191, 192] explored the high pressure behavior of Multiwalled-BNNTs (MWBNNTs) by Raman spectroscopy up to 12 GPa where they lost irreversibly the Raman signal. The results were interpreted as an amorphization of the structure. In a subsequent high pressure synchrotron X-ray diffraction study of MWBNNTs up to 19.1 GPa [193], it was shown that MWBNNTs remained crystalline up to the maximum pressure. In that work it was observed the irreversible appearance of new diffraction peaks from 3.2 GPa which were assigned to the w-BN phase. On the other side, Dong et al. [194] carried out *in situ* IR measurements at high pressure also in MWBNNTs up to 35 GPa. Comparing MWBNNTs with bulk h-BN it was observed that both samples undergo at $\sim$ 11 GPa a transformation towards the formation of sp^3 bonding, associated with the w-BN metastable phase [195]. At $\sim$ 23 GPa the transition is almost complete for bulk h-BN, whereas for MWBNNTs even at $\sim$ 35 GPa the transformation is far from complete. A two-step transformation mechanism for sp^3 bonding formation in MWBNNTs was proposed: first intertubular connections in bundles are formed (around 11 GPa) and secondly above 20 GPa where intratubular connections were supposed to become significant. Under decompression only the intratubular connexions remain.

To summarize, whereas theoretical works in BNNTs focus in the observation of pressure induced radial collapse transitions similarly to the known scheme in CNTs, none of the experiments performed up to now allow to evidence such transitions. All high pressure experiments on BNNTs concern MWBNNTs. In CNTs it not easy to provide experimental evidence on the radial collapse high pressure transformation of MWCNT, but it has been nevertheless recently provided in composite systems [196]. Experiments provide evidence of an structural evolution of MWBNNTs which includes the formation either of sp^3 bonding or even the transformation towards w-BN without a consensus on the pressure at which the transformation takes place. There is then a clear need for further experimental studies to clarify the high pressure structural evolution of BNMWNTs and try to establish if the parallel with the high pressure evolution in CNTs can be maintained or not. Our work combining *in situ* Raman spectroscopy and high-resolution TEM on recovered samples, provides a new insight in all these questions. We underline also that we have used for the first time according to our records TEM tomography to study high pressure nanomaterials from high pressures studies.

5.2.3 Results and discussion

We show in Fig.5.2 the Raman spectra of the tangential mode (TM) for the compression experiment from ambient pressure (outside of the pressure device) up to 36 GPa. This peak blue-shifts gradually up to ∼ 23 GPa, where it becomes very weak and cannot be further detected. The highest pressure spectrum at ∼ 36 GPa shows just the presence of a broad background signal. The TM signal was fitted using a Voigt profile including a background signal due to fluorescence (dashed lines). The intensity jump at the low energy side of the spectra is due to the diamond Raman peak contribution from the cell anvils. We may note that differences in intensity between the spectra are not significant due to the lack of a normalization signal.

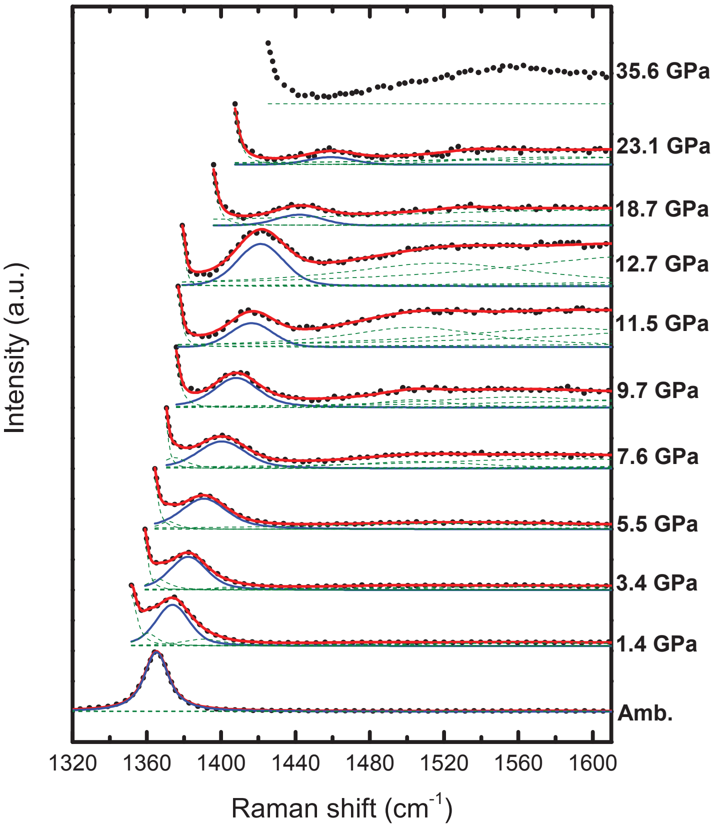

Figure 5.2 – Raman spectra of MWBNNTs during a compression run up to 36 GPa (black dots). Continuous lines (in red) supperposed to dots represent are the fitted function obtainned by considering Voigt curves fitting the BNMWNTs tangential mode (blue continuous line) and the background and diamond anvil contributions (green dashed lines).

In Fig.5.3(a), we have plotted the evolution of E_{2g} mode energy for the three different pressure runs with maximum pressures up to 7 GPa, 15 GPa and 36 GPa respectively. Each run corresponds to a different loading of the pressure cell with a fresh specimen. The evolution of the TM energy is linear in the full pressure range up to 24 GPa (maximum pressure in which we could detect it). The linear fitting on all grouped points in the graph provides a slope $\partial\omega_{E_{2g}}/\partial P = 4.02$

cm^{-1}/ GPa and ambient pressure intercept frequency at 1368± 1 cm^{-1} in good agreement with the TM frequency of 1365 ± 2 cm^{-1} measured outside of the cell. The obtained pressure slope for the E_{2g} is in good agreement with the values obtained in a previous work [191, 192]. Nevertheless we note that in the work of Saha et al[191] deviations from linearity were observed from 10 GPa and the TM signal was lost at 12 GPa, i.e., half pressure with respect to our measurements. In Fig.5.3 (b) is shown the corresponding pressure evolution of the Full Width at Half Maximum (FWHM) of the E_{2g} mode. The E_{2g} first enlarges rapidly up to around 8 GPa from where an abrupt decrease is observed. This dip in the evolution is followed by a plateau region for pressures beyond 12 GPa. The ambient pressure value of the FWHM in our sample (13 cm^{-1}) is significantly higher than in the case of Ref. [191] (∼ 9 cm^{-1}). This is also the case for the pressure evolution which in the case of Ref. [191] it evolves linearly up to 10 GPa with a maximum value of ∼ 14 cm^{-1} which is about half of our values for the same pressures. Differences in the sample's crystallinity and in the hydrostaticity of the used PTM can be at the origin of such observations. We should come later on this aspects after the study of the recovered samples.

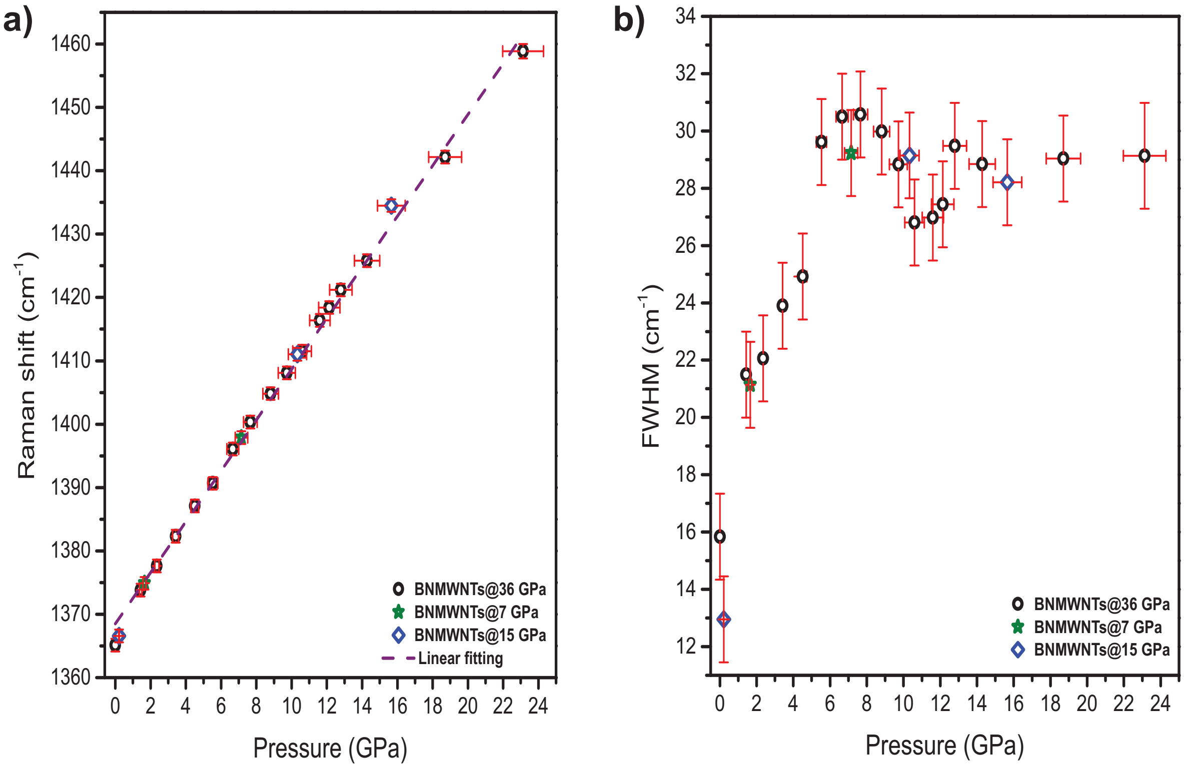

Figure 5.3 – High pressure evolution of the the E_{2g} tangencial mode in BN nanotubes. (a) frequency of the peak for 3 different experiments up to 7, 15 and 36 GPa. The dashed line corresponds to the linear fit of all the data. (b) corresponding FWHM evolution.

Raman spectra could be recorded for the recovered samples after pressure cycles up to 7.1, 15.6, 41.1 and 48.6 GPa. Their respective Raman spectra collected at ambient conditions outside the DAC are compared with the pristine sample in Fig.5.4(a). Within error bars there is no change in the E_{2g} position of the TM mode after all pressure cycles. Nevertheless some modifications can be noticed comparing the different spectra. The spectra from the pressure cycle up to 41.1

GPa and 48.6 GPa show the presence of a new broad band at $\sim 1280\ cm^1$. The same peak but much weaker can be already observed for the sample having been cycled up to 15 GPa but it is absent for the lower pressure points. In Fig.5.4(b) it is shown the E_{2g} FWHM for the recovered BNMWNTs and pristine sample TM peak. It is observed that the two first spectra (ambient and 7 GPa of cycling pressure) have a FWHM $\sim 16\ cm^{-1}$ while after cycling at higher pressure the E_{2g} broadens significantly concomitantly to the appearance of the new above referred peak. Figures 5.4(a and b) indicate then a change of regime taking place at 11 ± 4 GPa. Nevertheless, we have to admit that the FWHM evolution provides weak support to this transition, as a close to linear evolution could be also considered.

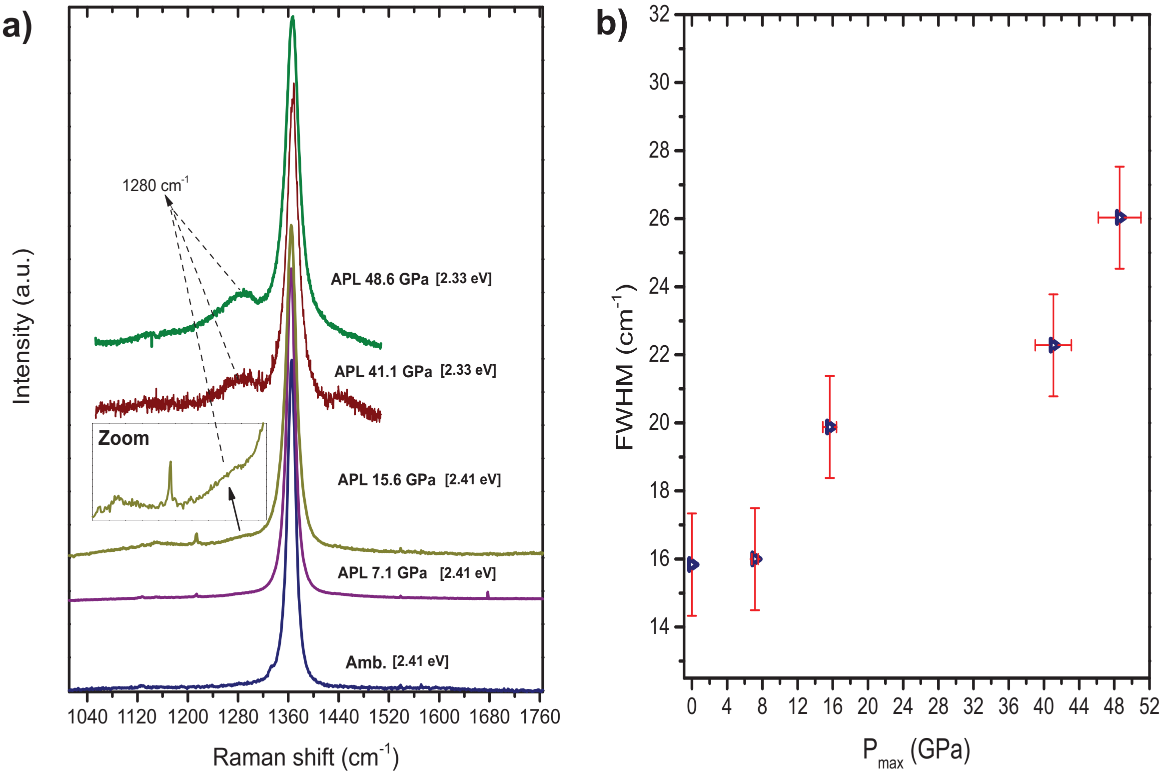

Figure 5.4 – Comparison of the Raman spectra of the BNNTs TM signal at ambient pressure and the corresponding signal after a pressure cycle with maximum pressure of 7.1, 15.6, 41.1 and 48.6 GPa. Spectra are vertically shifted for clarity. The excitation wavelength is indicated between brackets.

In order to obtain a better insight on the pressure evolution of BNMWNTs we have studied by TEM the pristine and the recovered samples. The most significant images are shown in Fig. 5.5 showing important changes in the tube morphology. At ambient conditions the BNMWNTs showed dark (or bright) spots along the tube axis which are well evident in panel a.1, b.1 and c.1 of the Figure. This apparently regular pattern has been associated to a double-helix hexagonal structure [197]. However, in contrast to this structural model, Golberg et al. [167] showed that the dark spots did not alternate periodically on opposite tube sides with a regular pitch. Images from the samples recovered after 7 GPa of pressure preserved the tube geometry as can be seen in Fig. 5.5 a.2. We nevertheless observed the presence of tubes presenting bamboo-like structure which we never observed in pristine samples (Fig. 5.5 a.2). In addition, in certain regions the tubes showed a periodic deformation along the tube (Fig. 5.5 b.2) which can be interpreted associated to a radial cross section modulation. Furthermore a local densification on the tube walls was also observed in some tubes as can be seen in Fig. 5.5 c.2. All changes observed in the 7 GPa sample become more pronounced for the tubes recovered after 15 GPa (Fig. 5.5 a-c.3). The sample recovered from a pressure cycle up to 36 GPa showed much more significant transformations (Fig. 5.5 a-d.4). In fact most tubes were extremely damaged as can be seen in Fig. 5.5 a-b.4. Nevertheless it was possible to observe some bamboo-like tubes (Fig. 5.5 c.4) and some zones presenting high densification as shown in Fig. 5.5 d.4.

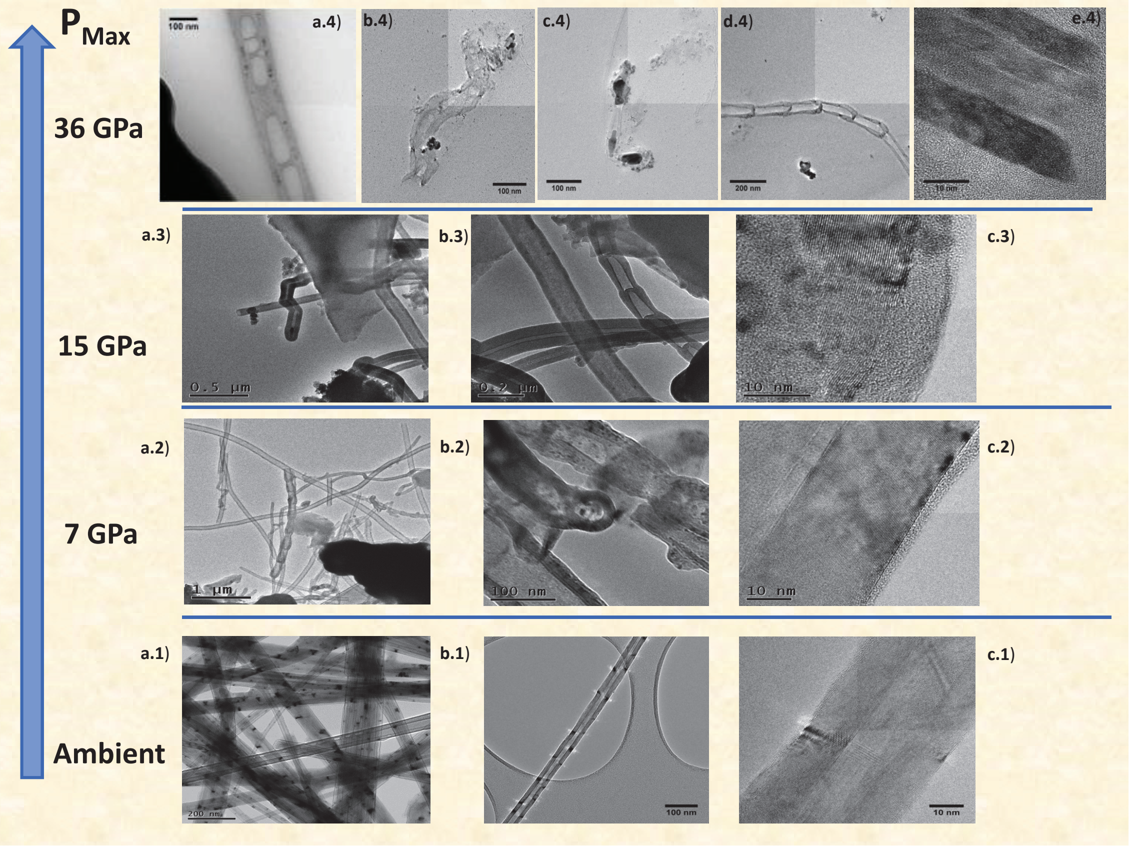

Figure 5.5 – HRTEM images of the pristine BNNTs sample and after pressure cycles up to 7, 15 and 36 GPa. Scales are provided in each image.

3D TEM tomography images were obtained for a MWBNNT at ambient pressure and for another tube recovered after a pressure cycle up to 36 GPa. The obtained views along the tube axis and cross-sections at different positions are shown in Fig. 5.6. We can observe that in both cases the internal cross-section morphologies evolve along the tube. The pristine tube showed the presence of encapsulated catalyst particles and multiple faceted rhombus polygonal internal cross-section with a modulated size. Polygonal cross-sections for all or part of MWBNNTs has been reported in a number works [197, 167, 168, 86, 198]. We should nevertheless note that these polygonal cross-section are hexagonal differing from our case in which they appear to be rhombic(as also observed in the Supporting Information of [198]). Rhombus cross-sections were also observed in the tube recovered from 36 GPa in which other morphologies (ovalized or highly deformed) were also present. We could also notice some highly disordered closed or bridged parts in the internal cross-section of the high pressure cycled tube.

In Figure 5.7 are shown different TEM views at various scales of a novel tube morphology produced after a pressure cycle up to 36 GPa. This very unique structure showed a new type of extremely interesting morphology. First we note that the tube presents a kind of irregular inner alveolar structure which reminds the recovered tube in Fig. 5.6 after pressure cycle or the one in Fig. 5.5.a.4 . Most interestingly we note that the tube wall is now divided in two regions. The external region (region A) is a multi-walled tubular structure made of about 40-50 tubes with an external diameter of about 110-120 nm and a thickness of about 15 nm. The intertube distance is of 0.35 nm. The internal region (region B) can be described as a domino stacking of one-closed-edge boron-nitride nanoribbons. The closed lobes have different hierarchical structures as can be appreciated in Fig. 5.7.d and Fig. 5.7.e. The lobe terminations are observed both in the internal and in the external sides and can be seen as multi-folded boron-nitride nanoribbons. In Fig. 5.7.d can be appreciated that there are some connection points between region A and region B, whereas in Fig. 5.7.e the two regions are well dissociated. The nano-ribbons form an angle of $\sim$ 15° with respect to the tube axis running all along the tube without interruption. This inclined structuration can be related to the spiral-type structure of polygonized BNNTs [197, 135].

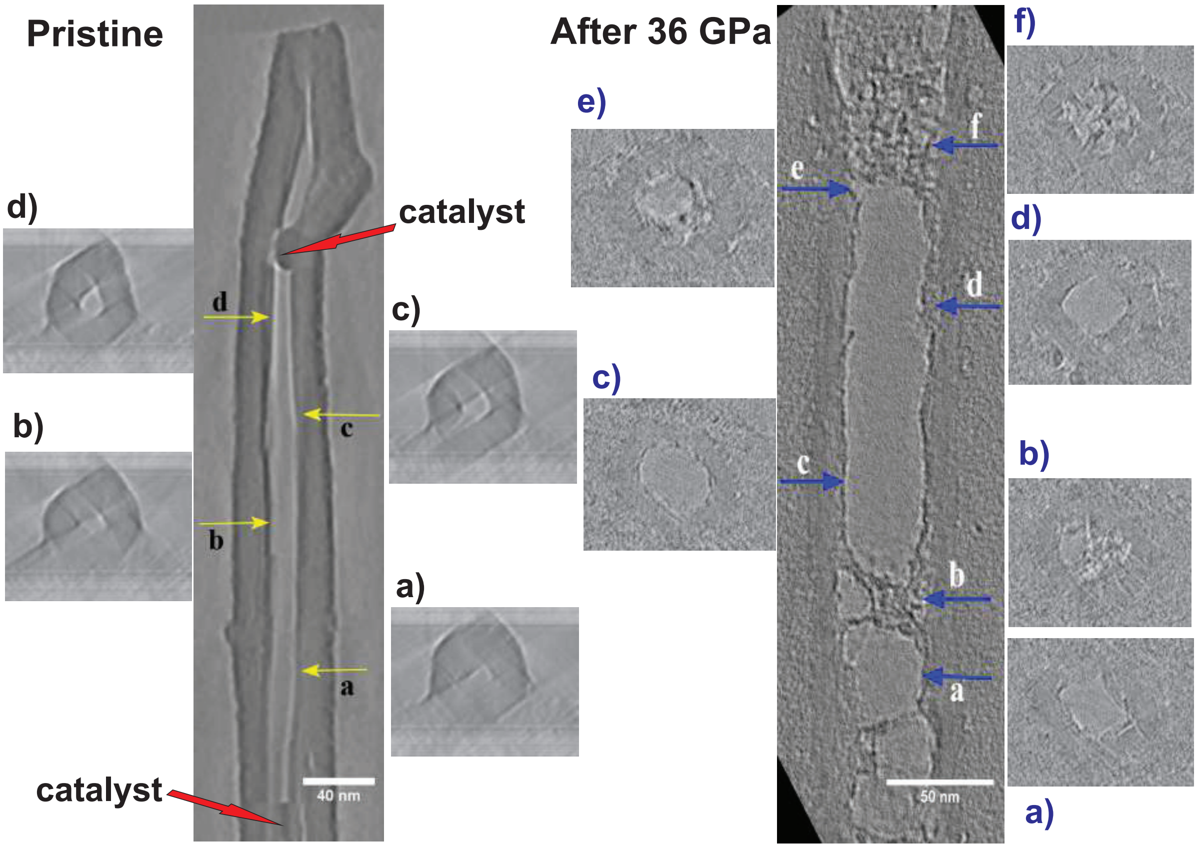

Figure 5.6 – HRTEM Tomography images of a pristine BNMWNT (left) and another tube after a pressure cycle of 36 GPa (right). The arrows show perpendicular cross sections along the tube labeled a to d for the pristine tube and a to f for the pressure cycled tube. The internal “diameter” of the tube in the non-closed regions evolves typically from 15 to 20 nm for the pristine tube (in the region between a and d) and between 36 and 40 nm (in the region between c and d) for the cycled tube. The average value of the external tube diameter is 52 and 66 nm for the pristine and the cycled tube respectively.

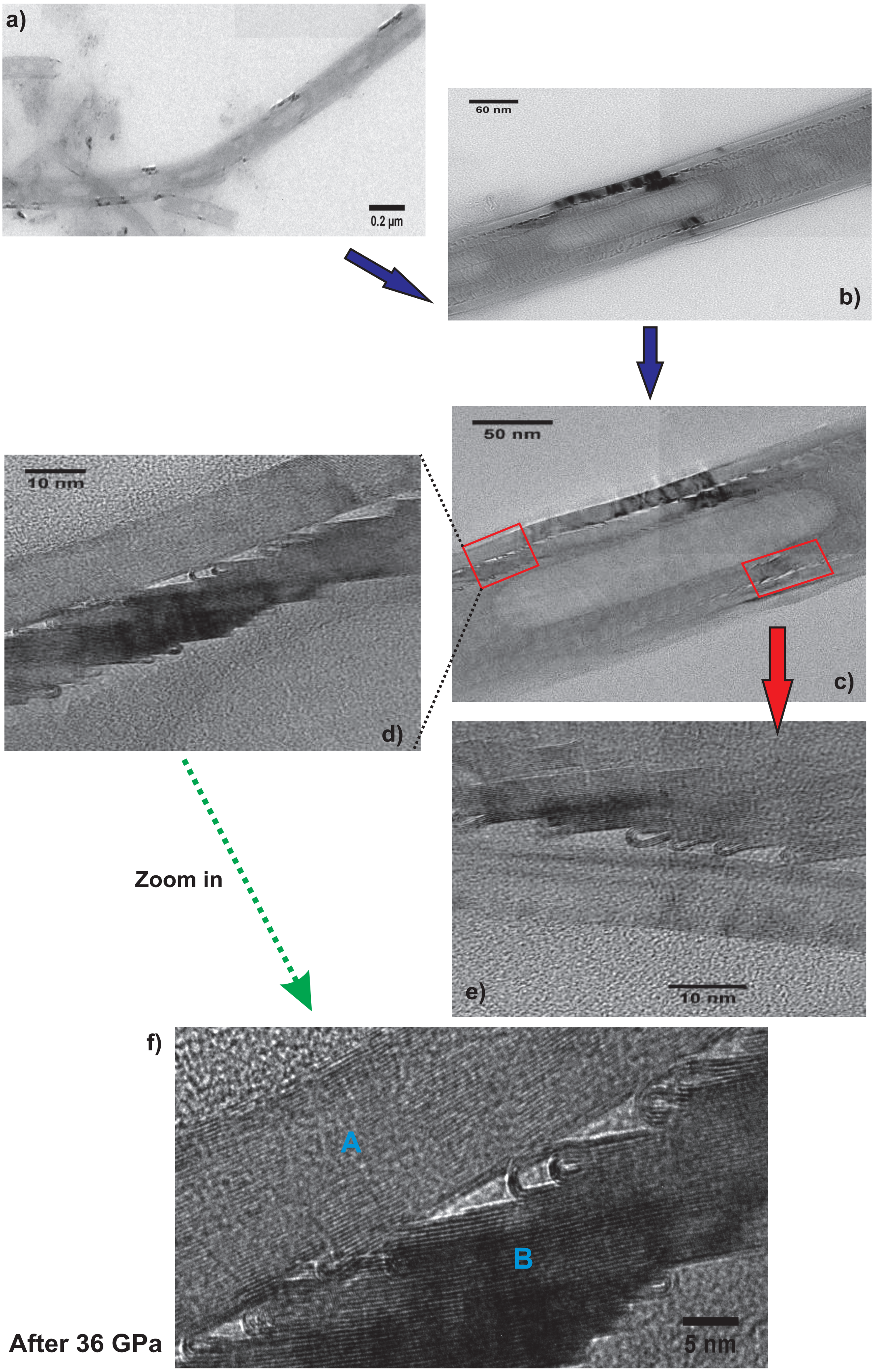

Figure 5.7 – HRTEM images of a particular pressure modified BNMWNT after a pressure cycle up to 36 GPa. a) Image of the several microns length tube showing several internal alveoli of irregular size and spacing. b) to e) detail of the structure at different scales.

These structures can be related to two-closed-edged Graphene Nanoribbons from Large-Diameter Collapsed Nanotubes [199].

Our TEM study on recovered samples after a pressure cycle show that boron nitride multi-wall nanotubes can survive pressure cycles up to pressures as high as at least 48.6 GPa (Figure 5.8(c)). Such high pressure conditions lead to different morphological changes in the tubes including the formation of alveolar structures with regular bamboo-like morphologies or with irregular alveoli, tube folding or highly damaged tubes including the formation of folded nano-ribbon dominoes internal structures. Some of those changes start to be observed for tubes cycled up to pressures of 7 GPa (Figure 5.8(a)-(b)).

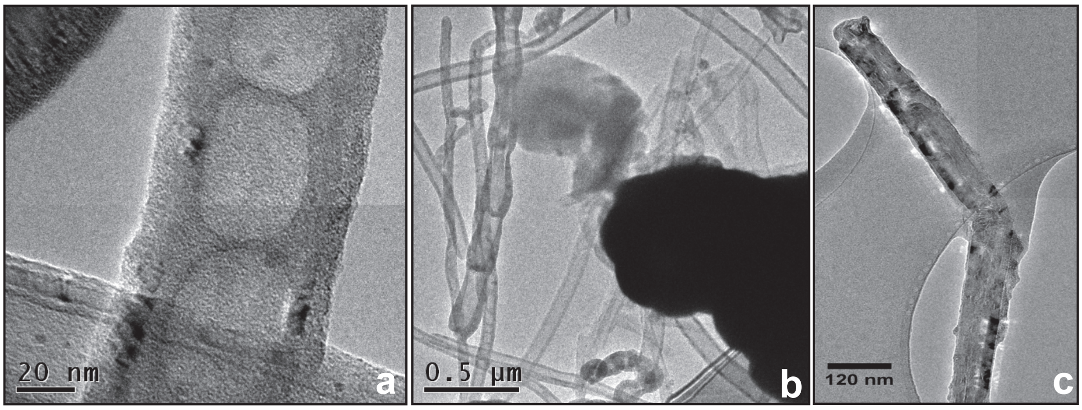

Figure 5.8 – a) and b) TEM images of BNNTs morphologies after pressure cycle of 7 GPa. The alveolar structures are also formed at low pressure. c) TEM image shows a BNNT after decompression of 49 GPa. The bar scales are provided in the images.

The high pressure Raman study shows strong modifications in the response of the E_{2g} h-BN phonon which start to take place from about 8 GPa. Those changes involve a change of regime in the FWHM evolution and the appearance of a new Raman mode at about 1280 cm^{-1}. This new mode, which is much weak, is visible in the spectra of samples cycled from 15.6 GPa and above (Fig. 5.3, double black dashed arrow).

As it was discussed in the introduction, various experimental works indicate the possible evolution of MWBNNTs towards sp^3 forms including w-BN [193, 194] and more clearly at h-BN bulk [195], in this sense we could relate the possible rehybridization (sp^2/sp^3) at MWBNNTs under cold compression to the w-BN phase by means of information provided in Fig.5.4. In addition, we may then interrogate ourselves about the possibility that the new Raman peak at 1280 cm^{-1} could be related with such type of transformation.

There are many theoretical calculations on the active Raman modes of the w-BN structure [200, 185, 177] which do not allow to discriminate the symmetry of a 1280 cm^{-1} mode in a w-BN structure. In fact, depending on calculations, w-BN A_1(TO) or E_1(LO) modes could be assigned to that observed Raman peak. However, for the evaluation more careful of this and other active modes, we need remind that in the Raman spectroscopy (as well as infrared) usually the vibration modes (phonons) close to the Γ point of the 1D Brillouin zone can be excited (due to stringent optical selection rules linked with the symmetry operations) and for systems with translational symmetry, e.g. quasi-one-dimensional systems as nanotubes (in particular for boron nitride nanotubes[88]), the "point group in the space group" determines through the selection rules which modes are active and which are not. In order to explain the Raman modes of the h-BN or w-BN structures, we need introduce the phonon dispersion via its phonon density of states. For this purpose, we invoke some works from literature.

Reich *et al.*[74] measured first- and second-order Raman scattering in cubic BN and h-BN at room temperature, of this study the experimentally observed frequencies were compared with their theoretical counterparts (calculated phonon modes). The results point out that for the critical points in the h-BN Brillouin zone, the frequency more similar to that of 1280 cm^{-1} should be by the experiment 1270 cm^{-1} (theory - 1290 cm^{-1}) coming of the transverse optical branch at M and K (TO(M-K) with M_2^+, M_3^-, K_1 and K_2 symmetry), which could be activated by cold compression. For cubic BN the experimental frequency observed is 1305 cm^{-1} (theory - 1285 cm^{-1}) assigned to LO(Γ) phonon branch, demonstrating at least a different experimental value from our. Nevertheless, we have bear in mind that our MWBNNTs (rolled up h-BN sheet) showed this new mode after the cold compression treatment and according to studies about the phase transformation in boron nitride the direct transformation between h-BN and c-BN is far less favorable than to w-BN [188, 186, 189] and additionally a study on the pressure dependence at high temperature of the transverse optical phonon (TO) (along with longitudinal optical phonon (LO)) of cubic boron nitride revealed a downshift for these modes at high pressure and temperature [201]. Therefore constraining the formation likelihood of this phase in our cycled samples.

Still on this subject, we could ascribe the new band at 1280 cm^{-1} as TO(M-K) mode activation of the pressure-induced h-BN, but when we assume the MWCNTs (as for h-BN bulk) experimental studies above-mentioned [195, 194, 193], they strongly point out a phase transformation from h-BN to w-BN under high pressure. Therefore, despite of the difficult to assign which phonon mode in the w-BN structure the new band belongs, it is reasonable attributed it to the w-BN metastable phase.

It is also important to note that the E_{2g} BNNT mode is preserved in our Raman experiments during compression up to 24 GPa. This observation seems to be consistent with the high resilience of the tube structure [202, 203]. Nevertheless, Figs. 5.4 clearly shows that non-reversible changes take place on the BNNT structure from pressures above ∼ 8 GPa. Our TEM images show structural modifications of the tubes, but no clear evidence of formation of w-BN. We have observed a number of structural evolutions on MWBNNTs under high pressure which include: i)the formation of bamboo-like structures (Fig. 5.5 b.2, b.3 and d.4), ii) the formation of alveolar structures (Fig. 5.5 a.4) iii)the formation of hybrid tubular/folded-nanoribbon (Fig. 5.7) which also presents an alveolar structure.

Our TEM tomography study (Fig 5.6) allows to see that the alveoli correspond to the presence of badly-organized matter inside the tubes. We propose that this could correspond to the breaking of the internal tubes leading to a non-folded h-BN ribbon structures. In that way, when the innermost tubes break, self-folding can lead to the particular structure of Fig. 5.7 or to alveolar structures when no self-folding takes place. The presence of alveoli in Fig. 5.7 would indicate that some tube-walls did not self-fold on breaking.

We can now discuss the reason leading to the pressure induced break of internal tubes and not to external. This can be considered as a consequence of the radial deformation of MWBNNTs under high pressure. In fact, such radial deformation, theoretically predicted for SWBNNTs imply a higher stress for the internal tubes. Why internal tube breaking mechanisms has been never observed in CNTs? Most probably this can be assigned to the additional stress term due to the BNNTs cross-section faceting. This faceting in BNNTs has found to be related to the interlayer lattice registry patterning, which arises from the interlayer electrostatic interactions of BN partly ionic bindings (polar nature), that favor the chiral angle correlations between layers [135].

We can then try to understand the different high pressure MWBNNT observed morphologies as related to the different possible schemes of the internal tubes polygonization. Fig.5.9 summarizes the proposed scheme of pressure transformation. For low polygonal order a symmetric breaking of the internal tubes may lead to the organized folding of the h-BN nanoribbons producing the bamboo-like structures. This would correspond to the case of an even polygon. In in the case of an n-polygon with n odd, pressure induced ovalization will not lead to a symmetric stress distribution in the internal tube. A less organized folding of the h-BN nanoribbons would lead to the alveolar structure. The case of the organized stacking of folded h-BN nanoribbons (c) could be related to the multiple fracture of high n-order polygon. In any case the observed structure clearly evidences the existence of a spiral ordering for the internal polygonized tubes [197, 135].

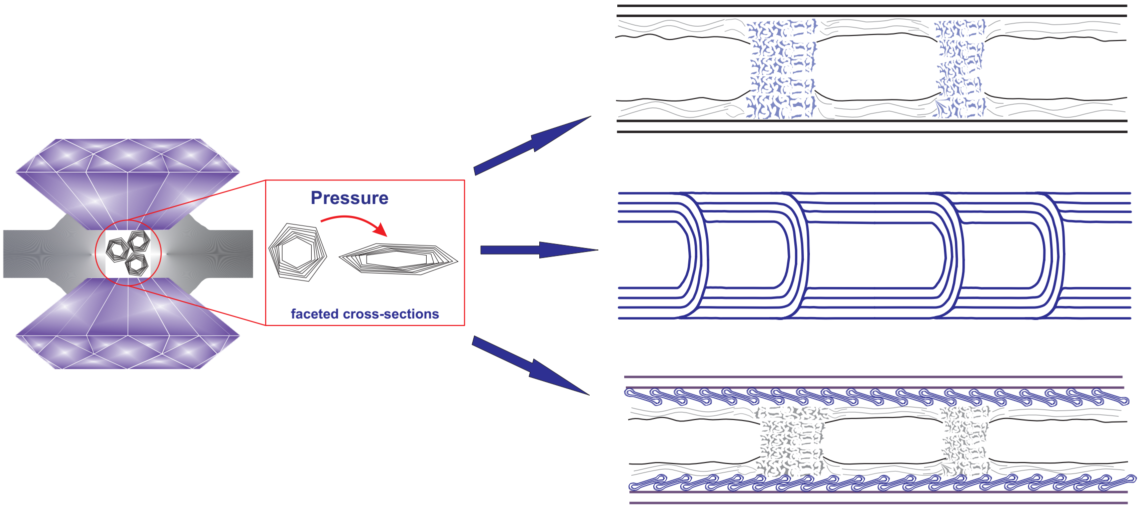

Figure 5.9 – Scheme illustrating the main morphologies for BNNTs after pressure cylce found in this work. On right side from up to down, we have respectively, the alveolar, bamboo-like and falling domino structures.

5.2.4 Conclusions

We have carried out a combined TEM and Raman high pressure study of multiwall boron nitride nanotubes. Irreversible changes in the morphology of the nanotubes take place from ∼7 GPa associated to an enlargement of the E_{2g} Raman peak profile (Fig. 5.3(b)). The presence of a new Raman non-assigned mode at 1280 cm^{-1}, after pressure cycles up to 41 and 49 GPa, indicates that some structural transformation takes place. Moreover after a pressure cycle up to 49 GPa it can still noted the contribution of the tangential mode with a broaden line width. This suggests that the BNMWNTs are partially reversible. Characterizations via TEM from the recovered samples not only are in agreement with Raman spectra results(Fig.5.8) but also allowed to provide a more completed picture letting us to identify three different morphologies. These morphological changes correspond to the formation of bamboo-like tubes or the transformation towards two different types of hybrid structures associated to the breaking of the internal tubes. These structures lead then to the formation of h-BN nanoribbons (Fig.5.9). The so formed internal h-BN nanoribbons could be found either in a non-organized arrangement leading to the observation of internal alveoli or in an organized stacking of folded h-BN nanoribbons. We can also underline the interest of the use of HRTEM tomography study on the recovered samples allowing to obtain a clear image about morphologically modified BN tubes by pressure.

General conclusion

We have investigated in this thesis, the effect of high pressure on the physical properties of few walls carbon nanotubes (single wall and triple wall) and also in multi wall boron nitride nanotubes. As a major objective we wanted to understand how the geometrical parameters such as size, number of walls or the atomic nature of the tube affect the radial stability of the tube and the tube stability itself. We have used Raman spectroscopy at resonant and non-resonant conditions as high pressure *in situ* as tool of investigation and we have frequently characterized the recovered materials after pressure via transmission electron microscopy in a deep level.

For the single walled carbon nanotubes (SWCNTs), we have studied chirality enriched samples letting us to focus on tubes centered on the 0.75 nm diameter. Our findings reveal that the collapse onset for the (6,5)-empty tubes takes place at $\sim$ 15 GPa. We were not able to identify a sign of collapse pressure for the (6,5)-filled tubes up to the maximum pressure of 50 GPa. Concerning the tube stability, chirality-enriched (6,5) filled tubes in bundles or individualized can endure pressure cycles higher than 50 GPa, but a considerable proportion begin damaged when inspected after this pressure cycle. We also show that the RBM frequencies at ambient conditions are strongly dependent on environmental interactions, for example, the PTM type or the residual molecules surrounding them. The RBM signal evolution of empty or filled (6,5) at high pressure is also affected by the tubes arrangement, i.e., if it is in bundles (signal distinguishable up to 7 GPa) or individualized (signal distinguishable above 15 GPa). In addition, the tubes tend to approach a graphite-like Raman evolution behavior beyond 50 GPa, reaching a complete irreversible instability at $\sim$ 80 GPa. In fact TEM images show that the nanotubes undergo irreversible transformations (unzipping), yielding quite disordered structures, such as turbostratic carbon and amorphous carbon. Finally, the tube mechanical instability seems to depend of the chirality with empty or filled (6,5) more unstable than (8,3) tubes.

In the study of triple walled carbon nanotubes (TWCNTs), we observed that the innermost tubes profiles loss the resonance with the pressure increase between 14.6 and 18.7 GPa. The innermost tubes contribute dominantly to the RBM spectra, thus making possible to discriminate the contribution of TWCNTs from its mixture with DWCNTs. Our measurements confirm that the normalized pressure derivatives of RBMs show a screening effect provided by the outer tubes to the innnermost ones.

The innermost tube diameter of TWCNTs spans from 0.58 to 0.94 nm, giving then a distribution having a central value of 0.76 nm, close to the diameter of the SWCNTs we have studied. Then we can use this study to see the effect of the number of walls on the pressure stability of CNTs. The three G^+ components evolution of TWCNTs as a function of pressure displayed a collapse onset at 21.7 GPa with an end at 36.8 GPa. The collapse process was interpreted as a sequential transformation following 3 steps, in which the two outer tubes reach a graphitic-like behavior at around 29 GPa, while the inner tube proceeds collapsing up to $\sim$ 37 GPa. Above 37 GPa all tubes follow the graphite-like regime. Far from the collapse region, between 60 GPa and 72 GPa, TWCNTs suffer an irreversible structural transformation. TEM images show the presence of nanoribbon-like structures originated from these transformations.

If we summarize the main results on the mechanical stability of SWCNTs and TWCNTs having similar inner diameters of ~ 0.75 nm, we observe that for SWCNTs a collapse pressure onset at ~ 15 GPa which seems to be complete at 30 GPa. For TWCNTs we observe a more complex collapse starting at ~ 22 GPa and completed at 37 GPa. It is then clear that the number of walls have an effect on the tube radial stability which cannot solely be described by a Lévy-Carrier or modifed Lévy-Carrier law with the internal diameter as variable as it has been recently proposed [56]. Concerning the tube irreversible transformation, they are observed between 50 and 80 GPa for SWCNTs and between 60 and 72 GPa for TWCNTs. Then, within the precision of our experiments, the tube irreversible transformation could take place in a similar pressure domain comprised between ~ 60 and 70 GPa for tubes of ~ 0.75 nm, independently of the number of walls. We may hypothesize that this assertion remains valid for higher number of walls as soon as the complete collapse pressure has already been attained, but this needs to be confirmed. The influence of the tube diameter on collapse pressure and tube irreversible transformations needs also to be clarified. Nevertheless, from the study of Alencar *et al.*[56], we may expect that the effect of the number of walls on the collapse pressure is reduced with increasing internal diameter.

In the last part of this thesis we have tried to get some insight on the effect of the tube atomic nature on its pressure stability. Boron nitride nanotubes were chosen for that study letting to introduce the effect of an iono-covalent bond. In boron nitride multiwalled nanotubes (BN-MWNTs), structural modifications were observed to take place from around 7 GPa. This result was associated with E_{2g} tangential mode and confirmed by TEM characterizations after pressure loading. The BN tubes studied here had in average 14 nm internal diameter and about 40 walls per tube. The Lévy-Carrier law (or its modified version discussed in previous chapters) would give a collapse pressure of only 50 bar for an equivalent SWCNTs of 14 nm internal diameter. We have nevertheless seen that the collapse pressure is strongly modified by the number of tube walls. We will need a study on a comparable MWCNT or to obtain a quantitative description of the evolution of the collapse pressure with the number of walls in carbon nanotubes in order to establish the effect of the atomic nature of the tube on pressure stability. For the BNMWNTs, after high pressure cycles up to 41 and 49 GPa the Raman spectra showed the new non-assigned vibrational modes, indicating some irreversible changes. The TEM characterizations of the recovered samples provided a major clarification concerning these structural transformations, showing by the first time new BNMWNTs morphologies h-BN complex nanoribbon structures or alveolar formations for the innermost tubes walls. We have also attempted by a simple scheme to address in a rational way these new morphologies. However, we expect that other experimental and theoretical studies can shed more light on these complex transformations.

Our studies allowed us also to verify the existence of some experimental difficulties, as the need of high-quality samples, the control of the environment, as well as the need of a precise characterization of samples after pressure loading including HRTEM. The study of individual and suspended nanotubes is probably one of the most promising approaches to circumvent a number of these problems.

It is worth here to mention that our understanding and control of these pressure-induced structural transformations of CNTs are also interesting in cutting-edge technologies as aerospace technologies (spacecraft, satellites), damping and armor projects. In case of the nanoribbons graphitic structures the potential applications are large, as in transparent conductive electrodes, energy storage, light-emitting diodes and field-effect transistors [149, 153]. In fact the pressure domain needed to modify the geometry and physical properties of nanotubes or to produce new nanoribbon structure can be compatible with industrially scalable processes in the case of use of large tube diameters which can make part of novel composite materials[196].

Annexes

A

Suplementary information of the Chapter 2

A.1 Experiments of Raman spectroscopy

A.1.1 SWCNTs

A series of *in situ* Raman experiments were performed in two (6,5)-SWCNTs sorts (precursor and chirality-enriched) at ambient conditions and high pressures, and being excited for three different laser energies. The Raman spectra were acquired using an Acton 2500i spectrometer with excitation source of 2.41 eV (argon-ion laser 514 nm), a LabRAM HR Evolution spectrometer with excitation energy of 2.33 eV (state solid laser 532 nm) and a LabRAM HR800 spectrometer with excitation energy of 2.18 eV (krypton-argon laser 568.2 nm). All laser beams were focused by a microscope objective lens 50x and the signals were dispersed by a 1800 groves/mm grating, providing spectral resolutions of 1 cm^{-1} (Acton 2500i), 0.6 cm^{-1} (LabRAM HR800) and 0.5 cm^{-1} (LabRAM HR Evolution). The laser power have been controlled in each experiment in order to avoid sample heating effects.

High pressures were achieved by means of pneumatic DACs, having culet sizes of 200 μm and 350 μm. The (6,5) SWCNTs were loaded in a steel gaskets with pierced hole in its center and sealed between the diamond anvils. However, the 4:1 ethanol:methanol mixture was used as pressure transmitting medium, only for experiments of the precursor CoMoCAT (SG65i, marketed by Sigma-Aldrich, diameter range: 0.7–0.9 nm, (6,5) percentage $\geq$ 40%) and chirality-enriched (6,5) nanotubes in buckypaper shape or bundles. In the particular case of the Top 2 solution (see more details in Chapter 3), which is constituted of water, polymers, surfactants and individualized (6,5) single wall carbon nanotubes, the own mixture worked as PTM. Small ruby chips were used to measure the pressure in the sample chamber via the ruby fluorescence line R1 [107]. With these configurations, the Raman experiments at high pressures were run up to 26 GPa, 40 GPa, 50 GPa and 80 GPa, besides further characterizations were accomplished after pressure loadings.

A.1.2 TWCNTs

Raman experiments were performed using a home-made optical system based on an Acton 2500i spectrometer with excitation energy of 2.41 eV (514.5 nm wavelength Argon laser). The laser power is controlled to get the best signal-to-noise ratio and to avoid temperature effects on the sample. The laser beam was focused by a 50x objective lens and the signal was dispersed by a grating of 1800 grooves/mm, resulting in a spectral resolution of $\pm 1\ cm^{-1}$. The Raman spectra of the recovered sample after pressure loading of 59.4 GPa were excited with the energy source of 2.33 eV (532nm wavelength state solid laser) and acquired by a LabRAM HR Evolution spectrometer, with a spectral resolution of about 0.5 cm^{-1}. The beam was focused onto the sample using a long work distance 50x Mitutoyo magnification objective lens.

High pressures were achieved by using a membrane diamond-anvil cell, having culet size of 200 μm and another of 350 μm for the experiment up to 34.6 GPa . The TWCNTs were loaded in a cylindrical pressure chamber, drilled in a pre-indented stainless steel gasket and placed between the two diamond anvils. NaCl powder was used as pressure transmitting medium (PTM) to avoid any accidental filling of the tubes [41]. The pressures into the chamber were calibrate by the standard ruby luminescence R1 line [107] of the small ruby chip place together with the sample and PTM.

A.1.3 Boron nitride multiwalled nanotubes

The BN-nanotubes were studied at high-pressure using *in situ* Raman spectroscopy with a membrane diamond-anvil cell (DAC) having diamond culets of 350 μm. Samples were inserted in a 120 μm hole drilled in a pre-idented stainless steel gasket (thickness after identation = 30 μm). A small ruby chip placed in the sample chamber was used as the *in situ* pressure gauge with the use of the ruby fluorescence method [107]. NaCl was used as pressure-transmitting medium (PTM). Raman spectra were collected in backscattering geometry with a home-built optical system and an Acton SpectraPro 2500i spectrometer with an spectral resolution of $\sim$2 cm^{-1}. The excitation energy was 2.41 eV (514.5 nm) provided by an air-cooled argon-ion laser, having a source power limited to 20 mW to avoid heating sample effects. A Mitutoyo 50x objective lens allowed to focus the laser beam to a spot size of 2 μm at the sample. Three *in situ* Raman experiments were performed up to maximum pressures of 7.1, 15.6, 36 GPa. The Raman spectra of the experiments up to pressures of 41.1 GPa and 48.6 GPa were measured only after the pressure cycles (out of the DAC), for this was used a LabRAM HR Evolution spectrometer (with a spectral resolution of $\sim$ 0.5 cm^{-1} and provided of a confocal system) and excited with a laser energy of 2.33 eV (532nm wavelength state solid laser). The laser beam was focused onto the samples using a long work distance 50x Mitutoyo magnification objective lens. In after all experiments the samples were gently recovered for further characterizations.

A.2 Experiments of transmission electron microscopy

All samples characterized in this section were transfered by means of procedure described in the subsection **2.3.2**: a dispersion in ethanol, followed by ultrasonication of low power and dropping on the TEM grid.

A.2.1 SWCNTs

The TEM characterizations were performed on a pristine sample from the stock and other recovered after pressure cycle up to 80 GPa by means of a TEM JEOL 2100 (LaB6 single crystal filament). The pristine sample was probed with an acceleration voltage of 80kV, while 200kV was used for the recovered one.

A.2.2 TWCNTs

Transmission electron microscopy studies were carried out in recovered samples after decompression of 72 GPa by a JEOL 2100 (LaB_6 single crystal filament) microscope operating at 120kV, in order to get the better resolution and same time to avoid as much possible the knock-on processes.

A.2.3 BNMWNTs

TEM observations of the as produced BNNTs as well as the pressure cycled samples were performed on a 200 keV field-emission high-resolution transmission electron microscope (TEM) JEOL JEM-2100F (Fig.2.7(a)). From the TEM images the inner diameter of the synthesized MWBNNTs ranges from 15 to 20 nm and the outer tube diameter from 40 to 80 nm. Some larger tubes can be also observed exceptionally.

TEM tomography series of tilted images were also taken for the pristine BN-nanotubes sample and for the cycled sample up to 36 GPa. For this, the JEOL JEM-2100F TEM was equipped with a Gatan Ultrascan 1000 CCD camera, using a magnification of 40000 for the pristine samples and of 80000 for the 36 GPa cycled sample. The specimens were rotated from $-60°$ to $66°$ in case of the pristine BN-nanotube and from $-60°$ to $63°$ for the recovered BN-nanotube. A Saxton tilt increment scheme (variable angular step allowing to improve 3D reconstruction with a reduced number of images in order to preserve the beam sensitive structure of the sample) was used. For the acquisitions control and 3D reconstructions, a JEOL TEMography software package was used. 3D visualization of the reconstructed structures were performed with ImageJ software [204].

Bibliography

[1] H.W. Kroto, J.R. Heath, S.C. O'Brien, R.F. Curl, and R.E. Smalley. C_{60} : Buckminsterfullerene. *Nature*, 318:162, 1985.

[2] S. Iijima. Helical microtubules of graphitic carbon. *Nature*, 354:56, 1991.

[3] S. Iijima and T. Ichihashi. Single-shell carbon nanotubes of 1-nm diameter. *Nature*, 363:603–605, 1993.

[4] D. S. Bethune, C. H. Klang, M. S. De Vries, G. Gorman, R. Savoy, J. Vazquez, and R. Beyers. Cobalt-catalysed growth of carbon nanotubes with single-atomic-layer walls. *Nature*, 363:605–607, 1993.

[5] R. Saito. *Physical properties of carbon nanotubes.* Icp, 1998.

[6] A. Jorio, M. S. Dresselhaus, and G. Dresselhaus. *Carbon nanotubes: advanced topics in the synthesis, structure, properties and applications.* Springer, 2008.

[7] Ado Jorio and Antonio G. Souza Filho. Raman studies of carbon nanostructures. *Annual Review of Materials Research*, 46(1):357–382, 2016.

[8] K. S. Novoselov, A. K. Geim, S. V. Morozov, D. Jiang, Y. Zhang, S. V. Dubonos, I. V. Grigorieva, and A. A. Firsov. Electric field effect in atomically thin carbon films. *Science*, 306(5696):666–669, 2004.

[9] Lydéric Bocquet and Roland R Netz. Nanofluidics: Phonon modes for faster flow. *Nature Nanotech.*, 10(8):657–658, 2015.

[10] Xuedan Ma, Sofie Cambré, Wim Wenseleers, Stephen K. Doorn, and Han Htoon. Quasiphase transition in a single file of water molecules encapsulated in (6,5) carbon nanotubes observed by temperature-dependent photoluminescence spectroscopy. *Phys. Rev. Lett.*, 118:027402, Jan 2017.

[11] Jan Prasek, Jana Drbohlavova, Jana Chomoucka, Jaromir Hubalek, Ondrej Jasek, Vojtech Adam, and Rene Kizek. Methods for carbon nanotubes synthesis-review. *J. Mater. Chem.*, 21:15872–15884, 2011.

[12] Robert Vajtai, editor. *Springer Handbook of Nanomaterials.* Number XXXVI, 1221. Springer-Verlag Berlin Heidelberg, 1 edition, 2013.

[13] R. Saito A. Jorio, M. Dresselhaus and G. F. Dresselhaus. *Raman Spectroscopy in Graphene Related Systems.* Wiley-VCH, 2011.

[14] J.N. Fuchs, M. O. Goerbig, and M. Potemski. Des électrons sans masse dans une feuille de carbone. *Images de la Physique (CNRS)*, pages 50–56, 2007.

[15] C. L. Kane and E. J. Mele. Electron interactions and scaling relations for optical excitations in carbon nanotubes. *Phys. Rev. Lett.*, 93:197402, Nov 2004.

[16] P.T. Araujo, P.B.C. Pesce, M.S. Dresselhaus, K. Sato, R. Saito, and A. Jorio. Resonance raman spectroscopy of the radial breathing modes in carbon nanotubes. *Physica E: Low-dimensional Systems and Nanostructures*, 42(5):1251 – 1261, 2010.

[17] H. Telg, J. Maultzsch, S. Reich, F. Hennrich, and C. Thomsen. Chirality distribution and transition energies of carbon nanotubes. *Phys. Rev. Lett.*, 93:177401, Oct 2004.

[18] R. Bruce Weisman and Sergei M. Bachilo. Dependence of optical transition energies on structure for single-walled carbon nanotubes in aqueous suspension: an empirical kataura plot. *Nano Letters*, 3(9):1235–1238, 2003.

[19] Vasili Perebeinos, J. Tersoff, and Phaedon Avouris. Scaling of excitons in carbon nanotubes. *Phys. Rev. Lett.*, 92:257402, Jun 2004.

[20] J. Jiang, R. Saito, K. Sato, J. S. Park, Ge. G. Samsonidze, A. Jorio, G. Dresselhaus, and M. S. Dresselhaus. Exciton-photon, exciton-phonon matrix elements, and resonant raman intensity of single-wall carbon nanotubes. *Phys. Rev. B*, 75:035405, Jan 2007.

[21] M. Machón, S. Reich, H. Telg, J. Maultzsch, P. Ordejón, and C. Thomsen. Strength of radial breathing mode in single-walled carbon nanotubes. *Phys. Rev. B*, 71:035416, Jan 2005.

[22] Valentin N. Popov, Luc Henrard, and Philippe Lambin. Electron-phonon and electron-photon interactions and resonant raman scattering from the radial-breathing mode of single-walled carbon nanotubes. *Phys. Rev. B*, 72:035436, Jul 2005.

[23] J. Jiang, R. Saito, Ge. G. Samsonidze, A. Jorio, S. G. Chou, G. Dresselhaus, and M. S. Dresselhaus. Chirality dependence of exciton effects in single-wall carbon nanotubes: Tight-binding model. *Phys. Rev. B*, 75:035407, Jan 2007.

[24] Eduardo B. Barros, Ado Jorio, Georgii G. Samsonidze, Rodrigo B. Capaz, Antônio G. Souza Filho, Josué Mendes Filho, Gene Dresselhaus, and Mildred S. Dresselhaus. Review on the symmetry-related properties of carbon nanotubes. *Physics Reports*, 431(6):261 – 302, 2006.

[25] C Thomsen and S Reich. Double resonant Raman scattering in graphite. *Phys. Rev. Lett.*, 85(24):5214–5217, 2000.

[26] V. Zólyomi and J. Kürti. Calculating the discrepancy between the stokes and anti-stokes raman d band of carbon nanotubes using double resonance theory. *Phys. Rev. B*, 66:073418, Aug 2002.

[27] James A. Elliott, Jan K. W. Sandler, Alan H. Windle, Robert J. Young, and Milo S. P. Shaffer. Collapse of single-wall carbon nanotubes is diameter dependent. *Phys. Rev. Lett.*, 92:095501, March 2004.

[28] Alfonso San-Miguel. Nanomaterials under high-pressure. *Chem. Soc. Rev.*, 35(10):876–889, 2006.

[29] Tiago F.T. Cerqueira, Silvana Botti, Alfonso San-Miguel, and Miguel A.L. Marques. Density-functional tight-binding study of the collapse of carbon nanotubes under hydrostatic pressure. *Carbon*, 69(0):355 – 360, 2014.

[30] Abraao C. Torres-Dias, Tiago F.T. Cerqueira, Wenwen Cui, Miguel A.L. Marques, Silvana Botti, Denis Machon, Markus A. Hartmann, Yiwei Sun, David J. Dunstan, and Alfonso San-Miguel. From mesoscale to nanoscale mechanics in single-wall carbon nanotubes. *Carbon*, 123:145 – 150, 2017.

[31] M. Motta, A. Moisala, Kinloch, and H. Windle. High performance fibres from dog bone carbon nanotubes. *Adv. Mater.*, 19(21):3721–3726, 2007.

[32] AK Sood, PV Teresdesai, DVS Muthu, R Sen, A Govindaraj, and CNR Rao. Pressure behaviour of single wall carbon nanotube bundles and fullerenes: A Raman study. *Phys. Status Solidi B*, 215(1):393–401, SEP 1999. International Conference on Solid State Spectroscopy - (ICSSS), Schwabisch Gmund, Germany, Sep 05-07, 1999.

[33] U.D. Venkateswaran, E.A. Brandsen, U. Schlecht, A.M. Rao, E. Richter, I. Loa, K. Syassen, and P.C. Eklund. High pressure studies of the raman-active phonons in carbon nanotubes. *Phys. Status Solidi B*, 223(1):225–236, 2001.

[34] U. D. Venkateswaran, A. M. Rao, E. Richter, M. Menon, A. Rinzler, R. E. Smalley, and P. C. Eklund. Probing the single-wall carbon nanotube bundle: Raman scattering under high pressure. *Phys. Rev. B*, 59:10928–10934, April 1999.

[35] M. J. Peters, L. E. McNeil, Jian Ping Lu, and Daniel Kahn. Structural phase transition in carbon nanotube bundles under pressure. *Phys. Rev. B*, 61:5939–5944, March 2000.

[36] S Karmakar, SM Sharma, PV Teredesai, DVS Muthu, A Govindaraj, SK Sikka, and AK Sood. Structural changes in single-walled carbon nanotubes under non-hydrostatic pressures: x-ray and raman studies. *New J. Phys.*, 5:143.1–143.11, October 2003.

[37] Mingguang Yao, Zhigang Wang, Bingbing Liu, Yonggang Zou, Shidan Yu, Wang Lin, Yuanyuan Hou, Shoufu Pan, Mingxing Jin, Bo Zou, Tian Cui, Guangtian Zou, and B. Sundqvist. Raman signature to identify the structural transition of single-wall carbon nanotubes under high pressure. *Phys. Rev. B*, 78(20):205411, November 2008.

[38] Mingguang Yao, Shuangchen Lu, Junping Xiao, Zhen Yao, Linhai Jiang, Tian Cui, and Bingbing Liu. Probing factors affecting the raman modes and structural collapse of single-walled carbon nanotubes under pressure. *physica status solidi (b)*, 250(7):1370–1375, 2013.

[39] C. Caillier, D. Machon, A. San-Miguel, R. Arenal, G. Montagnac, H. Cardon, M. Kalbac, M. Zukalova, and L. Kavan. Probing high-pressure properties of single-wall carbon nanotubes through fullerene encapsulation. *Phys. Rev. B*, 77(12):125418, 2008.

[40] Zu-Po Yang, Lijie Ci, James A. Bur, Shawn-Yu Lin, and Pulickel M. Ajayan. Experimental observation of an extremely dark material made by a low-density nanotube array. *Nano Lett.*, 8(2):446–451, 2008.

[41] Abraao C. Torres-Dias, Sofie Cambré, Wim Wenseleers, Denis Machon, and Alfonso San-Miguel. Chirality-dependent mechanical response of empty and water-filled single-wall carbon nanotubes at high pressure. *Carbon*, 95:442–451, 2015.

[42] Paul E. Lammert, Peihong Zhang, and Vincent H. Crespi. Gapping by squashing: Metal-insulator and insulator-metal transitions in collapsed carbon nanotubes. *Phys. Rev. Lett.*, 84:2453–2456, Mar 2000.

[43] Rodrigo B. Capaz, Catalin D. Spataru, Paul Tangney, Marvin L. Cohen, and Steven G. Louie. Hydrostatic pressure effects on the structural and electronic properties of carbon nanotubes. *Phys. Status Solidi B*, 241(14):3352–3359, 2004.

[44] Ahmad J. Ghandour, David J. Dunstan, Andrei Sapelkin, John E. Proctor, and Matthew P. Halsall. High-pressure raman response of single-walled carbon nanotubes: Effect of the excitation laser energy. *Phys. Rev. B*, 78:125420, Sep 2008.

[45] W. Shan, J. Wu, W. Walukiewicz, J. W. Ager, K. M. Yu, E. E. Haller, K. Kissell, S. M. Bachilo, R. B. Weisman, and R. E. Smalley. Pressure dependence of optical transitions in semiconducting single-walled carbon nanotubes. *physica status solidi (b)*, 241(14):3367–3373, 2004.

[46] J. Wu, W. Walukiewicz, W. Shan, E. Bourret-Courchesne, J. W. Ager, K. M. Yu, E. E. Haller, Kyle Kissell, Sergei M. Bachilo, R. Bruce Weisman, and Richard E. Smalley. Structure-dependent hydrostatic deformation potentials of individual single-walled carbon nanotubes. *Phys. Rev. Lett.*, 93:017404, Jul 2004.

[47] X. Ye, D. Y. Sun, and X. G. Gong. Pressure-induced structural transition of double-walled carbon nanotubes. *Phys. Rev. B*, 72:035454, Jul 2005.

[48] Xiaoping Yang, Gang Wu, and Jinming Dong. Structural transformations of double-walled carbon nanotube bundle under hydrostatic pressure. *Appl. Phys. Lett.*, 89(11):–, 2006.

[49] X. Yang and G. Wu. The study of structural, electronic and optical properties of double-walled carbon nanotube bundles under hydrostatic pressure. *EPL*, 81(4):47003, 2008.

[50] J. Arvanitidis, D. Christofilos, K. Papagelis, K. S. Andrikopoulos, T. Takenobu, Y. Iwasa, H. Kataura, S. Ves, and G. A. Kourouklis. Pressure screening in the interior of primary shells in double-wall carbon nanotubes. *Phys. Rev. B*, 71:125404, March 2005.

[51] J. Arvanitidis, D. Christofilos, K. Papagelis, T. Takenobu, Y. Iwasa, H. Kataura, S. Ves, and G. A. Kourouklis. Double-wall carbon nanotubes under pressure: Probing the response of individual tubes and their intratube correlation. *Phys. Rev. B*, 72:193411, Nov 2005.

[52] J. Arvanitidis and D. Christofilos. High pressure studies of the radial breathing modes in double-wall carbon nanotubes. *physica status solidi (b)*, 244(1):127–135, 2007.

[53] B. Anis, K. Haubner, F. Börrnert, L. Dunsch, M. H. Rümmeli, and C. A. Kuntscher. Stabilization of carbon nanotubes by filling with inner tubes: An optical spectroscopy study on double-walled carbon nanotubes under hydrostatic pressure. *Phys. Rev. B*, 86:155454, October 2012.

[54] B. Anis, F. Boerrnert, M. H. Ruemmeli, and C. A. Kuntscher. Role of the pressure transmitting medium on the pressure effects in DWCNTs. *Phys. Status Solidi B*, 250(12):2616–2621, DEC 2013.

[55] A. L. Aguiar, E. B. Barros, R. B. Capaz, A. G. Souza Filho, P. T. C. Freire, J. Mendes Filho, D. Machon, Ch Caillier, Y. A. Kim, H. Muramatsu, M. Endo, and A. San-Miguel. Pressure-induced collapse in double-walled carbon nanotubes: Chemical and mechanical screening effects. *J. Phys. Chem. C*, 115(13):5378–5384, April 2011.

[56] R.S. Alencar, Wenwen Cui, A.C. Torres-Dias, Tiago F.T. Cerqueira, Silvana Botti, Miguel A.L. Marques, O.P. Ferreira, Ch Laurent, A. Weibel, D. Machon, D.J. Dunstan, A.G.Souza Filho, and A. San-Miguel. Pressure-induced radial collapse in few-wall carbon nanotubes: A combined theoretical and experimental study. *Carbon*, 2017.

[57] A. Rubio, J.L. Corkill, and M.L. Cohen. Theory of graphitic boron nitride nanotubes. *Phys. Rev. B*, 49:5081–5084, 1994.

[58] X. Blase, L. X. Benedict, E. L. Shirley, and S. G. Louie. Hybridization effects and metallicity in small radius carbon nanotubes. *Phys. Rev. Lett.*, 72(12):1878–1881, 1994.

[59] Nasreen G. Chopra, R. J. Luyken, K. Cherrey, Vincent H. Crespi, Marvin L. Cohen, Steven G. Louie, and A. Zettl. Boron nitride nanotubes. *Science*, 269(5226):966–967, 1995.

[60] Wei-Qiang Han, Hua-Gen Yu, Chunyi Zhi, Jianbin Wang, Zhenxian Liu, Takashi Sekiguchi, and Yoshio Bando. Isotope effect on band gap and radiative transitions properties of boron nitride nanotubes. *Nano Letters*, 8(2):491–494, 2008. PMID: 18173295.

[61] Dmitri Golberg, Yoshio Bando, Yang Huang, Takeshi Terao, Masanori Mitome, Chengchun Tang, and Chunyi Zhi. Boron nitride nanotubes and nanosheets. *ACS Nano*, 4(6):2979–2993, 2010.

[62] Chunyi Zhi, Yoshio Bando, Chengchun Tang, and Dmitri Golberg. Boron nitride nanotubes. *Materials Science and Engineering: R: Reports*, 70(3–6):92 – 111, 2010.

[63] Kris J. Erickson, Ashley L. Gibb, Alexander Sinitskii, Michael Rousseas, Nasim Alem, James M. Tour, and Alex K. Zettl. Longitudinal splitting of boron nitride nanotubes for the facile synthesis of high quality boron nitride nanoribbons. *Nano Letters*, 11(8):3221–3226, 2011. PMID: 21608991.

[64] Y.; Ashrafi B.; Guan J.; Kim K. S.; O'Neill K.; Kingston C. T.; Simard B. Jakubinek, M. B.; Martinez-Rubi. Polymer nanocomposites incorporating boron nitride nanotubes, June 2015.

[65] D. Golberg, Y. Bando, M. Eremets, K. Takemura, K. Kurashima, and H. Yusa. Nanotubes in boron nitride laser heated at high pressure. *Applied Physics Letters*, 69(14):2045–2047, 1996.

[66] Oleg R. Lourie, Carolyn R. Jones, Bart M. Bartlett, Patrick C. Gibbons, Rodney S. Ruoff, and William E. Buhro. Cvd growth of boron nitride nanotubes. *Chemistry of Materials*, 12(7):1808–1810, 2000.

[67] Y. Chen, J.F. Gerald, J.S. Williams, and P. Willis. Mechanochemical synthesis of boron nitride nanotubes. In *Metastable, Mechanically Alloyed and Nanocrystalline Materials 1998*, volume 312 of *Materials Science Forum*, pages 173–178. Trans Tech Publications, 7 1999.

[68] Weiqiang Han, Yoshio Bando, Keiji Kurashima, and Tadao Sato. Synthesis of boron nitride nanotubes from carbon nanotubes by a substitution reaction. *Applied Physics Letters*, 73(21):3085–3087, 1998.

[69] A. Loiseau, F. Willaime, N. Demoncy, N. Schramchenko, G. Hug, C. Colliex, and H. Pascard. Boron nitride nanotubes. *Carbon*, 36(5):743 – 752, 1998. European Materials Research Society 1997 Meeting, Symposium A: Fullernes and Carbon based Materials.

[70] R. S. Lee, J. Gavillet, M. Lamy de la Chapelle, A. Loiseau, J.-L. Cochon, D. Pigache, J. Thibault, and F. Willaime. Catalyst-free synthesis of boron nitride single-wall nanotubes with a preferred zig-zag configuration. *Phys. Rev. B*, 64:121405, Sep 2001.

[71] M. Radosavljević, J. Appenzeller, V. Derycke, R. Martel, Ph. Avouris, A. Loiseau, J.-L. Cochon, and D. Pigache. Electrical properties and transport in boron nitride nanotubes. *Applied Physics Letters*, 82(23):4131–4133, 2003.

[72] J. S. Lauret, R. Arenal, F. Ducastelle, A. Loiseau, M. Cau, B. Attal-Tretout, E. Rosencher, and L. Goux-Capes. Optical transitions in single-wall boron nitride nanotubes. *Phys. Rev. Lett.*, 94:037405, Jan 2005.

[73] R. Arenal, O. Stéphan, M. Kociak, D. Taverna, A. Loiseau, and C. Colliex. Electron energy loss spectroscopy measurement of the optical gaps on individual boron nitride single-walled and multiwalled nanotubes. *Phys. Rev. Lett.*, 95:127601, Sep 2005.

[74] S. Reich, A. C. Ferrari, R. Arenal, A. Loiseau, I. Bello, and J. Robertson. Resonant raman scattering in cubic and hexagonal boron nitride. *Phys. Rev. B*, 71:205201, May 2005.

[75] Fawei Zheng, Gang Zhou, Shaogang Hao, and Wenhui Duan. Structural characterizations and electronic properties of boron nitride nanotube crystalline bundles. *The Journal of Chemical Physics*, 123(12):124716, 2005.

[76] X. Blase, A. Rubio, S.G. Louie, and M.L. Cohen. Stability and band gap constancy of boron nitride nanotubes. *EPL (Europhysics Letters)*, 28:335–340, nov 1994.

[77] G. Y. Guo, S. Ishibashi, T. Tamura, and K. Terakura. Static dielectric response and born effective charge of bn nanotubes from ab initio finite electric field calculations. *Phys. Rev. B*, 75:245403, Jun 2007.

[78] S. S. Coutinho, V. Lemos, and S. Guerini. Band-gap tunability of a (6,0) bn nanotube bundle under pressure: Ab initio calculations. *Phys. Rev. B*, 80:193408, Nov 2009.

[79] Wesdney S. Melo, Mauro B. Pereira, Humberto F. Silva Filho, and Silvete Guerini. Electronic properties of double wall bn nanotube under hydrostatic pressure: an ab initio study. *The European Physical Journal B*, 88(1):6, 2015.

[80] Chun-Wei Chen, Ming-Hsien Lee, and S J Clark. Band gap modification of single-walled carbon nanotube and boron nitride nanotube under a transverse electric field. *Nanotechnology*, 15(12):1837, 2004.

[81] Yong Jae Cho, Chang Hyun Kim, Han Sung Kim, Jeunghee Park, Hyun Chul Choi, Hyun-Joon Shin, Guohua Gao, and Hong Seok Kang. Electronic structure of si-doped bn nanotubes using x-ray photoelectron spectroscopy and first-principles calculation. *Chemistry of Materials*, 21(1):136–143, 2009.

[82] Yuri F. Zhukovskii, Sergei Piskunov, Jurijs Kazerovskis, Dmitry V. Makaev, and Pavel N. D'yachkov. Comparative theoretical analysis of bn nanotubes doped with al, p, ga, as, in, and sb. *The Journal of Physical Chemistry C*, 117(27):14235–14240, 2013.

[83] Yafei Li, Zhen Zhou, Dmitri Golberg, Yoshio Bando, Paul von Ragué Schleyer, and Zhongfang Chen. Stone−wales defects in single-walled boron nitride nanotubes: formation energies, electronic structures, and reactivity. *The Journal of Physical Chemistry C*, 112(5):1365–1370, 2008.

[84] Ruoxi Wang, Rongxiu Zhu, and Dongju Zhang. Adsorption of formaldehyde molecule on the pristine and silicon-doped boron nitride nanotubes. *Chemical Physics Letters*, 467(1):131 – 135, 2008.

[85] P. Jaffrennou, J. Barjon, T. Schmid, L. Museur, A. Kanaev, J.-S. Lauret, C. Y. Zhi, C. Tang, Y. Bando, D. Golberg, B. Attal-Tretout, F. Ducastelle, and A. Loiseau. Near-band-edge recombinations in multiwalled boron nitride nanotubes: Cathodoluminescence and photoluminescence spectroscopy measurements. *Phys. Rev. B*, 77:235422, Jun 2008.

[86] Aurélie Pierret, Hanond Nong, Frédéric Fossard, Brigitte Attal-Trétout, Yanming Xue, Dmitri Golberg, Julien Barjon, and Annick Loiseau. Role of structural defects in the ultraviolet luminescence of multiwall boron nitride nanotubes. *Journal of Applied Physics*, 118(23):234307, 2015.

[87] Ofir E. Alon. Symmetry properties of single-walled boron nitride nanotubes. *Phys. Rev. B*, 64:153408, Sep 2001.

[88] Ludger Wirtz, Angel Rubio, Raul Arenal de la Concha, and Annick Loiseau. Ab initio calculations of the lattice dynamics of boron nitride nanotubes. *Phys. Rev. B*, 68:045425, Jul 2003.

[89] Y. Xiao, X. H. Yan, J. X. Cao, J. W. Ding, Y. L. Mao, and J. Xiang. Specific heat and quantized thermal conductance of single-walled boron nitride nanotubes. *Phys. Rev. B*, 69:205415, May 2004.

[90] Valentin N. Popov. Lattice dynamics of single-walled boron nitride nanotubes. *Phys. Rev. B*, 67:085408, Feb 2003.

[91] B. Fakrach, A. Rahmani, H. Chadli, K. Sbai, and J.-L. Sauvajol. Raman spectrum of single-walled boron nitride nanotube. *Physica E: Low-dimensional Systems and Nanostructures*, 41(10):1800 – 1805, 2009.

[92] D. Sánchez-Portal and E. Hernández. Vibrational properties of single-wall nanotubes and monolayers of hexagonal bn. *Phys. Rev. B*, 66:235415, Dec 2002.

[93] Ludger Wirtz, Michele Lazzeri, Francesco Mauri, and Angel Rubio. Raman spectra of bn nanotubes: Ab initio and bond-polarizability model calculations. *Phys. Rev. B*, 71:241402, Jun 2005.

[94] E. Ghavanloo and S. A. Fazelzadeh. Raman radial breathing mode frequency of boron nitride nanotubes with bounded uncertain material properties. *IET Micro Nano Letters*, 10(11):617–620, August 2015.

[95] Raul Arenal, A C Ferrari, Stephanie Reich, Ludger Wirtz, J-Y Mevellec, Serge Lefrant, Angel Rubio, and A Loiseau. Raman spectroscopy of single-wall boron nitride nanotubes. 6:1812–6, 09 2006.

[96] Seung Yong Bae, Hee Won Seo, Jeunghee Park, Young Sang Choi, Ju Chul Park, and Soun Young Lee. Boron nitride nanotubes synthesized in the temperature range 1000–1200 °c. *Chemical Physics Letters*, 374(5):534 – 541, 2003.

[97] Chunyi Zhi, Yoshio Bando, Chengchun Tang, Dmitri Golberg, Rongguo Xie, and Takashi Sekigushi. Phonon characteristics and cathodolumininescence of boron nitride nanotubes. *Applied Physics Letters*, 86(21):213110, 2005.

[98] Yoke Khin Yap, editor. *B-C-N Nanotubes and Related Nanostructures (Lecture Notes in Nanoscale Science and Technology)*. Springer, 2009.

[99] C. Journet, WK Maser, P. Bernier, A. Loiseau, M. Lamy de La Chapelle, S. Lefrant, P. Deniard, R. Lee, and JE Fischer. Large-scale production of single-walled carbon nanotubes by the electric-arc technique. *Nature*, 388(6644):756–757, 1997.

[100] Neha Arora and N.N. Sharma. Arc discharge synthesis of carbon nanotubes: Comprehensive review. *Diamond and Related Materials*, 50(Supplement C):135 – 150, 2014.

[101] T. Guo, P. Nikolaev, A. G. Rinzler, D. Tomanek, D. T. Colbert, and R. E. Smalley. Self-assembly of tubular fullerenes. *J. Phys. Chem.*, 99(27):10694–10697, 1995.

[102] Peter J. F. Harris. *Carbon Nanotube Science*. CAMBRIDGE UNIVERSITY PRESS, 2009.

[103] Ronald Miletich, David R. Allan, and Werner F. Kuhs. High-pressure single-crystal techniques. *Reviews in Mineralogy and Geochemistry*, 41(1):445–519, 2000.

[104] S Klotz, JC Chervin, P Munsch, and G Le Marchand. Hydrostatic limits of 11 pressure transmitting media. *J. Phys. D: Appl. Phys.*, 42(7):075413, 2009.

[105] G. J. Piermarini, S. Block, and J.D. Barnett. Hydrostatic limits in liquids and solids to 100 kbar. *Journal of Applied Physics*, 44(12):5377–5382, 1973.

[106] Silvio Domingos Silva Santos. Estudo do espectro de fônons de sistemas ln2mo4o15 (ln = sm, la) sob condições extremas de pressão e temperatura. Master's thesis, Federal University of Pará, March 2014.

[107] H. K. Mao, J. Xu, and P. M. Bell. Calibration of the ruby pressure gauge to 800 kbar under quasi-hydrostatic conditions. *Journal of Geophysical Research: Solid Earth*, 91(B5):4673–4676, 1986.

[108] David B. Williams and C. Barry Carter. *Transmission Electron Microscopy*. Springer, Boston, MA, 2009.

[109] Jianwei Miao, Peter Ercius, and Simon J. L. Billinge. Atomic electron tomography: 3d structures without crystals. *Science*, 353(6306), 2016.

[110] Aude Stolz. *Systemes fonctionnels a base de carbone et interactions avec l eau. Du nano-confinement aux eponges super hydrophobes*. PhD thesis, Universite Claude Bernard Lyon 1, 2016.

[111] Navaneetha K Subbaiyan, Sofie Cambré, A Nicholas G Parra-Vasquez, Erik H Hároz, Stephen K Doorn, and Juan G Duque. Role of surfactants and salt in aqueous two-phase separation of carbon nanotubes toward simple chirality isolation. *ACS Nano*, 8:1619–1628, 2014.

[112] Per-Ake Albertsson. *Partition of Cell Particles and Macromolecules*. Wiley-Interscience, 1986.

[113] Navaneetha K Subbaiyan, A Nicholas G Parra-Vasquez, Sofie Cambré, Miguel A Santiago Cordoba, Sibel Ebru Yalcin, Christopher E Hamilton, Nathan H Mack, Jeffrey L Blackburn, Stephen K Doorn, and Juan G Duque. Bench-top aqueous two-phase extraction of isolated individual single-walled carbon nanotubes. *Nano Research*, 8(5):1755–1769, 2015.

[114] Jeffrey A. Fagan, Constantine Y. Khripin, Carlos A. Silvera Batista, Jeffrey R. Simpson, Erik H. Hároz, Angela R. Hight Walker, and Ming Zheng. Isolation of specific small-diameter single-wall carbon nanotube species via aqueous two-phase extraction. *Advanced Materials*, 26(18):2800–2804, 2014.

[115] Xiaojun Wei, Takeshi Tanaka, Yohei Yomogida, Naomichi Sato, Riichiro Saito, and Hiromichi Kataura. Experimental determination of excitonic band structures of single-walled carbon nanotubes using circular dichroism spectra. *Nature Communications*, 7:12899, 10 2016.

[116] Rafael N. Gontijo, Gustavo A.M. Sáfar, Ariete Righi, Rishabh M. Jain, Michael S. Strano, and Cristiano Fantini. Quantifying (n,m) species in single-wall carbon nanotubes dispersions by combining raman and optical absorption spectroscopies. *Carbon*, 115(Supplement C):681 – 687, 2017.

[117] Sofie Cambré, Bob Schoeters, Sten Luyckx, Etienne Goovaerts, and Wim Wenseleers. Experimental observation of single-file water filling of thin single-wall carbon nanotubes down to chiral index (5,3). *Phys. Rev. Lett.*, 104:207401, May 2010.

[118] M. J. Longhurst and N. Quirke. The environmental effect on the radial breathing mode of carbon nanotubes in water. *The Journal of Chemical Physics*, 124(23):234708, 2006.

[119] E. H. Hároz, J. G. Duque, W. D. Rice, C. G. Densmore, J. Kono, and S. K. Doorn. Resonant raman spectroscopy of armchair carbon nanotubes: Absence of broad G^- feature. *Phys. Rev. B*, 84:121403, Sep 2011.

[120] Hagen Telg, Juan G. Duque, Matthias Staiger, Xiaomin Tu, Frank Hennrich, Manfred M. Kappes, Ming Zheng, Janina Maultzsch, Christian Thomsen, and Stephen K. Doorn. Chiral index dependence of the g+ and g– raman modes in semiconducting carbon nanotubes. *ACS Nano*, 6(1):904–911, 2012. PMID: 22175270.

[121] Valentin N. Popov and Philippe Lambin. Radius and chirality dependence of the radial breathing mode and the g-band phonon modes of single-walled carbon nanotubes. *Phys. Rev. B*, 73:085407, Feb 2006.

[122] P. Puech, E. Flahaut, A. Sapelkin, H. Hubel, D. J. Dunstan, G. Landa, and W. S. Bacsa. Nanoscale pressure effects in individual double-wall carbon nanotubes. *Phys. Rev. B*, 73:233408, Jun 2006.

[123] M S Dresselhaus, Ado Jorio, A Filho, and Riichiro Saito. Defect characterization in graphene and carbon nanotubes using raman spectroscopy. 368:5355–77, 12 2010.

[124] Sehmus Ozden, Pedro A. S. Autreto, Chandra Sekhar Tiwary, Suman Khatiwada, Leonardo Machado, Douglas S. Galvao, Robert Vajtai, Enrique V. Barrera, and Pulickel M. Ajayan. Unzipping carbon nanotubes at high impact. *Nano Letters*, 14(7):4131–4137, 2014. PMID: 24915176.

[125] Kochling K. Boehm H. P. Fitzer, E. and H. Marsh. Recommended terminology for the description of carbon as a solid (iupac recommendations 1995). *Pure and Applied Chemistry*, 67(Supplement C):473–506, 2009.

[126] J. J. Guo, G. H. Liu, X. M. Wang, T. Fujita, B. S. Xu, and M. W. Chen. High-pressure raman spectroscopy of carbon onions and nanocapsules. *Applied Physics Letters*, 95(5):051920, 2009.

[127] Weiwei Zhang, Mingguang Yao, Xianhong Fan, Shijia Zhao, Shuanglong Chen, Chen Gong, Ye Yuan, Ran Liu, and Bingbing Liu. Pressure-induced transformations of onion-like carbon nanospheres up to 48 GPa. *J. Chem. Phys.*, 142:034702, 2015.

[128] R. S. Alencar, A. L. Aguiar, A. R. Paschoal, P. T. C. Freire, Y. A. Kim, H. Muramatsu, M. Endo, H. Terrones, M. Terrones, A. San-Miguel, M. S. Dresselhaus, and A. G. Souza Filho. Pressure-Induced Selectivity for Probing Inner Tubes in Double- and Triple-Walled Carbon Nanotubes: A Resonance Raman Study. *J. Phys. Chem. C*, 118(15):8153–8158, APR 17 2014.

[129] Hiroyuki Muramatsu, Daisuke Shimamoto, Takuya Hayashi, Yoong Ahm Kim, Mauricio Terrones, Morinobu Endo, and Mildred S. Dresselhaus. Bulk synthesis of narrow diameter and highly crystalline triple-walled carbon nanotubes by coalescing fullerene peapods. *Advanced Materials*, 23(15):1761–1764, 2011.

[130] Y. Zhao, J. Wei, R. Vajtai, P.M. Ajayan, and E.V Barrera. Iodine doped carbon nanotube cables exceeding specific electrical conductivity of metals. *Scientific Reports*, 1(83), 2011.

[131] Thomas Ch. Hirschmann, Paulo T. Araujo, Hiroyuki Muramatsu, Xu Zhang, Kornelius Nielsch, Yoong Ahm Kim, and Mildred S. Dresselhaus. Characterization of bundled and individual triple-walled carbon nanotubes by resonant raman spectroscopy. *ACS Nano*, 7(3):2381–2387, 2013. PMID: 23311296.

[132] Thomas Ch. Hirschmann, Paulo T. Araujo, Hiroyuki Muramatsu, Joaquin F. Rodriguez-Nieva, Max Seifert, Kornelius Nielsch, Yoong Ahm Kim, and Mildred S. Dresselhaus. Role of intertube interactions in double- and triple-walled carbon nanotubes. *ACS Nano*, 8(2):1330–1341, 2014. PMID: 24456167.

[133] Thomas Ch. Hirschmann, Mildred S. Dresselhaus, Hiroyuki Muramatsu, Max Seifert, Ursula Wurstbauer, Eric Parzinger, Kornelius Nielsch, Yoong Ahm Kim, and Paulo T. Araujo. $G^{'}$ band in double- and triple-walled carbon nanotubes: A raman study. *Phys. Rev. B*, 91:075402, Feb 2015.

[134] D. Levshov, T. X. Than, R. Arenal, V. N. Popov, R. Parret, M. Paillet, V. Jourdain, A. A. Zahab, T. Michel, Yu. I. Yuzyuk, and J.-L. Sauvajol. Experimental evidence of a mechanical coupling between layers in an individual double-walled carbon nanotube. *Nano Letters*, 11(11):4800–4804, 2011. PMID: 22007874.

[135] Itai Leven, Roberto Guerra, Andrea Vanossi, Erio Tosatti, and Oded Hod. Multiwalled nanotube faceting unravelled. *Nat Nano*, 11(12):1082–1086, December 2016.

[136] Tobias Hertel, Axel Hagen, Vadim Talalaev, Katharina Arnold, Frank Hennrich, Manfred Kappes, Sandra Rosenthal, James McBride, Hendrik Ulbricht, and Emmanuel Flahaut. Spectroscopy of single- and double-wall carbon nanotubes in different environments. *Nano Letters*, 5(3):511–514, 2005. PMID: 15755104.

[137] D. Christofilos, J. Arvanitidis, G. A. Kourouklis, S. Ves, T. Takenobu, Y. Iwasa, and H. Kataura. Identification of inner and outer shells of double-wall carbon nanotubes using high-pressure raman spectroscopy. *Phys. Rev. B*, 76:113402, Sep 2007.

[138] P. Puech, H. Hubel, D. J. Dunstan, A. Bassil, R. Bacsa, A. Peigney, E. Flahaut, C. Laurent, and W. S. Bacsa. Light scattering of double wall carbon nanotubes under hydrostatic pressure: pressure effects on the internal and external tubes. *Phys. Status Solidi B*, 241(14):3360–3366, 2004.

[139] P. Puech, H. Hubel, D. J. Dunstan, R. R. Bacsa, C. Laurent, and W. S. Bacsa. Discontinuous tangential stress in double wall carbon nanotubes. *Phys. Rev. Lett.*, 93:095506, Aug 2004.

[140] A. L. Aguiar, A. San-Miguel, E. B. Barros, M. Kalbáč, D. Machon, Y. A. Kim, H. Muramatsu, M. Endo, and A. G. Souza Filho. Effects of intercalation and inhomogeneous filling on the collapse pressure of double-wall carbon nanotubes. *Phys. Rev. B*, 86:195410, Nov 2012.

[141] Vikram Gadagkar, Prabal K. Maiti, Yves Lansac, A. Jagota, and A. K. Sood. Collapse of double-walled carbon nanotube bundles under hydrostatic pressure. *Phys. Rev. B*, 73:085402, Feb 2006.

[142] A. Merlen, N. Bendiab, P. Toulemonde, A. Aouizerat, A. San Miguel, J. L. Sauvajol, G. Montagnac, H. Cardon, and P. Petit. Resonant raman spectroscopy of single-wall carbon nanotubes under pressure. *Phys. Rev. B*, 72:035409, July 2005.

[143] D. I. Levshov, T. Michel, R. Arenal, H. N. Tran, T. X. Than, M. Paillet, Yu. I. Yuzyuk, and J.-L. Sauvajol. Interlayer dependence of g-modes in semiconducting double-walled carbon nanotubes. *The Journal of Physical Chemistry C*, 119(40):23196–23202, 2015.

[144] Wenwen Cui, Tiago F. T. Cerqueira, Silvana Botti, Miguel A. L. Marques, and Alfonso San-Miguel. Nanostructured water and carbon dioxide inside collapsing carbon nanotubes at high pressure. *Phys. Chem. Chem. Phys.*, 18:19926–19932, 2016.

[145] Shujie You, Mattias Mases, Ilya Dobryden, Alexander A. Green, Mark C. Hersam, and Alexander V. Soldatov. Probing structural stability of double-walled carbon nanotubes at high non-hydrostatic pressure by raman spectroscopy. *High Pressure Res.*, 31(1):186–190, 2011.

[146] P.A. Djondjorov, V.M. Vassilev, and I.M. Mladenov. Analytic description and explicit parametrisation of the equilibrium shapes of elastic rings and tubes under uniform hydrostatic pressure. *Int. J. Mech. Sci*, 53:355–364, 2011.

[147] Kosynkin D. V., Higginbotham A. L., Sinitskii A., Lomeda J., Dimiev A., Price B. K., and Tour J. M. Longitudinal unzipping of carbon nanotubes to form graphene nanoribbons. *Nature*, 458:872–876, April 2009.

[148] Liming Xie, Hailiang Wang, Chuanhong Jin, Xinran Wang, Liying Jiao, Kazu Suenaga, and Hongjie Dai. Graphene nanoribbons from unzipped carbon nanotubes: Atomic structures, raman spectroscopy, and electrical properties. *Journal of the American Chemical Society*, 133(27):10394–10397, 2011. PMID: 21678963.

[149] S Jovanovic, T Da Ross, A Ostric, D Tosic, J Prekodravac, Z Markovic, and B Todorovic Markovic. Raman spectroscopy of graphene nanoribbons synthesized by longitudinal unzipping of multiwall carbon nanotubes. *Physica Scripta*, 2014(T162):014023, 2014.

[150] Joonwon Lim, Uday Narayan Maiti, Na-Young Kim, Rekha Narayan, Won Jun Lee, Dong Sung Choi, Youngtak Oh, Ju Min Lee, Gil Yong Lee, Seok Hun Kang, Hyunwoo Kim, Yong-Hyun Kim, and Sang Ouk Kim. Dopant-specific unzipping of carbon nanotubes for intact crystalline graphene nanostructures. *Nature Communications*, 7:10364, January 2016.

[151] Yan-Sheng Li, Jia-Liang Liao, Shan-Yu Wang, and Wei-Hung Chiang. Intercalation-assisted longitudinal unzipping of carbon nanotubes for green and scalable synthesis of graphene nanoribbons. *Scientific Reports*, 6:22755, 2016.

[152] Liying Jiao, Li Zhang, Xinran Wang, Georgi Diankov, and Hongjie Dai. Narrow graphene nanoribbons from carbon nanotubes. *Nature*, 458(7240):877–880, 2009.

[153] Sehmus Ozden, Leonardo D. Machado, ChandraSekhar Tiwary, Pedro A. S. Autreto, Robert Vajtai, Enrique V. Barrera, Douglas S. Galvao, and Pulickel M. Ajayan. Ballistic fracturing of carbon nanotubes. *ACS Applied Materials & Interfaces*, 8(37):24819–24825, 2016. PMID: 27564421.

[154] Jeremy R. Patterson, Yogesh K. Vohra, Samuel T. Weir, and Jagannadham Akella. Single-wall carbon nanotubes under high pressures to 62 gpa studied using designer diamond anvils. *Journal of Nanoscience and Nanotechnology*, 1(2):143–147, 2001.

[155] V.D. Blank, V.N. Denisov, A.N. Kirichenko, N.A. Lvova, S.Y. Martyushov, B.N. Mavrin, D.M. Popova, M.Yu. Popov, E.V. Tat'yanin, and A.A. Zakhidov. Nanostructured superhard carbon phase obtained under high pressure with shear deformation from single-wall nanotubes hipco. *Physica B: Condensed Matter*, 382(1):58 – 64, 2006.

[156] E. Y. Pashkin, A. M. Pankov, B. A. Kulnitskiy, I. A. Perezhogin, A. R. Karaeva, V. Z. Mordkovich, M. Y. Popov, P. B. Sorokin, and V. D. Blank. The unexpected stability of multiwall nanotubes under high pressure and shear deformation. *Applied Physics Letters*, 109(8):081904, 2016.

[157] M.S. Dresselhaus, G. Dresselhaus, A. Jorio, A.G. Souza Filho, and R. Saito. Raman spectroscopy on isolated single wall carbon nanotubes. *Carbon*, 40(12):2043 – 2061, 2002.

[158] A. Jorio, A. G. Souza Filho, G. Dresselhaus, M. S. Dresselhaus, A. K. Swan, M. S. Ünlü, B. B. Goldberg, M. A. Pimenta, J. H. Hafner, C. M. Lieber, and R. Saito. G-band resonant raman study of 62 isolated single-wall carbon nanotubes. *Phys. Rev. B*, 65:155412, March 2002.

[159] A. Jorio, C. Fantini, M. S. S. Dantas, M. A. Pimenta, A. G. Souza Filho, Ge. G. Samsonidze, V. W. Brar, G. Dresselhaus, M. S. Dresselhaus, A. K. Swan, M. S. Ünlü, B. B. Goldberg, and R. Saito. Linewidth of the raman features of individual single-wall carbon nanotubes. *Phys. Rev. B*, 66:115411, September 2002.

[160] A Jorio, M A Pimenta, A G Souza Filho, R Saito, G Dresselhaus, and M S Dresselhaus. Characterizing carbon nanotube samples with resonance raman scattering. *New J. Phys.*, 5(1):139, 2003.

[161] A. Jorio, M. A. Pimenta, A. G. Souza Filho, Ge. G. Samsonidze, A. K. Swan, M. S. Ünlü, B. B. Goldberg, R. Saito, G. Dresselhaus, and M. S. Dresselhaus. Resonance raman spectra of carbon nanotubes by cross-polarized light. *Phys. Rev. Lett.*, 90:107403, March 2003.

[162] D. Bischoff, J. Güttinger, S. Dröscher, T. Ihn, K. Ensslin, and C. Stampfer. Raman spectroscopy on etched graphene nanoribbons. *Journal of Applied Physics*, 109(7):073710, 2011.

[163] Kiran M. Subhedar, Indu Sharma, and Sanjay R. Dhakate. Control of layer stacking in cvd graphene under quasi-static condition. *Phys. Chem. Chem. Phys.*, 17:22304–22310, 2015.

[164] Chengchun Tang, Yoshio Bando, Tadao Sato, and Keiji Kurashima. A novel precursor for synthesis of pure boron nitride nanotubes. *Chem. Commun.*, pages 1290–1291, 2002.

[165] Chunyi Zhi, Yoshio Bando, Chengchun Tan, and Dmitri Golberg. Effective precursor for high yield synthesis of pure bn nanotubes. *Solid State Communications*, 135(1):67 – 70, 2005.

[166] Yang Huang, Jing Lin, Chengchun Tang, Yoshio Bando, Chunyi Zhi, Tianyou Zhai, Benjamin Dierre, Takashi Sekiguchi, and Dmitri Golberg. Bulk synthesis, growth mechanism and properties of highly pure ultrafine boron nitride nanotubes with diameters of sub-10 nm. *Nanotechnology*, 22(14):145602, 2011.

[167] D. Golberg, M. Mitome, Y. Bando, C.C. Tang, and C.Y. Zhi. Multi-walled boron nitride nanotubes composed of diverse cross-section and helix type shells. *Applied Physics A*, 88(2):347–352, 2007.

[168] Aurelie Pierret. *Propriétes structurales et optiques de nanostructures III-N semiconductrices à grand gap. Nanofils d AlxGa1-xN synthetises par epitaxie par jets moleculaires et nanostructures de nitrure de bore.* PhD thesis, Universite Pierre et Marie Curie, 2013.

[169] Jonathan N. Coleman, Umar Khan, Werner J. Blau, and Yurii K. Gun'ko. Small but strong: A review of the mechanical properties of carbon nanotube–polymer composites. *Carbon*, 44(9):1624 – 1652, 2006.

[170] Meng Zheng, Xiaoming Chen, In-Tae Bae, Changhong Ke, Cheol Park, Michael W. Smith, and Kevin Jordan. Radial mechanical properties of single-walled boron nitride nanotubes. *Small*, 8(1):116–121, 2012.

[171] Meng Zheng, Changhong Ke, In-Tae Bae, Cheol Park, Michael W Smith, and Kevin Jordan. Radial elasticity of multi-walled boron nitride nanotubes. *Nanotechnology*, 23(9):095703, 2012.

[172] J Xiao, B Liu, Y Huang, J Zuo, K-C Hwang, and M-F Yu. Collapse and stability of single- and multi-wall carbon nanotubes. *Nanotechnology*, 18(39):395703, 2007.

[173] Y. Kinoshita, S. Hase, and N. Ohno. Flattening-induced electronic changes in zigzag single- and multi-walled boron nitride nanotubes: A first-principles dft study. *Phys. Rev. B*, 80:125114, Sep 2009.

[174] I. Loa. Raman spectroscopy on carbon nanotubes at high pressure. *Journal of Raman Spectroscopy*, 34(7-8):611–627, 2003.

[175] R. Geick, C. H. Perry, and G. Rupprecht. Normal modes in hexagonal boron nitride. *Phys. Rev.*, 146:543–547, Jun 1966.

[176] E. Borowiak-Palen, T. Pichler, G. G. Fuentes, B. Bendjemil, X. Liu, A. Graff, G. Behr, R. J. Kalenczuk, M. Knupfer, and J. Fink. Infrared response of multiwalled boron nitride nanotubes. *Chem. Commun.*, pages 82–83, 2003.

[177] Yongqing Cai, Litong Zhang, Qingfeng Zeng, Laifei Cheng, and Yongdong Xu. Infrared reflectance spectrum of {BN} calculated from first principles. *Solid State Communications*, 141(5):262 – 266, 2007.

[178] Steven Prawer and Robert J. Nemanich. Raman spectroscopy of diamond and doped diamond. *Philosophical Transactions of the Royal Society of London A: Mathematical, Physical and Engineering Sciences*, 362(1824):2537–2565, 2004.

[179] F. P. Bundy and R. H. Wentorf Jr. Direct transformation of hexagonal boron nitride to denser forms. *The Journal of Chemical Physics*, 38(5):1144–1149, 1963.

[180] T. Soma, A. Sawaoka, and S. Saito. Characterization of wurtzite type boron nitride synthesized by shock compression. *Materials Research Bulletin*, 9(6):755 – 762, 1974.

[181] A. V. Kurdyumov, V. L. Solozhenko, and W. B. Zelyavski. Lattice parameters of boron nitride polymorphous modifications as a function of their crystal-structure perfection. *Journal of Applied Crystallography*, 28(5):540–545, Oct 1995.

[182] P.B. Mirkarimi, K.F. McCarty, and D.L. Medlin. Review of advances in cubic boron nitride film synthesis. *Materials Science and Engineering: R: Reports*, 21(2):47 – 100, 1997.

[183] M. I. Eremets, K. Takemura, H. Yusa, D. Golberg, Y. Bando, V. D. Blank, Y. Sato, and K. Watanabe. Disordered state in first-order phase transitions: Hexagonal-to-cubic and cubic-to-hexagonal transitions in boron nitride. *Phys. Rev. B*, 57:5655–5660, Mar 1998.

[184] Vladimir L. Solozhenko, Daniel Häusermann, Mohamed Mezouar, and Martin Kunz. Equation of state of wurtzitic boron nitride to 66 gpa. *Applied Physics Letters*, 72(14):1691–1693, 1998.

[185] Nobuko Ohba, Kazutoshi Miwa, Naoyuki Nagasako, and Atsuo Fukumoto. First-principles study on structural, dielectric, and dynamical properties for three bn polytypes. *Phys. Rev. B*, 63:115207, Mar 2001.

[186] W. J. Yu, W. M. Lau, S. P. Chan, Z. F. Liu, and Q. Q. Zheng. Ab initio study of phase transformations in boron nitride. *Phys. Rev. B*, 67:014108, Jan 2003.

[187] Lili Yu, Bin Gao, Zhi Chen, Chuantao Sun, Deliang Cui, Chengjian Wang, Qilong Wang, and Minhua Jiang. In situ ftir investigation on phase transformations in bn nanoparticles. *Chinese Science Bulletin*, 50(24):2827–2831, 2005.

[188] Eunja Kim and Changfeng Chen. First-principles study of phase stability of bn under pressure. *Physics Letters A*, 319(3):384 – 389, 2003.

[189] Hongbo Wang, Quan Li, Tian Cui, Yanming Ma, and Guangtian Zou. Phase-transition mechanism of h-bn → w-bn from first principles. *Solid State Communications*, 149(21):843 – 846, 2009.

[190] Jun Liu, Yogesh K. Vohra, John T. Tarvin, and Suresh S. Vagarali. Cubic-to-rhombohedral transformation in boron nitride induced by laser heating: In situ raman-spectroscopy studies. *Phys. Rev. B*, 51:8591–8594, Apr 1995.

[191] Surajit Saha, D.V.S. Muthu, D. Golberg, C. Tang, C. Zhi, Y. Bando, and A.K. Sood. Comparative high pressure raman study of boron nitride nanotubes and hexagonal boron nitride. *Chemical Physics Letters*, 421(1–3):86 – 90, 2006.

[192] Surajit Saha, Vikram Gadagkar, Prabal K. Maiti, D. V. S. Muthu, D. Golberg, C. Tang, C. Zhi, Y. Bando, and A. K. Sood. Irreversible pressure-induced transformation of boron nitride nanotubes. *Journal of Nanoscience and Nanotechnology*, 7(6):1810–1814, 2007.

[193] D.V.S. Muthu, A.E. Midgley, E.A. Petruska, A.K. Sood, Y. Bando, D. Golberg, and M.B. Kruger. High-pressure effects on boron nitride multi-walled nanotubes: An x-ray diffraction study. *Chemical Physics Letters*, 466(4–6):205–208, 2008.

[194] Zhaohui Dong and Yang Song. Transformations of cold-compressed multiwalled boron nitride nanotubes probed by infrared spectroscopy. *The Journal of Physical Chemistry C*, 114(4):1782–1788, 2010.

[195] Yue Meng, Ho-Kwang Mao, Peter J. Eng, Thomas P. Trainor, Matthew Newville, Michael Y. Hu, Chichang Kao, Jinfu Shu, Daniel Hausermann, and Russell J. Hemley. The formation of sp3 bonding in compressed bn. *Nat Mater*, 3:111–114, 2004.

[196] Félix Balima, Sylvie Le Floch, Christophe Adessi, Tiago F.T. Cerqueira, Nicholas Blanchard, Raúl Arenal, Annie Brûlet, Miguel A.L. Marques, Silvana Botti, and Alfonso San-Miguel. Radial collapse of carbon nanotubes for conductivity optimized polymer composites. *Carbon*, 106:64–73, 2016.

[197] Ayten Celik-Aktas, Jian-Min Zuo, James F. Stubbins, Chengchun Tang, and Yoshio Bando. Double-helix structure in multiwall boron nitride nanotubes. *Acta Crystallographica Section A*, 61(6):533–541, Nov 2005.

[198] Dmitri Golberg, Pedro M. F. J. Costa, Oleg Lourie, Masanori Mitome, Xuedong Bai, Keiji Kurashima, Chunyi Zhi, Chengchun Tang, and Yoshio Bando. Direct force measurements and kinking under elastic deformation of individual multiwalled boron nitride nanotubes. *Nano Letters*, 7(7):2146–2151, 2007.

[199] Chenguang Zhang, Ksenia Bets, Seung Soo Lee, Zhengzong Sun, Francesca Mirri, Vicki L. Colvin, Boris I. Yakobson, James M. Tour, and Robert H. Hauge. Closed-edged graphene nanoribbons from large-diameter collapsed nanotubes. *ACS Nano*, 6(7):6023–6032, 2012. PMID: 22676224.

[200] Krystian Karch and Friedhelm Bechstedt. Ab initio. *Phys. Rev. B*, 56:7404–7415, Sep 1997.

[201] Alexander F. Goncharov, Jonathan C. Crowhurst, J. K. Dewhurst, and S. Sharma. Raman spectroscopy of cubic boron nitride under extreme conditions of high pressure and temperature. *Phys. Rev. B*, 72:100104, Sep 2005.

[202] Jonathan Garel, Itai Leven, Chunyi Zhi, K.S. Nagapriya, Ronit Popovitz-Biro, Dmitri Golberg, Yoshio Bando, Oded Hod, and Ernesto Joselevich. Ultrahigh torsional stiffness and strength of boron nitride nanotubes. *Nano Letters*, 12(12):6347–6352, 2012. PMID: 23130892.

[203] Xianlong Wei, Ming-Sheng Wang, Yoshio Bando, and Dmitri Golberg. Tensile tests on individual multi-walled boron nitride nanotubes. *Advanced Materials*, 22(43):4895–4899, 2010.

[204] C. A. Schneider, W. S. Rasband, and K. W. Eliceiri. Nih image to imagej: 25 years of image analysis. *Nature Methods*, 9:671–675, 2012.

Carbon nanotubes and boron nitride nanotubes under high pressure

Abstract: This thesis work focuses on the structural stability of well-characterized carbon and boron nitride nanotubes under very high pressures both including their in situ study as well as after the pressure cycle. We try to provide in this way a first approach to determine the role of parameters as composition (C or BN), number of walls or diameter on the limit stability of nanotube structures.

In the two first chapters, we provide a basic description of the theoretical aspects related to carbon nanotubes, we address their main synthesis methods as well as the experimental techniques used in this thesis to study these systems. In the three following chapters, we describe the structural evolution of three systems i) low diameter (6,5) chirality enriched single wall nanotubes ii) triple-wall carbon nanotubes and iii) multiwall boron nitride nanotubes. The maximum pressure attained in these studies were of 80, 72 and 50 GPa respectively.

Both the radial collapse of the structure and the mechanical stability of the tubular structure under very high pressure are addressed in the study. In particular, after their collapse, the low-diameter (6,5) single walled carbon nanotubes can be preserved up to 50 GPa and above this value the tubes undergo an irreversible structural transformation. On its side, the triple wall systems could be detected up to $\sim$ 60 GPa but their transformed irreversibly at 72 GPa. Finally boron nitride tubes have a low mechanical stability when compared with their carbon counterparts. Under high pressures they present transformations at different pressures to a variety of structural morphologies, some of them having been detected for the first time in this work.

Keywords: Carbon nanotubes, Boron nitride nanotubes, Raman spectroscopy, Transmission electron microscopy, High pressures, 1D systems, phase transitions

---

Nanotubes de carbone et de nitrure de bore sous haute pression

Résumé : Dans ce travail de thèse nous avons étudié la stabilité structurale à très haute pression de nanotubes de carbone et de nitrure de bore à la fois in situ et après cycle de pression. Nous essayons de cette manière une première approche pour déterminer le rôle de paramètres comme la composition (C or BN), nombre de parois ou diamètre dans la limite de stabilité de la structure des nanotubes.

Les deux premiers chapitres de la thèse nous permettent de faire une introduction aux aspects fondamentaux relatifs aux propriétés des nanotubes de carbone, suivie d'une présentation des méthodes de synthèse ainsi que des techniques expérimentales utilisées dans cette thèse. Les trois chapitres suivants permettent de présenter l'évolution structurale des trois systèmes étudiés: a) Des nanotubes de carbone monoparois de faible diamètre enrichis en chiralité (6,5), b) nanotubes de carbone triple-parois, et c) des nanotubes de nitrure de bore à parois multiple. Les pressions maximales de ces études ont été de 80, 72 et 50 GPa respectivement.

Le collapse radial de la structure et la stabilité tubulaire des nano-objets ont été au centre de nos recherches. En particulier, les nanotubes de carbone à simple parois de chiralité (6,5) peuvent être préservés jusqu'à 50 GPa, pression à la quelle a lieu une transformation irréversible. De leur côté, les nanotubes à 3 parois ont pu être détectés jusqu'à environ 60 GPa, présentant en suite une transformation irréversible à 72 GPa. Enfin, les nanotubes de nitrure de bore ont montré une plus faible stabilité mécanique face à leurs analogues carbonés. De plus ils présentent une évolution vers toute une variété de morphologies, parmi lesquelles certaines ont été observées pour la première fois dans ce travail de thèse.

Mots clefs : Nanotubes de carbone, nanotubes de nitrure de bore, spectroscopie Raman, Micrcosopie Électronique à Transmission, Hautes Pressions, Systèmes 1D, transitions de phase